UNIVERSIDAD DE GUANAJUATO

CAMPUS IRAPUATO – SALAMANCA
DIVISION DE INGENIERIAS

EXPERIMENTAL STUDY ON THE PERFORMANCE OF A SINGLE SOFC DURING INTERNAL REFORMING

THESIS

TO OBTAIN THE DEGREE OF:

MASTER OF SCIENCE IN MECHANICAL ENGINEERING

PRESENTING:

SILVA MOSQUEDA DULCE MARIA

DIRECTORS:

DR. FRANCISCO ELIZALDE BLANCAS

DR. STEPHEN J. MCPHAIL

SALAMANCA, GUANAJUATO. SEPTEMBER 2019

ABSTRACT

As an interesting integrated system in the framework of distributed power generation, solid oxide fuel cell (SOFC) systems with internal reforming have the potential to become an economically competitive technology, exploiting its significantly higher electrical efficiency compared to existing technologies. Yet, SOFCs high operating temperature enables internal reforming of hydrocarbon fuels, therefore allowing the suppression of external reforming. Evidently, this brings benefits in terms of system complexity, cost reduction and faster load response. Nonetheless, usually direct exposure to large amounts of methane favors SOFC anode degradation. The number and the complexity of the intertwined chemical, electrochemical and thermo-fluid dynamic mechanisms driving the energy conversion of reformate fuels into electrical power and heat call for more accurate analysis tools and techniques that allow for a deeper understanding of the physicochemical processes occurring within the cell, so as to correctly address the role of these mechanisms in the immediate and endurance performance and to overcome most of the degradation issues currently hindering the maturity of this technology.

Therefore, in the present work a combined experimental and numerical investigation towards methane reforming with different gas compositions is presented. Steam methane reforming has been investigated from the perspective of methane conversion, hydrogen yield, power delivered, and cell stability. Different ratios between methane, steam, carbon dioxide, carbon monoxide and hydrogen were used in order to simulate different grades of methane internal reforming in the SOFC.

Experimentally, it is reported an extensive characterization of commercial anode-supported single cells by means of electrochemical impedance spectroscopy (EIS) and the distribution of relaxation times (DRT) method, polarization (I-V) curves and gas composition and temperature analyses in open-circuit voltage (OCV) and under loading conditions for three different reformate compositions. Simultaneous gas and temperature analyses were carried out throughout the anode by means of an in-house built validated spot-sampling set-up. These measurements were carried out *in-operando* conditions, in order to correlate the thermal and chemical phenomena occurring in the anode under determined conditions. Additionally, in order to analyze the effect on the performance and stability of these planar intermediate temperature (IT) SOFC systems under internal reforming, a long-term test has been also carried out. Also in this case, to correlate the evolution in the cell performance with specific thermo-fluid-physicochemical processes, localized gas analyses and temperature measurements were frequently carried out using the very particular and innovative spot-sampling set-up, as well as EIS and I-V curves. The impedance spectra have been also analyzed through the DRT method and the cell study complemented with a post-mortem analysis.

Furthermore, a comprehensive zero-dimensional (0D) model of the tested samples, incorpo-

rating thermodynamic equilibrium and some experimental parameters, has been also validated by confronting the simulated polarization curves with the experimental ones. Thermodynamic equilibrium modeling was employed to determine the concentrations of each gas species in the equilibrium state. This model has demonstrated to be a compelling tool to characterize the performance of the cells while establishing the bases to follow and analyze the effects of potential degradation phenomena and predict the electrical output of the cell under pre-determined operating conditions.

The modeling and experimental results, both, showed that at 650 °C, above 90% of methane conversion is achieved in most of the cases. Furthermore, the experimental data and modeling results are also consistent in the equilibrium approach and the reactions and physicochemical phenomena that occur in the cell under the analyzed conditions.

Hence, a systematic synergistic approach between the experimental measurements, the use of novel analysis tools and techniques –as the deconvolution of impedance spectra by means of the DRT method and *in-operando* gas and temperature analyses –and modeling theory has proved to be instrumental for the estimation of parameters describing the electrochemical properties of planar anode-supported SOFCs, operating in the IT range (650-700°C), and in elucidating the thermochemical phenomena for a better comprehension of the most important reaction processes that determine the performance of the cell. An additional 2D model, based on finite differences and combined with some experimental results, has been also implemented for a mapping of the current density distribution over the anode.

Chemical and thermal mapping of the anode have been obtained under different operating conditions, highlighting the evolution, competition and impact of the different reactions with a spatial resolution. The DRT method applied to EIS measurements allowed the recognition of the single physicochemical processes, their contribution to the overall performances, and the evaluation of degradation effects. Hence, the obtained results have provided a clearer picture of the most important factors or parameters affecting the overall performances of SOFC cells fed with reformate fuels, opening new perspectives for the investigation of SOFC systems.

Nonetheless, this experimental work can be considered as one of the first steps towards understanding the interplay and evolution between various physicochemical phenomena occurring in relatively large-area cells, since these novel *in-situ* and *in-operando* techniques, still limited to few facilities around the world, are still at its early stage, and several testing and technical challenges remain, especially concerning the design. Therefore, some modeling investigations on the system design and thermo-fluids, as well as more experimental testing still need to be carried out.

"Everything will be okay in the end. If it's not okay, then it's not the end"
—John Lennon

ACKNOWLEDGMENTS

Many people deserve a heartfelt thank you now that this project reaches its pinnacle. However, the work hereby presented could not have been written without the advice of my supervisor, Dr. Francisco Elizalde Blancas and the essential support of my co-supervisor, Dr. Stephen J. McPhail, who have taught me professional and personal values that will accompany me forever. Thank you to you both for your project guidance and crucial technical assistance. *If I have seen further it is by standing on the shoulders of giants — Isaac Newton*

A very special thank you to Francesca Santoni, Davide Pumiglia and Carlos Boigues Muñoz, for their superb technical assistance, time, friendship and precious contribution to this thesis with their professional advice.

I also would like to thank Massimiliano Della Pietra, Marco Graziadio and Andi Mehmeti for their warm welcoming from the very first day in ENEA, their friendship and support, which were critical to this study.

Special thanks to my thesis committee. The effort and time you put in to reviewing this work is much appreciated, and your suggestions significantly helped to improved its completeness.

I extend my gratitude to ENEA, UG and CONACYT for giving me this opportunity and providing financial support towards completion of this research.

I would like to dedicate this work and make a special mention to my beloved husband, for placing his trust in me and being there always supporting me, whose love, patience, encouragement and selfless perseverance afforded me the opportunity to pursue my goals. Thank you Juan Pedro Perez Trujillo, for everything you have done for me and for making special every moment of my life with you.

I would also like to express my gratitude towards my family for their great love, with a special mention to my mother for the encouragement, infinity love, and for being always there supporting me towards the completion of this work.

And last but not least, gratitude goes to all my friends, who directly or indirectly helped me to complete this work.

To you all, my gratitude for ever...

Contents

1 INTRODUCTION **1**

1.1 Motivation for the investigation 1

1.2 Objective and scope of the thesis 3

2 FUNDAMENTALS AND LITERATURE REVIEW **5**

2.1 Introduction to fuel cells 5

2.2 Solid oxide fuel cells 7

2.2.1 Operating principles and concepts 7

2.2.2 Reversible cell potential and thermodynamic fundamentals 9

2.2.3 Voltage loss mechanisms 12

2.2.4 Fuel flexibility and internal reforming 14

2.3 Previous research on SOFCs and reformate-fed SOFCs 18

2.3.1 Experimental characterization 18

2.3.2 SOFC Modeling 27

3 BASICS OF THE IMPLEMENTED CHARACTERIZATION TECHNIQUES AND ANALYSIS TOOLS **33**

3.1 Polarization curves 33

3.1.1 Current-voltage measurements 33

3.1.2 I-V characteristics 34

3.2 Electrochemical impedance spectroscopy 36
3.2.1 Principles of EIS 36
3.2.2 EIS measurements on SOFCs 38
3.2.3 Distribution of relaxation times method 42
3.3 Gas chromatography 46
3.4 Other analysis tools 50
3.4.1 SEM and EDS techniques 50

4 EXPERIMENTAL CAMPAIGN, TESTING PROCEDURES AND TEST STATION DESCRIPTION 51

4.1 Internal reforming experimental campaign 51
4.2 Single cell test station and experimental materials 52
4.2.1 Tested samples 52
4.2.2 Multisampling set-up 54
4.3 Cell assembly and testing procedure 58
4.3.1 Cell assembly 58
4.3.2 Single cell testing procedure 61
4.3.3 Experimental conditions for the analysis tools 63
4.4 Multisampling set-up validation 65
4.4.1 Testing conditions 65
4.4.2 Validation results 66
4.5 Testing conditions of the study cases 69
4.5.1 Low internal reforming 69
4.5.2 Intermediate internal reforming 70
4.5.3 Complete internal reforming 71
4.5.4 Long-term operation 72

5 RESULTS AND DISCUSSION **74**

5.1 Experimental results on the internal reforming experimental campaign 74

5.1.1 Electrochemical performance 74

5.1.2 Processes identification from the DRT analysis 82

5.1.3 Gas composition analyses 89

5.1.4 Thermal analysis 116

5.2 Numerical and experimental comparison of the three internal reforming grades . . 130

5.2.1 Comparison with the electrochemical 0D model 131

5.2.2 Current density distribution through the model based on finite differences . 141

5.3 Single cell long-term operation under internal reforming 145

5.3.1 Polarization curves and electrochemical analysis 148

5.3.2 Thermal analysis 154

5.3.3 Gas analyses 157

5.3.4 Post-mortem analysis 160

5.3.5 Effect of the testing procedure on the cell performance 165

6 CONCLUSIONS AND RECOMMENDATIONS FOR FUTURE WORK **167**

6.1 Conclusions 167

6.2 Future work and recommendations 174

Appendices **176**

A MODELS DESCRIPTION **177**

A.1 Electrochemical zero-dimensional model 177

A.1.1 Internal reforming model 178

A.1.2 Electrochemical model 180

A.2 Finite-difference model 184

NOMENCLATURE **187**

CONTRIBUTIONS **192**

Bibliography 193

List of Figures

3.1 *Schematic representation of the I-V characteristics of a SOFC (adapted from Ref. [31]). It indicates the regions in which the different polarization losses (irreversibilities) are predominant.* . . . 35

3.2 *Typical Nyquist plot of a single SOFC under hydrogen operation. Z' represents the real axis and $-Z''$ the imaginary axis.* . . . 39

3.3 *L-curve for Tikhonov Regularization, adapted from [43].* . . . 44

3.4 *Imaginary component of impedance and DRT spectrum, taken from [43].* . . . 45

3.5 *Kramers-Kronig test results for the EIS measurement performed on a tested single cell sample. Red dots are related to the real part of the impedance, while blue dots are related to the imaginary part.* . . . 46

3.6 *Typical chromatogram from a gas analysis.* . . . 48

3.7 *GC system at ENEA research center.* . . . 49

4.1 *Elcogen cells tested in this work, where anode (in green) and cathode (in black) can be distinguished.* . . . 53

4.2 *P & I diagram of the single cell test station.* . . . 54

4.3 *Schematic illustration of the multisampling set-up.* . . . 56

4.4 *Top view of the a) anodic case, b) anodic GDP, where the different coordinates are shown and c) anodic case and GDP showing the distribution of the 11 sampling points and the flow direction.* . . . 57

4.5 *Assembling procedure.* . . . 61

4.6 *Sampling points for the gas analyses: a) cell inlet, b) cell outlet and c) anode.* . . . 65

4.7 *Performance comparison between tested cells via the novel set-up and scaled 15-cell stack obtained in CUTEC lab at a) 650 °C and b) 700 °C.* 67

4.8 *Polarization curves in pure hydrogen of a second-generation Elcogen's single cell obtained using a gold mesh grid as anodic current collector and after system improvements (red line), compared to those obtained from an Elcogen 15-cell stack tested by CUTEC lab, scaled and in the same operating conditions (green line), and a first-generation single cell obtained using a Crofer mesh grid as anodic current collector and previous to the set-up improvements (blue line).* 68

5.1 *Polarization curves comparison at 650 and 700 °C for a) LIR, b) IIR and c) CIR.* . . 75

5.2 *I-V and power density curves comparison for all the compositions at a) 650 °C and b) 700 °C.* 77

5.3 *Electrochemical spectra comparison under LIR, IIR and CIR at a) 650 °C and b) 700 °C.* 79

5.4 *a) EIS and b) DRT comparison at 650 vs 700 °C for IIR composition.* 84

5.5 *a) EIS and b) DRT comparison at 650 vs 700 °C for LIR composition.* 85

5.6 *a) EIS and b) DRT comparison at 650 vs 700 °C for CIR composition.* 86

5.7 *DRT comparison at a) 650 °C and b) 700 °C.* 88

5.8 *Species variation along the cell for LIR at 650 °C and a) OCV, b) 15 A and c) 30 A.* 90

5.9 *Compositions comparison at OCV, 15 A and 30 A along the cell for LIR at 650 °C for a) H_2, b) H_2O, c) CH_4, d) CO and e) CO_2.* 92

5.10 *Species distribution throughout the cell for LIR at OCV and 650 °C: a) H_2, b) H_2O, c) CH_4, d) CO and e) CO_2.* 93

5.11 *Species distribution throughout the cell for LIR at 15 A and 650 °C: a) H_2, b) H_2O, c) CH_4, d) CO and e) CO_2.* 95

5.12 *Species distribution throughout the cell for LIR at 30 A and 650 °C: a) H_2, b) H_2O, c) CH_4, d) CO and e) CO_2.* 97

5.13 *Species variation along the cell for IIR at 650 °C and a) OCV, b) 15 A and c) 30 A.* 100

5.14 *Compositions comparison at OCV, 15 A and 30 A along the cell for IIR at 650 °C for a) H_2, b) H_2O, c) CH_4, d) CO and e) CO_2.* 101

5.15 *Species distribution throughout the cell for IIR at OCV and 650 °C: a) H_2, b) H_2O, c) CH_4, d) CO and e) CO_2.* . . . 102

5.16 *Species distribution throughout the cell for IIR at 15 A and 650 °C: a) H_2, b) H_2O, c) CH_4, d) CO and e) CO_2.* . . . 104

5.17 *Species distribution throughout the cell for IIR at 30 A and 650 °C: a) H_2, b) H_2O, c) CH_4, d) CO and e) CO_2.* . . . 106

5.18 *Voltage fluctuations comparison during time for CIR at 650 °C and a) 15 A and b) 30 A.* . . . 109

5.19 *Species variation along the cell for CIR at 650 °C and a) OCV, b) 15 A and c) 25 A.* 110

5.20 *Compositions comparison at OCV, 15 A and 25 A along the cell for CIR at 650 °C for a) H_2, b) H_2O, c) CH_4, d) CO and e) CO_2.* . . . 111

5.21 *Species distribution throughout the cell for CIR at OCV and 650 °C: a) H_2, b) H_2O, c) CH_4, d) CO and e) CO_2.* . . . 112

5.22 *Species distribution throughout the cell for CIR at 15 A and 650 °C: a) H_2, b) H_2O, c) CH_4, d) CO and e) CO_2.* . . . 113

5.23 *Species distribution throughout the cell for CIR at 25 A and 650 °C: a) H_2, b) H_2O, c) CH_4, d) CO and e) CO_2.* . . . 115

5.24 *LIR temperature profiles comparison at a) OCV-650 °C, b) OCV-700 °C, c) 15 A-650 °C and d) 30 A-650 °C.* . . . 117

5.25 *LIR contour-plot comparison at 650 °C and a) OCV, b) 15 A and c) 30 A.* . . . 119

5.26 *IIR temperature profiles comparison at a) OCV-650 °C, b) OCV-700 °C, c) 15 A-650 °C and d) 30 A-650 °C.* . . . 120

5.27 *IIR contour-plot comparison at 650 °C and a) OCV, b) 15 A and c) 30 A.* . . . 121

5.28 *CIR temperature profiles comparison at a) OCV-650 °C, b) OCV-700 °C, c) 15 A-650 °C and d) 25 A-650 °C.* . . . 123

5.29 *CIR contour-plot comparison at 650 °C and a) OCV, b) 15 A and c) 25 A.* . . . 124

5.30 *Contour-plot comparison at 650 °C and OCV for a) LIR, b) IIR and c) CIR.* . . . 125

5.31 *Contour-plot comparison at 700 °C and OCV for a) LIR, b) IIR and c) CIR.* . . . 126

5.32 *Contour-plot comparison at 650 °C and 15 A for a) LIR, b) IIR and c) CIR.* . . . 127

5.33 *Contour-plot comparison at 650 °C and 30 A for a) LIR, b) IIR and c) CIR.* 128

5.34 *Zero dimensional algorithm.* 131

5.35 *Numerical and experimental comparison of the polarization curves at 650 °C for a) LIR, b) IIR, and c) CIR.* 132

5.36 *Numerical and experimental comparison of the different overpotentials at 650 °C for a) LIR, b) IIR, and c) CIR.* 133

5.37 *Numerical and experimental comparison of the polarization curves at 700 °C for a) LIR, b) IIR, and c) CIR.* 134

5.38 *Numerical and experimental comparison of the different overpotentials at 700 °C for a) LIR, b) IIR, and c) CIR.* 135

5.39 *Molar rate of CH_4 reacting as a function of current density at a) 650 °C and b) 700 °C according to the equilibrium constant of the internal reforming reaction.* 136

5.40 *Molar rate of CO reacting as a function of current density at a) 650 °C and b) 700 °C according to the equilibrium constant of the water-gas shift reaction.* 137

5.41 *Numerical and experimental comparison of the cell electrical power, and efficiency at 650 and 700 °C for a) LIR, b) IIR and c) CIR.* 139

5.42 *MATLAB algorithm, part 1.* 141

5.43 *MATLAB algorithm, part 2.* 142

5.44 *Numerical current density distribution throughout the cell for LIR at 650 °C and a) 15 A and b) 30 A.* 143

5.45 *Numerical current density distribution throughout the cell for IIR at 650 °C and a) 15 A and b) 30 A.* 144

5.46 *Numerical current density distribution throughout the cell for CIR at 650 °C and a) 15 A and b) 25 A.* 145

5.47 *Cell voltage variation with some representative events during its operation at 248 $\mathrm{mA \cdot cm^{-2}}$ ($FU = 43\%$) and 650 °C.* 146

5.48 *Polarization curves recorded during the test and corresponding to the fuel flow composition specified in Table 4.10.* 148

5.49 *Nyquist plots or EIS at OCV condition recorded during all the characterizations, showing mainly a big increase in the intermediate frequency arc.* 150

5.50 *Increase of the internal and polarization electrical resistance over time, obtained from the impedance spectra.* 151

5.51 *Individual increase of the overpotentials with time.* 152

5.52 *DRT identification processes according to [30, 90, 94], where the most significant difference is found for the cathode-related processes.* 153

5.53 *Temperature profiles of the 11 sampling points in the anode during the stability test. For the distribution of the sampling points throughout the anode, please refer to Fig. 4.4.* 155

5.54 *Cell voltage and average anode temperature during the test in OCV and at* 248 $\mathrm{mA/cm^2}$. 155

5.55 *Experimental temperature contours at a) OCV-0h, b) OCV-460h, c) 30A-0h, and d) 30A-460h.* 157

5.56 *Concentration temporal and spatial variation under load and at OCV; a) H_2 variation, b) H_2O variation, c) CH_4 variation.* 159

5.57 *SEM micrographs of the anode functional layer after the test. Note that no significant microstructural changes developed during the test.* 160

5.58 *EDS results after the test of Sr segregation/diffusion and chromium poisoning, corresponding to the central section of the a) LSC cathode surface, and b) cross-section, both corresponding to the region 4 indicated in the images.* 161

5.59 *EDS results after the long-term test corresponding to the outlet cross-section.* . . . 162

5.60 *Cell cracks at the outlet corners showing a particular pattern on the failure mode.* . 163

5.61 *Cathode gas diffusion plate (GDP) after the test showing the same two corresponding rusty zones to those with the zone failure/cracks.* 164

A.1 *Schematic representation of the anode discretization.* 185

List of Tables

3.1 Characteristics of the columns according to the different detectors of the GC system. 49

4.1 Internal methane reforming experimental campaign. 52

4.2 Technical data of the new generation anode-supported cells (ASC-400B) from Elcogen AS. 53

4.3 Reference composition ("H_2 reference") used during the experimental campaign. . 64

4.4 CUTEC composition tested for the test bench validation. 66

4.5 LIR or reformate syngas no AOGR composition. 69

4.6 Experimental conditions under which the analysis techniques are implemented for the LIR and IIR compositions. 70

4.7 IIR or reformate syngas AOGR composition. 70

4.8 CIR composition. 71

4.9 Experimental conditions under which the analysis techniques are implemented for the CIR composition. 72

4.10 Tested IIR gas composition and cell operating temperature during the long-term test. 73

5.1 Cell performance and EIS results at both temperatures for the three tested compositions. 81

5.2 Comparison of the measured and calculated inlet and outlet compositions for LIR at OCV, 15 A and 30 A. 98

5.3 Comparison of the measured and calculated inlet and outlet compositions for IIR at OCV, 15 A and 30 A. 107

5.4 Comparison of the measured and calculated inlet and outlet compositions for CIR at OCV, 15 A and 25 A. 116

5.5 Summary of the thermal analysis for the three analyzed compositions at the three loading conditions. 129

5.6 Comparison of the outlet gas compositions for the three analyzed compositions at 15 A and 650 °C. 138

Chapter 1

INTRODUCTION

1.1. Motivation for the investigation

It has been internationally established that in the coming decades world oil reserves will rapidly decline, which will result in a strong impact on the economy of those countries that have not developed alternative energy generation technologies. As a part of this scenario, a radical change in the global energy sector and the transition from an oil-based economy to a hydrogen-based economy has been proposed in various scientific circles [1, 2].

Furthermore, the actual world energy system is facing even more critical challenges [3]. The historical combination of oil-derived fuels and combustion engines requires urgent alternatives to meet the 2 °C global warming limit recently defined [4]. The development of more efficient and environmentally friendly energy sources has gained vital importance to avoid a legacy of irreversible environmental damage for future generations.

In recent years, great efforts have been made to reduce the impact of human activity on the environment and reduce the amount of pollutants in the atmosphere. The efforts have covered several scientific and technological aspects, including the use of alternative fuels that have become essential [4–8], and the development of new power generation systems, which do not pose a risk to the environment. These systems must satisfy the requirements of zero - or very low - emissions of polluting waste into the atmosphere and to have high conversion efficiencies [9]; i.e. they need to become more flexible and nimble while fulfilling the obligations set by the directives on the use of renewable forms of energy, the reduction of carbon dioxide emissions, and fuel consumption in traffic.

In the outlook of the transition to the carbon-free society, researchers show much interest in fuel

cells, and more particularly in solid oxide fuel cells (SOFCs). This interest is driven by technical, and environmental advantages offered by these devices including the quest for higher performance characteristics, efficiencies, reliability, durability and clean power generation.

However, the attractiveness of a SOFC relates principally to its solid-state nature, high operating temperature and fuel flexibility. Thanks to the advantages in thermodynamics and kinetic terms related to the temperature effects, the SOFC technology can widely compete with other type of cells [10]. The high operating temperature and its fuel flexibility, owed to the catalytic activity of the anode materials, allow for internal reforming of hydrocarbons or hydrocarbon-derived fuels, which can be directly reformed into hydrogen-rich gases inside the cell by using the heat generated through the electrochemical reactions, eliminating the requirement for a separate fuel reformer, generating high-quality heat for energy conversion or other uses, thus increasing the system efficiency, simplifying the overall system design, and improving the process economics [9, 11].

Amongst hydrocarbon fuels, methane has attracted much attention for direct operation of SOFCs, being the most studied alternative fuel due to availability and possible internal reforming. As the simplest hydrocarbon, methane is the principal component of natural gas [7]. Natural gas is a key energy vector in all the world, since it is a widely available fuel and it possesses lesser challenges than heavier hydrocarbons [4, 12, 13]. However, other advantages that methane fuel in SOFCs possess are the increased efficiency, its production through renewable sources, and the absence of combustion avoiding emissions (e.g., NOx, SOx) as well as its coupling with carbon capture and storage technologies to prevent the CO_2 emissions to the atmosphere.

Nonetheless, direct exposure to large amounts of methane favors SOFC anode degradation [14–17]. Fuel flexibility in SOFCs possesses problems in terms of their thermal management and non-homogeneity of the chemical gradients. Because steam reforming is a strongly endothermic reaction, it may cause severe temperature gradients in the cell. Nonuniform temperature distributions not only lead to the cracking of the ceramic materials in the SOFC but also accelerate the degradation of the cell.

Additionally, a key technical issue that has limited the development and deployment of this transformative technology is its high operating temperature, resulting in higher systems costs and performance degradation rates, as well as slow start-up and shutdown cycles, this latter limiting dramatically its applicability in portable power and transportation markets.

Over the past decade, there has been a strong drive to lower the operating temperature of the SOFCs, and considerable progress has been achieved in bringing the temperature down to an intermediate temperature range, from 600 to 800°C [6, 16, 18–20]. However, the main difficulty with intermediate temperature solid oxide fuel cells (IT-SOFCs) is the significant decline in performance, mainly owed to lower ion conduction of the electrolyte, and to a strong cathode polarization [18].

Besides, even at these temperatures, materials are not immune to corrosion and reaction with other cell components, facing problems of chemical stability of various cell components.

Solid oxide fuel cells have not yet evolved to current megawatt-scale commercial power plants because their still existing limitations [21]. However, when operating SOFCs under internal reforming, they provide a promising option for energy production, improving the economic benefits. Stable and safe operation of SOFC systems fed with syngas is currently an issue, the endurance performance of the cell can be hindered, even to the point of critical failure. The number and the complexity of the intertwined chemical, electrochemical and thermo-fluid dynamic mechanisms driving the energy conversion of syngas into electrical power and heat call for more accurate analysis tools and techniques so as to correctly address the role of these mechanisms in the immediate and endurance performance, and thus going beyond the state-of-art.

In this context, *in-operando* analysis tools are potentially suitable techniques, still limited to few facilities around the world [22], for a real-time analysis allowing to follow local changes, that complemented with other techniques, can improve our understanding on the fuel cells mechanisms and reforming processes.

To this day, the progress for a further improvement of anode supported cells has been partly constrained by an incomplete understanding of the multi-physics phenomena occurring in the anode while internal reforming as well as the physical origin and share of the individual polarization processes controlling the cell performance. Little is known about the complex interfacial electrochemistry and thermochemistry, the physicochemical processes occurring within the cell and it is also difficult to diagnose problems and optimize cell performance [23–25]. Therefore, optimal design and operation of SOFCs systems with internal reforming still require experimental testing that include an accurate description of reforming processes, as well as a lot of improvements concerning the SOFC research in order to understand the underlying mechanisms of SOFCs and to overcome most of the degradation issues currently hindering the maturity of this technology.

1.2. Objective and scope of the thesis

By carrying out experiments *in-situ* and *in-operando* conditions via a very particular set-up that allows for localized gas compositions and temperature measurements throughout the anode, the present study aims to evaluate the electrochemical performance and thermochemical behavior on commercial planar-type anode-supported IT-single SOFCs during internal reforming of methane.

This should lead to a detailed mapping of the temperature and composition on the anode, and in turn, to better insights of how the reactions proceed across the SOFC for an accurate description

of the reforming process; resulting in an in-depth comprehension of the physicochemical processes occurring within the cell and their effect on the overall performances, as well as the thermal and chemical gradients arising during the operation, and the degradation effects caused by a long-term operation.

This study further aims to numerically and experimentally compare the performance of these commercial intermediate-temperature cells running under three different grades of internal reforming, namely: low internal reforming, intermediate internal reforming and complete internal reforming; in order to determine under which conditions it is possible to achieve the best tradeoff in terms of syngas/H_2 production (within the cell), electrical power generation and degradation rate of the cell.

Chapter 2

FUNDAMENTALS AND LITERATURE REVIEW

2.1. Introduction to fuel cells

A fuel cell is an electrochemical energy-conversion device which directly converts the chemical energy of a fuel into useful electrical energy with water and heat as by-products [10, 26]. The basic reactants (hydrogen and oxygen) power the electrochemical reaction. Although fuel cells can not store chemical energy, unlike batteries, they can produce power continuously as long as fuel and oxygen are available [27].

The electrochemical combination of reactants takes place in stages on separate porous electrodes: anode and cathode. An ion-conducting electrolyte, separating the two electrodes, allows the flow of charged ions formed by the reaction from one electrode to the other to maintain the overall charge balance. It also provides a physical barrier to prevent the mixing of the fuel and oxidant gas streams and prevents the two electrodes to come into electronic contact by blocking the electrons [23]. The reduction reaction of oxygen, at the cathode, and the oxidation of fuel, at the anode, give rise to a potential difference (voltage), which drives the electrons through an external load. The ions, from the cathode, diffuse and migrate through the electrolyte to complete the electrical circuit in the cell.

By avoiding the highly irreversible direct combustion as an intermediate step, this electrochemical process is inherently efficient and much cleaner than combustion technologies, actually, depending on the fuel source, produces zero or near-zero polluting emissions. Among other benefits that fuel cells provide, these include lower maintenance costs, high reliability, silent operation, and high-quality uninterrupted power. Furthermore, since the electrical energy is converted directly

from the chemical energy in the fuel cell, this latter is not limited by the thermodynamic limit of the Carnot cycle. Hence, fuel cells can, at least theoretically, achieve a higher efficiency than the internal combustion processes [26, 28].

Fuel cells are a unique technology that can fit into a range of categories –primary, backup, or off-grid power generation scaled to fit any need (ranging from kilowatts to megawatts), as well as power for motive operations– and provide a wide range of benefits. A benefit of fuel cells that has been extremely attractive lately is that they operate in water balance. Fuel cells do not require any external water [12, 29], as all the water needed is generated and utilized within the system.

Fuel cells are generally classified by the chemical characteristics of the electrolyte employed, because the electrolyte determines the kind of chemical reaction taking place in the cell. Thus, today, there are six main different types [10]: Proton Exchange Membrane Fuel Cell (PEMFC), Direct Methanol Fuel Cell (DMFC), Alkaline Fuel Cell (AFC), Phosphoric Acid Fuel Cell (PAFC), Molten Carbonate Fuel Cell (MCFC) and Solid Oxide Fuel Cell (SOFC). However, the DMFC is named after the fuel instead of the electrolyte and is sometimes a subcategory of the PEMFC. Each of them works on the same principle and performs the same purpose, i.e., converting hydrogen and oxygen into electrical power and sometimes heat.

Based on the working temperature, fuel cells are also categorized into low and high-temperature. The SOFC and the MCFC belong to the high-temperature fuel cells.

By far the greatest research interest throughout the world has been focused on proton exchange membrane and solid oxide fuel cells. However, SOFCs offer significant further advantages compared to other types of fuel cells with respect to their fuel flexibility. While the more common PEMFCs require hydrogen fueling, solid oxide fuel cells can oxidize essentially any fuel [18,30,31], from hydrogen to hydrocarbons or hydrocarbon-derived fuels to even carbon .

In addition to their fuel flexibility, the high operating temperature (600°C- 1000°C) allows for internal reforming, this is, hydrogen can be directly produced from hydrocarbon fuels in the interior of the SOFCs thanks to the high catalytic activity of the anode materials (Nickel content) along with their low susceptibility; promoting rapid electro-catalytic reactions with non-precious metals and producing high quality byproduct heat for co-generation. Therefore, regarding the efficiency of SOFC systems under these premises, the efficiencies can reach up to 70% [23], making SOFCs extremely useful in large, high-power applications such as full-scale industrial stations and large-scale electricity-generating stations.

The key technical issue that has limited the development and deployment of this transformative technology is, in fact, its high operating temperature, resulting in higher systems costs and performance degradation rates, as well as slow start-up and shutdown cycles, this latter limiting dramat-

ically its applicability in portable power and transportation markets. Over the past decade, there has been a strong drive to lower the operating temperature of SOFCs, and considerable progress has been achieved in bringing the temperature down to an intermediate temperature range of 600 to 800°C [18, 20]. However, the main difficulty with IT-SOFCs is the significant decline in performance, mainly owed to lower ion conduction of the electrolyte, and to a strong cathode polarization. Besides, even at these temperatures, materials are not immune to corrosion and reaction with other cell components, facing problems of chemical stability of various cell components.

2.2. Solid oxide fuel cells

2.2.1. Operating principles and concepts

The solid oxide fuel cell, as the name suggests, relies on a complete solid-state structure that uses an oxide ceramic material as electrolyte. The conventional SOFCs operate at high temperature (above 700 or 800°C) in order to enable diffusion of O^{2-} through the electrolyte.

Owed to the high operating temperatures, they do not require noble catalysts to activate the reaction. Nevertheless, SOFC technology is very demanding from a materials standpoint. SOFCs are composed of all-solid-state materials, and this solid-state character puts no fundamental restriction on the cell configuration. Fuel cells are being designed and constructed in several ways, however, the most common geometries are planar and tubular [23, 32]. In addition, depending on the supporting layer, there are four types of planar SOFCs: electrolyte-supported, anode-supported, cathode-supported and, the more recently developed, metal-supported [33]. Each configuration has its strengths and limitations. However, concerning the first three types, anode-supported cells tend to show the best performance; allowing for significantly thinner electrolytes and thus, considerably reducing the overall internal resistance of the cell. This type of cells, also, have allowed to reduce operating temperatures to the intermediate temperature range [18]. Thus, anode-supported cells are being intensively developed by both industrial and academic researchers. Nevertheless, the mechanical properties and stability of this type of cells tend not to be satisfying because cracking or delamination related to thermal gradients and mechanical stresses can sometimes be an issue [32].

A SOFC consists of three major components: two porous electrodes (cathode and anode) and a hard-ceramic and nonporous electrolyte with conductivity-based O^{2-}. The vast majority of SOFCs use a zirconia-based electrolyte, typically yttria-stabilized zirconia (YSZ), because of its superior stability. Although it is a good oxygen-ion conductor, it is far from having the highest conductivity. It is well known that there are many interesting and sometimes highly compelling alternative SOFC electrolyte, anode, and cathode materials, however, the discussions of SOFCs materials are mainly

focused on YSZ-based electrolytes in combination with Ni-YSZ anodes and lanthanum strontium manganite (LSM) cathodes, since these materials meet most of the electrode requirements. A general overview of the most common SOFC electrolyte, electrodes, and catalyst materials highlights the dual requirement for high performance and high stability of the SOFC materials. Any fuel cell material candidate (whether it is an electrolyte, electrode, or catalyst material) must not only deliver high performance but also be stable and durable in the fuel cell environment [23, 27]. However, because fuel cell environments are often quite harsh, meeting these dual requirements is challenging.

The operation principle of a SOFC involves reduction of molecular O_2 at the cathode, diffusion of the resulting O^{2-} through the electrolyte, and oxidation of the fuel by oxygen ions at the anode. On the anode side, the gaseous fuel, usually H_2, is oxidized, and two electrons are released, Eq. (2.1). The electrons flow through the external electrical circuit to be used as power. On the cathode side, oxygen, usually carried by air, reacts with incoming electrons, and ions O^{2-} are formed, Eq. (2.2). The oxygen ions migrate through the electrolyte and combine with hydrogen on the anode side, Eq. (2.1), to form water.

Hence, the electrochemical processes on the anode and cathode side can be expressed as follows:

$$H_2 + O^{2-} \longrightarrow H_2O + 2e^- \,(\text{anode}) \tag{2.1}$$

$$\frac{1}{2}O_2 + 2e^- \longrightarrow O^{2-} \,(\text{cathode}) \tag{2.2}$$

Combining the two half reactions, Eq. (2.1) with Eq. (2.2), the overall electrochemical reaction can thus be described as follows:

$$H_2 + \frac{1}{2}O_2 \longrightarrow H_2O \qquad \Delta H^0_{298K} = -286\,\text{kJ}\cdot\text{mol}^{-1} \tag{2.3}$$

The electrochemical reaction of hydrogen, Eq. (2.3), is an exothermic reaction.

For hydrocarbon fuels, usually the electrochemical reaction of hydrogen is taken into account by assuming that methane is consumed only in the steam-reforming process and the carbon monoxide in the subsequent water-gas shift reaction, and not in the electrochemical reaction [34].

It is widely reported that the electrochemical reactions mainly occur at the triple-phase boundary (TPB). The TPB is assumed to be located at the electrode/electrolyte interfaces on which the electrochemical reactions take place and where the electrode, the electrolyte and the gas phase meet.

TPB characteristics have a large influence on the electrochemical performance of the cell since it is thought as the active area. Some studies have estimated that the TPB region has a limited extension of 5-20 μm from the electrolyte surface [35, 36], while others report a very thin zone within 1 μm from the electrode/electrolyte interface. Consequently, in electrode-supported cell modelling the TPB is frequently assumed as a layer of negligible thickness at the interface.

2.2.2. Reversible cell potential and thermodynamic fundamentals

In a perfect world, we could harness all of the enthalpy released by a chemical reaction to do useful work. Unfortunately, thermodynamics tells us that this is not possible. Only a portion of the energy evolved by a chemical reaction can be converted into useful work. For electrochemical systems (e.g., fuel cells), the Gibbs free energy (G) gives the maximum amount of energy that is available to do electrical work, thus representing the exploitable energy potential, or work potential, of the system.

As the Gibbs free energy –which is a function of state– is the key to the work potential of a reaction, it is necessary to give its mathematical definition, which is:

$$G = H + TS \tag{2.4}$$

Differentiating this expression, holding temperature constant (isothermal process, $dT = 0$) and writing this relationship in terms of molar quantities:

$$\Delta\hat{g} = \Delta\hat{h} + T\Delta\hat{s} \tag{2.5}$$

Thus, for an isothermal reaction, $\Delta\hat{g}$ can be computed in terms of $\Delta\hat{h}$ and $\Delta\hat{s}$.

Then, the maximum amount of electrical work per mole unit that a system can perform in a constant-temperature, constant-pressure process is given by the negative of the Gibbs free-energy difference for the process. For a reaction, this equation can be written as:

$$\frac{W_{elect}}{n_{rxn}} = -\Delta\hat{g}_{rxn} \tag{2.6}$$

The constant-temperature, constant-pressure assumption used to obtain this expression is not really as restrictive as it seems. The only limitation is that the temperature and pressure do not vary during the reaction process. In fact, it is important to realize that Eq. (2.6) is valid for different

values of temperature and pressure as long as these values are not changing during the reaction process [27]. Since fuel cells at steady state usually operate under isobaric (constant-pressure) and isothermal (constant-temperature) conditions, its use is reasonable.

On the other hand, the potential of a system to perform electrical work is measured by voltage (also called electrical potential). Then, the theoretical maximum potential difference in a fuel cell is given by the reversible cell potential, which is obtained under thermodynamically reversible conditions.

As any other chemical or electrochemical device, fuel cells are driven by reactions involving consumption of reactants and generation of products. Hence, consider Eq. (2.7), which represents a generic reaction involving two reactants and two products:

$$b\mathrm{B} + c\mathrm{C} \rightleftharpoons m\mathrm{M} + n\mathrm{N} \tag{2.7}$$

where b, c, m, and n are the stoichiometric coefficients of the reactant species B and C, and of the products M and N, respectively.

In the chemistry field, the Gibbs free energy also expresses the tendency of a reaction to occur under constant temperature and pressure conditions, i.e., the spontaneity of a reaction. When $\Delta G < 0$ the reaction is said to be spontaneous (energetically favorable) hence it is shifted towards the products formation, when $\Delta G = 0$ the reaction is in equilibrium, and when $\Delta G > 0$ the reaction is nonspontaneous (energetically unfavorable) and is shifted towards the formation of reactants.

Although spontaneous reactions are energetically favorable, spontaneity is not a guarantee that a reaction will occur, nor either indicates how fast it will occur. Many spontaneous reactions do not occur because they are impeded by kinetic barriers. The rate at which electricity can be produced from a fuel cell is limited by several kinetic phenomena. Thus, it is necessary to understand how the electrical work capacity of a fuel cell is translated into a cell voltage.

When the amounts (concentrations) of chemical species in a fuel cell are changed, the free energy of the system is also changing. This change in free energy in turn changes the reversible voltage of the fuel cell. The chemical potential measures how the Gibbs free energy of a system changes. However, since the chemical potential is related to concentration through activity a, the Gibbs free energy can be expressed in terms of the activities of the reactants and products, namely:

$$\Delta\hat{g} = \Delta\hat{g}^0 + RT \ln\left(\frac{a_M^m \cdot a_N^n}{a_B^b \cdot a_C^c}\right) \tag{2.8}$$

Where $\Delta\hat{g}^0$ is the standard-state molar free-energy change for the reaction (representing the lumped standard-state chemical potential terms), R is the ideal gas constant, T the operating temperature, the subscript represents the species involved in the electrochemical reaction, and the superscript its stoichiometric coefficient.

For electrochemical devices, and thus for electrochemical reactions, the electrical potential difference E between two electrodes is related to $\Delta\hat{g}$ by the following equation:

$$\Delta\hat{g} = -n_e F E \tag{2.9}$$

where n_e is the number of electrons transferred in the reaction and F is the Faraday's constant.

Combining Eq. (2.8) and Eq. (2.9) allows to see how the reversible cell voltage varies as a function of chemical activity:

$$E = -\frac{\Delta\hat{g}^0}{n_e F} - \frac{RT}{n_e F}\ln\left(\frac{a_M^m \cdot a_N^n}{a_B^b \cdot a_C^c}\right) \tag{2.10}$$

The high operating temperatures of SOFCs (700-900 °C) and the relatively low operating pressures (1-3 bar) allow to approximate the behavior of the gas species or chemical components as an ideal behavior, i.e. as ideal gases [28, 37]. Since the activity of the species depends on its chemical nature, consequently, for an ideal gas, the chemical activity can be computed as $a_i = p_i/p_{std}$, where p_i is the partial pressure of the gas species i and p_{std} is the standard-state pressure (1 atm). Thus, considering the overall reaction for the oxidation of H_2 reported in Eq. (2.3), where $n_e = 2$, the OCV takes on the following expression [38]:

$$E_N = -\frac{\Delta G^0}{2F} - \frac{RT}{2F}\ln\left[\frac{y_{H_2O}}{y_{H_2} \cdot y_{O_2}^{0.5}}\left(\frac{p}{p_{std}}\right)^{-0.5}\right] \tag{2.11}$$

Although Eq. (2.11) should be used to determine the OCV, an equivalent and simplified form of this expression, expressed in terms of the partial pressures of the gas species involved in the electrochemical reaction, is generally used instead [27, 39]. However, such an expression should be carefully used, since it arises when accepting $p_{std} = 1atm$ and thus $a_i = p_i$. Hence, Eq. (2.10) becomes:

$$E_N = -\frac{\Delta G^0}{2F} - \frac{RT}{2F}\ln\left(\frac{p_{H_2O,bulk}}{p_{H_2,bulk} \cdot p_{O_2,bulk}^{0.5}}\right) \tag{2.12}$$

where $p_{k,bulk}$ denotes the partial pressure of species i in the bulk composition, i.e. the composition under open-circuit voltage.

This important result is known as the Nernst equation. The Nernst equation outlines how reversible electrochemical cell voltages vary as a function of species concentration, gas pressure, and so on; thus, giving the maximum theoretical potential difference in an electrochemical device, i.e. the theoretical maximum voltage that a cell could achieve given a specific set of operating conditions. This equation is the centerpiece of fuel cell thermodynamics.

Therefore, the theoretical OCV of a fuel cell can be calculated by assessment of the Nernst potential, Eq. (2.11) or Eq. (2.12). However, because the OCV is a measurement of the potential that develops between the anode and the cathode when there is zero net current, at OCV, theoretically there are no products being formed as there is no net oxygen ions transfer across the electrolyte. According to Eq. (2.11) and/or Eq. (2.12), as the partial pressure of the reactants approach 0, the Nernst potential tends to infinity, making the Nernst potential of dry hydrogen at OCV undefined. However, in reality the OCV is limited by the amount of O_2 leaking into the anode chamber forming water. Very small variations in oxygen partial pressure at the anode result in a large change in the OCV of the cell [40]. Because of this, humidified H_2 (typically 0.97% H_2 / 3% H_2O, mole basis) is used since the presence of H_2O at the anode defines the Nernst potential.

2.2.3. Voltage loss mechanisms

When a fuel cell is loaded with an electric current, i.e., under operating conditions, the cell is affected by several irreversible processes which induce potential losses, decreasing the cell voltage below the thermodynamically predicted (Nernst-voltage). This is, the cell potential is reduced from the theoretical OCV by internal irreversible overpotentials which depend on the current and derive mainly from the following three mechanisms [23]:

1. *Ohmic overpotential:* It occurs principally during the transport of oxygen ions across the electrolyte and electronic transport in electrodes and metallic interconnects. It is caused by the ionic and electrical resistances through the conducting materials within the cell.
   The overall ohmic resistance, R_{ohm}, is the sum of each individual ohmic contribution (ionic, electronic, and contact resistance). According to Ohm's law, the ohmic overpotential, η_{ohm}, linearly increases with the current density j as:

$$\eta_{ohm} = j \cdot R_{ohm} \tag{2.13}$$

   However, in planar SOFCs, the main contribution to ohmic losses is due to the solid electrolyte. Therefore, it is generally valid to consider the main ohmic contribution to the voltage

loss equal to that related to the solid electrolyte [41]. Unlike electrolyte-supported cells where the electrolyte thickness takes on values of up to 200 µm, the electrolyte thickness in anode-supported cells usually is only around 10 µm. Therefore, the ohmic resistance can be reduced, still rendering possible the operation of this configuration in the IT range [42].

2. *Activation overpotential:* It is associated with overcoming the energy barriers at the electrochemically active sites (TPB) which prevent reactions taking place spontaneously. Thus, the larger the activation energy, the bigger the energy supply needed from the reactants to surpass these barriers. However, the higher the temperature, the higher the probability for reactants to gain the necessary activation energy, and thus reducing the overpotentials.
   A commonly used equation for describing the influence of activation overpotential on current density is the well-known Butler-Volmer equation [27, 43]:

$$j = j_{0,el}\left[exp\left(\alpha_{el}\frac{n_e F \eta_{act,el}}{RT}\right) - exp\left(-(1-\alpha_{el})\frac{n_e F \eta_{act,el}}{RT}\right)\right] \tag{2.14}$$

   where $j_{0,el}$ is the exchange current density of the corresponding electrode (anode or cathode), which is dependant on the partial pressure and temperature and are in turn, defined applying an Arrhenius-type equation for both anode and cathode exchange current densities, n_e represents the number of transferred electrons (in this case $n_e = 2$), α_{el} the charge transfer coefficient at the electrode, and $\eta_{act,el}$ the activation overpotential of the corresponding electrode (anode or cathode). The charge transfer coefficient is an indicator of the symmetry of the activation energy barrier when a positive or negative overpotential is applied [27].

3. *Concentration overpotential:* It occurs at high current densities or high fuel utilizations, the requirement for reactants in the active zones (TPB) exceeds the gas capability of diffusing through the porous electrodes to these active sites, resulting in an undersupply of fuel or oxygen causing a plummet in the cell voltage. This is caused by slow diffusion from the bulk of the gas through the porous electrodes.
   By applying Ficks first law and based on the Nernst-equation, the concentration-based voltage drop, $\eta_{conc,el}$, can be estimated as [41, 42]:

$$\eta_{conc,an} = \frac{RT}{2F}\ln\left(\frac{1 + \dfrac{RTL_{an}}{2FD^{eff}_{H_2O}p_{H_2O,an}P_0}\cdot j}{1 - \dfrac{RTL_{an}}{2FD^{eff}_{H_2}p_{H_2,an}P_0}\cdot j}\right) \tag{2.15}$$

$$\eta_{conc,cat} = \frac{RT}{4F} \ln \left(\frac{1}{1 - \frac{RTL_{cat}\left(1 - p_{O_2,cat}/p\right)}{4FD_{O_2}^{eff} p_{O_2,cat} P_0} \cdot j} \right) \tag{2.16}$$

where L_{an} and L_{cat} denote the effective thickness of the diffusion layer on the anode and cathode side respectively. D_i^{eff} is the effective molecular diffusion coefficient, which is a function of the microstructural properties (pore-size, porosity and tortuosity) of the underlying diffusion layer. The absolute pressure is denoted by p $(p = 1 \cdot atm)$ and P_0 represents a conversion factor from [atm] to [Pa], $p_{H_2,an}$, $p_{H_2O,an}$, and $p_{O_2,cat}$ are the known partial pressures of hydrogen, water and oxygen, respectively, in the gas channel.

Since electrolytes are never perfect fully dense gas barriers, they lead to fuel crossover from anode to cathode reducing the maximum theoretical voltage. Furthermore, these are never ideal electrical insulators, therefore internal currents appear which further increase the Ohmic losses. Both effects –fuel crossover and internal currents– can be lumped together creating the so-called leakage overpotential (η_{leak}), nevertheless these are neglected in many occasions as their effect is insignificant when compared with the rest of current-dependent overpotentials [1].

Therefore, three principal mechanisms losses: ohmic, activation, and concentration, are generally considered [44–46]. The last two are generated at both, anode and the cathode side, while the ohmic losses encompass the ohmic behavior of all the conducting phases. Thus, the resulting cell voltage under operation will be then expressed as follows:

$$V_{cell} = E_N - \eta_{ohm} - (\eta_{act,an} + \eta_{act,cat}) - (\eta_{conc,an} + \eta_{conc,cat}) \tag{2.17}$$

where E_N is the Nernst potential or OCV, $\eta_{act,an}$ and $\eta_{act,cat}$ the activation overpotentials in anode and cathode respectively, η_{ohm} the ohmic overpotential, $\eta_{conc,an}$ and $\eta_{con,cat}$ the concentration overpotentials in anode and cathode.

2.2.4. Fuel flexibility and internal reforming

Hydrogen and syngas are today considered important fuels in future energy systems. However, due to the lack of a widespread hydrogen distribution infrastructure and to difficulties in hydrogen storage, fuel cell systems must rely on conventional (hydrocarbon) fuels in the immediate future [31]. Amongst hydrocarbon fuels, CH_4 has attracted much attention for direct operation of SOFCs

since it is the main constituent of natural gas, being this latter a widely available fuel that possesses lesser challenges than heavier hydrocarbons [13].

Among other advantages that the use of methane fuel in SOFCs possess are: 1) the increased efficiency, 2) the absence of combustion avoiding emissions, and 3) the transition aspects that it represents to deploy SOFC technology, e.g. the use of biogas in the future, synthetic methane, or other renewable fuels. Regarding the first point, electrical efficiencies as high as 74% (based on the LHV) have been demonstrated using steam-reformed methane as fuel, while converting more than 90% of the fuel in a single-pass. With hydrogen, efficiencies slightly above 60% (LHV) have been attained at 94% of fuel utilization [47]. About the second aspect, systems based on SOFC technology and fueled with natural gas can help to restrict the emission of other pollutants (e.g., NOx, SOx) [48], in fact, these systems are characterized by low NOx emissions. Additionally, although hydrocarbons fuel reforming does not eliminate carbon dioxide during the process, it does reduce the emissions as compared to the burning of conventional fuels, and in this sense, carbon capture and storage become a possibility to prevent the CO_2 emissions to the atmosphere. And finally, regarding the third aspect, biogas, mostly consisting of methane and carbon dioxide, is a potentially clean and renewable energy resource, and is readily available from a variety of waste streams such as landfill, sewage sludge, farm residues, and industrial effluents. Therefore, the use of biogas in the internal reforming SOFCs might become a key solution for energy and environmental problems of today.

In fact, generation of hydrogen from renewable sources has been already planned as an alternative. To the present day, industrial H_2 and syngas are almost exclusively generated from steam reforming of hydrocarbon fuels as natural gas [31, 49]. It is estimated that 95% of hydrogen production in the United States comes from this process [40].

Amongst the major types of reforming processes, steam reforming is a well-established and common process to produce H_2 and syngas for fuel cells [50], being the oldest and the most vital route to convert CH_4 into H_2.

The conditions for steam reforming of natural gas are very similar to the operating conditions of a SOFC. In addition to fuel flexibility, in high-temperature fuel cells (700 – 1100°C) as SOFC systems, hydrogen gas can either be directly supplied and electro-oxidized in the cell to produce electricity or first produced via fuel reforming (i.e., chemically processed through a conversion of hydrocarbon fuel into a hydrogen-rich gas) and then electro-oxidized by the fuel cell to produce electricity. Hence, the reforming process can occur inside the fuel cell itself (internal reforming) rather than in a separate chemical reactor outside the fuel cell (external reforming).

From both processes, internal reforming has a major benefit on the electrical efficiency of the overall system, as the heat required to sustain the endothermic reforming reaction can be provided

by the electrochemical reaction in the cells [1]. This is, the overall heat production is about twice the heat consumed by the steam reforming reaction, thus, in the internal reforming process, the cooling required by the cell (which is usually achieved by flowing excess gas through the cathode in the case of external reforming systems) will be much smaller for internal reforming systems.

This has led to various elegant internal reforming concepts that have been applied to the high temperaure fuel cell technologies, MCFC and SOFC. These two approaches are usually referred to as direct (DIR) and indirect (IIR) internal reforming.

In direct internal reforming, the reforming reactions take place directly on the anode (at the catalysts surface inside the cell), thanks to the catalytic activity of the dispersed Ni particles and nickel content in the anode, along with the low susceptibility of the SOFC systems. The advantage of DIR is not only that it offers good heat transfer but there is also chemical integration, i.e., product steam from the electrochemical reaction can be used for the reforming reaction. In principle, the endothermic reaction can be used to help controlling the temperature of the cells, reducing the air flow requirement for cell cooling. Nevertheless, this effect is not enough to completely offset the heat produced by the electrochemical reaction, and management of the temperature gradients is an issue [51, 52].

On the other hand, indirect internal reforming, also known as integrated reforming, involves conversion of methane by upstream reformers positioned in close thermal contact with the cells. With IIR, the reforming reaction and electrochemical reactions are separated. IIR suffers from the fact that heat is transferred well only from cells adjacent to the reformers and steam for the reforming must be raised separately [1].

Depending on the applications, either the DIR or the IIR conversion can be applied. Nevertheless, IIR is generally preferred due to the significant thermal and concentration gradients that arise when methane is reformed directly (DIR) at the anode [34] which can risk the stability of the entire system [1,41]. This is because steam reforming is a strongly endothermic reaction which may cause severe temperature gradients in the cell and nonuniform temperature distributions, not only leading to the cracking of the ceramic materials in the SOFC but also accelerating the degradation of the cell. Therefore, when a DIR reaction is employed in a SOFC, the thermal management of the cell becomes a very important and challenging issue, being crucial for the effective and safe operation of SOFCs.

Then, for methane, the steam reforming process is described as follows: at the anode, the methane and water vapor in the fuel gas are adsorbed into the nickel-based anode and are combined to produce H_2 and CO, according to Eq. (2.18). To increase the H_2 yield, Le Chatelier's principle suggests that operating the reaction with excess water vapor would help shift the reactions equilibrium to favor H_2 production. Thus, to further increase the H_2 yield, the CO produced can be

shifted to H_2 via a second reaction, Eq. (2.19). This means that when CO in the presence of water vapor is catalytically shifted to CO_2, additional hydrogen is produced. Such reactions are the steam reforming reaction itself and the associated water-gas shift reaction, Eq. (2.18) and Eq. (2.19), respectively [31].

$$CH_4 + H_2O \rightleftharpoons 3\,H_2 + CO \qquad \Delta H^0_{298K} = +206\,\mathrm{kJ}\cdot\mathrm{mol}^{-1} \tag{2.18}$$

$$CO + H_2O \rightleftharpoons CO_2 + H_2 \qquad \Delta H^0_{298K} = -41\,\mathrm{kJ}\cdot\mathrm{mol}^{-1} \tag{2.19}$$

The steam reforming reaction – Eq. (2.18) – is strongly endothermic (consumes heat, $\Delta H_r = 206\,\mathrm{kJ/mol}$) and proceeds in the presence of a Ni catalyst, while the WGS – Eq. (2.19) – is mildly exothermic (produces heat, $\Delta H_r = -41\,\mathrm{kJ/mol}$) and it proceeds much faster than the steam-reforming reaction [27].

The endothermic steam methane reforming (SMR) reaction is thermodynamically favored at high temperatures and low pressures. In industry, the steam reforming and the water-gas shift (WGS) reaction are jointly carried out at temperatures above 700 °C over nickel-based catalysts. However, since the water-gas shift reaction is a weakly exothermic reversible reaction, with increasing temperature the reaction rate increases but the conversion of reactants to products becomes less favorable. Due to its exothermic nature, high carbon monoxide conversion is thermodynamically favored at low temperatures, more specifically, below 500 °C, since above this value the WGS reaction is no longer spontaneous [53]. Despite the thermodynamic favorability at low temperatures, the reaction is kinetically favored at high temperatures. The water-gas shift reaction is sensitive to temperature, with a tendency to shift towards reactants as temperature increases due to Le Chateliers principle [27]. Consequently, operating a high-temperature direct hydrocarbon fuel cell requires a delicate balance between the thermodynamics of the reactions (which are more favorable at lower temperatures) and the kinetics of the reactions (which improve at higher temperatures).

When an SOFC is fed with a hydrocarbon mixture as syngas, several different reactions, both of chemical and electrochemical nature, occur. However, usually it is assumed that methane is consumed only in the steam-reforming process and not in the electrochemical reaction [17]. Under these assumptions, the steam reforming of natural gas typically has a H_2 yield of 76% on a dry, molar basis (i.e., no water vapor is in the outlet gas stream). The WGS reaction can increase the H_2 yield by about 5% [27].

Nonetheless, along with the electrochemical oxidation of H_2, Eq. (2.3), and the aforementioned steam reforming and water-gas shift reactions other mechanisms are theoretically possible,

depending on the conditions of temperature, gas compositions, cell materials, and operating point at which the SOFC works. Equilibria like the methane cracking and the Boudouard reaction may be present forming carbon deposits. The carbon deposition issue is one of the main drivers behind the exploration of some of the alternative anode materials.

If the steam to carbon ratio (S/C) is very low, it will produce coke deposits in the typical conversion process. From the chemical equations a steam to carbon ratio of two is required to prevent carbon from depositing on the catalyst. However, in practice a S/C ratio of two will not prevent carbon accumulation on the catalyst. Generally, the ratio is kept above 2.5, more often above 3.0 to avoid carbon deposition [27, 54]. However, it is not unusual, in industry to see S/C ratios of 6.5 and greater [40].

However, adding steam (increasing the S/C) has its own disadvantages because it can accelerate Ni agglomeration and it can reduce the overall efficiency of the process by diluting the fuel. Because of the S/C greater than two, the resulting mixture can still contain a large amount of water (can be as high as 50 mol%). Some of or all the water will need to be removed to increase the fuel concentration. Some water left over may be beneficial as water will help remove carbon deposited on the anode. The produced gas is termed syngas, which is referred to a gas mixture composed mostly of H_2, CO, H_2O with some CO_2 and CH_4. Several factors influence the final composition [40], including but not limited to the S/C ratio, reactor size, catalyst, and temperature.

The operation of SOFCs with syngas has been widely studied in literature [15], but a clear comprehension of the occurrence of all these reactions and their pathway is still missing, especially due to the lack of analysis tools able to provide information directly in-operando. Hence, optimal design and operation of such a system requires SOFC models and experimental testing that include accurate description of reforming processes.

2.3. Previous research on SOFCs and reformate-fed SOFCs

2.3.1. Experimental characterization

Solid oxide fuel cell technology has made significant progress in the past 30 years and is currently in the early commercialization stage [21]. Operation of multicell planar stacks up to more than 50000 hours, and a degradation rate as low as 0.2%/1000 hours have been reported [55].

In these achievements, testing of electrodes have provided detailed insight into the electrochemical performance and its correlation with several parameters such as gas composition, exact chemical composition of electrode materials, and the effect of specific structures on the electro-

chemical performance and durability; all electrode-specific information as elegantly shown in literature [56–63]. Testing of full cells complicates the set-up, test procedures and analyses of the results, but on the other hand, it provides insight into the effect of parameters such as high current density, i.e., overpotential gradients and current density gradient along the fuel flow direction due to fuel utilization as shown many times in recent years [23, 51, 64–74].

In the past, most of the SOFC research and development (R&D) has been performed on single cell level on laboratory scale, where the cells have been electrochemically characterized mainly by I-V curves, EIS and long-term measurements [46]. However, in recent years also innovative measuring techniques such as in-situ Raman spectroscopy [75], electrode segmentation [66, 67] or *ex-situ* and *in-situ* computer tomography and other techniques [63, 76] are being employed. Recently, *in-situ* and *in operando* measurements have been conducted for SOFCs under various conditions [55, 64]. These novel techniques allow for a more real and in depth analysis of the phenomena occurring in fuel cells while their operation, e.g. gas analyses under high and real steam contents, unlike what is usually reported in the literature (dry basis) [51, 77, 78] owed to the complexity that involves performing such analyses under wet conditions. These R&D activities have been very helpful for understanding better the electrochemical behavior, the reaction mechanisms, the overpotentials and the degradation effects of SOFC single cells at different operating conditions.

Typical DC (polarization curves) and AC (impedance spectroscopy) characterization methods for electrodes and cells are found in the literature [45, 79–88]. The electrochemical impedance analysis is widely adopted to investigate the frequency response of SOFCs systems by *in-situ* diagnosis [85, 89–91]. From such analyses, a comprehensive and more theoretical description of different polarization overpotentials, as well as a breakdown of losses are given.

However, the major drawback of impedance spectra is related to the difficulty to distinguish clearly each single physicochemical process that occurs in the cell due to many processes involved and that partly overlap in frequency range. Hence, impedance spectra at different gas compositions are used to analyze the dependency of the different polarization losses on gas composition, and usually gas changes in "one electrode sided" are used to separate which impedance contributions originate from each of the electrodes for a full cell test. The impedance spectra are typically analyzed in terms of equivalent circuit models applying a complex non-linear least squares (CNLS) fitting routine [84, 92–95], through analysis of differences in impedance spectra (ADIS) [58, 82], by gas shift impedance spectroscopy [25] or via the distribution of relaxation times (DRT) technique [61, 63, 85, 90].

Recently, the distribution of relaxation times is regarded as a powerful representation of EIS, exhibiting the state-of-the-art frequency resolutions to resolve electrochemical processes. Some of the very first attempts for SOFCs characterization through this technique are reported by Leonide et

al. [42, 79, 92]. However, there have been a number of publications where the DRT and approaches to unfold a DRT from impedance spectra are discussed [89]. To date, DRT has been successfully employed in the study of physicochemical processes occurring in anode-supported SOFCs operating in humidified hydrogen [85, 94] or in reformate fuel [84, 96], in tubular SOFCs [97], and in the study of degradation and stability analysis [90, 98, 99]. Besides, taking advantages of *in-situ*, fast-response, and non-destructive attributes, DRT analysis has proved to be a new technique for quantification of SOFC electrode microstructures [63].

Usually, the impedance analyses are supported by postmortem microscopy investigations. A variety of analysis techniques based on spectroscopy can be and have been applied for SOFC characterization such as secondary ion mass spectroscopy (SIMS) [100], Raman spectroscopy [101], and spectroscopy based on X-rays such as energy dispersive spectroscopy (EDS) [86, 98, 102] or x-ray diffraction (XRD) [86, 100, 103]. Scanning electron microscopy (SEM) is widely used for studying SOFC on a nano-and micrometer scale [96, 100, 101] and for investigation of aging and degradation of cells [86, 98, 102, 103].

In recent years, combined focused ion beam (FIB) milling and SEM imaging have also been used to make 3D reconstructions of electrode structures [52] leading to very detailed and quantitative information on the active TPB lengths, particle size distributions, tortuosity, etc. in a given electrode structure. Over the last decade, there have also been several examples of applying transmission electron microscopy (TEM) for the analysis of SOFC [103] which enables, e.g., investigation of nano-sized impurities in the electrode structures and formation of undesirable secondary phases.

Thousands of reports can be found in literature on electrochemical testing of SOFC electrodes [63, 104–109], cells [92, 110–114], and short-stacks [115–118]. Due to the easiness and because of historical reasons, almost all reported cell tests have been galvanostatic (constant current) tests. Additionally, as there is no general agreement on test protocols even inside regions such as USA or the European Union (EU) [119, 120], it is particularly important to note that the testers carefully report the obtained fundamental parameters, such as area-specific resistance (ASR), activation energy (E_a) and polarization losses [58, 83, 92, 94, 121–126], and provide the exact test conditions for the study to minimize misleading interpretations and inappropriate comparison of electrochemical test results.

Usually cell tests are conducted with very low fuel and air utilizations [45, 64, 67, 70, 74, 86, 104, 112, 127], because these are easier to perform than the realistic tests with high fuel utilization [51, 68, 99]. Also, because of the homogeneity regarding temperature, species distribution, current density, etc., that can be achieved, button cell tests are used to derive the electrochemical fit parameters, which are the pre-exponential factors and activation energies [42, 121], which then are used in

simulations in order to reproduce experimental data.

Different designs for test housing and cell assembly are reported [51, 64, 73, 76, 78, 96, 128, 129] but based on similar concepts, i.e., the cell sandwiched between gas distributors and current collecting foils and applying sealing to avoid mixing of fuel and air.

In SOFC research, the anode design has been extensively investigated [94,130]. To date, various design options and fabrication approaches for SOFC have been proposed and developed for single cells and multicell stacks, however, anode supported is generally the most favorable design [131]. Additionally, the planar configuration has emerged as the most common and more widely studied. To date, most of the built and demonstrated systems are based on planar stacks. The planar design has become the dominant configuration through the combination of the following developments and advancements [55]: a) thin-electrolyte anode-supported cell design, b) fabrication of green thin electrolytes on anode supports by conventional ceramic processing techniques, c) reduced temperature ($\leq$ 800°C) operation for anode supported cells and use of metallic interconnects, and d) demonstration of extraordinary performance for anode-supported cells.

For stack testing, there are several examples on results –experimental and modeling– that illustrate the importance of awareness of the choice of flow design and geometries, i.e. cross-flow, co-flow and counter-flow, when considering temperature profiles [70, 132–134]. The effect of chosen flow geometry will be much smaller when considering single cell tests compared to testing of large stacks.

On the other hand, in recent years, research efforts on fuel cells have been addressed on the development of multifuel reformers with particular emphasis toward the potential use of non-traditional fuels. Among these, syngas and/or methane for fuel cell system applications have been of great interest [135–137]. With syngas mixtures fed to the anode of the SOFC and mainly using anode-supported button cells [11, 13, 113, 135, 138], the interest lies in understanding the multi-physics phenomena and optimizing the geometric and operation parameters of the SOFC, while avoiding operating and fuel conditions that can lead to or accelerate degradation processes.

In literature are found extensive investigations about internal reforming from the perspective of methane conversion [6, 117], hydrogen yield [11, 139–141] and solid carbon formation [96, 112, 142–145]. However, most of these works are based on high temperature SOFCs. Considerable research has been done regarding the electrochemical performance of SOFCs operated with carbon-based fuels (natural gas, coal gas, etc.), kinetic studies on carbon deposition and dependency of SOFCs performance on fuel composition (hydrogen vs. methane) and fuel utilization, etc. The evaluation of recycling and reusing the exhaust gas from SOFCs under methane reforming, to evaluate the enhancement of the fuel utilization of methane and the effects of some components of exhaust gas, e.g. H_2 and CO_2, on the performance of the cell, have been also carried out [11, 17, 128, 146].

In the internal reforming process of SOFCs, when CO and H_2 are both present in the fuel stream the mechanism becomes even more complex because of parallel charge transfer, water-gas shifting, and the involvement and interaction of additional gaseous and adsorbed species. Hence, sometimes, the electrochemical oxidation of hydrogen and carbon monoxide on the anode side are taken into account [147] by assuming that methane is consumed only in the steam-reforming process and not in the electrochemical reaction.

Research about CO electrochemical oxidation is much less spread-out than H_2 electrochemical oxidation. However, it is generally agreed that the electrochemical reaction rate of CO is lower than that of H_2. According to experimental results using a nickel-patterned anode on YSZ by Sukeshini et al. [148], the reduced output power obtained from a porous anode was a combination of slow CO electrochemical kinetics and increased resistance to transport CO to reaction sites because the relatively heavy CO molecules are characterized by a lower diffusivity than their lighter H_2 counterparts. Therefore, in real systems not only CO will be slower to reach the TPB, but it will also be slower to react there. This observation agrees with that of Matsuzaki and Yasuda [149] who found that the electrochemical oxidation rate of H_2 was 1.9-2.3 times faster than that of CO at 750°C, and 2.3-3.1 times faster at 1000°C. However, the authors concluded that even though the CO electro-oxidation rate is slower than H_2, for systems using CO-dominant fuels, CO electrochemical oxidation may play a non-negligible role as a parallel charge-transfer pathway to H_2 electro-oxidation. Nonetheless, there is no general agreement on the mechanism for CO electrochemical oxidation for H_2-CO mixtures, especially under different operating conditions [147, 150].

Regarding the direct electrochemical oxidation of methane in a SOFC, it was first reported in detail by Steele et al. [151], who observed that methane could be effectively converted into CO_2 and H_2O on oxide-based anodes. Ceria was also mentioned as a particularly good candidate for an anode material for the direct electrochemical oxidation of methane. Park et al. [152, 153] also reported direct oxidation of CH_4 in SOFCs, concluding that the direct electrochemical oxidation of dry methane can be achieved in SOFCs with $Cu/CeO_2/YSZ$ anodes with reasonable performances. More recently, Park et al. [153] reported on the direct electrochemical oxidation of various hydrocarbons (methane, ethane, 1-butene, n-butane, and toluene) at 700 °C and 800 °C with a composite anode of copper and ceria (or samaria-doped ceria). They demonstrate stable operation without carbon formation in the anode. Murray et al. [154] reported the direct electrochemical oxidation of nearly pure CH_4 in SOFCs using a ceria-based anode, which resulted in power densities up to $0.37\,W/cm^2$ at 650°C. Therefore, although methane has been successfully oxidized electrochemically, the susceptibility to carbon formation and poor power densities have prevented the application of this simple fuel in practical applications.

Very few experimental studies on large area planar SOFCs have been reported with respect to temperature distribution on cells. Lim et al. [51] experimentally investigated the effect of endother-

mic internal steam reformation of methane and exothermic fuel cell reaction on the temperature of a planar-type anode-supported SOFC as a function of current density and fuel utilization. Using 30 thermocouples inserted through the cathode of a large-area cell (22 cm $\times$ 33 cm), the authors concluded that a moderate condition with regards to thermal gradient on the cell correspond to high fuel utilization and low current density. Guan et al. [155] experimentally measured temperature distribution inside 3-cell SOFC stack with five thermocouples under various operating conditions. It was found that the discharging current had a great impact and the gas flow rate had a slight impact on the temperatures of unit cells. Besides, the relationship between temperatures and cell performance showed that the worse the cell performance, the higher the cell surface temperature.

Santoni et al. [74] report an experimental study of commercial cells where the gas composition along with temperature measurements under internal reforming are analyzed. The experiments have been carried out *in operando* conditions, where 11 sampling points in the anode side allow the analysis.

Some other authors, such as Lanzini et al. [137] and Razbani et al. [70] have also experimentally reported the temperature distribution over planar-type anode-supported SOFCs under internal reforming and various operating conditions.

Research on internal reformin has mainly focused on the improvement of anode materials as well. In recent years, many researchers have been developing SOFC anodes for operating on hydrocarbon fuels [4, 7, 16, 150], where the development of new porous anode [156] for the direct utilization of hydrocarbon fuels has attracted extensive interest [8, 156].

Two main strategies have been developed to allow the use of such fuels (methane) in SOFC. The first one is the addition of an oxidizing agent to the fuel stream to prevent the thermodynamic conditions that favor carbon deposition. Usually, water is the most common choice [17, 51, 74, 137, 142, 157, 158], however some studies have reported SOFCs running on methane by adding air or CO_2 [158, 159]. The second strategy is to modify or substitute the traditional Ni-based cermet anode to allow stable operation of SOFCs without fuel dilution. Different materials have been reported, including various cermets and ceramic anodes. However, such anodes usually exhibit either low electronic conductivity or low catalytic activity.

Investigations on Ni-YSZ anodes have focused on kinetics of internal reforming of hydrocarbons [15, 77, 78, 93, 160], influence of microstructure [108, 161, 162], and their electrochemical performance as electrode [50, 73, 158, 159]. The suitability of this material as a catalyst for this reaction is confirmed. It has been shown that no alternative anode than the state-of-the-art nickel cermet anodes can provide enough activity for steam reforming [4, 6] without the need for additional catalyst; however, anode degradation may occur.

A large volume of research focused on the production of hydrogen via the reforming of methane has been recently reported. The recent progress, challenges, and new approaches for improving the performance in direct fueling with methane (or related fuels) of SOFCs with nickel-based cermet anodes, is comprehensively reviewed [7, 16, 163].

Tremendous efforts have been devoted to improve the coking resistance, sulfur resistance, and redox stability of methane and other hydrocarbons fueled over nickel-based anodes of SOFCs. Strategies to suppress coke formation over nickel cermet anodes include: 1) addition of oxygen containing gases into the anodic feeding gas to increase the oxygen-to-carbon ratio (O/C) and thereby to avoid coke formation thermodynamically [7, 159]; 2) promotion of the carbon elimination reaction by increasing the polarization current [145, 164, 165]; 3) introduction of another metal(s) into the nickel cermet anode to modify the surface of the nickel particles or form an alloy-ceramic anode [8]; 4) application of an anode catalyst layer to alter gas distribution within the anode and to increase catalytic activity for the reforming/partial oxidation of methane; 5) tailoring of the ceramic phase in the anode; 6) modification of the anode structure and anode surface with other active oxide(s) [6, 8, 166] or using anode barrier layers [159]. Most of the these strategies brought about enhanced resistance to coking but suffered from one or several drawbacks, such as low activity, poor electrical conductivity, bad chemical compatibility, and so on. Hence, Ni-based cermet anodes are still one of the most attractive anodes for SOFCs in the case of their catalytic activity and coking behavior towards methane or some other hydrocarbons [4, 6].

As concluded in several works, the simplest way to suppress coke formation over a fuel cell anode that operates on methane fuel is via a thermodynamic approach that involves the addition of oxygen-containing gases into the fuel gas to increase the O/C ratio. S/C ratios greater than the thermodynamic minimum have been demonstrated to be necessary to avoid carbon deposition and structural damage to the anode. In some cases, however, the experimental S/C ratio needed for effectively avoiding coke formation has been drastically different from that predicted from the thermodynamic calculations. Such a discrepancy can be explained by the fact that thermodynamic calculations only provide insight into the expected equilibrium conditions and do not account for the impact of reaction kinetics.

Although the introduction of steam into fuel gas can reduce coke formation thermodynamically, it can also detrimentally affect the operational stability of the anode, and thus the overall cell efficiency, by facilitating the sintering of nickel particles, which, in turn, affects the catalytic activity and coking behavior of the anodes. For example, King et al. [162] found that methane conversion over a NiYSZ cermet anode catalyst under steam reforming conditions was significantly reduced from an initial value of 78% to 9% after the fuel cell was operated for 120 h at an S/C ratio of 3.0 at 700°C. Contributions of nickel particles to the catalytic activity were detected. Thus, it was concluded that care should be taken in suppressing coke formation by simply increasing the steam

content in the fuel gas.

As already mentioned, some researchers have also attempted to suppress the coke formation over nickel cermet anodes by adding O_2 or CO_2 into the methane fuel gas; however, progress in this area remains slow [7, 158, 159, 167]. The challenge is that the amount of oxidant added should be kept to a minimum because an increase in the amounts of such oxidants may increase the polarization resistances and reduce the power density. Furthermore, an excessive amount of oxygen also increases the risk of re-oxidation of the Ni-based anodes, which results in an irreversible effect on the operational stability of the cell.

To date, research about SOFCs with hydrocarbon as fuel is mainly focused on oxygen ions conducting SOFC (O-SOFC). However, recently, the internal reforming of methane has been also integrated into proton conducting solid oxide fuel cells (H-SOFCs) operating with hydrocarbon fuels, where the theoretical [168] and experimental feasibility [166] of this approach has been demonstrated. Additionally, a very remarkable interest in SOFCs operated in reverse mode (solid oxide electrolysis cells or SOECs) has arisen. The SOEC has been considered and developed for hydrogen and syngas production for commercial and other uses [10, 55]. Solid oxide electrolysis cells for the production of H_2 or H_2/CO by means of H_2O electrolysis or H_2O/CO_2 co-electrolysis, has been reported. Therefore, advancements in SOECs will continue to leverage progress in SOFC technology.

Anode-supported SOFCs accumulating more than 700 h of stable operation on dry ethanol [4] and 200 h on ethylene glycol (EG)-steam mixtures [5] have been also reported. However, a key technical issue that has limited the development and deployment of this transformative technology is its high operating temperature, resulting in higher systems costs and performance degradation rates, as well as slow start-up and shutdown cycles [169].

Over the past decade, there has been a strong drive to lower the operating temperature of the SOFCs, and considerable progress has been achieved in bringing the temperature down to an intermediate temperature range of 600 to 800°C [6, 16, 18, 19, 170]. However, the main difficulty with IT-SOFCs is the significant decline in performance. Besides, even at these temperatures, materials are not immune to corrosion and reaction with other cell components [100], facing problems of chemical stability of various cell components.

Fuel impurities are reported to drastically reduce the electrochemical performances of the cell, both at the intermediate temperature [101] and in the high temperature range [60,61], affecting both activation and mass transport processes. Actually, it can be found from H_2S poisoning tests simulating H_2S contamination of biogas, that 1 ppm H_2S caused about 9% voltage drop and about 40% decrease in reaction rate of internal reforming [171]. From post-mortem analyses, the formation of some phases affecting the anode activity have been observed [61, 101], which has allowed to

associate the poisoning phenomena with changes in the microstructure.

The degradation mechanisms of SOFCs have been also extensively studied, however most experimental studies have been conducted on button cell or small-size level and at high operating temperatures [5,6,80,85,86,108,159,166,169,172,173]. In fact, there are few studies that have reported data concerning performance, degradation and durability of large-area planar cells [51, 70, 81], mainly because they are time-and resources-consuming.

Particularly, the redox stability of state-of-the-art Ni anodes and cracking of the electrolyte are the major drawbacks for the anode supported cells under redox-cycling conditions [7, 60]. A redox cycle can occur for several reasons such as: thermal cycle of a SOFC system during shut down and start-up operations, due to system failures e.g. in electronic devices, cutting-off gas supply, leakage through a sealing, and high fuel dilution or local fuel starvation. However, in terms of anode degradation, a strong interaction between several parameters has been indicated.

Besides, the presence of water at the cathode is not from a fundamental point of view expected to have an influence on SOFC performance. However, several studies have shown that humidity can have a negative effect resulting in a severe voltage drop [25, 65, 82, 105, 174]. All these phenomena are associated with serious volume change, leading to an irreversible volume expansion and changes in the microstructure [175]. In the case of anode degradation, the major causes are attributed to the agglomeration of Ni particles [20] and carbon deposition [7, 8].

Nevertheless, there is no published consensus in this field [163, 169, 174]. Some authors report massive degradation [6, 65, 85, 86, 172], while some others report no significant degradation [45, 80, 81, 126].

In addition to simple performance tests and long-term durability tests [20,60,80,82,98,101,105, 125, 174], other test variations have been unintentionally carried out because of technical problems with the cell test set-up [65, 81, 86, 117, 118, 126, 169, 176]. Such tests were redox tests, thermal cycling and electrical load cycling, which have allowed to evaluate the single cells long-term stability. Redox test and thermal cycling, by nature, often end with a mechanical break-down of the cell, which will allow oxygen or air to mix with the fuel gases. Examples of redox testing [86, 169], electrical load testing [177] and thermal cycling [80, 102, 169] can be easily found in literature, while the case of fuel-cell-electrolysis-cell-mode cycling tests are rarer [35, 116].

Hitherto, identification of the degradation mechanisms has been mainly possible by post-mortem analysis, underlining the difficulty of recognizing them in operando. Most of the techniques used for post-mortem analysis are now developed for in-situ analysis and/or time-resolved measurements. This trend, however, rather recently (developed mainly over the last decade), is still limited to few facilities around the world [22].

2.3.2. SOFC Modeling

Since direct measurements of the characteristic variables (e.g., local temperature, local concentration, local current density, etc.) of an operating SOFC are difficult because of the high temperature, narrow channel gaps, and small flow rates; several researchers have adopted the numerical approach as an effective tool to obtain detailed information about the SOFC technology [34, 178]. Hence, to date several improvements of SOFCs have been conducted based on modeling and simulation studies with the aim of achieving better performance [179–186] and looking for fuel cell optimization [168], where anode-supported SOFC has been generally the most studied design [94, 185, 187–190].

On the modeling of SOFC systems there is a great deal of available literature where many types of modeling approaches can be found, ranging from simple 0-D electrochemical [191–193] cells to quasi-2-D unit cells [194, 195] or to complex 3-D cells and stacks [168, 196–198]. Most of these models are one or two-dimensional with different simplifications and assumptions among them.

Different methods, length scales and multiscale model integration are reported. The finite element method (FEM) and finite volume method (FVM) are used to model SOFCs at the macroscale level. COMSOL Multiphysics [196], based on the FEM, as well as FLUENT [9], based on the FVM, are examples of the most common commercial codes employed for the analysis of SOFCs at different scales.

Therefore, the current state-of-the-art in SOFC modeling is to use computational fluid dynamics (CFD) to solve the transport equations and couple the solution to an electrochemical model. In terms of methodology for the modeling, some models can be compared. Most of the investigated models [180, 183–186, 199, 200] use the finite volume method to solve the governing equations. Most authors [180, 184–186, 199–201] include a parametric study to test their models, but comparison with experimental data is not common. Regarding the flow configuration co- [200], counter- [185, 202] as well as cross flow [183] can be found in the literature.

Most authors [183–185, 199, 201] do not include material characteristics that are dependent on temperature. However, in some cases the conductivity is defined as temperature dependent [180, 199], while the other material characteristic parameters are still defined only at one temperature. All investigated models include governing equations for mass transport, most of them [183, 185, 186, 199–201] for momentum transport, some of them for energy [183, 199, 200] and ionic transport [180, 184–186, 200]. Pramuanjaroenkij et al. [200] included simultaneously the governing equations for mass-, energy-, momentum-, and ionic transport. Models are developed with different aims at component, cell or stack level, and calculations considering entire fuel cell systems can be also found in the literature [203]. However, owing to the heavy computational load, the computational

domain of most CFD-based two-and three-dimensional simulations of fuel cells is generally limited to a single module or channel. On the other hand, steady-state conditions are applied in a majority of the models developed so far [182].

Most reported models restricted validation to a single set of experiments, at one specified temperature [168]. Additionally, it is common to assume that the current density is uniform over the entire electrode [204], which is basically only valid as long as the fuel consumption is uniform along the flow channel. In some other models the total pressure gradient inside the anode is normally assumed to be negligible [204, 205]. It is common to assume laminar flow with a small pressure change for fuel cell gas channels due to the low velocities compared to the air flow [206]. Hence, the flow direction is often assumed to be constant, and flow field predictions are made in a rather simple manner by considering only the mass balance. This simplification allows to avoid the calculation of the pressure field and greatly reduces the computational cost and complexity [185], enabling simulations to be performed at a relatively low computational load. However, a constant flow direction or laminar flow cannot always be ensured, particularly in complicated systems where considerable temperature variations are expected.

Numerous studies on the thermal fluid dynamics and electrochemistry of SOFCs have been conducted in recent years. However, most of them are based on computational modeling [16, 34, 115, 175, 196, 207] while very few on experimental studies [51, 66, 208]. Most of the works based on numerical simulations with internal reforming report much higher temperature differences along and across the cell than those reported experimentally under almost the same operating conditions. Such discrepancies in the temperature differences are attributed by some authors to the different thermal boundary conditions (adiabatic, isothermal and radiation heat exchange) that the models use.

Since heat transfer inside SOFCs includes various aspects such as convective heat transfer between the solid surfaces and the gas streams, conduction heat transfer in solid and porous structures; a very common method in SOFC modeling is to employ a local temperature equilibrium (LTE) approach, which assumes the same temperature for gas-and solid phase [181, 200]. However, when some typical conditions found in the porous SOFC electrodes bring this assumption into question: 1) very low Reynolds number, 2) presence of volumetric heat generation, and 3) large difference in thermal conductivities between the gas and solid phases; a local temperature non-equilibrium (LTNE) approach is employed [209] in order to predict the temperature difference between the solid- and gas phases within the porous electrodes.

On the other hand, SOFCs are examined from different points of view: as an electrochemical generator in a viewpoint of electrochemical reactions at continuum level [170], as a heat and mass exchanger in a perspective of fluid dynamics and transport phenomena [196], or as a chemical reac-

tor in viewpoints of chemical reactions depending on fuel composition and heat effects associated with the electrochemical conversion [205].

The focus and the selected scale (system, stack, cell, component or functional materials) differ significantly between different models, as described in the open literature. For example, two approaches for defining the electrochemical reactions can be found in the literature, either as source terms in the governing equations [180, 181] or as interface conditions defined at the electrode/-electrolyte interfaces [182–185, 207]. When the interface condition approach is applied, the ionic resistance in the electrodes is neglected and the electrochemical reactions reduce to the interface conditions in the governing equations for heat, mass and momentum transport. Hence, selection of either approach will affect the governing equations.

Usually, because of the usage of the Nernst equation, which considers the partial pressure of steam at TPB in the denominator of the logarithmic term, Eq. (2.11) or Eq. (2.12), a small amount of steam needs to be fed at the inlet of the fuel channel along with the gas composition, just for practical simulation of most of the numerical models. This is, to validate model simulations with experiments under pure H_2, the inlet composition at the fuel channel is usually 3% H_2O + 97% H_2, while the experiments used pure H_2. This initial guess is found to have a very minor effect on the OCV [168].

Regarding mass transport, Fick's model is the simplest diffusion model used for dilute or binary systems [200]. In the literature the Stefan-Maxwell model is commonly used to calculate the diffusion in a multi-component system [182, 210]. In some references the Stefan-Maxwell model is combined with the Knudsen diffusion term (frequently called the Dusty-Gas model or extended Stefan-Maxwell equation) [181, 184, 196, 211–213] to predict the collision effects between the gas molecules and the solid porous material. In other models this effect is neglected [214]. Besides, to account for the increased diffusion length due to the tortuous paths of real pores in the porous materials, different approaches can be found [186].

Shi et al. [215] developed a 2D CFD model, including phenomena of heat, mass, ion, and electron transport as well as electrochemical reactions. Electrode properties were taken into account by linear functionally graded porosity as well as nonlinear distributions according to their porous electrode features. Also, Ni et al. [216] studied composite electrodes, but at the microscale level, and their model predicts the overpotential losses by capturing the coupled mass transfer and the electrochemical reactions. A 2D isothermal mechanistic model for a SOFC button cell was developed by Shi et al. [217], including polarization effects, molecular and Knudsen diffusion, gas transport, ionic and electronic conduction, surface diffusion of intermediate species and electrochemical reactions. Kanno et al. [218] and Iwai et al. [219] introduced a concept of different tortuosity factors for the transport of ions, electrons and gas-phase molecules, i.e., the real (average) transport distance

for the ions and the electrons within the electrodes was evaluated and applied in the simulation. The tortuosity factors can be calculated, for example, by the lattice Boltzmann method.

Concerning internal reforming, sophisticated numerical models for DIR-SOFCs can be also found [34, 69, 113, 141, 196, 202, 220]. Approaches to model electrochemical as well as internal reforming reactions are also discussed in detail [16].

For instance, Andersson et al. [170] have developed a model considering fluid flow, mass-and heat transfer for a single cell IT-SOFC. A fully coupled CFD model (COMSOL Multiphysics) was developed to describe an intermediate temperature SOFC single cell, including governing equations for heat, mass, momentum and charge transport as well as kinetics considering the internal reforming and the electrochemical reactions of only hydrogen. It was found that 60 % of the polarizations occur in the anode, 10 % in the electrolyte and 30 % in the cathode.

Iwai et al. [34] also developed a numerical model for an anode-supported intermediate-temperature direct-internal-reforming (DIR) planar SOFC to simultaneously solve quasi-three-dimensional multicomponent gas flow fields, temperature fields, and electric potential/current fields. The steam-reforming reaction of methane, the water-gas shift reaction, and the electrochemical reactions of hydrogen and carbon monoxide were taken into account. Such model applies the volume-averaging method to the flows in SOFC passages and it was assumed that a porous material was inserted in the passages as a current collector. This assumption was made in order to reduce the computational time and cost by avoiding a full 3D simulation while maintaining the ability to solve the flow, pressure fields, and thermal field in the streamwise and spanwise directions. By varying the pre-reforming rate it was indicated that the effects of DIR may be controlled by tuning the pre-reforming rate of the fuel introduced into the cell. However, a direct comparison of the model with experimental data was not possible because the authors claim that an experimental counterpart to the problem considered in their study was not available in the literature until then.

Several electrochemical models about internal reforming [9, 34, 72, 94, 128, 129, 131, 190, 192, 194, 196, 202, 221–225] predict the I-V behavior, overpotentials and performance of anode-supported single SOFCs at high temperatures. However, a few models based on intermediate-temperature fuel cells behavior prediction are reported [34, 72, 202]. Some models encounter difficulties in the prediction of polarization losses caused by activation and gas diffusion, particularly over a sufficiently broad range of operating conditions [191], mainly because of the usage of parameters that are either generally estimated under largely simplifications and assumptions or taken from literature [193]. This is, although most of these models are based on physical equations such as the Butler-Volmer equation for determining the activation polarization or Fick's model for determining diffusion polarization, these equations often must be simplified to a much too large extent. The Butler-Volmer equation is substituted by a linear function and the Tafel equation. The partial pressure dependen-

cies of the exchange current densities are largely simplified or only a constant value is used for the exchange current density.

An early polarization model, involving the Butler-Volmer equation, was developed by Chan et al. [193] to describe the activation overpotential instead of using simplified expresions such as the Tafel equation. Patcharavorachot et al. [226] developed a pure electrochemical reaction model, i.e., neglecting the mass and the heat transport, the fluid flow and the internal reforming reactions. Bessler et al. [227] studied electrochemistry of SOFC anodes, focusing on the nickel/yttria-stabilized zirconia (Ni/YSZ) materials, and the electrochemical reactions were described in multi-steps in the Arrhenius form. The Butler-Volmer equations are often used to describe the overpotential/current density relationship, however, a more detailed approach was developed by Bessler et al. [228] to include an elementary-kinetic multistep description of electrochemistry with coupled surface chemistry, charge-transfer reactions, physical representation of the electric potential steps and other transport phenomena. On the other hand, in the above-mentioned models, only pure hydrogen is considered for the electrochemical reactions at the fuel side, i.e., it is assumed that carbon monoxide and methane are fully reformed to hydrogen before the electrochemical reactions occur.

Some models are also compared in terms of internal reforming reaction mechanisms and involved gas species. It is also found that comparison with experimental data is rare. Several kinetic expressions considering the steam reforming reaction are developed in the literature. The reaction order varies significantly between the models and they usually originate from fitting experimental data. However, most of the models [192, 221, 229–233] use an equilibrium approach both for the water-gas shift reaction and steam reforming reaction.

In several models, it is common to use an inlet concentration considering 30% pre-reformed natural gas [229, 230, 232, 233], while the ratio of water to methane has been varied in some others [231, 234] to study the effect of gradual vs. direct internal reforming reactions. Some models consider only hydrogen electrochemical oxidation [170], others consider hydrogen and carbon monoxide oxidation [147].

Different approaches for defining the water-gas shift reaction can be found in literature: 1) global reaction mechanism that considers reaction in the anode only [181, 229], 2) global reaction mechanism that considers reaction in the anode and in the fuel channel [231], and 3) a more advanced reaction mechanism that includes catalytic surface reaction kinetics for steam reforming, water-gas shift reaction and the Boudouard mechanism [194, 212].

Reforming and shifting reactions proceed through homogeneous and heterogeneous elementary thermochemical reaction steps. Homogeneous elementary chemistry is well developed in the combustion literature. Hecht et al. [160] proposed an elementary heterogeneous reaction mechanism for CH_4 on Ni-based catalysts. The reaction mechanism consists of 42 reactions among 6 gas-phase

and 12 surface-adsorbed species. The full mechanism covers the global aspects of steam reforming, dry reforming, the water-gas shift (forward and reverse), and carbon deposition (Boudouard reactions). This mechanism was later improved by Janardhanan and Deutschmann [212] and adopted by Zhu et al. [235], and more recently, by Santarelli et al [128].

Menon et al. [168] developed a computational model to investigate proton-conducting SOFCs (H-SOFCs) with direct internal reforming, employing also a 42-step elementary heterogeneous mechanism for Ni catalysts. The performance of the cell was analyzed by assuming the co-flow planar cell to be adiabatic. In a quasi-2-D planar cell model a parametric analysis was performed. The dependence of temperature distribution on cell voltage, cell length, specific catalytic area of the anode has been illustrated. The analysis also investigated species transport within the whole cell.

However, most of the studies treat the reforming and water gas shift reaction as global reactions occurring in a single step. A few investigations consider detailed kinetics in a surface reaction mechanism of the steam reforming reaction and water gas shift reaction. It is frequently stated in literature [192, 202, 221, 231] that the water-gas shift reaction should be considered to be in (or very close to) equilibrium state.

A review on the reaction kinetics of internal reforming of hydrocarbons was given by Mogensen et al. in [15], from which it is concluded that there are large differences in the published kinetic expressions for the steam reforming reactions. Vakouftsi et al. [236] developed a 3D CFD model for a planar SOFC, including mass transport, electrochemical reactions and global scale kinetic expressions for the steam methane reforming and the water-gas shift reaction in the Arrhenius form. Nagel et al. [232] studied the relations between mass, heat and charge transport within SOFCs, using a finite volume method, considering different fuel gas compositions. A dynamic SOFC model, including mass and energy balances, electrochemical reactions and internal reforming reaction kinetics, was developed by Aguiar et al. [202] to study load step-changes

Finally, the widely spread problem of thermal stresses and big temperature gradients close to the inlet have been also analyzed through modeling with different approaches: such as 1) lowering the operating temperature to an intermediate range to reduce the steam reforming reaction rate [237], 2) recycling a part of the anode gas to obtain a dilution of the fuel [11, 238], where the rate of reforming reactions decreases, due to the decrease in fuel concentration. A 50% recycling has resulted in sufficient steam for the reforming reactions, and 3) design of the anode material with the aim of decreasing the steam reforming activity [8].

Chapter 3

BASICS OF THE IMPLEMENTED CHARACTERIZATION TECHNIQUES AND ANALYSIS TOOLS

3.1. Polarization curves

3.1.1. Current-voltage measurements

A typical result from a single cell test is a polarization curve also called current-voltage curve (I-V curve). Generally, I-V curve measurements are used to quantitatively describe the overall performance of a fuel cell system, providing data over a large polarization range.

The polarization curve is the most employed electrochemical diagnostic technique used to characterize the overall immediate performance of SOFC cells. The I-V curve allows to comprehensively distinguish the irreversibilities in electrochemical devices under determined operating conditions (i.e. temperature, fuel composition, etc.) hence, resulting in a useful technique to assess the operation of the system.

It consists in the measurement of the cell voltage by varying the current generated and extracted from an external load. It provides information about the general electrical response of the cell over the range of currents investigated, and hence it is a valuable instrument to assess the dependency of the cell performance to the operating conditions, but it can also suggest hints about the effect of the different polarization losses by examining the different portions of the plot.

As above-mentioned, the I-V curve shows the output voltage of the fuel cell for a given current

density loading. Fuel cell I-V curves are usually measured with a potentiostat/galvanostat system. This system draws a fixed current from the fuel cell and measures the corresponding output voltage. By slowly stepping the current demand, the entire I-V response of the fuel cell can be determined. However, reliable I-V curve measurements of fuel cells require that the following important points must be considered [27]: a) steady state must be ensured, and b) the test conditions should be carefully controlled and documented.

Steady state means that the voltage and current readings do not change with time. When current is demanded from a fuel cell, the voltage of the cell drops to reflect the higher losses associated with producing current. However, this voltage drop is not instantaneous, it can take seconds, minutes, or even hours for the voltage to reach a steady-state value. This delay is due to subtle changes, such as temperature changes and reactant concentration changes that take time to propagate through the fuel cell. Usually, the larger the fuel cell, the slower the approach to steady state. Hence, current or voltage measurements recorded before a fuel cell reaches steady state will be artificially high or artificially low.

For large fuel cell systems, I-V curve testing can be a tedious, time-consuming process. Often, measurements are made galvanostatically. In steady-state galvanostatic I-V measurements, the current of the fuel cell is held fixed in time and the steady-state value of the fuel cell voltage is recorded after a long equilibration time, i.e., the fuel cell is subjected to a given current load, then the voltage response is monitored until it no longer changes significantly in time, and finally this voltage is recorded. Then, the current load is increased to a new predetermined value and the procedure is repeated. Frequently, time constraints only permit $10-20$ points along the fuel cells I-V curve to be acquired. Although the data are coarse, it is generally sufficient to outline the fuel cells performance.

3.1.2. I-V characteristics

The effect of the different loss mechanisms, already discussed in Chapter 2, on the actual output voltage of a real SOFC during loading is shown qualitatively in the following Fig. 3.1. As can be seen, even at open circuit condition (OCV), the cell voltage is lower than the theoretical Nernst voltage V_{th}, thermodynamically predicted by Eq. (2.9) (where it is referred as E). This difference ($V_{th} - OCV$) may be caused by different parasitic losses [31, 42], for example undesired electron leaks across the electrolyte or even gas leakage (imperfect gas tightness) of the system. These causes induce an unwanted fuel-utilization already at open circuit, thus lowering the Nernst voltage. Deviations of up to 5% from the theoretical OCV are acceptable for an adequate operation of the SOFC [43].

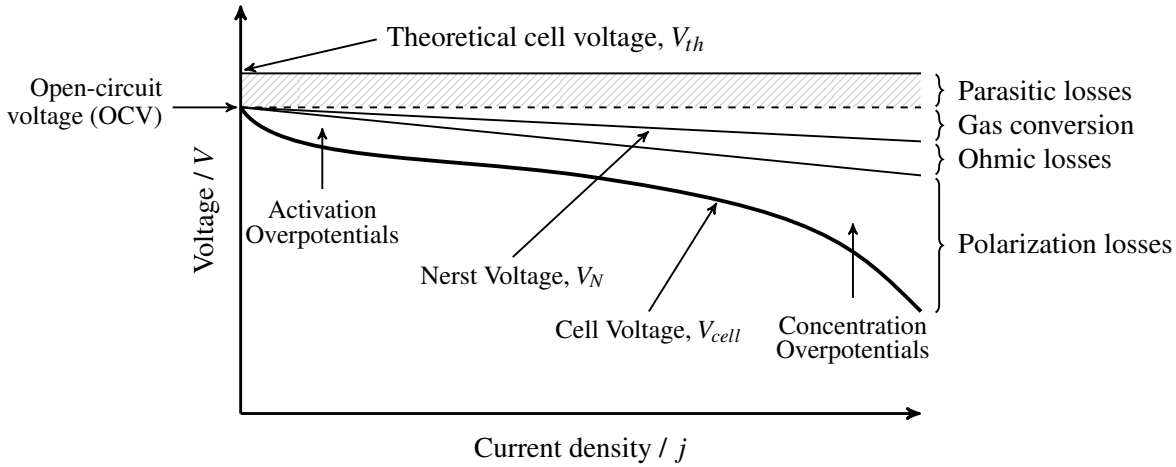

Figure 3.1. *Schematic representation of the I-V characteristics of a SOFC (adapted from Ref. [31]). It indicates the regions in which the different polarization losses (irreversibilities) are predominant.*

A second cell voltage drop caused by the fuel utilization is the so-called gas conversion loss. When a current load is applied to the cell, the measured cell voltage experiences a further decrease. Under operation of the fuel cell, the applied current density converts part of the fuel and the oxidant. The fuel conversion at the anode involves a decrease of the H_2 concentration along with an increase of the H_2O concentration. At the cathode, part of the O_2 is consumed, resulting in a decreased p_{O_2}. As a consequence, following Eq. (2.10) the Nernst-voltage V_N will decrease by increasing current density. Hence, V_N represents the driving force for the overall cell reaction and is therefore also called the electromotive force ($e.m.f.$).

It has to be pointed out that this voltage decrease is immanent in operation of the cell and has to be regarded as fuel utilization rather than as an actual loss process [31].

The two remaining losses responsible for the characteristic S-type shape of the I-V curve depicted in Fig. 3.1 are the ohmic and polarization losses. The polarization loss is the sum of the activation and concentration polarization. The strong (nonlinear) voltage drop at low current density is mainly caused by activation losses, related to the overcoming of the activation energies for the electrochemical reactions at the electrodes. The acuteness of this drop can therefore be used to potentially pinpoint criticalities in the fuel cell charge transfer mechanisms.

In the medium current range, the overall loss is dominated by the ohmic overpotential loss, therefore a more or less linear decrease of the cell voltage with increasing current density is observed. Because the electrolyte is by far the layer presenting the lowest conductivity, this region is often exclusively associated to this element. From the slope of this straight line, the physical quantity known as area-specific resistance (ASR) can be estimated in order to compare the overall performances of different cells.

At high current densities, the output voltage of the fuel cell once again drops rapidly due to mass-transport limitations at the electrodes (gas diffusion or concentration polarization). When high current densities are required from the cell, an under-supply of reactants in the active regions of the cell occurs, which is caused by the mass transport limitations of gases through the electrode layers or by simple fuel starvation. It should be highlighted that operation of the SOFC in this region should be avoided by all means because it induces rapid material degradation.

The discussed loss processes exhibit different dependencies on the operating parameters (temperature, concentrations of H_2 and H_2O in the fuel and O_2 concentration in the oxidant gas). Thus, a variation of the operating parameters results in differences in the characteristic shape of the measured I-V curves [46, 64]. Hence, although the fact that the I-V curve is somewhat a rudimentary technique, it still can provide inestimable information about the health of the fuel cell and its components.

3.2. Electrochemical impedance spectroscopy

3.2.1. Principles of EIS

Everyone knows that Ohm's law defines the electrical resistance in terms of the ratio between voltage, V, and current, I. However, the use of this well-known relationship is limited to only one circuit element -the ideal resistor.

However, the real world contains circuit elements that exhibit much more complex behavior. These elements force us to leave the simple concept of resistance, and in its place, use the impedance concept, a more general circuit parameter. Like resistance, impedance is a measure of the ability of a system to impede the flow of electrical current, but unlike resistance, impedance can deal with time -or frequency- dependent phenomena.

In an analogous way to Ohm's law, impedance Z is given by the ratio between a time-dependent voltage and a time-dependent current as follows:

$$Z = \frac{V(t)}{i(t)} \tag{3.1}$$

Electrochemical impedance spectroscopy is a very sensitive technique that maps an electrochemical system response to the application of a periodic small alternating current (AC) signal carried out at different frequencies. The EIS method takes advantage from the fact that the diverse physicochemical processes taking place in an electrochemical system differ in their characteristic

time constant and therefore each one is exhibited at different frequencies [239].

The most common and standard approach to measure the dynamic behavior (impedance) of an electrochemical system is by applying a small sinusoidal voltage (or current) perturbation, $V(t) = V_0 cos(\omega t)$, to the interface and monitoring the phase shift and amplitude, or real and imaginary parts, of the resultant current (or voltage) response, $i(t) = i_0 cos(\omega t - \phi)$, through the system [42]. In these expressions, $V(t)$ and $i(t)$ are the potential and current at time t, V_0 and i_0 are the amplitudes of the voltage and current signals, and $\omega = 2\pi f$ is the radial frequency.

In general, the current response of a system may be shifted in phase compared to the voltage perturbation. This phase shift effect is described by ϕ. This is, the current response will pose the same period (frequency) as the voltage perturbation but will generally be phase shifted by an amount ϕ.

Following Eq. (3.1), the sinusoidal impedance response of a system is:

$$Z = \frac{V_0 cos(\omega t)}{i_0 cos(\omega t - \phi)} = Z_0 \frac{cos(\omega t)}{cos(\omega t - \phi)} \tag{3.2}$$

Alternatively, the impedance of the system can be expressed as a complex number as follows [27]:

$$Z(\omega) = \frac{V_0 e^{j\omega t}}{i_0 e^{(j\omega t - j\phi)}} = Z_0 e^{j\phi} = Z_0(cos\phi + jsin\phi) \tag{3.3}$$

Where its real and imaginary components are expressed, respectively, as:

$$Re[Z(\omega)] = Z'(\omega) = Z_0 cos\phi \tag{3.4}$$

$$Im[Z(\omega)] = Z''(\omega) = Z_0 sin\phi \tag{3.5}$$

However, impedance is only defined for systems that satisfy contemporaneously the conditions of causality, linearity and time-invariance; i.e. only if the studied system satisfies such conditions, the mathematical properties above-mentioned can be applied. Although electrochemical systems are usually non-linear, this problem is circumvented by using small-signal voltage perturbations in impedance measurements. This signal is generally small enough to confine us to a pseudo-linear segment of the cell's I-V curve. In a linear (or pseudo-linear) system, the current response to a sinusoidal potential will be a sinusoid at the same frequency but shifted in phase [27, 42].

On the other hand, impedance measurements are generally performed for a discrete quantity of frequency values in a defined frequency range and the recorded impedance values are usually plotted in the complex plane. If the real part is plotted on the X-axis and the imaginary part on the Y-axis of a chart, the resulting curve is known as *Nyquist plot*.

Another popular graphic representation of the impedance is the *Bode plot*, that depicts the dependency on the imposed frequency of the impedance modulus or the phase shift. Unlike the Nyquist plot, the Bode plot does show frequency information. However, impedance data are most often plotted as a Nyquist plot.

3.2.2. EIS measurements on SOFCs

While the I-V curve provides general quantification of fuel cell performance and only the overall losses can be identified, a more sophisticated test is required to accurately differentiate between all the major sources of loss in a fuel cell. In this task, EIS is the most widely used technique by which a breakdown of losses can be made unfolding complex electrochemical systems such as a SOFC.

Solid oxide fuel cells couple very diverse mechanisms and processes making them non-linear systems. Hence, in normal EIS practice, a small (1-20 mV) AC signal is applied to the cell [27, 42, 240], in such a way that the response of the cell can be considered linear, causal and time invariant, and so the mathematical properties and impedance concept can be applied.

In this work the fulfillment of the above-mentioned preconditions was verified by applying the Kramers-Kronig (K-K) relations, which will be latter discussed.

A frequency response analyzer (FRA) imposes the small amplitude AC signal to the SOFC and measures the amplitude of the response signal and the phase shift between voltage and current.

Furthermore, since EIS measurements are carried out in a defined range of frequencies and for a finite number of points, in order to obtain the maximum possible information from the phenomena driving the operation of SOFCs, these measurements should be performed from very high frequencies (c.a. 100 kHz) to very low frequencies (10 mHz or below) at relatively short intervals (at least 10 points per decade on a logarithmic scale).

Recalling Eq. (3.4) and Eq. (3.5), the output signal from the SOFC can be divided into a real and an imaginary part, and these can be plotted generating a Nyquist plot, Fig. 3.2, from which the electrical u ohmic resistance (R_0) and the polarization resistance (R_{pol}) can be discerned.

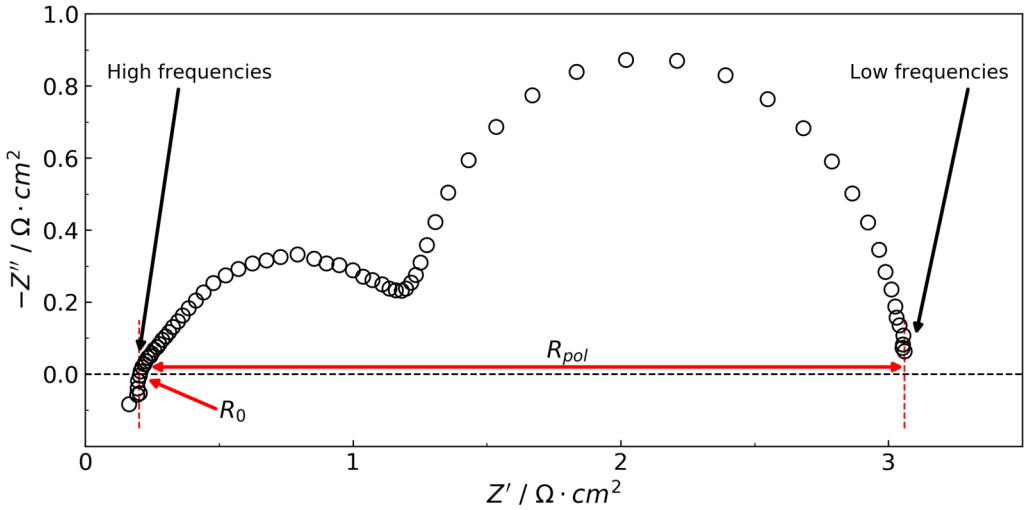

Figure 3.2. *Typical Nyquist plot of a single SOFC under hydrogen operation. Z' represents the real axis and $-Z''$ the imaginary axis.*

The high frequency intercept (for $\omega \to \infty$) with the real axis (Z') corresponds to the purely ohmic resistance R_0 of the cell, whereas the intercept at the lower frequency (for $\omega \to 0$) is identical to the total cell resistance. The difference between the low and high frequency intercept is the so-called polarization resistance R_{pol} of the cell. R_{pol} accounts for all the activation and mass transport losses of both the anode and cathode sides, meanwhile the total cell resistance is the sum of each single polarization resistance caused by the loss mechanisms explained in chapter 2.

Further information can be given by accepting the general assumption that the small arc appearing in the high frequency region is related to the fast charge transfer mechanism involved in the electrochemical reactions at the anode and at the cathode, which is considered valid for SOFC cells [241].

By similar considerations, the bigger arc appearing in the low frequency region is often associated to the mass transport losses related to the gas diffusion in the porous matrix of the electrodes; it is therefore a measure of the diffusion resistance which causes the voltage to rapidly drop at high current densities.

On the other hand, regarding the ohmic resistance, R_0, a new concept is introduced: the Area-Specific Resistance (ASR). The area-specific resistance is a common measure to judge the performance of an electrochemical system. It is the ohmic resistance normalized by the cell active area (AA_{cell}) to a square-centimeter, i.e. it is based on 1 cm^2 [23], so that the units for the ASR is Ωcm^2 [242].

ASR accounts for the fact that fuel cell resistance scales with area, thus allowing fuel cells of different sizes to be compared. It is calculated by multiplying the fuel cell ohmic resistance R_{ohmic}

or R_0 by its active area:

$$ASR = AA_{cell} \cdot R_0 \tag{3.6}$$

It is generally necessary to use area-normalized fuel cell resistances when discussing ohmic losses [27]. By using ASR, ohmic losses can be calculated from current density as:

$$\eta_{ohmic} = j \cdot ASR \tag{3.7}$$

A well-performing electrochemical system is characterized by a small ASR, e.g., for tests that are closer to fundamental research (e.g. single cell tests) degradation is often expressed as an increase of area specific resistances [163]. Values for the ASR are often found in the literature. However, when using literature data for ASR, it is important to verify its definition since some researchers also include the activation and concentration polarization as well as the ohmic polarization in the ASR definition [243, 244].

The ASR is a function of the cell design, material choice, manufacturing technique, and, operating conditions. Nonetheless, in an impedance spectrum of a fuel cell, the ohmic resistance is invariant with gas concentration, while the part of the impedance that is related to mass transport and kinetics changes markedly with anode feed composition. Hence, the ASR is a key performance parameter, especially in high-temperature fuel cells, where the ohmic losses often dominate the overall polarization of the cell.

Even though the information obtainable from the analysis of Nyquist plots provides quantitative measurement about the polarization losses, nothing can be said about which process, anodic or cathodic, is predominant on a given amount of polarization loss; moreover, since the EIS response appears very extended, it is difficult to clearly visualize the contributions of single physicochemical processes to the total polarization resistance, hence hindering a deep and complete comprehension of the evolution of these processes and their dependency to the operating conditions of the cell.

Additionally, impedance spectra obtained on a full SOFC (or even a half-cell or symmetric cell) are difficult to interpret due to many processes involved and partly overlap in frequency range for these processes. Therefore, at least the following three aspects should be considered when applying electrochemical impedance spectroscopy for analysis of SOFC: 1) proper impedance spectroscopy measurements, 2) intelligent use of different test conditions to analyze differences in contribution of losses, and 3) modeling the experimental impedance data to obtain the quantification of the breakdown of losses [119].

Regarding aspect 1, this includes measurements in the relevant frequency range, i.e., typically from 100 kHz to 0.1 Hz for SOFCs with an appropriate number of points recorded per frequency decade (i.e., 10-15 points per decade) if quantitative analysis is desired. Frequencies should be set to minimize effects of electronic noise from other electronic devices in the cell test rig. Furthermore, the amplitude of the AC signal for the impedance measurements should be adjusted to be small enough to provide a small perturbation in the linear region of the system and still be large enough for a reasonable signal-to-noise ratio. Of course, the signal-to-noise ratio will be also optimized by running many cycles at the same frequency, e.g., 5-50 cycles depending on frequency range and time available for the measurement. Measuring an EIS spectrum takes time (often up to many hours), since the system being measured must be at a steady state.

Regarding aspect 2, intelligent use of impedance spectroscopy at different test conditions provides valuable information on different processes constituting the total loss. Impedance spectra at different temperatures but same gas compositions will enable the calculations of the activation energies and typically enable the separation of non-thermally activated processes from thermally activated processes. Impedance spectra at different gas compositions can be used to analyze the different polarization losses dependency on gas composition and "one electrode sided" gas changes can be used to separate which impedance contributions originate from each of the electrodes for a full cell test.

The use of impedance spectra at different gas compositions can provide qualitative but model-independent, electrode-specific information on different impedance contributions and assist in the analysis of which electrode -or both electrodes- that degraded during long-term testing and provide information regarding the approximate summit frequencies for several of the different losses contributing to the total polarization loss for the full SOFC.

Regarding aspect 3, to quantitatively characterize the different impedance contributions, EIS data are typically analyzed in terms of equivalent circuit models applying a complex non-linear least squares (CNLS) fitting routine. However, a complementary way of analyzing impedance spectra is via distribution of relaxation times (DRT). The latter method will be discussed later in this chapter.

There will be cases where it is not possible to perform a breakdown of the losses of a full SOFC based on the measured impedance spectra, e.g., because of overlapping impedance contributions or quality of the spectra. However, there can still be useful information to obtain from the impedance spectra in terms of the ohmic resistance and the total polarization resistance of the SOFC.

3.2.3. Distribution of relaxation times method

Recently, the distribution of relaxation times is regarded as a powerful representation of EIS, exhibiting the state-of-the-art frequency resolutions to resolve electrochemical processes [63]. Similar to Nyquist and Bode representations, DRT is another representation of complex impedance.

The impedance of high-performance batteries and fuel cells usually contains a number of physicochemical processes related to different loss mechanisms in the cathode, electrolyte, anode and their interfaces. In this task, the distribution of relaxation times method allows deconvoluting the impedance data providing a high frequency resolution that enables clear distinction between the many processes contributing to the total polarization loss. Hence, the output signal of an electrochemical cell is correlated to diverse physicochemical processes occurring at distinctive relaxation times and with different strengths.

Therefore, by applying DRT each electrochemical process is resolved by its intrinsic time constant. The magnitude of each process is assigned as a specific share of the overall polarization resistance.

The relation between the impedance spectrum $Z(\omega)$ and the distribution function of relaxation times $\gamma(\tau)$, which is for sake of simplicity often displayed as a distribution $g(f)$ vs. the relaxation frequencies, is given by Eq. (3.8) [90, 91].

$$Z(\omega) = R_0 + Z_{pol}(\omega) = R_0 + R_{pol}\int_0^{\infty} \frac{\gamma(\tau)}{1+j\omega\tau} d\tau \tag{3.8}$$

where Z_{pol} is the polarization impedance, R_0 and R_{pol} are respectively the overall electrical resistance and polarization resistance of the cell, $\omega = 2\pi f$ the angular frequency of the input signal, and τ the continuous relaxation time.

However, the complex function, Eq. (3.8), can be divided into a real part (Z') and an imaginary part (Z''). Thus, in the frequency domain and in the discrete form, the SOFC cells real and imaginary impedances can be expressed by means of Eq. (3.9) and Eq. (3.10) respectively, both of them linked by means of the Kramers-Kronig relations [43, 85].

$$Z'(\omega) = R_0 + R_{pol}\sum_k \frac{1}{1+(\omega\tau_k)^2} a_k \tag{3.9}$$

$$Z''(\omega) = R_{pol}\sum_k \frac{\omega\tau_k}{1+(\omega\tau_k)^2} a_k \tag{3.10}$$

where τ_k is the relaxation time of process k, and a_k is the contribution of process k to the total polarization loss.

The relation between the real and imaginary functions makes that only one of them is needed to obtain the relaxation-time distribution function (a_k). In this work the imaginary part of the data has been employed attending to the ease of handling one single set of data (R_{pol}) rather than two (R_0 and R_{pol}). Consequently, rewriting Eq. (3.10) in matrix form and introducing the constant R_{pol} value into the distribution vector (i.e. $b_k = R_{pol}a_k$) gives [85, 89]:

$$\begin{pmatrix} Z_1'' \\ \vdots \\ Z_n'' \end{pmatrix} = \begin{pmatrix} \frac{-\omega_1\tau_1}{1+(\omega_1\tau_1)^2} & \cdots & \frac{-\omega_1\tau_n}{1+(\omega_1\tau_n)^2} \\ \vdots & \ddots & \vdots \\ \frac{-\omega_n\tau_1}{1+(\omega_n\tau_1)^2} & \cdots & \frac{-\omega_n\tau_n}{1+(\omega_n\tau_n)^2} \end{pmatrix} \begin{pmatrix} b_1 \\ \vdots \\ b_n \end{pmatrix} \tag{3.11}$$

which for simplicity will be expressed as follows:

$$\mathbf{Z''} = \mathbf{Kb} \tag{3.12}$$

The mathematical problem with the above-mentioned approach arises from the inversion of Eq. (3.8), an ill-posed problem (Fredholm integral) that requires special methods to be solved [90]. Eq. (3.12) is also an example of a Fredholm integral equation of the first kind with a product Kernel (**K**), making the direct extraction of (**b**) a mathematically ill-posed problem. Ill-posed problems arise when the solution is very sensitive to small variations in the components of the input vector (i.e. unstable with respect to measurable errors) [85, 90]. Even if there are numerous methods which can solve these kind of inversion problems, the most renowned and reliable one is the Tikhonov regularization algorithm [85, 90, 91]. The Tikhonov regularization only requires one important parameter, the regularization parameter (λ), to dampen the effects of the contributions from data errors and rounding errors which dominate the solution. This method provides a solution for the following minimization problem, Eq. (3.13), with smoothness as a secondary condition, significantly improving the quality and reliability of the DRT with limited error sources and good stability vs. noise in the measured spectra.

$$\min_b \{\|\mathbf{Kb} - \mathbf{Z''}\|_2^2 + \lambda^2\|\mathbf{b}\|_2^2\} \tag{3.13}$$

λ is the self-consistent regularization parameter that constrains and determines the smoothness of **b**. Thus, since the solution to the previous minimization problem, given by Eq. (3.14), is gov-

erned by λ, the shape of features in the distribution function highly depends on the value of the regularization parameter: too small values result in artificial meaningless peaks while too large values tend to over-smooth the shape of $\mathbf{b}$, hence suppressing valuable information. This is, low values can cause erroneous oscillations not related to the physicochemical processes of the system, whereas high values may result in features not clearly distinguishable [91]. Therefore, in the case of excellent data quality or synthetic data; a small regularization parameter can be used - for noisy data the regularization parameter has to be increased to suppress false peaks and oscillations in the DRT.

$$\mathbf{b} = \left(\mathbf{K}^T\mathbf{K} + \lambda^2\mathbf{I}\right)^{-1}\mathbf{K}^T\mathbf{Z}'' \tag{3.14}$$

where $\mathbf{I}$ is the identity matrix.

A general rule for the choice of the regularization parameter does not exist, however, various methods have been developed for the selection of optimal regularization parameters (e.g. Discrepancy Principle, L-curve, Cross-Validation) the L-curve being the most extended one in applied mathematics due to its robustness and ability to treat perturbations consisting of correlated noise [85, 89]. The L-curve is basically a trade-off curve between two quantities that ought to be controlled contemporaneously: data fitting and contribution from data errors. In this method, a plot of the solution norm versus the regularization parameter provide an L-shape curve whose corner allowed to identify the suitable parameter. This is, the optimum value of λ corresponds to the angle or corner of the L-shaped curve, which is the point where the residual norm and the solution norm have a minimum value contemporarily. Considering the particular example from Fig. 3.3, the optimum value is in the proximities of $\lambda = 0.01$.

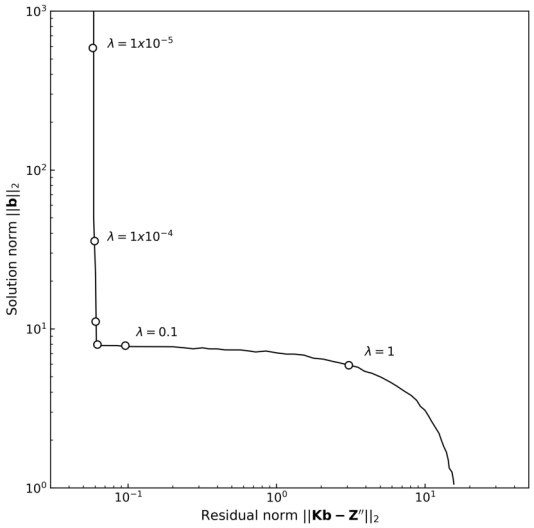

Figure 3.3. *L-curve for Tikhonov Regularization, adapted from [43].*

Therefore, in the present work the Tikhonov regularization algorithm and the optimum value of the regularization parameter have been solved implementing an already developed, by an ENEA's PhD student [43], in-house program run in MATLAB®. Nevertheless, there are several commercial and user-free computer programs running on different platforms which allow the solution of the Tikhonov regularization algorithm, e.g. Ftikreg [85, 90].

Fig. 3.4 illustrates the distribution function (dashed line) obtained from the DRT analysis and the imaginary part of the impedance (continuous line). A definite number of peaks rise over the zero line, being each one of these peaks (or cluster of them) the response of a specific physical or chemical process to the AC input signal of the EIS. Thus, it shoud be noted that the area beneath the DRT curve represent the resistance of the cell.

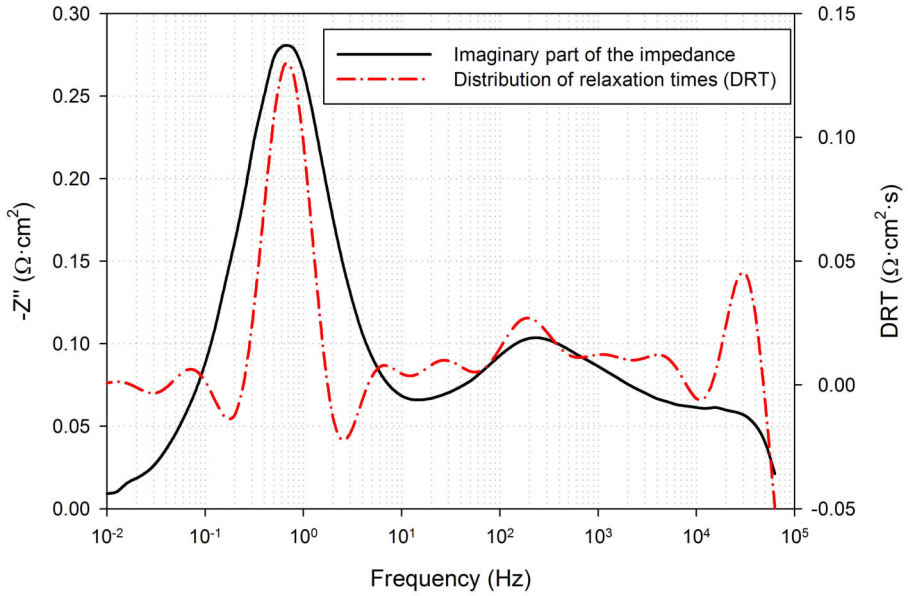

Figure 3.4. *Imaginary component of impedance and DRT spectrum, taken from [43].*

It is important to underline that the quality of the experimental data plays a fundamental role in obtaining an interpretation of the DRT plots. If the experimental spectra are affected by instrumental interference that cause a loss in the linearity of the EIS response, scattered signals appear in the EIS spectra that will be converted into ghost peaks in the DRT plots, hampering a correct identification and analysis of the processes. Therefore, high quality impedance spectra are required for proper DRT analysis.

In this work the fulfillment of the above-mentioned preconditions was verified by applying the so-called Kramers-Kronig (K-K) relations. The K-K relations are used to evaluate EIS data quality. They demand that causal, complex plane spectral data shows dependence between magnitude and

phase. The K-K relations will always be true for EIS data that is linear, causal, and stable.

Hence, a Kramers-Kronig test basically assesses the validity of the K-K relationships through all the frequency range examined. In this work, the K-K test was performed by means of the Kramers-Kronig test for Windows [245], software developed by B.A. Boukamp et al. [246].

An example of the residual errors plot of such a test is shown in Fig. 3.5. The distribution of the points (red dots for the real part and blue dots for the imaginary part of the impedance) is random for all the frequency range, so when the maximum error lies below 5%, the experimental data can be considered reliable.

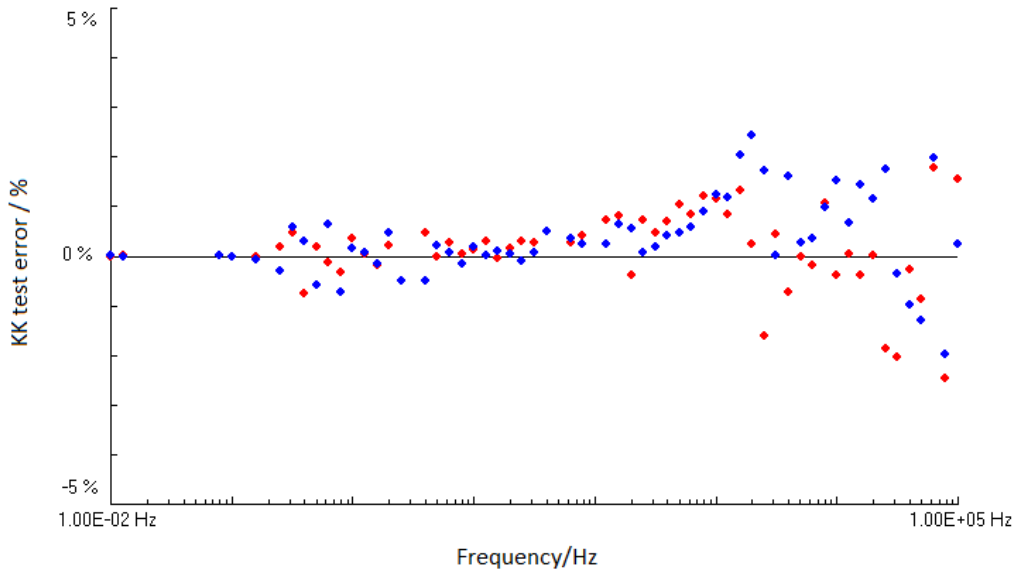

Figure 3.5. *Kramers-Kronig test results for the EIS measurement performed on a tested single cell sample. Red dots are related to the real part of the impedance, while blue dots are related to the imaginary part.*

It should be mentioned that in some cases, especially when high water contents are fed to the cell, the low-frequency region of the spectra is affected by a more significant error, but being still acceptable.

As it will be explained in the discussion of experimental results, all the EIS measurements were carried out in OCV conditions, which have resulted acceptable according to the K-K test.

3.3. Gas chromatography

Gas chromatography (GC) is an analytical technique used for the analysis of the gas mixtures composition. Data from this technique can be used to determine the mole fractions of the gaseous

products from the reactions taking place in the fuel cell. This technique has been already applied when analyzing gas compositions in SOFCs. However, most analyses in the literature are often reported on a dry basis [51, 77, 78]. In a dry product analysis, the mole fractions are given for all gaseous products except the water vapor [28].

The GC technique is based on the different retention (elution) times that the different gas species possess when they pass through a stationary phase (solid phase), carried by a mobile phase (gas carrier). When a known volume of gaseous sample is injected into the inlet of the column, the carrier gas (usually an inert gas such as helium) sweeps the molecules of the chemical species through the column. The rate at which the gas species (molecules) pass along the column depends on the strength of adsorption, which in turn depends on the type of molecule, various physical and chemical properties and on the interaction with the stationary phase materials. Since each type of molecule has a different rate of progression, the several components of the sample mixture are separated as they progress along the column and reach the end of the column at different times (retention time). A specific detector (e.g., thermal conductivity detector -TCD-, flame ionization detector -FID-) is used to monitor the outlet stream from the column; thus, the time at which each component reaches the outlet and the amount of that component can be determined. The mixture components are identified (qualitatively) by the order in which they emerge (elute) from the column and by the retention time. The comparison of retention times is what gives GC its analytical usefulness. A more detailed description of the GC technique can be found elsewhere [247].

For GC analyses, a key point is the method employed, i.e., the conditions in which the GC equipment (gas chromatograph) operates for a given analysis. Method development involves determining what conditions are adequate or ideal for the required analysis. Conditions which can be varied to accommodate a required analysis include inlet temperature, detector temperature, column temperature and temperature program, carrier gas and carrier gas flow rates, the column stationary phase, diameter and length, inlet type and flow rates, sample size and injection technique. Depending on the detector(s) installed on the GC, there may be a number of detector conditions that can also be varied.

The result of this kind of analysis is called a chromatogram, Fig. 3.6. It provides a spectrum of peaks from the sample, related to the gas species forming the mixture, and detected as a function of the retention time.

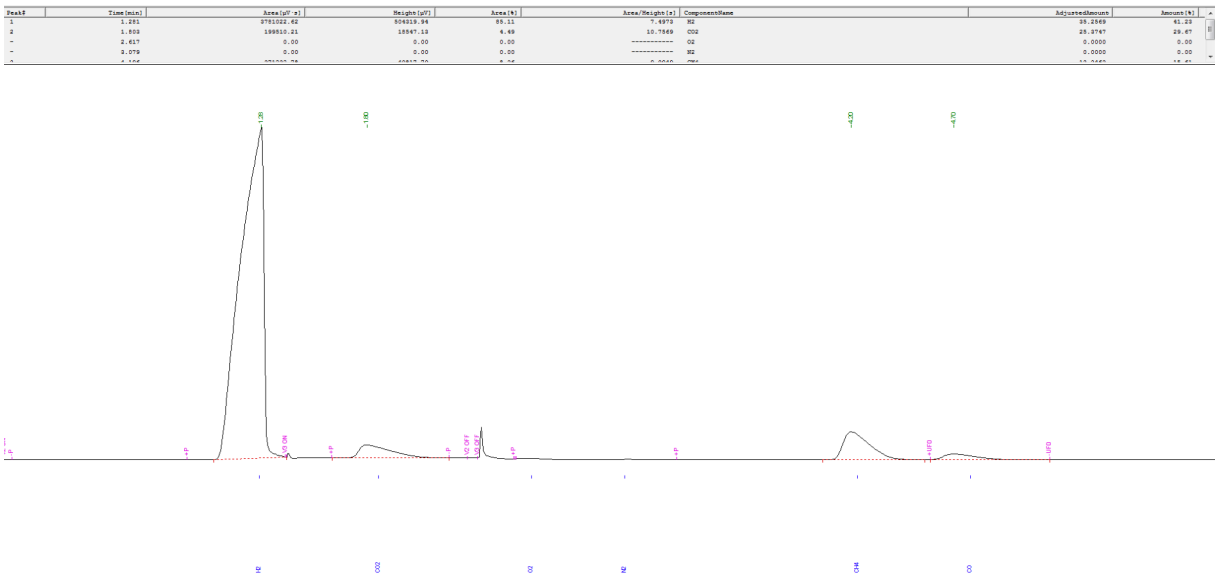

Peak#	Time [min]	Area [µV * s]	Height [µV]	Area [%]	Area/Height [s]	ComponentName	AdjustedAmount	Amount [%]
1	1.281	9781022.62	904319.94	85.11	7.4973	N2	35.2569	41.23
2	1.809	199810.21	18547.13	6.49	10.7769	CO2	25.0767	29.67
-	2.617	0.00	0.00	0.00	----------	O2	0.0000	0.00
-	3.079	0.00	0.00	0.00	----------	N2	0.0000	0.00

Figure 3.6. *Typical chromatogram from a gas analysis.*

From a chromatogram, qualitative data can be obtained. The area under a peak is proportional to the amount of a single gas species (analyte) present in the chromatogram. Hence, by the integration of the peak obtained by GC, the concentration of the gas species in the original sample can be determined. On a percentage basis: the ratio between the areas of two peaks will be equal to the ratio of their concentration in the gas mixture. The concentration of any compound can be calculated through a calibration curve created by finding the response for a series of concentrations of each gas species using a standard. Regarding the retention time of single species, qualitative data can be obtained based on literature data (most often employing databases within the analysis software provided with the instrument).

The GC system at ENEA research center, Fig. 3.7, consists of two gas chromatographers CLARUS 680 (PerkinElmer) customized by ARNEL. They were adapted with an auto-sampler and special columns that allow to analyze the gas samples *in-operando*, i.e., under real steam contents in fuel cells, unlike what is generally reported in the literature when this type of analysis is included. The whole system consists of 4 detectors: two universals (Thermal Conductivity Detector-TCD with a sensibility: 100 ppb), one specific for hydrocarbons (Flame Ionization Detector-FID with a sensibility of 1 ppb) and one for Sulphur compounds (Flame Photometric Detector-FPD with a sensibility of 0,001 ppb) [248]; thus, allowing different and very particular kind of analyses. Both GCs consist of 2 different kind of detectors (TCD-FPD and TCD-FID), with specific columns each. Therefore, depending on the type of gas analysis and the components in the mixture, one detector or the other one is employed. Table 3.1 indicates some characteristics of the columns corresponding to the different detectors that integrate the GC system, including the compounds that can be detected.

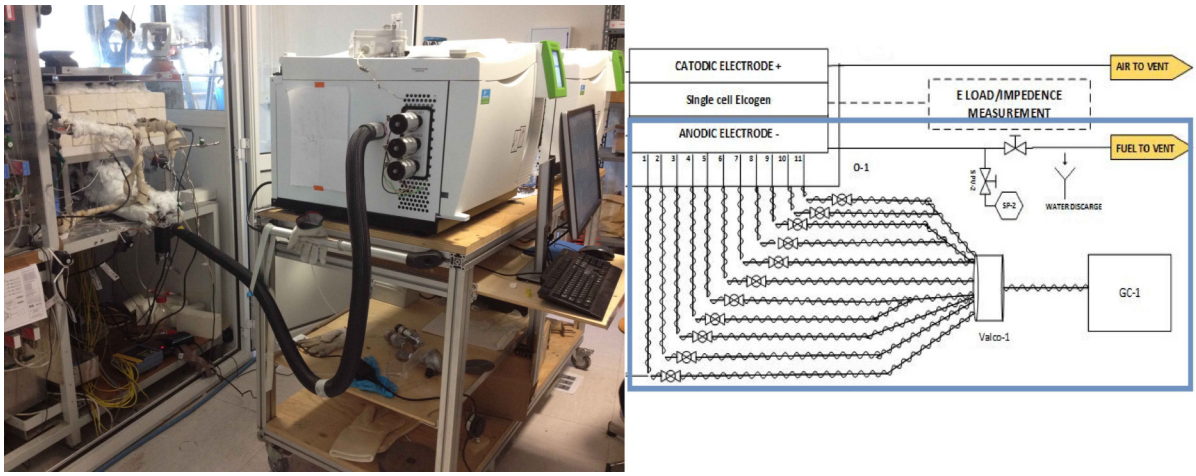

Figure 3.7. *GC system at ENEA research center.*

This configuration allows to perform *in-operando* gas composition analyses of the anode, allowing qualitative and quantitative analysis, showing on this way the evolution of the chemical and electrochemical reactions during the process. It is a very particular system in the world. This GC system has been already employed for the analysis of specific compounds present in the fuel supplied to the fuel cells (e.g., H_2, CO, CO_2, CH_4, H_2O, N_2, O_2 and different kind of contaminants such as Sulphur compounds and siloxanes) [64, 74].

Table 3.1. Characteristics of the columns according to the different detectors of the GC system.

Thermal conductivity detectors-TCD	Column I: HayeSep Q and Molecular Sieve 5A. Compounds: Specific for the analysis of matrix compounds (H_2, CO_2, N_2, CO, CH_4, O_2). Column II: Hayesep P. Compounds: Specific for the analysis of NH_3 and H_2O.
Flame Ionization Detector-FID	Column: Elite-5 Capillary Column 0.53 mm. Compounds: Specific for the analysis of Hydrocarbons (CH_4, Benzene, Toluene, Naphthalene etc.) and Siloxanes: (D4-D5-L2).
Flame Photometric Detector-FPD	Column: Silica Bond Plot capillary column 0,32 mm. Compounds: Specific for the analysis of Sulphur compounds (H_2S, COS, DMS, SO_2, CH_3SH, EtSH, THT).

Hence, in the gas analyses for the present work the GC with the TCD-FPD detectors is used, from which the TCD detector with its corresponding columns (Haysep Q and Molecular Sieve 5A) were employed.

3.4. Other analysis tools

3.4.1. SEM and EDS techniques

Scanning Electron Microscopy (SEM) allows for visual observation of an area of interest in a completely different way from that of the naked eye or even normal optical microscopy. SEM magnifies a specific sample region using a high energy focused beam of electrons. When the beam of electrons hits the sample, it causes secondary electrons to be released from the sample which are detected to provide an image based off the topography of the surface [249].

The sample region evaluated with SEM analysis can be also analyzed to determine the specific elements that comprise the sample by Energy Dispersive X-Ray Spectroscopy (EDS). X-rays are also released from the surface of the sample that carry a unique energy signature that are specific to elements found in the sample [250]. EDS provides data about the chemical composition of the sample and provides additional data about the features that are observed in the SEM micrographs. This combined technique is referred to as SEM-EDS or SEM-EDX analysis.

Backscattered electron images in the SEM display compositional contrast that results from different atomic number elements and their distribution [251]. EDS allows identifying what those particular elements are and their relative proportions (e.g., atomic %).

Hence, SEM-EDS analysis being a great method for determining particle sizes and elemental composition, it is also a go-to analytical technique for performing nano-characterization. It allows for the ”inspection” of areas of interest in a much more informative way. Contamination and failure analysis are common situations in which SEM analysis pared with EDS is very valuable [98, 101].

In the fuel cells field, SEM/EDS analysis are carried out as a post-test or post-mortem analysis on tested cell, in order to identify degradation processes on the cell components. This tool allows an in-depth analysis of the samples down to the micron and submicron scale. Hence, such analyses are usually performed to verify hypothesis or drawn conclusions based on other analysis and techniques applied during cells operation, such as the impedance analysis. Therefore, investigation of the microscopic features on particular samples enables a comprehensive evaluation of the morphological evolution due to the operating conditions and degradation phenomena.

For the present work, electrodes surfaces were examined using a JEOL JSM-5510LV SEM, and the evaluation of the chemical composition was performed by means of the combined technique SEM/EDS analysis.

Chapter 4

EXPERIMENTAL CAMPAIGN, TESTING PROCEDURES AND TEST STATION DESCRIPTION

4.1. Internal reforming experimental campaign

An experimental campaign is proposed in order to compare the performance of commercial single cells running under three different grades or cases of internal reforming, namely: low internal reforming (LIR), intermediate internal reforming (IIR) and complete internal reforming (CIR), determining under which conditions is possible to achieve the best tradeoff in terms of syngas/H_2 production (within the cell), electrical power generation and degradation rate of the cell.

Accordingly, Table 4.1 summarizes the proposed experimental campaign. The molar or volume percentage (mol% or vol%) for each gas species forming the gas mixtures and the total flows per square centimeter (normalized total flows) fed to the anode and cathode under the three different gas compositions proposed, simulating the three grades of internal reforming already-mentioned, are presented.

For each case, tests have been carried out at two different temperatures: 650 °C and 700 °C, and at three different loading conditions: OCV, 15 A and 25 or 30 A. The highest loading condition has been defined according to the polarization curves obtained under each composition. Each test, corresponding to the experimental campaign, was initiated from a reference composition, which is also shown in Table 4.1, referred as H_2 reference.

Additionally, in order to evaluate the degradation rate and stability of these commercial single

cells, as well as to prove the multisampling set-up under continuous or uninterrupted operation, an endurance performance test under IIR composition at 650 °C is carried out.

Table 4.1. Internal methane reforming experimental campaign.

	Anode		Cathode			
	Composition [%]	Total flow† [Nml/min · cm^2]	Composition [%]	Total flow† [Nml/min · cm^2]		
	$N_2/H_2/CO/CO_2/CH_4/H_2O$		AIR		T [°C]	i [A]
LIR	0/57/6/8/2/27	4.8	100	18.5	650/700	0/15/30
IIR	0/31/4/23/12/30	4.8	100	18.5	650/700	0/15/30
CIR	0/0/0/0/22.4/77.6	4.5	100	18.5	650/700	0/15/25
Ref. ‡	50/50/0/0/0/0	8.6	100	18.5	–	–

† Normalized total flows, i.e., per cm^2 of active area. Based on IUPAC Former, ISO 10780 Normal Conditions: P=101.325 kPa and T=273.15 K

‡Reference composition or H_2 reference

The experimental conditions for each particular case will be more extensively discussed in section 4.5.

To carry out the proposed experimental campaign, an innovative and very particular single SOFC test bench is used (fully described in section 4.2.2), which enables the simultaneous sampling of temperature and localized gas compositions in the anode in order to collect data on the evolution of anode reactions along the surface during internal reforming.

4.2. Single cell test station and experimental materials

4.2.1. Tested samples

A new generation of commercial intermediate-temperature solid oxide fuel cells (IT-SOFCs), manufactured by Elcogen AS (Tallinn, Estonia), are tested in this study. This kind of cells are based on a 405±20 µm-thick supporting and active NiO/YSZ cermet anode, a 3/6 µm-thick YSZ electrolyte, and a 12±5 µm-thick lanthanum strontium cobaltite (LSC) cathode with a gadolinum-doped ceria (GDC) barrier, as summarized in Table 4.2. The standard size of these anode supported planar-type cells is 12x12 cm with an active area of 11x11 cm^2, determined by the cathode area (see Fig. 4.1).

Table 4.2. Technical data of the new generation anode-supported cells (ASC-400B) from Elcogen AS.

Component	Material	Thickness [µm]	Standard size [cm]	Suggested operating temperature [°C]
Anode	NiO/YSZ	405±20 †	12x12	600-750
Electrolyte	YSZ	3/6	12x12	
Barrier	GDC	12±5 ‡	12x12	
Cathode	LSC		11x11	
Total (cell)	–	415±45	12x12	

† Half cell: anode support layer+anode functional layer+electrolyte

‡ Cathode+barrier

The anode substrate is produced by tape casting of NiO/YSZ suspensions; upon this substrate, the electrolyte layer is deposited by tape casting a dense YSZ suspension and sintered to form a dense film. The GDC diffusion barrier and the LSC cathode layer are applied by subsequent screen printing and sintering processes.

Figure 4.1. *Elcogen cells tested in this work, where anode (in green) and cathode (in black) can be distinguished.*

Elcogen AS is currently the only company in the world capable of manufacturing low temperature, ceramic SOFC cells and stacks. Elcogen's SOFC technology can already begin to operate at 600 °C while other SOFCs require 750 °C or even 900 °C. A much lower operating temperature allows fuel cell stack and system manufacturers to use low-cost materials (at the cell, stack and system level) and components, which are not practical at higher operating temperatures. Reduced system costs, facilitated by these low-cost materials, are a critical component of bringing SOFCs to the mass market.

4.2.2. Multisampling set-up

The proposed experimental campaign is carried out through a single cell test station equipped with an innovative spot-sampling set-up that allows for *in-situ* and *in-operando* characterization of the anode processes of single SOFCs via simultaneous gas analysis and temperature measurements. This experimental facility or test unit consists of two main parts: 1) gas dosing and humidification system and 2) the innovative spot-sampling set-up, as shown in the piping and instrumentation (P&I) diagram in Fig. 4.2.

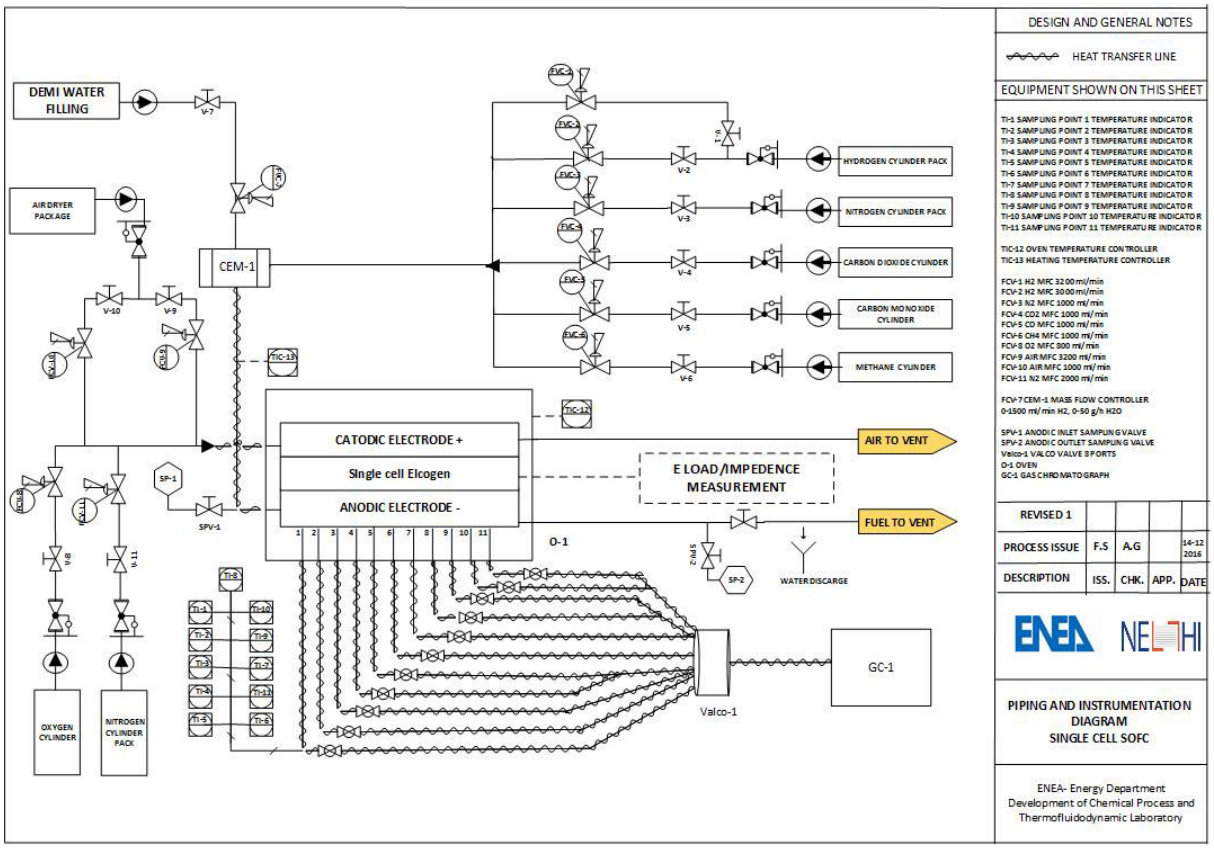

Figure 4.2. *P & I diagram of the single cell test station.*

4.2.2.1. Gas dosing and humidification system

The gas dosing and humidification system consists of a set of Bronkhorst® mass flow controllers that regulate the inlet gas flow rates of H_2, CO, CO_2, CH_4 and N_2 to the anode, and air to the cathode. Cathode flow can be further enriched or depleted in its oxygen content by means of N_2 and O_2 mass flow controllers specifically for the cathode side. Regarding humidification system of the anode, a liquid flow meter (FCV7) and a controlled evaporator and mixer (CEM) are used to adjust and deliver the required water content in the fuel gas.

The single cell test station is equipped with a temperature programmed furnace, in which the single cell housing is inserted. Eleven sampling capillary tubes merge from the bottom of the furnace, and converge to a multi-port valve, which selectively drives the gas mixture coming from each single sampling spot to a gas-chromatograph. Inside each capillary tube, a thermocouple is inserted, ending in the immediate proximity of the corresponding holes. To reduce the pressure drop on the cell and to avoid the mixing of the gas coming from different spot samplings, each capillary line is also equipped with a single control valve.

In order to prevent water condensation, anodic and cathodic inlet pipelines, anode outlet and capillary sampling lines are all trace heated using XtremeFlex® cloth and BriskHeat® HSTAT silicon rubber heating tapes. The inlet lines are heated from the point of water injection up to the furnace entry, mainly to pre-heat the gas mixture. Anode exhaust is driven to a hermetic glass container for the water condensation, and the exhaust gas is then led to the vent. The cathode exhaust is driven to the vent as well.

To record polarization curves, the test station is equipped with a Kikusui PLZ664WA electronic load connected in series with a Delta Elektronika SM-30-100D power supply, measuring the cell potential by means of a TTi 1604 digital multimeter, and with a Solartron 1260 Impedance Gain/Phase Analyzer module coupled with a Solartron 1287 Electrochemical Interface for the electrochemical impedance spectroscopy measurements.

4.2.2.2. Multisampling set-up

The core of the system, the innovative spot-sampling or multisampling set-up (shown in detail in Fig. 4.3), enables the measurement of temperature and gas compositions using eleven sampling points distributed throughout the anode allowing to collect data on the evolution of anodic reactions. Simultaneous temperature measurements and gas chromatography are employed to detect the variation of thermodynamic and chemical conditions across the anode in steady state and in real time. Consequently, chemical and temperature gradients are available and can be recorded during selected modes of operation of the cell.

The particular location of each sampling point, Fig. 4.4, was chosen in such a way as to minimize interference in the flow pattern across the anode, but maximizing the spatial information of the measurements. Thus, allowing to investigate the evolution of chemical reactions occurring during the operation of the cell, identified with a spatial resolution covering the whole surface of the anode. Sampling settings are tailored to analyze representative specimens of anode gas without altering local conditions. Moreover, as previously mentioned, the novel cell housing allows for full electrochemical characterization through I-V curves and EIS, maximizing the data output from a given experiment without affecting significantly the cell response during characterization.

The design of the spot-sampling set-up is depicted in Fig. 4.3. It consists of several components separated by several frame-shaped layers of gaskets. This multi-layer configuration is meant to provide both gas tightness and electrical insulation of the SOFC cell from the housing.

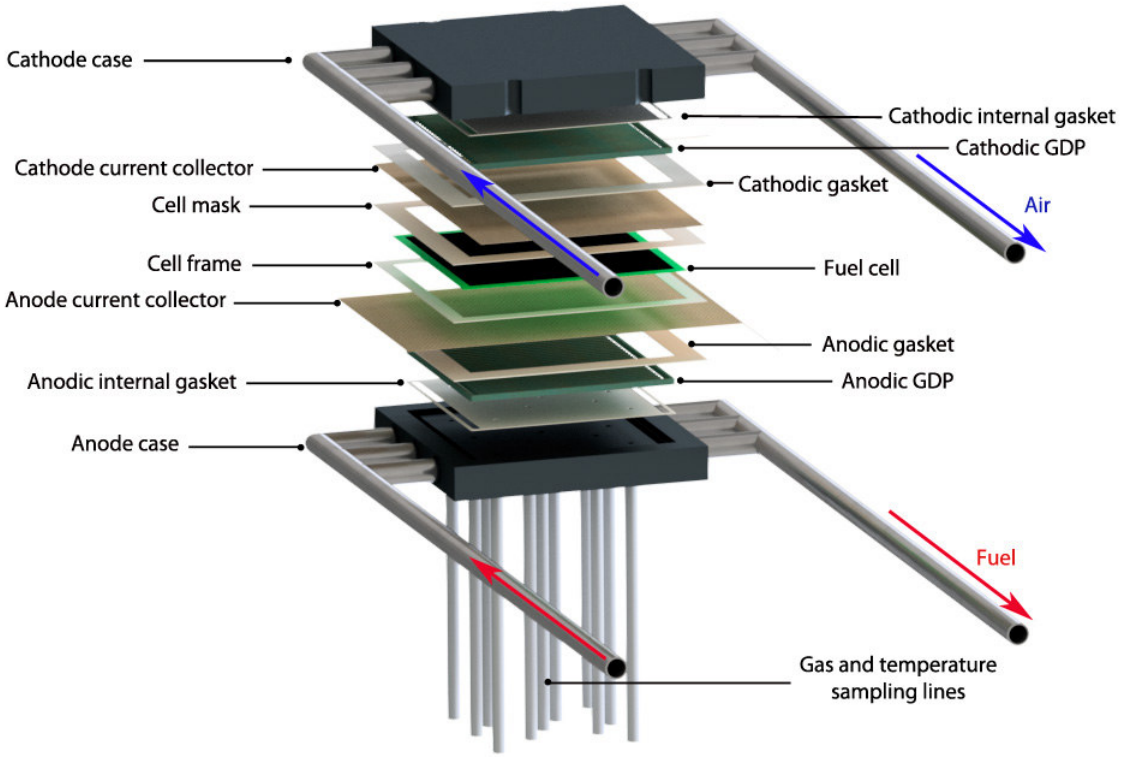

Figure 4.3. *Schematic illustration of the multisampling set-up.*

Anodic and cathodic cases are made of AISI 310S stainless steel. The gas inlet and outlet pipes are made of Inconel, which is a material supposed to form a thick and stable passivating oxide layer on its surface, avoiding chromium evaporation and, thus, cell contamination. The anodic case is located at the bottom of the set-up. It has been drilled throughout the surface for the gas sampling, as shown in Fig. 4.4a. Hence, gas sampling is performed via a set of 11 capillary tubes made of AISI 310S stainless steel, provided by Sulfinert®, and welded perpendicularly in correspondence with the drilled points. Meanwhile, localized temperature measurements can be achieved by means of 11 type-K thin thermocouples inserted inside the capillary tubes and positioned in the proximity of each spot. The cathodic case is the top of the multisampling set-up where a mechanical load is directly applied in order to ensure good contact between the electrodes and the current collectors as well as to avoid gas leakages from the system.

Inside the anodic and cathodic cases, grooved gas distribution plates (GDPs) made of AISI 310S stainless steel, heat treated and coated with insulating Al_2O_3 to generate electrical insulation and to avoid Cr evaporation, provide parallel gas distribution in co- or counter-flow. However, for the

present work, only the co-flow configuration has been adopted. The anodic GDP poses a set of the same 11 holes, Fig. 4.4b, to allow the localized gas sampling and temperature mapping in the anode.

As can be seen in Fig. 4.4c, two groups of three holes are distributed along the y-axis, in the proximity to gas inlets and outlets. In this way, it is possible to analyze the initial and final compositions coming from the anode, both from the corners and in the middle. Along the gas flow direction, x-axis, the gas composition can be monitored in 7 progressive axial locations, resulting in an efficient mapping of the surface composition and temperature.

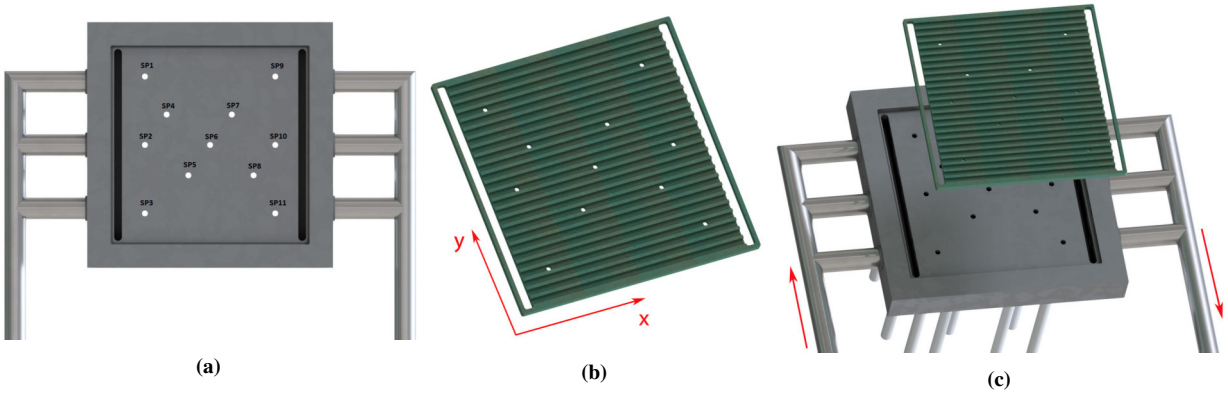

Figure 4.4. *Top view of the a) anodic case, b) anodic GDP, where the different coordinates are shown and c) anodic case and GDP showing the distribution of the 11 sampling points and the flow direction.*

Between each GDP and the corresponding electrode (cathode or anode), a gold mesh grid (Gold M-Grid 120x180 mm, thickness 0.2 mm, gold purity 99.99%, grid max mesh aperture 1.4x0.92 mm), provided by Fiaxell SOFC Technologies™, is used as current collector. In one side of the gold mesh, a set of Pt wires for current collection are welded very close to each other and twisted altogether forming a bundle, while in the opposite side a single Pt wire is welded for the measurement of the cell potential. The current collectors are manufactured to be completely flat, ensuring a good contact with the cell electrodes.

As previously mentioned, to ensure gas tightness, electrical insulation, alignment of the system components, and to guarantee a good contact between the electrodes and the current collectors, a set of 7 Thermiculite® gaskets, shaped as required by hand-cut, are employed in the whole set-up. They are made of Thermiculite® 866LS and Thermiculite® CL87 with different thicknesses, provided by Flexitallic.

The eleven sampling lines, carefully heated to avoid water condensation from the gas sample, are linked to a Clarus 680 GC Perkin-Elmer gas chromatograph through a multi-port valve (8 and 11 ports) to analyze the gas composition online. The GC equipment is fitted with specific columns for the compounds studied (Haysep Q and Molecular Sieve 5A) and a thermal conductiv-

ity detector (TCD). It should be noted that owing to the low volume required for the gas sampling ($10\,\mathrm{ml}\cdot\mathrm{min}^{-1}$), compared to the overall anode flows (from 500 up to $2000\,\mathrm{Nml}\cdot\mathrm{min}^{-1}$), stable performances of the cell are ensured during the gas sampling and composition analyses. Temperature samplings in the same points are performed by a set of type-K thermocouples connected to a data logger acquisition system (YOKOGAWA XL 100 data logger), acquiring simultaneously the temperature of each thermocouple up to every 500 ms.

This experimental set-up is particularly important for the direct fuelling of IT-SOFCs with syngas, where the dynamic processes of internal reforming and water-gas shift reactions can create severe local gradients of temperature and gas compositions, inducing stresses and possible carbon deposition.

Single cell tests are carried out on commercial IT-SOFCs fed with simple hydrogen, methane and selected syngas compositions in order to assess the thermochemical response of the SOFC at different current densities and create a detailed spatial mapping of critical hotspots correlated with operating conditions and inlet gas compositions. It is thus possible to identify areas within the operational space that are conducive to better uniformity of conditions, presumed to enhance SOFC durability, allowing to provide recommendations for fuel pre-conditioning processes as well as SOFC operation modes. Eventually, it is envisaged to establish a real-time spatial mapping with key parameters that are easily monitored in a real SOFC system.

Hence, experimental data will be useful to investigate internal reforming phenomena occurring on the cell plane. Along with a simple 0D model and a 2D numerical model, they are expected, e.g. to give a map of the current density distribution in the anode and to predict thermodinamically the outlet compositions in order to compare them with those obtained experimentally and from ChemCAD™.

4.3. Cell assembly and testing procedure

4.3.1. Cell assembly

The assembly procedure for each tested single cell has been carried out manually as following described:

Step 1. The set of gaskets for the entire set-up is manually shaped, Fig. 4.5a. The set consists of 7 gaskets in total: two gaskets, 1 anodic and 1 cathodic (both made of Thermiculite CL87, 0.62 mm); a cell frame (Thermiculite 866LS, 0.4 mm); a cell mask (Thermiculite CL87, 0.35 mm); and three internal gaskets, 1 for the anode side (thermiculite 8666LS, 0.4 mm)

and two for the cathode side (thermiculite 866LS, 0.4 mm and thermiculite CL87, 0.35 mm). Two internal gaskets are necessary for the cathode side in order to avoid an existing misalignment error coming from the manufacturing process of the cathode case.

Step 2. After cleaning the anode case until getting a soft surface, it is positioned into the furnace, with the gas sampling lines emerging from the bottom, outside the furnace. The ends of these capillary lines are closed by means of valves. On the top of the anodic case, the so-called internal anodic gasket is fixed using a spray glue (3M Scotch-Weld™ 77 multipurpose spray adhesive), as shown in Fig. 4.5b. Then, the anodic gas distribution plate is placed into its slot, Fig. 4.5c.

Step 3. The so-called anodic gasket is also fixed, as shown in Fig. 4.5d. Then the anodic current collector is placed on the gas distribution plate, Fig. 4.5e, followed by the so-called cell frame, Fig. 4.5f, in which the single cell (anode side in green and cathode side in black) is placed, as seen in Fig. 4.5g. Hence, two more gaskets are placed at this level: one surrounding the cell, the previously mentioned cell frame, Fig. 4.5f, and the so-called cell mask, covering the electrolyte exposed on the cathode side, i.e. the non-active area of the cell (green part) and just keeping visible the cell active area to avoid short circuiting of the electrodes, as shown in Fig. 4.5h.

Step 4. The cathode current collector is then positioned in contact with the cathode, but perpendicular to the anode current collector, as shown in Fig. 4.5i. This configuration is adopted in order to avoid possible short circuit caused by the bending or contact of the current collectors and wires.

Step 5. In this step, the two cathodic internal gaskets are fixed in the cathodic case using the same adhesive as for the other gaskets, Fig. 4.5j. Then, the cathodic gas distribution plate is placed into its slot, Fig. 4.5k, but using a special scotch tape for high temperature, which helps to keep the cathodic GDP in its place when the cell arrangement is closed. Also, the so-called cathodic gasket is fixed in the cathode case as shown in Fig. 4.5l.

Step 6. Finally, the cathodic case is placed on the top of the cathode current collector, closing and completing in this way the cell arrangement, Fig. 4.5m. Then, a mechanical load is placed over the set-up, Fig. 4.5n, Fig. 4.5o and Fig. 4.5r, and a contact test between current collectors and cases, to ensure electrical insulation, is performed. The furnace is completed and built with alumina bricks, Fig. 4.5o and Fig. 4.5p, and insulated with fiberglass, Fig. 4.5q and Fig. 4.5r.

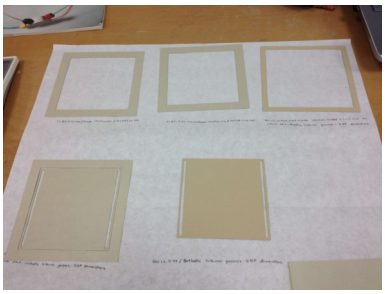

(a) *Thermiculite gaskets, shaped as required by hand cut.*

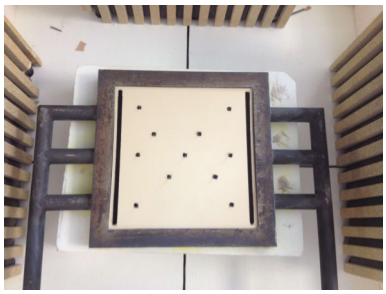

(b) *Anodic internal gasket (Thermiculite 866LS, 0.4 mm).*

(c) *Anodic gas distribution plate (GDP).*

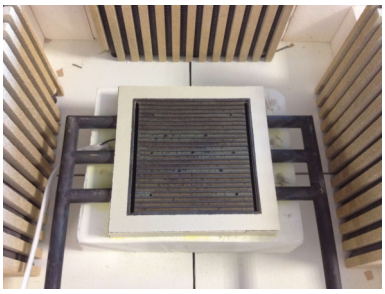

(d) *Anodic gasket (Thermiculite CL87, 0.62 mm).*

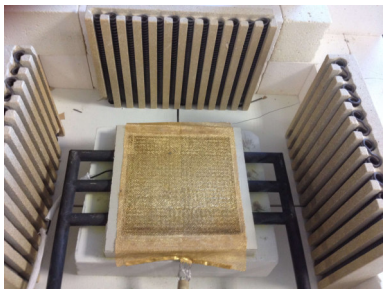

(e) *Anodic current collector (ACC).*

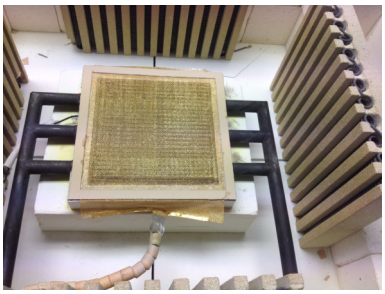

(f) *Cell frame (Thermiculite 866LS, 0.4 mm).*

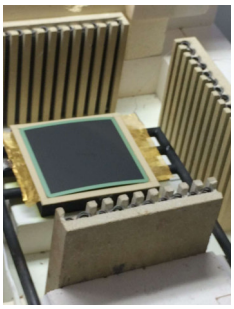

(g) *Single SOFC (anodic side in green and cathodic side in black).*

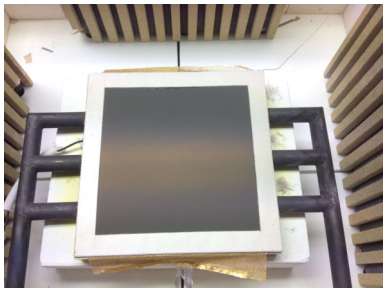

(h) *Cell mask (Thermiculite CL87, 0.35 mm).*

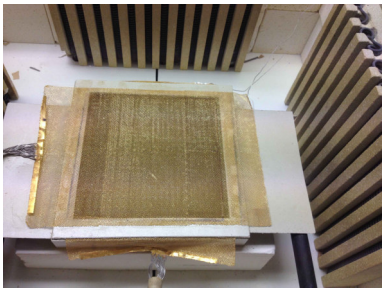

(i) *Cathodic current collector (CCC).*

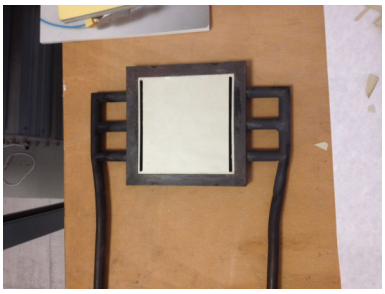

(j) *Cathodic internal gaskets (Thermiculite 866LS, 0.4 mm and Thermiculite CL87, 0.35 mm).*

(k) *Cathodic GDP.*

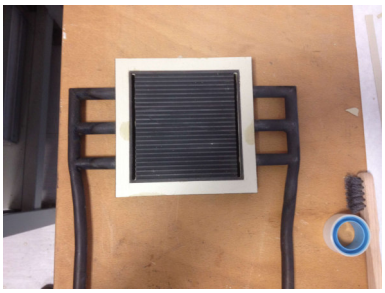

(l) *Cathodic gasket (Thermiculite CL87, 0.62 mm).*

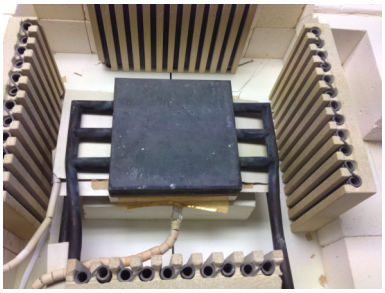

(m) *Complete cell arrangement.*

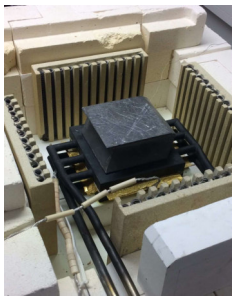

(n) *Mechanic load for the cell contact test.*

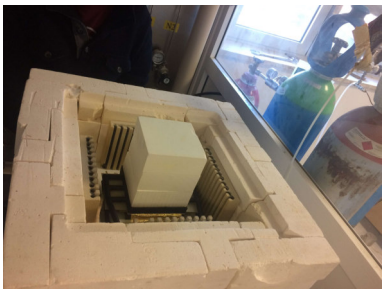

(o) *Alumina compacted blocks over the cathode surface, used as mechanical load.*

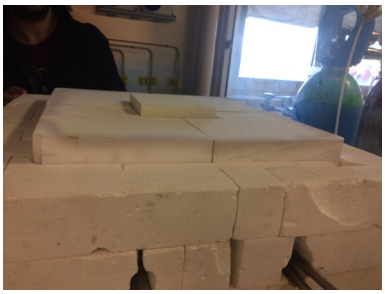

(p) *Closing of the cell housing.*

(q) *Furnace insulation.*

(r) *Final arrangement.*

Figure 4.5. *Assembling procedure.*

4.3.2. Single cell testing procedure

4.3.2.1. Cell start-up

The start-up procedure for each single cell basically consists of the following three phases:

1. *Heating phase*: After mounting the cell in the furnace, the single cell sample is heated from room temperature to 700 °C at a rate of $0.5\,^{\circ}\mathrm{C}\cdot\mathrm{min}^{-1}$ under $500\,\mathrm{Nml}\cdot\mathrm{min}^{-1}$ of pure N_2 to the anode and $500\,\mathrm{Nml}\cdot\mathrm{min}^{-1}$ of air to the cathode.

2. *Reduction phase*: The NiO in the anode and support layer is then reduced at 700 °C using 10% H_2 balanced with N_2, under a total anode volume flow rate of $1113\,\mathrm{Nml}\cdot\mathrm{min}^{-1}$ (corresponding to $1000\,\mathrm{Nml}\cdot\mathrm{min}^{-1}$ of N_2 and $113\,\mathrm{Nml}\cdot\mathrm{min}^{-1}$ of H_2) and $1000\,\mathrm{Nml}\cdot\mathrm{min}^{-1}$ of air to the cathode for about two hours. All the flow changes are always made gradually.
   In this phase, it is normal to perceive a slight temperature increase owed to the reduction phenomenon and the possible existing leakages. However, if the temperature increase is significant, it could be possible that there is a serious leakage problem and possibly the oxygen is reaching the anode in such a way that there is a direct combustion taking place in this electrode, which is probably causing such a big temperature change. If so, this effect increases in the subsequent phases because of the increase in the quantity of H_2 feed to the anode.

3. *Activation phase*: The cell is subsequently activated in pure H_2 at $500\,\mathrm{Nml}\cdot\mathrm{min}^{-1}$ to the anode and $500\,\mathrm{Nml}\cdot\mathrm{min}^{-1}$ of air to the cathode, for about half an hour.

4.3.2.2. Preliminary testing in the cells

After the activation step, the following preliminary testing is carried out for the first acceptance trials to determine whether the cell is valid for further testing or not.

- *CUTEC* @ 700 °C: At the same temperature of the previous phase (activation), i.e. at 700 °C, the H_2 flow in the anode is gradually increased to 986 Nml/min and the air in the cathode changed to 2196 Nml/min, corresponding to the so-called CUTEC composition. Once the cell voltage stabilized under this composition, i.e. when the cell reached the steady state, then the cell performance is evaluated through an EIS in OCV and an I-V curve, respectively recorded.
- *CUTEC* @ 650 °C: Under the same composition, the cell is subsequently cooled down to 650 °C and again characterized with an EIS and I-V curve. The implementation of the electrochemical spectra and polarization curves is described in the following section 4.3.3.

Once the cells are preliminary tested, from the preliminary testing results, the first acceptance trials of the cell are carried out. Firstly, the two resulting I-V curves for each single cell, (CUTEC @ 650 and 700 °C), are always compared with those obtained by a NELLHI Partner, CUTEC lab (CUTEC-Institut GmbH), for an Elcogen 15-cell stack but scaled to one single cell tested under the same operating conditions. Based on this comparison, i.e., according to the difference between both curves, a very first decision can be made.

Then, regarding the resulting OCV, if the voltage loss is below 5%, according to Eq. (4.1), the gas leakages are considered to be negligible and the corresponding cell is valid for further testing.

$$\Delta E_N(\%) = \frac{E_{N,th} - E_{N,meas}}{E_{N,th}} \times 100 \tag{4.1}$$

ΔE_N denotes the voltage loss due to leakage, $E_{N,th}$ is the theoretical Nernst voltage calculated by means of Eq. (2.9) and $E_{N,meas}$ is the experimentally measured cell potential, i.e. the OCV.

Finally, if the cell is considered valid for further testing, then the reference composition (already mentioned in section 4.1, Table 4.1) is set, and the experimental campaign initiates under this composition.

4.3.3. Experimental conditions for the analysis tools

4.3.3.1. EIS measurements

The electrochemical activity of the electrodes by electrochemical impedance spectroscopy is monitored only at OCV condition, using a Solartron 1260 Impedance Gain/Phase Analyzer module coupled with a Solartron 1287 Electrochemical Interface. The applied frequency sweep ranges from 100 kHz to 10 mHz, while the voltage signal amplitude is 10-20 mV.

EIS spectra are always recorded prior to polarization curves, with intervals of time of about one hour between one technique and other, in order to avoid possible effects on the results of the subsequent technique, caused by a possible disruption of the cell steady state owed to the previous experimental technique. Hence, it is important to highlight that all measurements or cell evaluations with the different employed experimental techniques are always performed when the system has reached the steady state. This condition is assured by monitoring the anode temperature and cell voltage changes over time.

The quality evaluation of the EIS data is carried out by means of the Kramers-Kronig test for Windows, as already mentioned in the previous chapter, and later analyzed using the DRT technique.

4.3.3.2. I-V curves recording

Current-voltage curves are performed using the Kikusui PLZ664WA electronic load connected in series with a Delta Elektronika SM-30-100D power supply, increasing the current at a rate of $0.1\,\mathrm{A}\cdot\mathrm{s}^{-1}$, from OCV condition to about 30 A or 40 A, depending on the composition of the gas fuel.

In the present study, the polarization curves are mainly recorded in the low-current-density region in order to keep the cell working safely and to avoid possible stresses that can affect the cell integrity for the subsequent testing.

4.3.3.3. Temperature measurements

Assuring the condition of steady state in the tested cells, temperature analyses are carried out during at least three consecutive hours under each condition, recording simultaneously the temperature of each thermocouple every second through a YOKOGAWA XL 100 data logger acquisition system.

In order to follow the evolution of the steady state condition and the temperature changes under each analyzed condition, a reference composition is set, Table 4.3 (corresponding to the composition also shown in Table 4.1), from which each test of the experimental campaign begins.

Table 4.3. Reference composition ("H_2 reference") used during the experimental campaign.

	Molar percentage[%]	Flow [Nml/min]
Anode		
H_2	50	520
N_2	50	520
Cathode		
Air	100	2240

Hence, beginning from the reference composition at the temperature of interest (650 °C or 700 °C), temperature acquisitions are carried out as follows:

- *In OCV condition*: It is recorded by switching the composition from the reference composition (or hydrogen reference) to the composition of interest, and leaving the cell to reach the steady state under open-circuit voltage condition.
- *Under loading condition*: It is recorded by switching the corresponding cell condition from OCV to the current value of interest and leaving the cell to reach the steady state under the corresponding loading condition.

4.3.3.4. Gas analyses

The gas analyses are always carried out at the inlet, Fig. 4.6a, in order to verify the inlet composition; throughout the anode, via the sampling points, Fig. 4.6b; and at the cell outlet, Fig. 4.6c. For each gas sampling, a volumetric flow rate of $10\,\mathrm{ml}\cdot\mathrm{min}^{-1}$ is taken. Each gas measurement lasts about 6 min and they are carried out at a constant temperature. The GC oven temperature is set to 70 °C while for the inlet line is 80 °C.

Gas analyses are carried out using a Clarus 680GC, fitted with a thermal conductivity detector (TCD) and adapted with an auto-sampler and a special column for the studied compounds (Haysep Q and Molecular Sieve 5A), which additionally allows to analyze the gas samples under real steam contents.

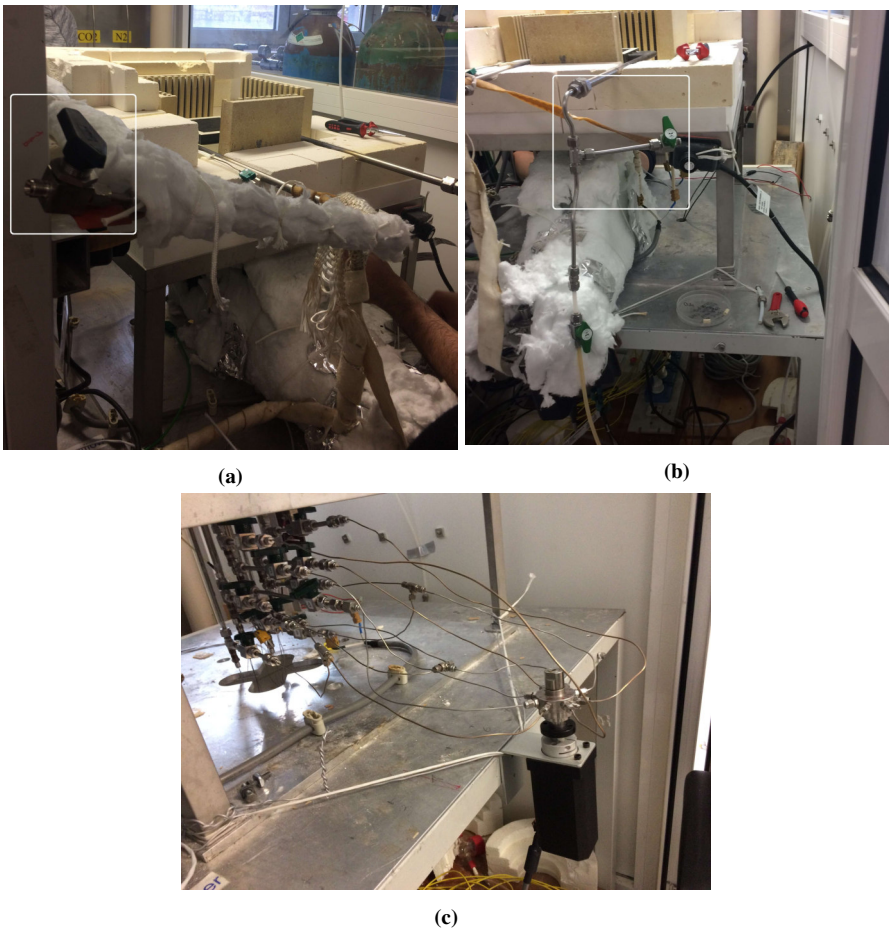

Figure 4.6. *Sampling points for the gas analyses: a) cell inlet, b) cell outlet and c) anode.*

4.4. Multisampling set-up validation

4.4.1. Testing conditions

Seeking to achieve the novel set-up validation, an anode-supported single cell (962-25-B-400), with the technical specifications already described in section 4.2.1, is tested at two different temperatures: 650 and 700 °C through polarization curves in pure hydrogen (CUTEC composition). The corresponding I-V curves were compared to those obtained by CUTEC Lab (CUTEC- Institut GmbH, a partner of the NELLHI project) in an Elcogen 15-cell stack but scaled to one single cell tested under the same operating conditions. The gas flows and composition corresponding to CUTEC composition are reported in Table 4.4, while the cell start-up procedure has been indicated in detail in section 4.3.2.

Table 4.4. CUTEC composition tested for the test bench validation.

	Molar percentage[%]	Flow [Nml/min]
Anode		
H_2	100	986
Cathode		
Air	100	2196

At both temperatures, 650 and 700°C, polarization curves are obtained as described in section 4.3.3: from OCV condition to 45 A at a rate of 0.1 $A\,s^{-1}$.

From the evaluation of the voltage loss/leakages for the first acceptance trials of the tested cell, according to Eq. (4.1), it remained, in both cases, below the 5% established to consider the cell acceptable for further testing, being 3.8% and 4.1% at 650 and 700 °C, respectively.

4.4.2. Validation results

One of the main achievements during this work is the validation of this new multisampling set-up by comparison of the polarization curves obtained for a single cell with the actual set-up at 650 and 700 °C vs those obtained in CUTEC lab.

In Fig. 4.7a and Fig. 4.7b it is respectively shown the comparison at 650 °C and 700 °C between the polarization curves obtained with the multisampling set-up and that of the scaled 15-cell stack obtained in CUTEC lab (hereinafter called as "the reference"). It can be observed that, in both cases, a slight OCV mismatch and voltage difference along the polarization curves are still present between both curves.

At 650 °C with the actual set-up there is an OCV deviation of ca. 38 mV, below the reference, representing a difference of 3.1%, and an average voltage difference of 10.7 mV along the I-V curve. At 700 °C there is an OCV deviation of ca. 28.5 mV, still below the reference, representing a difference of 2.4%, and an average voltage difference of 12.5 mV along the curve.

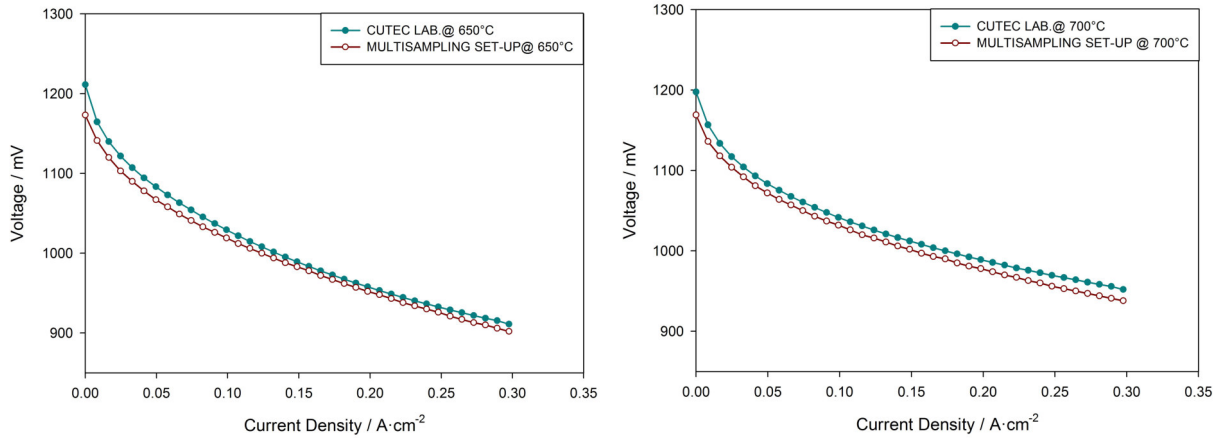

Figure 4.7. *Performance comparison between tested cells via the novel set-up and scaled 15-cell stack obtained in CUTEC lab at a)* 650 °C *and b)* 700 °C.

Comparing these differences with those obtained during the first trials for the set-up validation [64], carried out at 650 °C, a substantial improvement is observed, see Fig 4.8. Accordingly, the best polarization curve (blue line) obtained until then from a first-generation cell and before the set-up improvements, shows an OCV deviation of ca. 33 mV below the reference, representing a difference of 2.7%. Even though this OCV deviation is lower than the obtained after the set-up improvements at the same conditions, an average voltage difference of 34 mV along the I-V curve was obtained, which is significantly higher than those currently achieved. This was however imputable to the internal resistance increase owed to the Crofer 22H stainless steel anodic current collector used during those tests. In fact, the difference between such polarization curve and the other ones is more pronounced in the ohmic region, where it can be observed that the slopes of the curves, related to the ASR of the system, are different.

Therefore, for the current tests a significant decrease in the internal resistance of the system was achieved by changing the Crofer mesh employed as anode current collector to a gold mesh grid. In addition to the gold mesh anodic current collector, all the system insulation has been enhanced by implementing heating tapes and fiberglass in most of the system lines. These set-up improvements, in general, have enhanced the quality of the results obtained, reducing the impact of the set-up into the cell's response, as also confirmed through a comparison of the first works produced via this novel set-up [64, 74], before and after improvements, respectively.

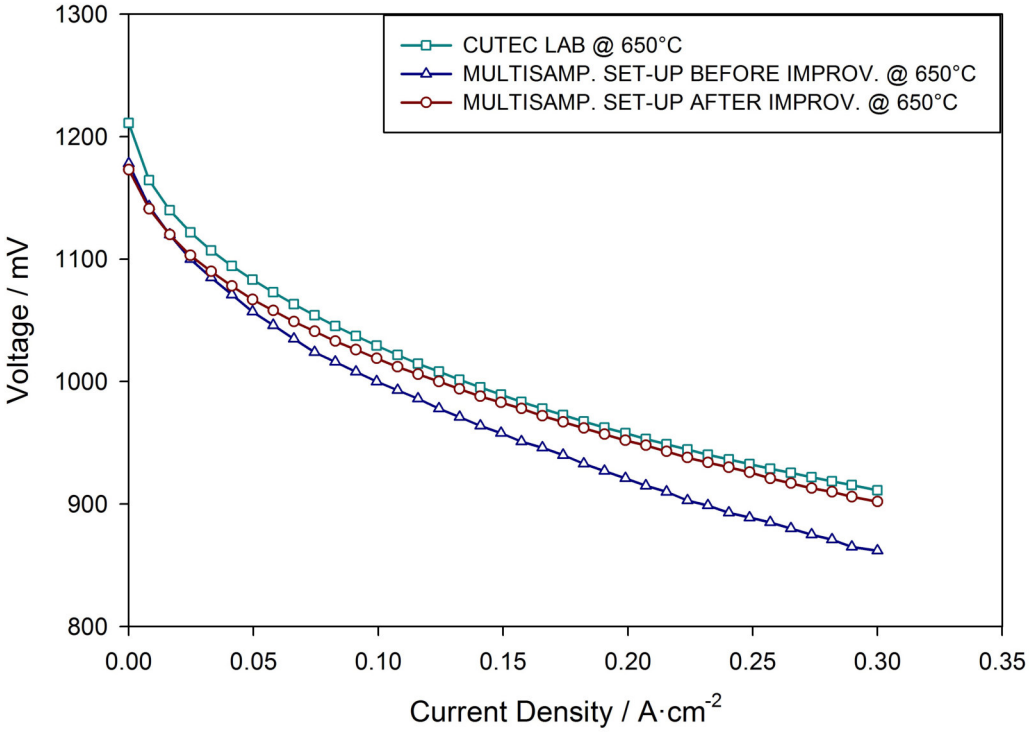

Figure 4.8. *Polarization curves in pure hydrogen of a second-generation Elcogen's single cell obtained using a gold mesh grid as anodic current collector and after system improvements (red line), compared to those obtained from an Elcogen 15-cell stack tested by CUTEC lab, scaled and in the same operating conditions (green line), and a first-generation single cell obtained using a Crofer mesh grid as anodic current collector and previous to the set-up improvements (blue line).*

Regarding the slightly lower but still existing OCV mismatch, it can be mainly owed to the inherently less gas-tight assembly in a single-cell configuration than that of a stacked assembly which leads to the presence of gas leakages because a mismatch in the layers positioning, imperfections of the gaskets or because of the manual assembling process itself. This strongly highlights the need of a system improvement but in terms of the mechanical load system as well as in the assembling procedure. Another reason could be a possible longer stabilization period of the cell after the activation phase. In fact, after about 250 hours of cell operation on the set-up after improvements, the OCV under CUTEC composition increased up to 1220 mV, resulting even higher than the reference one.

Therefore, although an OCV mismatch is still present, very similar polarization curves are obtained, which to a greater extent validates the multisampling set-up.

4.5. Testing conditions of the study cases

The completion of the following described experimental campaign is carried out by means of two more anode-supported samples: SC 949-24-B-400, employed for the experimental campaign itself and SC 978-29-B-400, employed for the long-term operation. Both cells, with the technical specifications already described in section 4.2.1, proceed from the same batch. Nevertheless, a preliminary performance characterization is carried out on each cell in order to assure comparability of the tested samples and for the subsequent experimental results.

4.5.1. Low internal reforming

The first case, low internal reforming (LIR), corresponds to a pre-reformate gas mixture with the lowest quantity of methane and the highest quantity of hydrogen of the three proposed compositions. It simulates a syngas composition that results from the natural gas reforming process using Nickel as catalyst at 600 °C without Anode Off-Gas Recirculation (syngas no AOGR). The corresponding flows and molar compositions employed under this composition are reported in Table 4.5.

Table 4.5. LIR or reformate syngas no AOGR composition.

	Molar percentage[%]	Flow [Nml/min]
Anode		
H_2	57	333
CO	6	35
CO_2	8	47
CH_4	2	12
H_2O	27	158
Cathode		
Air	100	2240

The experimental techniques under LIR composition are implemented under the following conditions: EIS measurements in OCV condition and polarization curves are recorded at 650 and 700 °C. At 650 °C, gas composition and temperature measurements in each sampling point are performed under three different conditions: OCV, 15 A and 30 A, corresponding the latter two to 124 mA/cm^2 and 248 mA/cm^2 of current density and to 25% and 50% of fuel utilization, respec-

tively. However, because of time reasons, for all the three compositions, at 700 °C and solely in OCV condition, only temperature measurements are carried out (see Table 4.6).

Table 4.6. Experimental conditions under which the analysis techniques are implemented for the LIR and IIR compositions.

	I-V curve	EIS	Temperature measurements			Gas analyses		
		OCV	OCV	15A	30A	OCV	15A	30A
650 °C	✓	✓	✓	✓	✓	✓	✓	✓
700 °C	✓	✓	✓	✗	✗	✗	✗	✗

The general testing procedure is as already indicated in section 4.3.2, while the implementation of the experimental techniques, i.e. EIS measurements, polarization curves, gas analyses and temperature measurements, is carried out as previously described in section 4.3.3.

4.5.2. Intermediate internal reforming

Intermediate internal reforming composition, also corresponds to a pre-reformate gas mixture but with an intermediate quantity of methane and hydrogen from the three proposed compositions (S/C=2.5), simulating a syngas composition obtained from the natural gas reforming process using Nickel as catalyst at 600 °C and with Anode Off-Gas Recirculation (syngas AOGR). The corresponding flows and compositions are reported in Table 4.7.

Table 4.7. IIR or reformate syngas AOGR composition.

	Molar percentage[%]	Flow [Nml/min]
Anode		
H_2	31	180
CO	4	23
CO_2	23	135
CH_4	12	71
H_2O	30	173
Cathode		
Air	100	2240

These former two fuel gas compositions (LIR and IIR) are proposed from the NELLHI project,

from which, until then, there were some preliminary tests which could be used for comparative purposes.

As also summarized in Table 4.6, the experimental techniques under this composition are implemented under the following conditions: EIS measurements in OCV condition and polarization curves are recorded at 650 and 700 °C. At 650 °C, gas composition and temperature measurements in each sampling point are performed under three different conditions: OCV, 15 A and 30 A corresponding the later two to 124 mA/cm^2 and 248 mA/cm^2 of current density and to 21.5% and 43% of fuel utilization, respectively. However, because of time reasons, at 700 °C and solely in OCV condition, only temperature measurements are carried out.

4.5.3. Complete internal reforming

The third case, complete internal reforming (CIR), is a fuel composition consisting of pure methane and steam (S/C=3.5). The corresponding flows and compositions are reported in Table 4.8.

Table 4.8. CIR composition.

	Molar percentage[%]	Flow [Nml/min]
Anode		
CH_4	22.4	122
H_2O	77.6	422
Cathode		
Air	100	2240

This case, CIR, is proposed in order to evaluate the cell performance under the highest possible quantity of methane through evaluation of the hydrogen production and avoiding the problem of carbon deposition. Furthermore, it is sought to compare the cell performance as a reformer comparing the experimental gas mixtures at the outlet of the cell with the theoretical ones.

As summarized in Table 4.9, the experimental techniques under this composition are implemented under the following conditions: EIS measurements in OCV condition and polarization curves are recorded at 650 and 700 °C. At 650 °C, gas composition and temperature measurements in each sampling point are performed under three different conditions: OCV, 15 A and 25 A corresponding the later two to 124 mA/cm^2 and 206 mA/cm^2 of current density and to 21.5% and 36% of fuel utilization, respectively. However, because of time reasons, at 700 °C and solely in

OCV condition, only temperature measurements are carried out.

Table 4.9. Experimental conditions under which the analysis techniques are implemented for the CIR composition.

	I-V curve	EIS	Temperature measurements			Gas analyses		
		OCV	OCV	15 A	25A	OCV	15A	25A
650 °C	✓	✓	✓	✓	✓	✓	✓	✓
700 °C	✓	✓	✓	✗	✗	✗	✗	✗

As can be seen, unlike the previous two cases, for CIR, the test at the maximum current corresponds to 25 A instead of 30 A, which is owed to a cell stability reason under this composition, as will be further discussed in the results chapter.

4.5.4. Long-term operation

Endurance performance tests, as explored in [81,102], are necessary in order to maintain system integrity, durability, and lifespan. Therefore, in the last part of the experimental campaign, an endurance performance test under intermediate internal reforming composition is carried out in order to evaluate the performance and durability of these commercial single cells, as well as to evaluate the multisampling set-up stability and integrity under uninterrupted operation.

IIR composition has been selected for the long-term operation because, from the three studied gas mixtures, it resulted to be the most promising option in terms of power delivered, yielding the highest performance. Additionally, its technical applicability goes further because of representing an anode off-gas recirculation mixture, where the main drivers of this condition are the increased fuel efficiency and the independence of the external water supply for the fuel pre-reforming process [252–254].

For the long-term operation a new single cell sample (978-29-B-400) is employed. The general test sequence (start-up and preliminary testing) is as described in section 4.3.2. Afterwards, the fuel flow is changed to the simulated intermediate internal reforming composition to characterize the cell with an I-V curve, an EIS, and with anode temperature measurements and gas analysis in OCV. And finally, during the cell operation (under load and IIR composition), the cell is regularly characterized (at 0 h and every 100-150 h), carrying out gas analyses under load, EIS in OCV, temperature measurements in both OCV and under load, and I-V curves. The last characterization is performed prior to cooling the cell down. The cell cooling is carried out during at least 24 hours under the composition set during the reduction phase.

The evolution and changes in cell performance are investigated by holding the cell for about 500 h at 650 °C and under a constant current mode of 30 A corresponding to a current density of 248 mA/cm^2 and a fuel utilization (FU) of 43%. The single cell is fed with the IIR gas mixture consisting of 31% H_2, 23% CO_2, 12% CH_4, 4% CO and 30% H_2O supplied to the anode (S/C=2.5), at a flow rate of 582 Nml/min, whereas air is supplied to the cathode at a flow rate of 2240 Nml/min, as it is indicated in Table 4.10.

Table 4.10. Tested IIR gas composition and cell operating temperature during the long-term test.

Gas mixture	Molar fraction	Flow rate [Nml/min]	Operating temperature[†]
Anode			650 °C
H_2	0.31	180	
CO	0.04	23	
CO_2	0.23	135	
CH_4	0.12	71	
H_2O	0.30	173	
Cathode			
Air	–	2240	

[†] Operating temperature in OCV condition

EIS, I-V curves, gas analyses and temperature measurements are also implemented as already described in section 4.3.3. After fully cooling the cell down, it is then analyzed by SEM/EDS post-mortem analysis, in order to complement and confirm the results obtained through the characterization tests.

Chapter 5

RESULTS AND DISCUSSION

5.1. Experimental results on the internal reforming experimental campaign

This section presents the experimental results obtained during the experimental campaign described in Chapter 4, regarding the comparison of the electrochemical performance and thermochemical behavior of commercial fuel cells under internal reforming analyzing composition and temperature effects. Through the analysis of polarization curves and electrochemical spectra, the general electrochemical performance of such cells is discussed. Then, in order to identify the number, the nature and the evolution of the different physicochemical processes, it is presented a discussion of the different processes occurring inside the cell through the DRT method applied to the impedance spectra of the three analyzed compositions. Finally, the results of the gas and thermal analyses are respectively presented and discussed, aiming to study the chemical and thermal gradients in the anode due to the evolution of the multiple reactions at the different operating conditions.

5.1.1. Electrochemical performance

5.1.1.1. Polarization curves

Fig. 5.1 shows the experimental comparison of the I-V curves at 650 °C and 700 °C corresponding to the three tested compositions: LIR, IIR and CIR. Since the open-circuit voltage depends on the nature of the fuel supplied and, to a small extent, on the temperature, among others; firstly, the I-V characteristics are analyzed considering the temperature effect and consequently, the fuel composition.

As expected and as it is observed, the OCV decreases with rising the temperature. This effect is owed to the loss of Gibbs free energy with increasing the temperature. Accordingly, the recorded OCV under LIR composition, Fig. 5.1a, decreased from 1008 mV at 650 °C to 994 mV at 700 °C, resulting in a voltage difference at OCV (ΔV) of 14 mV. For the IIR case, Fig. 5.1b, the measured OCV reduced from 1010 mV at 650 °C to 997 mV at 700 °C, representing a ΔV of 13 mV; while for the CIR case, Fig. 5.1c, the ΔV resulted in 19 mV, decreasing the OCV from 981 mV at 650 °C to 962 mV at 700 °C. Although the compositions of LIR and IIR are relatively different, it is observed that the measured OCVs and the ΔVs are nearly the same in both cases, while for CIR the OCV is significantly lower and the ΔV higher. The lower OCV under the highest methane containing atmosphere is attributed to the greater humidity of the corresponding gas mixture, as will be later discussed.

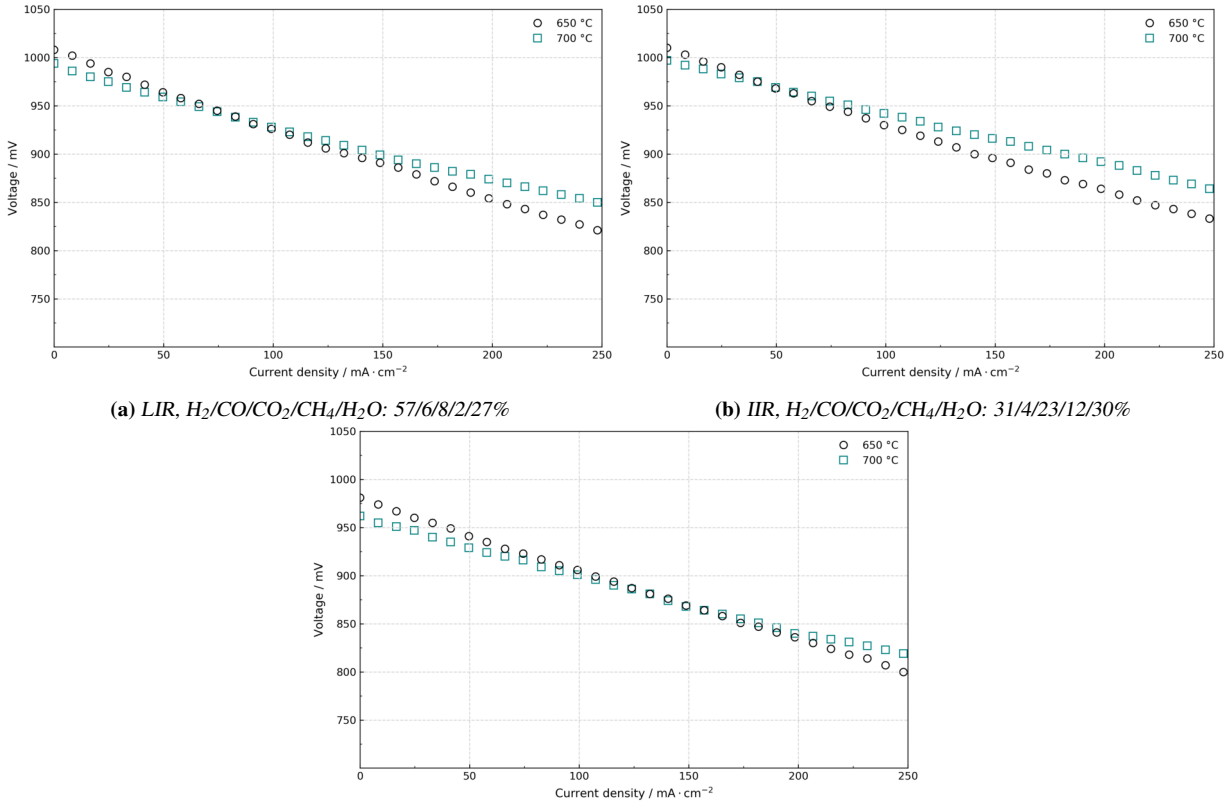

(a) *LIR, H_2/CO/CO_2/CH_4/H_2O: 57/6/8/2/27%*

(b) *IIR, H_2/CO/CO_2/CH_4/H_2O: 31/4/23/12/30%*

(c) *CIR, CH_4/H_2O: 22.4/77.6%*

Figure 5.1. *Polarization curves comparison at 650 and* 700 °C *for a) LIR, b) IIR and c) CIR.*

Furthermore, it is observed from the polarization curves that the lower the temperature the higher the slope of the I-V curves. This is because the conductivity of the electrolyte decreases when temperature decreases, increasing in consequence, the internal resistance of the cell. Thus, comparing the slopes of the I-V curves for the LIR case result in a value of ca. -0.573 Ωcm^2 at 700 °C and ca. -0.749 Ωcm^2 at 650 °C, giving an increase of about 23.5%. For the IIR case, the I-V

slope increases from ca. -0.529 $\Omega\,cm^2$ at 700 °C to ca. -0.704 $\Omega\,cm^2$ at 650 °C, resulting in a rise of about 24.9%. And finally, for the CIR case, the slope increases from ca. -0.584 $\Omega\,cm^2$ at 700 °C to ca. -0.718 $\Omega\,cm^2$ at 650 °C resulting in an increment of about 18.7% when reducing the operating temperature from 700 °C to 650 °C.

The values of the slope give a general picture of how the voltage changes respect to the current density, while the minus sign just indicates that the voltage is decreasing while current increases. Accordingly, from the three analyzed compositions at 650 °C and 700 °C, it is obtained that under IIR composition the voltage drops more slowly when increasing the current density, as the comparison of the values above suggests. Besides, regarding the percentage slope change between 650 °C and 700 °C, the IIR composition also resulted with the highest percentage change, indicating that when the operating temperature is increased there is a greater improvement in the cell performance under IIR than under LIR or CIR.

Nevertheless, it should be pointed out that the latter result may be influenced by the fact that the I-V curves under LIR and CIR at 700 °C were performed when the cell was showing a significant degradation, which in fact has been reflected in more distant intersection points (intersection points at higher current density values) between the I-V curve at 650 °C and 700 °C for both compositions, compared to the intersection point under IIR. This is, the intersection point between 650 °C and 700 °C for IIR is found at ca. 41.3 $mA\,cm^{-2}$, while for LIR it occurs at ca. 74 $mA\,cm^{-2}$ and for CIR at ca. 157 $mA\,cm^{-2}$. Although the OCV decreases when rising the temperature, according to Eq. (2.12), it should be a point from which there is an improvement or advantage of operating the cell at higher temperatures, which is related to the rate or enhancement of the chemical kinetics of the different reactions. Hence, the shifting of the IV curves intersection points towards higher current densities under LIR and CIR may be an effect of the cell degradation detected at 700 °C, since the intersection point for all the three compositions should appear, at least in theory, around almost the same value ($\sim$35 $mA\,cm^{-2}$).

Additionally, from Fig. 5.2, corresponding to the three I-V curves comparison at both temperatures, it is observed a greater difference at 700 °C than at 650 °C for the I-V curves under LIR and CIR respect to the I-V curve under IIR. This is, while an average voltage deviation of $\sim$6 mV and $\sim$27.5 mV along the whole polarization curves for LIR-IIR and CIR-IIR is respectively obtained at 650 °C, at 700 °C this average deviation respect to the IIR I-V curve increased to $\sim$13.7 mV and $\sim$43.5 mV for LIR and CIR, respectively. Such quantities represent an increase of 126% for LIR and about 59% for CIR. As above-mentioned, these figures are owed to an experienced cell degradation, which usually had been occurring after a certain number of operative hours. However, this degradation issue will be further discussed and clearly shown in the following (EIS) section.

On the other hand, regarding the fuel composition effect, it is expected that the OCV also

decreases under a higher water content in the fuel. This is explained because at OCV, theoretically there are no products being formed as there is no net oxygen ions transfer across the electrolyte. According to Eq. (2.12), as the partial pressure of the reactants approach 0, the Nernst potential tends to infinity, making the Nernst potential of dry hydrogen at OCV undefined. In reality, the OCV is limited by the amount of O_2 leaking into the anode chamber forming water. Hence, humidified H_2 is used since the presence of H_2O at the anode defines the OCV. According to Eq. (2.12), as the partial pressure of water in the fuel increases, the OCV decreases. Therefore, for LIR and IIR whose compositions of H_2O are 27 and 30%, respectively, the measured OCV is nearly the same (1008 and 1010 mV), while for CIR whose H_2O content is more than 75% the OCV resulted in only 981 mV at 650 °C.

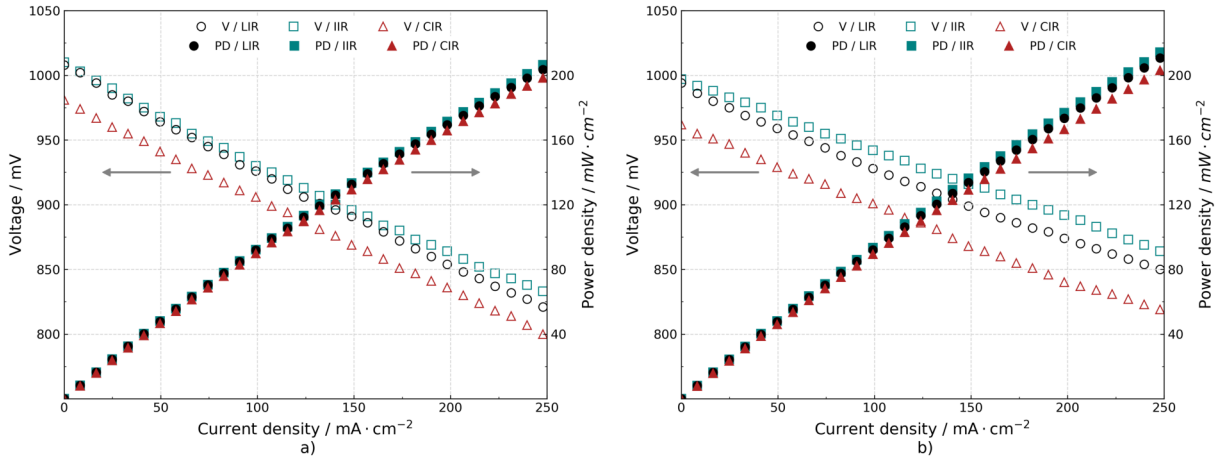

Figure 5.2. *I-V and power density curves comparison for all the compositions at a)* 650 °C *and b)* 700 °C.

It is also well-known that at low current densities there is a characteristic exponential decay of the I-V curve due to the dominance of activation losses, and that such non-linearity increases with decreasing temperature. However, the constant linear behavior observed at both temperatures in all the polarization curves, either from Fig. 5.1 or Fig. 5.2, without the expected exponential decay at very low current densities is also owed to the high water content in the three tested compositions; which is in accordance with Willich [255] and Subotic et al. [112], who have pointed out that the higher the water content the less pronounced is the exponential behavior at low current densities. This statement is also shown when comparing the I-V curves either from Fig. 5.1 or Fig. 5.2 with those from Fig. 4.8, where in this later, there is no water in the supplied fuel and the exponential behavior owed to the dominance of activation overpotentials at low current densities is noticeable.

Hence, differences between the polarization curves for the operation under humidified gas mixtures and dry gas are obvious in the range of low current densities, and it may be explained by the combined effect of the Nernst voltage and the activation losses. As above-mentioned, the partial pressure of water in the gas mixture has a significant impact on the Nernst voltage, whereby the

increasing amount of water vapor brings the polarization curve to the linear behavior.

Moreover, with higher water contents, the voltage of the cell is less stable, which is assumed to be owed to an unstable water vaporization or condensation at the cell outlet [256]. Actually, this voltage instability has been mainly experienced when recording the CIR polarization curve, which has the highest content of H_2O from the three compositions ($\sim$75%), showing voltage fluctuations in OCV of up to $\sim$25 mV and under load of up to $\sim$600 mV. However, in the case of hydrocarbon fuels (e.g. methane), such fluctuations can be observed because there are several competing and parallel oxidation and reforming processes which can give rise to different voltages, even in OCV. Hence, depending on the steam-to-carbon ratio, pressure, temperature, etc., different voltages with some fluctuations can be observed.

Although OCV is not an accurate indicator of the cell performance, it is clearly seen from a comparison of the three I-V curves at 650 °C and at 700 °C, Fig. 5.2, that changes in the OCV also signify a change of the chemical species at the electrodes, which are determined, in this case, by the reforming and shifting reactions. Actually, as observed under IIR composition, even when the mole percentage of H_2 entering the cell is lower than that of LIR, at steady state, the resulting I-V curves are closely the same. In contrast, the lower voltage and performance under the highest methane containing atmosphere may be attributed to a more marked competence of the processes occurring simultaneously and in parallel (oxidation of H_2, reforming and shifting reaction) over the Ni/YSZ anode, resulting in a significant instability of the cell under this composition.

In addition to the polarization curves, Fig. 5.2 shows the corresponding power densities delivered under each composition. By a comparison of the performance of the three analyzed gas mixtures, it can be seen that in terms of delivered power, the composition that yields the highest performance corresponds to the IIR followed by the LIR and the CIR. However, the difference in the power density delivered is not significant, even when considering the total cell power, e.g. at the maximum recorded current density, 30 A, the cell yields: 24.62 W, 24.98 W and 23.99 W at 650 °C, and 25.5 W, 25.9 W and 24.57 W at 700 °C under LIR, IIR and CIR, respectively. As earlier mentioned, for CIR composition, the flow rate of steam was about twice that of methane so that the partial pressure of water vapor at the anode increased, resulting in a lower OCV. This lower open-circuit voltage was the main reason for the slightly lower power density under CIR composition.

Therefore, in terms of fuel composition, it is observed that adding more CH_4 to the fuel mixture and as long as it contains H_2, the cell performance improves up to be comparable to that obtained under an inlet mixture with a higher H_2 content, which is owed to the huge H_2 production through the promotion of the reforming and shifting reactions.

5.1.1.2. EIS results

Fig. 5.3 shows the comparison of the electrochemical impedance spectra of the cell operation under the three analyzed reformate compositions at a) 650 °C and b) 700 °C. It is particularly observed that the shape of the measured EIS spectra under reformate operation are different to the typical one under hydrogen operation. Whereas this latter is characterized by only two distinctive arcs, Fig. 3.2, the spectra under reformate operation are characterized by three arcs, as also reported in [30]. Accordingly, the shapes of the impedance plots reflect the variation of many factors and parameters in SOFCs, such as in this case, the fuel composition.

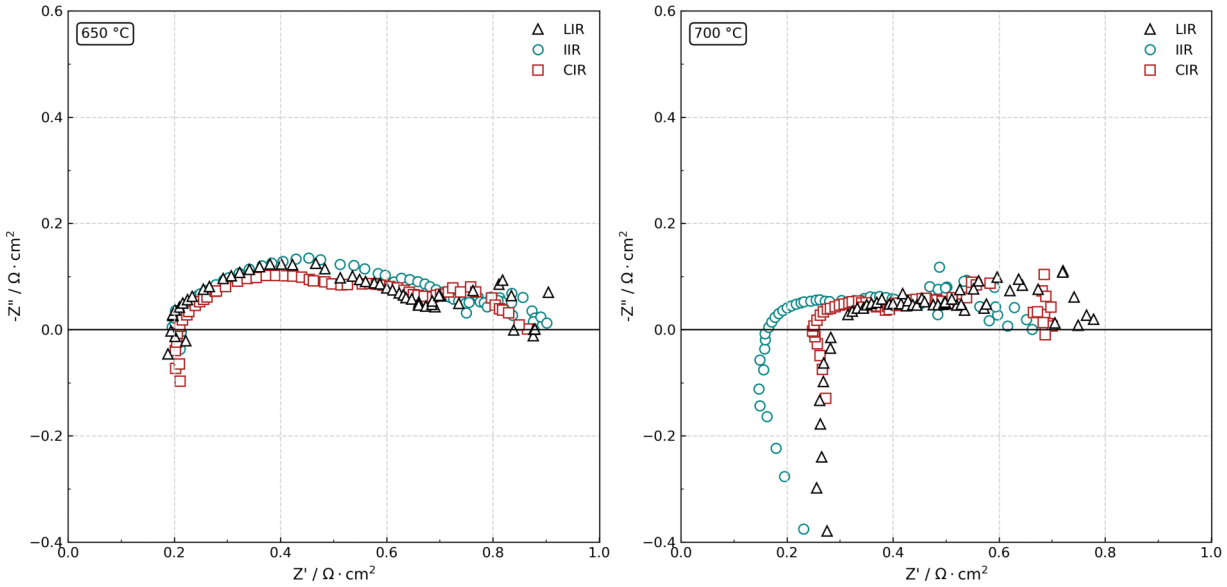

(a) **(b)**

Figure 5.3. *Electrochemical spectra comparison under LIR, IIR and CIR at a)* 650 °C *and b)* 700 °C.

However, from Fig. 5.3a it is observed that, in spite of the difference in the fuel composition, at 650 °C the recorded spectra are quite similar in shape and size. In effect, as expected, the ohmic resistance of the cell (R_0) is not dependent on the anode fuel composition. Thus, the high-frequency intersection of the measured spectra with the real axis (ASR, whose relation with R_0 is given by Eq. (3.6)) at 650 °C is nearly the same for the three operating fuel compositions. Under LIR, the measured ASR is 194.3 mΩcm^2 at an average steady state temperature (T_{avg}) of 651.7 °C. Under IIR, the corresponding ASR is 197.6 mΩcm^2 at $T_{avg} = 646.2$ °C. And finally, under CIR, the ASR at $T_{avg} = 644.9$ °C corresponds to 208.4 mΩcm^2.

As observed, the average steady state temperatures are slightly different for the three analyzed cases, decreasing while increasing the CH_4 content under the corresponding composition, which is owed to the reforming grade. However, this point will be further discussed in the thermal analysis.

The important thing here is just to highlight that even under very small differences in temperature the slight ASR differences vary according to the expected trend of the ASR with temperature. This is, it is known that the lower the cell operating temperature the higher the ASR. In this case, the average steady state temperature of the cell decreases in the following order: LIR, IIR and CIR, while the ASR increases in the same order. This fact strongly highlights the accuracy and reliability of the data obtained at 650 °C, suggesting that this kind of analysis have been carried out in a suitable way.

Regarding the polarization resistance (R_{pol}), it is observed that, also, despite the difference in the fuel compositions the polarization resistances are closely the same. Accordingly, the measured polarization resistance, which includes both anode and cathode contributions, are: 664.3, 676.2 and 657 $m\Omega cm^2$ at 650 °C under LIR, IIR and CIR, respectively. These results represent a polarization resistance $\sim$19 $m\Omega cm^2$ and $\sim$7 $m\Omega cm^2$ higher under IIR and LIR than under CIR, respectively. These results strongly indicate that the polarization resistance decreases with the addition of H_2O, as also reported by Miao et al. [257] and Lim et al. [51]. The differences between the polarization resistance under LIR and IIR are not considered owed to the very similar H_2O content, in addition to the fact that under such water contents the spectra at low-frequencies tend to be very scattered (as observed in all the spectra), which may be affected by a more significant error. Nevertheless, when also comparing the R_{pol} from the EIS under dry H_2 (Fig. 3.2) and any of the spectra under reformate operation, it is evident how R_{pol} decreases drastically with the addition of H_2O, suggesting that proper addition of H_2O enhances the diffusion phenomena and reduces the activation losses, as also reported in [112].

In contrast, from a comparison of the spectra at 700 °C, Fig. 5.3b, it is evident that the ASR (or the internal resistance of the cell) is quite different under the three tested compositions: 293.7 $m\Omega cm^2$ under LIR, 162.9 $m\Omega cm^2$ under IIR and 249.4 $m\Omega cm^2$ under CIR. Such differences are owed to an experienced cell degradation, as already mentioned when analyzing the I-V curves. It should be pointed out that this degradation had been also observed in previous tested cells, and it was generally experienced after certain number of operative hours. Accordingly, the spectra and I-V curves at 650 °C were recorded at 21, 46 and 53 hours of cell operation, while at 700 °C were recorded at 305, 215 and 310 hours for LIR, IIR and CIR, respectively.

Since the results under IIR at 700 °C still resulted consistent because of showing the expected tendency of reducing the ASR with temperature, from 197.6 $m\Omega cm^2$ at 650 °C to 162.9 $m\Omega cm^2$ at 700 °C, it is suggested that the cell degradation started after those 215 hours of operation. Hence, the results influenced by the cell degradation correspond to the obtained under LIR and CIR at 700 °C, while those considered still reliable include the recorded in the first 215 hours of the cell operation. Regarding the polarization resistance, it is observed that for all the three cases, it does not show a significant difference. Thus, this experienced cell degradation has been mainly reflected

in an increase of the ohmic resistance, as actually observed in Fig. 5.3b.

On the other hand, Table 5.1 summarizes the electrochemical performance of the cell based on the results of the EIS and polarization curves. It is noteworthy how the total cell resistance, R_{cell}, obtained from data fitting of the I-V curves, seems to approach to the total cell resistance obtained from EIS, R_T, at the corresponding temperature. The existing difference is because of the different, static and dynamic, nature of the techniques under which each value is obtained: R_{cell} comes from a static technique (I-V curve), while R_T is obtained from a dynamic one (EIS).

Table 5.1. Cell performance and EIS results at both temperatures for the three tested compositions.

Composition	**T** [°C]	**OCV** [mV]	**PD** [mW/cm^2]	**ASR** [$m\Omega cm^2$]	**R_{pol}** [$m\Omega cm^2$]	**R_T** [$m\Omega cm^2$]	**R_{cell}** [$m\Omega cm^2$]
LIR: H_2/CO/CO_2/CH_4/H_2O:	650	1008	203.5	194.3	664.3	858.6	748.5
57 / 6 / 8 / 2 / 27%	700	994	210.7	293.7	484.4	778.1	572.5
IIR: H_2/CO/CO_2/CH_4/H_2O:	650	1010	206.5	197.6	676.2	873.8	703.7
31 / 4 / 23 / 12 / 30%	700	997	214.2	162.9	476.4	639.4	528.5
CIR: CH_4/H_2O:	650	981	198.3	208.5	657	865.5	718.5
22.4 / 77.6%	700	962	203.1	249.4	436.4	685.7	584.4

OCV: open-circuit voltage

PD: power density at 30 A corresponding to 50, 43 and 43% of FU for LIR, IIR and CIR, respectively

ASR: area-specific resistance from EIS

R_{pol}: polarization resistance from EIS

R_T: Total cell resistance from EIS, $R_T = ASR + R_{pol}$

R_{cell}: Total cell resistance from I-V curves (data fitting from OCV to 30 A)

Then, according to the results shown in Table 5.1, R_{pol} and R_T decreased with temperature in all the three cases, despite the significant increase in the *ASR* under LIR and CIR at 700 °C. Actually, at 700 °C, R_{pol} is closely the same for the three cases, showing a respective difference of 48 and 40 $m\Omega cm^2$ higher for LIR and IIR respect to CIR. Hence, even at 700 °C it is observed that R_{pol} decreases with a greater H_2O content, as previously stated. Moreover, whilst the decrease in the ASR with temperature observed for IIR represents 17.5%, the R_{pol} difference between 650 °C and 700 °C, for the three compositions are: 179.9, 199.8 and 220.6 $m\Omega cm^2$, representing a respective decrease for LIR, IIR and CIR of 27.1, 29.5 and 33.5% when increasing the operating temperature by 50 °C. These figures indicate that the cell polarization resistance, mainly caused by activation in both electrodes, is the major limiting factor of single cell performance, especially at low and intermediate temperature.

Regarding the cell performance, it is observed that at 30 A the differences in the power density delivered under the three compositions are not far different. However, when comparing the cell

performance at a same fuel utilization, the power density delivered under the different compositions seems to show a more marked difference. For example, at a FU of 43%, corresponding to 26 A under LIR and 30 A under IIR and CIR, the power density delivered is 181.1 mW/cm^2 at 650 °C and 186 mW/cm^2 at 700 °C, representing a total cell power of 21.9 W and 22.5 W, respectively, under LIR composition. Thus, when comparing the total power yielded at the same FU for the three compositions, it is obtained: 21.9, 24.9 and 23.9 W at 650 °C and 22.5, 25.9 and 24.5 at 700 °C under LIR, IIR and CIR, respectively, representing a difference of 12.2% and 3.9% in the power delivered under LIR and CIR below to that delivered under IIR at 650 °C, which yielded the highest power from the three analyzed compositions at both temperatures. At 700 °C, the differences in percentage respect to IIR are 13.1% for LIR and 5.1% for CIR, below the power delivered under the already mentioned composition.

Despite the intermediate operating temperature and the differences in the reformate compositions, the average cell power delivered from these planar commercial SOFCs is comparable to those reported in [51, 117, 202, 257, 258].

Therefore, although the polarization resistance is not the lowest one under IIR, this composition shows the best electrochemical performance in terms of power delivered, compared to the LIR and CIR composition. IIR composition represents an anode off-gas recirculation mixture, so that the obtained results from the electrochemical analysis are found very promising in terms of technical applications. Furthermore, it has been observed that employing only wet methane or high methane containing atmospheres, can be hindered by the fact that increasing the amount of CH_4 means increasing also the quantity of steam in order to avoid carbon deposition. Nonetheless, operating under high water contents is a big deal since it makes really difficult the analysis and the cell operation, and in the worst of the cases, being a rate-determining step of the overall processes owed to water clogging effects, as will be later discussed.

5.1.2. Processes identification from the DRT analysis

5.1.2.1. Temperature comparison

The physicochemical processes occurring in the cell are now identified by analyzing the impedance spectra and calculating their corresponding distribution of relaxation times. The different processes are identified based on published works about DRT analyses on ASC. Hence, for a more detailed description on the identification of these processes, the reader is referred to [84, 85, 92, 259].

Seeking to firstly analyze the temperature effect on the individual processes of the cell, Fig. 5.4a gives a comparison of the impedance spectra under IIR composition at 650 and 700 °C, while their corresponding DRT are depicted in Fig. 5.4b. It is firstly presented the analysis under this

composition since, as above-mentioned, this is the only one for which the results of the analyses at both temperatures are considered reliable owed to degradation issues under which the other two compositions at 700 °C were performed. Thus, it is possible to identify correctly the thermally activated processes from this analysis and then, from the analyses of the other two compositions at both temperatures, differentiate the degradation-related processes from the thermally-activated ones. The dependence on the operating temperature usually distinguishes diffusion polarization processes, with low temperature dependence, from thermally activated activation polarization processes.

It can be seen from Fig. 5.4a that under reformate operation, unlike H_2 operation, the dominating arc corresponds to the high-frequency semi-circle, ranging from 50.1 kHz to 50.1 Hz at 650 °C and from 9 kHz to 50.1 Hz at 700 °C. In fact, this high-frequency arc, which is related to the fast charge transfer mechanism involved in the electrochemical reactions at both electrodes [240,241] is smaller when rising the temperature, suggesting an enhancement of the charge transfer and activation mechanisms when increasing the operating temperature. Furthermore, as already-mentioned, the low/intermediate-frequency region is characterized by two distinctive arcs. In addition to the semicircle at ca. 10 Hz, another semicircle appears at frequencies below 2 Hz for reformate operation. In the Nyquist plots from SOFC systems under typical H_2 operation, the low-frequency arc is often associated to the mass transport losses related to the diffusion of the gases in the porous matrix of the electrodes. However, due to the lack of a straightforward correlation between the impedance plot and the SOFC properties and operative conditions, it is not easy to come to a complete agreement on the interpretation of the intermediate/ low-frequency arcs from the impedance plot, especially because of the multiple phenomena occurring under reformate operation. What is completely clear is that the additional semicircle has been always identified only under reformate operation.

Unlike in the impedance curve, where the individual polarization processes overlap, up to six processes can be clearly distinguished in the calculated DRT (black line from Fig. 5.4b), giving more insight on the single physicochemical processes that form the measured impedance arcs. The polarization processes that have been identified and characterized under operation with hydrogen as fuel and air as oxidant [85,92] are identified here as well. However, depending on the fuel type and the operating temperature, the characteristic frequency of each process may result slightly or considerably shifted. This phenomenon can be related to the effect of a different surface chemistry experienced, as suggested by Zhu et al. [259]. The two high-frequency processes, $P_{1,an}$ and $P_{2,an}$, are ascribed to the gas diffusion coupled with the charge transfer mechanism and ionic transport within the anode functional layer. The high-frequency process in the cathode, $P_{3,cat}$, is associated with the oxygen surface exchange kinetics of LSC as well as the diffusivity of oxygen ions within the LSC bulk, owed to its dependency on the O_2 content in the cathode stream [85]. The mass

transfer processes, $P_{4,an}$ and $P_{5,an}$, are caused by a gas-phase diffusion in the pores of the Ni/YSZ-anode substrate. Characteristic of this process are its two peaks in the DRT, as also suggested by Leonide et al. [92].

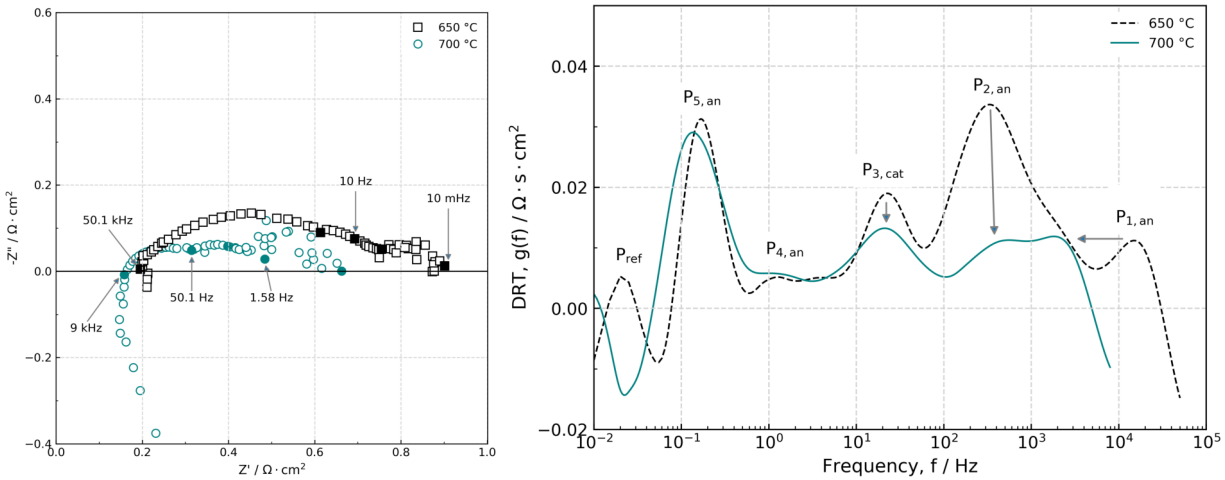

Figure 5.4. *a) EIS and b) DRT comparison at 650 vs* 700 °C *for IIR composition.*

Additionally, there is a sixth process visible at frequencies below 0.1 Hz, P_{ref}. This process is scarcely reported in the literature [31, 84]. However, due to its occurrence under reformate operation, it is called reformate process, P_{ref}.

It is evident that the processes $P_{1,an}$, $P_{2,an}$ and $P_{3,cat}$ are all characterized by a pronounced thermal activation since their amplitude is affected by a modification in the temperature: the intensity of the peak of $P_{2,an}$ and $P_{3,cat}$ decreases around 65% and 30%, respectively, when increasing the temperature by only 50 °C. Meanwhile, processes $P_{4,an}$ and $P_{5,an}$ show, by contrast, a negligible dependency on the operating temperature. It is interesting to note how the reforming process P_{ref} in addition to $P_{1,an}$ shift significantly to lower characteristic frequencies when increasing the operating temperature. Remembering the fact that the area beneath the DRT curve represents the resistance of the cell [260], and consequently the area beneath each process represents the individual contribution of such a process to the total cell resistance, it is observed that not only an amplitude decrement represents an enhancement but also a shift to lower characteristic frequencies of the processes. Accordingly, if the amplitude is similar but the process is shifted to lower frequencies, it means that the frequency range over which it should be integrated is lower, thus the final area and consequently the contribution to the cell resistance should be lower. Therefore, as expected, P_{ref} and $P_{1,an}$ also show a temperature dependence but mainly reflected in a frequency shift. Most of these features are in completely agreement with other works carried out on button ASC reported in the literature [84,85].

For the case of LIR, Fig. 5.5a, the shape of the spectra seems to be characterized by only two

arcs, as in the case of H_2 operation. The high-frequency arc ranging from 50.1 and 6.3 kHz at 650 °C and 700 °C, respectively, to 7.94 Hz, and the low-frequency arc ranging from 7.94 Hz to 10 mHz. However, it seems to be present a subtle change at ca. 200 Hz making doubtful whether the other semicircle at ca. 10 Hz is also present or not. This apparent difference in the EIS shape under LIR may be related to the fact that its CH_4 content is very low (∼2%), as well as that of CO and CO_2 (∼6% and ∼8%), making either the phenomenon of methane internal reforming or the subsequent WGS reaction practically imperceptible.

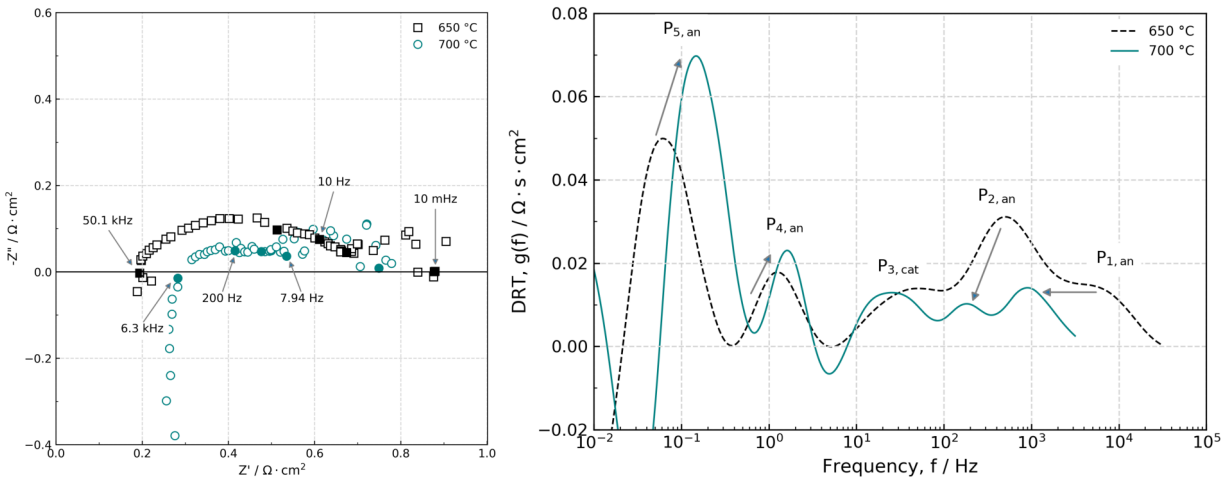

(a) **(b)**

Figure 5.5. *a) EIS and b) DRT comparison at 650 vs* 700 °C *for LIR composition.*

From a comparison of the spectra at both temperatures it is also observed an enhancement in the high-frequency arc and therefore in the related physicochemical processes when rising the temperature. However, not in the same way for the apparent low-frequency arc which may be owed to a worsening of the related phenomena in this frequency range because of the experienced cell degradation. On the other hand, the issue of the higher internal resistance at 700 °C has been already discussed.

Regarding the DRT for this case, Fig. 5.5b, it is evident that unlike the case of IIR, all processes seem to be characterized by a pronounced thermal activation: the intensity of the peak of $P_{2,an}$ and $P_{3,cat}$, decreases around 67% and 8%, respectively, while the intensity of $P_{4,an}$ and $P_{5,an}$ increases around 29% and 36%, respectively, when increasing the temperature from 650 °C to 700 °C. Such behavior is rather related to the cell degradation, which in fact mainly points to the fuel electrode processes. Additionally, it is observed that $P_{1,an}$ does not show a significant change in its amplitude but does show a shift to lower frequencies as in the IIR case. $P_{2,an}$ in addition to showing an effect in its amplitude also shifts to lower frequencies, in contrast to $P_{4,an}$ and $P_{5,an}$ which shift to higher frequencies when increasing the operating temperature. All these features, perfectly agree with the

characteristics observed in the spectra comparison.

It is also interesting to observe how the reforming-related process, P_{ref}, is not visible under this composition (LIR), which is attributed to the very low internal reforming activity because of the fuel composition (very low CH_4 content in the fuel mixture), as also concluded from the EIS analysis and as it will be further shown in the gas and thermal analyses.

On the other hand, Fig. 5.6a shows the spectra comparison under CIR composition. From this plot it is observed how the shape of the spectra under CIR is more similar to that under IIR since the three semicircles are clearly visible: the high frequency arcs, ranging from 22.5 and 14 kHz at 650 and 700 °C, respectively, to 200 Hz; the intermediate frequency arcs ranging from 200 Hz to 1.58 Hz, and the low frequency one ranging from 1.58 Hz to 10 mHz. Again, despite the cell degradation, it is observed a decrease with temperature mainly in the high and intermediate arcs which means an enhancement in the related physcochemical processes.

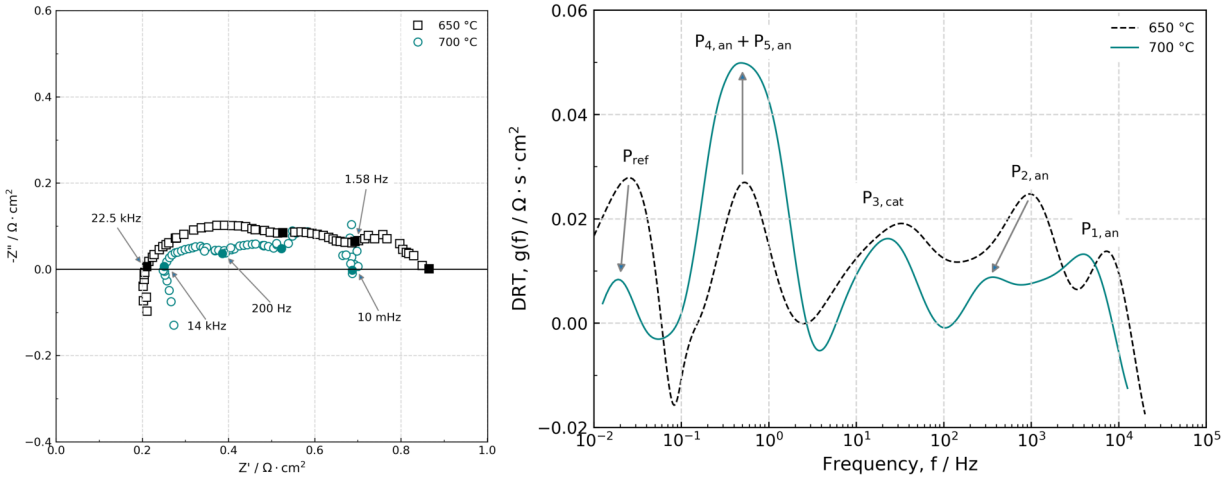

(a) **(b)**

Figure 5.6. *a) EIS and b) DRT comparison at 650 vs* 700 °C *for CIR composition.*

From the DRT, Fig. 5.6b, it is observed how the high frequency processes $P_{1,an}$ and $P_{2,an}$ are affected qualitatively and quantitatively (in a very similar way) as in the other two discussed cases. Actually, $P_{2,an}$ decreases also around 65% while $P_{1,an}$ mainly shifts to lower frequencies with increasing the temperature. Regarding the physicochemical processes occurring at the cathode, $P_{3,cat}$, these still show an enhancement of around 14% when increasing the temperature. However, when comparing with the temperature effect under IIR, the cathode-related phenomena under LIR and CIR do show a slight worsening because of the cell degradation.

Overall, the distribution of relaxation times under CIR shows the same temperature effect in the processes as under LIR, which is explained, as previously mentioned, by the cell degradation

when characterizing under these both compositions at 700 °C. The main differences come from the reforming proces, P_{ref}, and the mass transfer processes in the Ni/YSZ-anode substrate, $P_{4,an}$ and $P_{5,an}$. For the first one, it is observed how under this composition the peak related to the reforming process is very noticeable, showing a highly pronounced thermal activation by a decrease in its amplitude (∼60%) when increasing the temperature. In other words, the impact of P_{ref} on the overall polarization resistance of the cell is less significant at higher temperatures and becomes more relevant for lower temperatures. Regarding $P_{4,an}$ and $P_{5,an}$ it is observed how under this composition those two peaks became only one ($P_{4,an}$ + $P_{5,an}$). Although $P_{4,an}$ and $P_{5,an}$ became a single peak, it also shows a high increase in its amplitude, around 85%, when increasing the temperature, thus, making evident the cell degradation through this process. Therefore, it is suggested that mainly the anode is the electrode responsible of the cell degradation since the phenomena that worsen when increasing the cell temperature are identified at the characteristic frequencies where the anode processes take place.

5.1.2.2. Fuel comparison

Regarding fuel comparison, at 650 °C it is observed from Fig. 5.7a that the characteristic frequency of the high frequency process $P_{1,an}$ results closely the same for all the three compositions, while the process $P_{2,an}$ changes slightly its characteristic frequency when the fuel composition is changed. This evidence suggests that, compared to process $P_{1,an}$, the process $P_{2,an}$ is more influenced by the molecular properties of the fuel species. Since the ionic transport within the YSZ lattice should be, at least in theory, not influenced by the fuel properties, it can be supposed that $P_{1,an}$ is related to the ionic transport phenomenon, while the process $P_{2,an}$ is most likely ascribable to the charge transfer process in the oxidation reaction. Accordingly, Son et al. [261] reported a DRT analysis carried out on Ni-YSZ anodes (half cell) and Bertei et al. [262] on anode-supported LSCF/GDC/YSZ/Ni:YSZ SOFC. In both analyses, they separated the two contributions in the DRT plots related to the electrochemical oxidation of H_2, ascribing the highest frequency process to the ionic transport within the YSZ matrix, and the second one at a lower frequency to the charge transfer mechanism involved in the electrochemical oxidation of H_2. Nevertheless, in this case, further and more specific investigations are needed to confirm this assumption, since both processes are deeply correlated, and sometimes convoluted with each other, in addition to the multiple phenomena because of the complex analyzed mixtures.

Additionally, the dependency of the peak $P_{2,an}$ on the fuel composition is typical for mass transport processes. It is reported in literature that the two above-mentioned high-frequency processes ($P_{1,an}$ and $P_{2,an}$) may experiment a mass transport limitation arising from an insufficient anode functional layer (AFL) porosity. However, this contribution is frequently negligible for AFL layers thinner than 8 µm, and becomes unimportant during the first 100 hours of cell operation, due to the

development of an open porosity in the AFL [42].

Regarding $P_{3,cat}$, it is clearly visible that the cathode-related processes exhibit a relatively low dependence on the variation of the fuel composition, which in fact is observed at both temperatures, Fig. 5.7a and Fig. 5.7b. In contrast, the anodic low-frequency polarization processes, $P_{4,an}$, $P_{5,an}$ and P_{ref} exhibit continuous shifts and amplitude changes for the variation of the fuel gas composition.

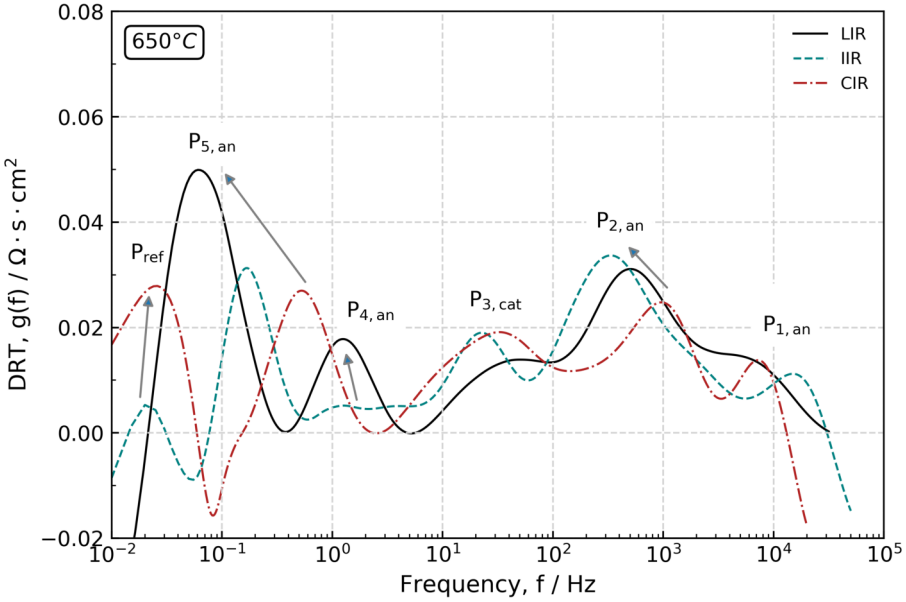

(a)

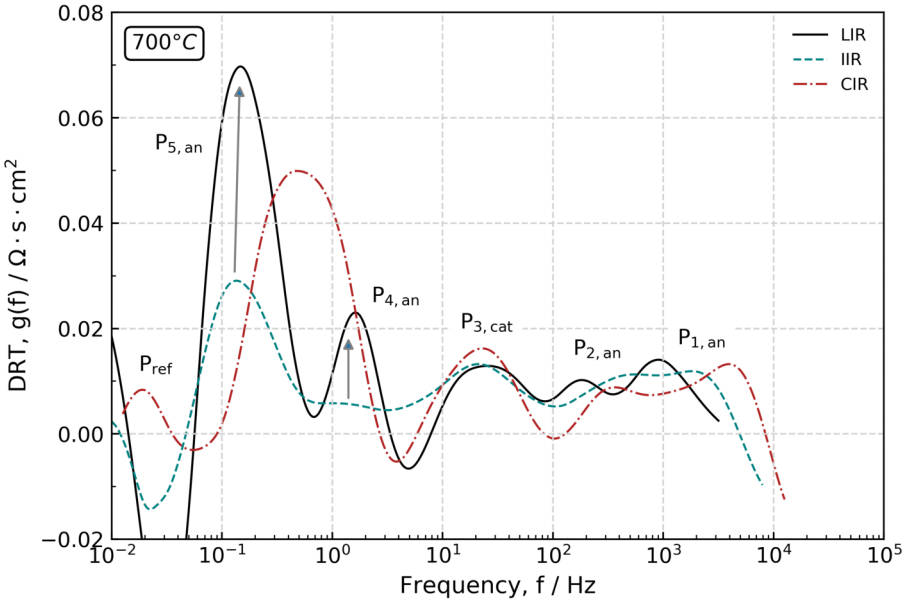

(b)

Figure 5.7. *DRT comparison at a)* 650 °C *and b)* 700 °C.

The observed behavior indicates that for reformate fueled ASCs, the low frequency polarization process $P_{4,an}$ + $P_{5,an}$ has to be attributed to the diffusion of H_2/H_2O, while P_{ref} is dominated by the diffusion of $CH_4/CO_2/CO$. In terms of reforming chemistry, the LIR gas mixture seems to be inert, i.e., no reforming reactions seem to occur, due to the low CH_4 content. This indicates that the reforming reactions, which theoretically are excited during EIS measurements even in OCV, are appearing as a single process, as observed under IIR and CIR gas mixtures. The last statement completely differs to that reported by A. Kromp [31]. However, it is important to clarify that, unlike the present study, the indicated author does not include the effect of CH_4 on his analyzed mixtures, in addition to carry out his studies on button cells which may change by far the phenomena occurring in the cell and, consequently, the obtained results.

Accordingly, the significant dependency of the reforming process, P_{ref}, on the reformate gas mixture and temperature allows to ascribe such process to both the reforming and shifting processes, as also indicated by Lyu et al. [263]. Meanwhile, Kromp et al. [84] and Zhu et al. [259] observed a power law dependency of this process to the gas composition and ascribed this novel DRT feature to the occurrence of the water-gas shift reaction coupled with the gas-phase diffusion of CO and CO_2 within the porous anode structure. Nevertheless, it is again remembered that in both studies the authors did not include CH_4 in the fuel mixtures, unlike the present study. Thus, analogously, a similar attribution can be given to the process P_{ref} observed in the present study, i.e., ascribe it to the steam methane reforming process in addition to the WGS reaction coupled with the gas-phase diffusion of CH_4, CO and CO_2 through the anode. However, also in this case, further and more specific experimental investigations are required in order to prove this attribution.

Finally, considering the reliability of the data at 650 °C and the degradation issues on the data at 700 °C, most of the analyses about the fuel variation have been done based on the data at 650 °C. Nevertheless, in the DRT at 700 °C it is observed a similar qualitative behavior in some of the different processes. In fact, it is observed that also at 700 °C, Fig. 5.7b, the polarization processes $P_{1,an}$, $P_{2,an}$ and $P_{3,cat}$ just exhibit a slight sensitivity on the gas composition of the fuel. In contrast, $P_{4,an}$+$P_{5,an}$ under LIR and CIR exhibit a much higher sensitivity than on the DRT comparison at 650 °C which in fact is attributed to the cell degradation.

5.1.3. Gas composition analyses

5.1.3.1. LIR

The mole or volume percentage distributions along the main flow direction over the anode for hydrogen, water, methane, carbon monoxide and carbon dioxide in a) OCV, b) 15 A and c) 30 A under LIR composition are shown in Fig. 5.8, while the corresponding comparison for each species

variation under the three different current values is depicted in Fig. 5.9.

Although both H_2 and CO can be directly oxidized electrochemically, only H_2 is considered as the electrochemically active species in the present study. This approach is based upon the commonly used assumption that CO is preferentially oxidized via the water-gas shift process [34, 264]. It is generally agreed that the electrochemical oxidation rate of CO on Ni-YSZ electrodes is lower than that of H_2 [72, 149, 222]. Additionally, there is strong evidence that for reformate fuels, only H_2 is electrochemically oxidized at the Ni/YSZ anode. It has been shown that even for reformate fuels with a high share (90%) of CO/CO_2, still H_2 is preferred for the electrochemical oxidation [30, 147], implying that CO is subsequently oxidized when it is converted to H_2 via the water-gas shift reaction.

Hence, according to Fig. 5.8 and Fig. 5.9, it is observed that when current is drawn, the molar composition of hydrogen decreases along the flow direction, mainly due to the electrochemical reaction. Nevertheless, in OCV, it is observed a similar or constant hydrogen composition along the anode, which is attributed to the low reforming activity caused by the low methane content in the LIR gas mixture. At 15 A, Fig. 5.8b, it is observed a slight decrease in the mole composition of hydrogen, while at 30 A, Fig. 5.8c, due to the increase in the FU, it is evident a more pronounced drop of this species, mainly in the second half of the cell.

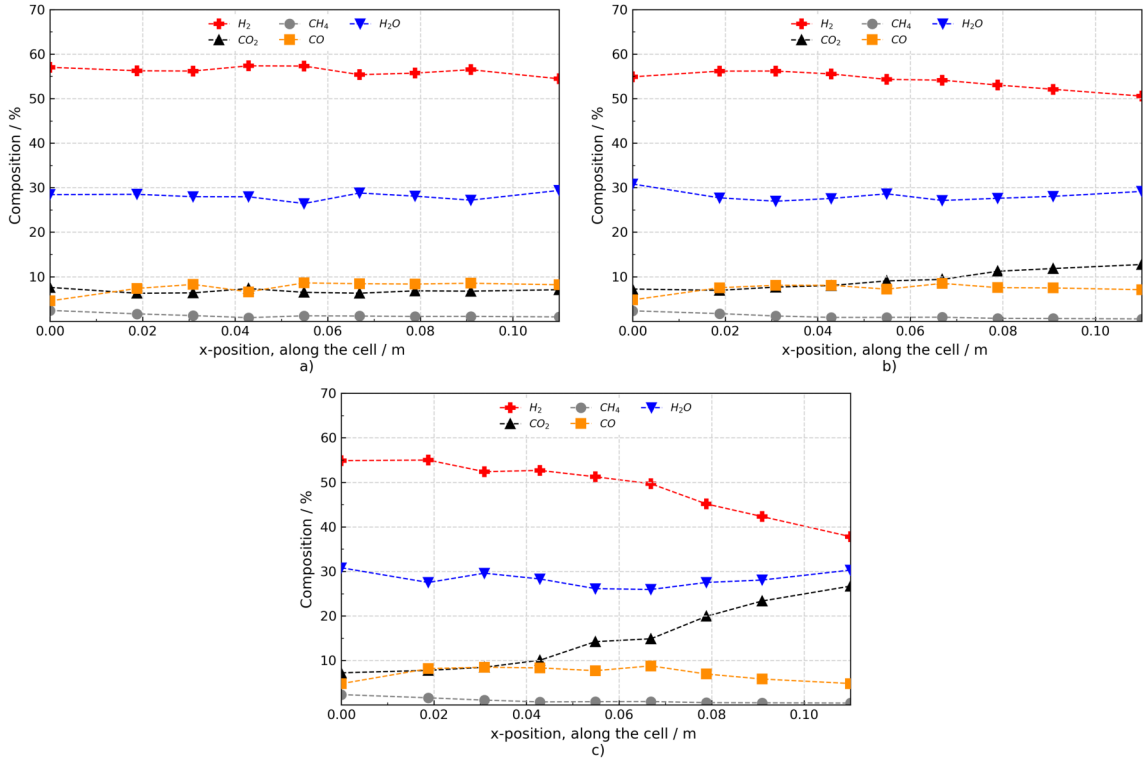

Figure 5.8. *Species variation along the cell for LIR at* 650 °C *and a) OCV, b) 15 A and c) 30 A.*

Since water is generated through the electrochemical reactions and consumed in the reforming reactions (SMR+WGS), it would be expected under load that the mole distribution for water exhibits a large difference throughout the anode. The latter, because the water molecules need to be transported back through the porous media from the active electrochemical reaction zones to the locations for the reforming reactions, and then, to the fuel channel to be transported out of the cell. Nevertheless, it is observed that in all the three cases, Fig. 5.9b, the water content remains almost constant along the cell. In the case of OCV it is justified, as above mentioned, owed to the very low grade of internal reforming, in addition to the absence of electrochemical activity. However, at 15 A and 30 A, it is also observed how the corresponding water compositions remain practically constant along the flow direction, in spite of increasing the current, Fig. 5.9b. That is, even when it is supposed that water is forming under load due to the electrochemical activity, and not being consumed because of the insignificant reforming activity, it is still observed basically the same constant composition as in OCV.

This unexpected trend may result from the way in which H_2O has being quantified. In fact, as mentioned in section 3.3, the GC system that is able to quantify H_2O was not used for the present analyses due to some technical issues with it. Therefore, H_2, CO, CO_2 and CH_4 were the only directly quantified species from the GC, while H_2O has been indirectly quantified or just calculated as the difference between the total, 100%, and the sum of the measured percentage of all the other species. Hence, since the H_2O composition is directly coupled to the measurement of the concentration of the other species, so if there is an issue with CO_2 measurement this would directly reflect in the H_2O concentration. Otherwise, the constant H_2O concentration under load could be the resulting effect of SMR + WGS (consume H_2O) + electrochemical oxidation (generates H_2O).

On the other hand, carbon monoxide is generated in the reforming reaction and consumed by the WGS reaction, according to Eq. (2.18) and Eq. (2.19), respectively. Thus, correspondingly to the methane content in the gas mixture, the CO mole composition initially increases in the flow direction for all the three cases: OCV, 15 A and 30 A. However, as the operating current increases, a more noticeable CO decrease close to the outlet or downstream region of the cell is evident, Fig. 5.9d. Meanwhile, carbon dioxide is generated in the WGS reaction and transported back through the anode to the fuel channels, and further flows out of the cell with the exhaust fuel stream, unless the occurrence of the reverse water-gas shift (r-WGS) reaction, where CO_2 is consumed. Therefore, the observed CO decrease along with the growth of the CO_2 amount, Fig. 5.9e, strongly suggest the occurrence of the WGS reaction under load.

Nonetheless, at 30 A, a considerable increase in the molar composition of the CO_2 is observed. This increase is not quantitatively correspondent with the occurrence of the shifting reaction, nor the CO oxidation reaction as one might think, because there is no way in which such a big quantity of CO_2 is produced. Thus, it is deduced that some issues with the quantification of some species, in

addition to H_2O, have occurred.

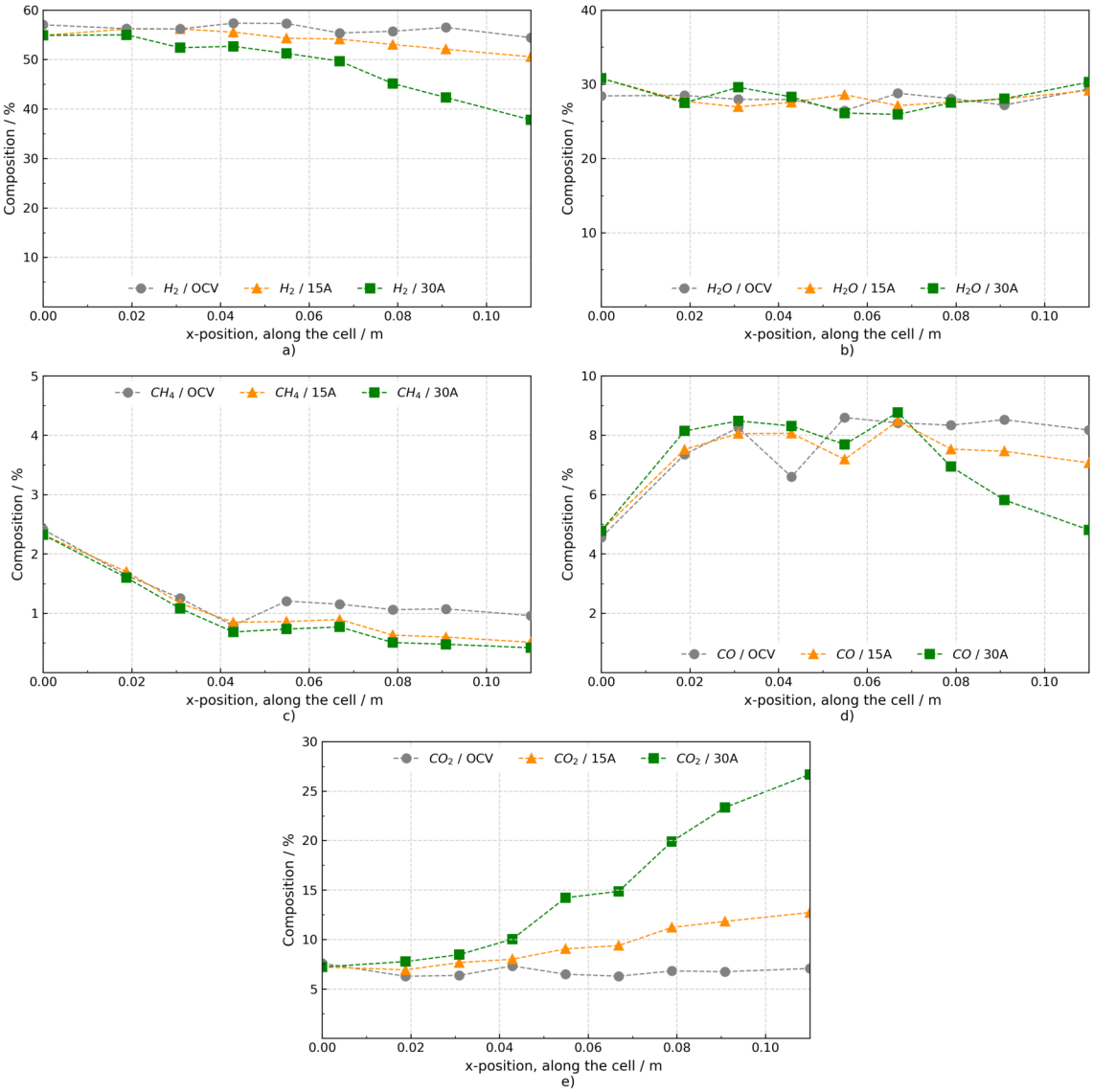

Figure 5.9. *Compositions comparison at OCV, 15 A and 30 A along the cell for LIR at* 650 °C *for a) H_2, b) H_2O, c) CH_4, d) CO and e) CO_2.*

For methane, a clear decrease in the mole composition along the flow direction can be seen. It should be noted that, despite the intermediate operating temperature of the cell, most methane is converted into hydrogen and CO, and even more when the current density is increased, Fig. 5.9c.

Furthermore, from Fig. 5.10 to Fig. 5.12, the contour plots of the species distribution in steady state under LIR at OCV, 15 A and 30 A are depicted.

Accordingly, analyzing the species distribution in OCV, Fig. 5.10, it is observed an apparent uneven species distribution over the anode. However, it should be noted that because of the low

CH_4, CO and CO_2 content in the corresponding gas mixture, the variation in the mole percentage of the species throughout the anode is only ∼2.7% for H_2, ∼3.9% for H_2O, ∼0.8% for CH_4, ∼2.5% for CO, and ∼1.1% for CO_2, which compared to the other two analyzed reformate gas mixtures under the same OCV condition, can be considered insignificant.

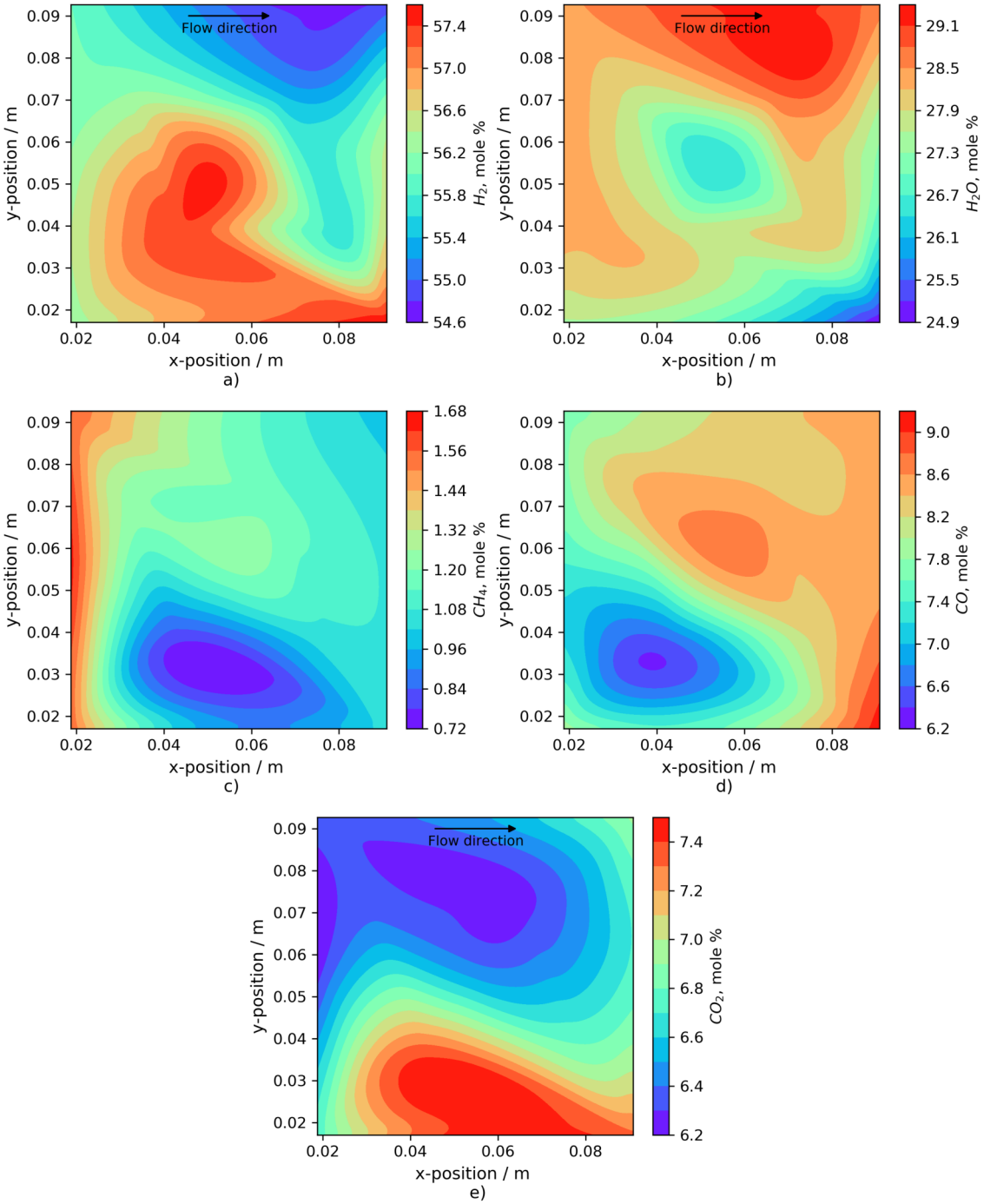

Figure 5.10. *Species distribution throughout the cell for LIR at OCV and 650 °C: a) H_2, b) H_2O, c) CH_4, d) CO and e) CO_2.*

The slight H_2 and CO_2 decrease respect to the inlet composition, mainly observed in the upper half of the cell, along with a correspondent CO and H_2O increase in the flow direction, observed in nearly the same region of the anode, strongly suggest the occurrence of the reverse water-gas shift reaction in OCV condition. Meanwhile, the correspondent mild decrease of CH_4 together with the CO and a localized H_2 increase, observed for this latter in the lower half of the anode, clearly show the occurrence of the steam methane reforming reaction.

In contrast, from Fig. 5.11, it is observed that under 15 A, the general species distribution changes from that observed at OCV. The corresponding increase or decrease for some species in the flow direction becomes more uniform than in OCV, which suggests a more uniform activity of the reacting species. Additionally, the variation in the mole percentage of the species distribution through the anode changes slightly from those obtained under OCV, being $\sim$5.3% for H_2, $\sim$2.3% for H_2O, $\sim$1.2% for CH_4, $\sim$1.6% for CO and $\sim$6.5% for CO_2.

Owed to the multiple reactions occurring under loading conditions and because of the presence of some species as reagent in some reactions and at the same time as products in others, it becomes harder to determine whether a reaction is occurring or not. However, analyzing the H_2 decrease along the flow direction, it is certainly attributed to the hydrogen electrochemical reaction. The CH_4 distribution remains very similar as in the case of OCV, i.e., showing a gradual decrease of methane in the flow direction, with the difference that a bit more CH_4 is forced to react under current than in OCV. This latter due to an increase in the fuel utilization, or in other words, in the demand of H_2 fuel that is produced through SMR.

In the case of CO_2, it is observed a gradual increase in the flow direction, while the CO shows a more uneven mole distribution but a general increase from its inlet composition because of the reforming reaction. However, the clear decrease of the CO mole percentage in the lower half of the anode, along with the marked CO_2 increase and H_2O decrease in the same region, strongly suggest the occurrence of the WGS reaction dominating in that region; whereas the SMR clearly shows its dominance in the inlet region of the cell, as observed from Fig. 5.11c.

Like in the case of 15 A, the contours of species distribution at 30 A, Fig. 5.12, show a quite similar qualitative distribution. Not in the same way for the variation in the mole percentage of the species over anode, which, as expected, increases more than at 15 A. Nevertheless, for some species (H_2 and CO_2), the composition change is not quantitatively correspondent to the applied current, it is rather much more considerable, as can be seen from the following figures, discerned from the corresponding contours of species: $\sim$17.4% for H_2, $\sim$5.6% for H_2O, $\sim$1.2% for CH_4, $\sim$4% for CO, and $\sim$19.1% for CO_2.

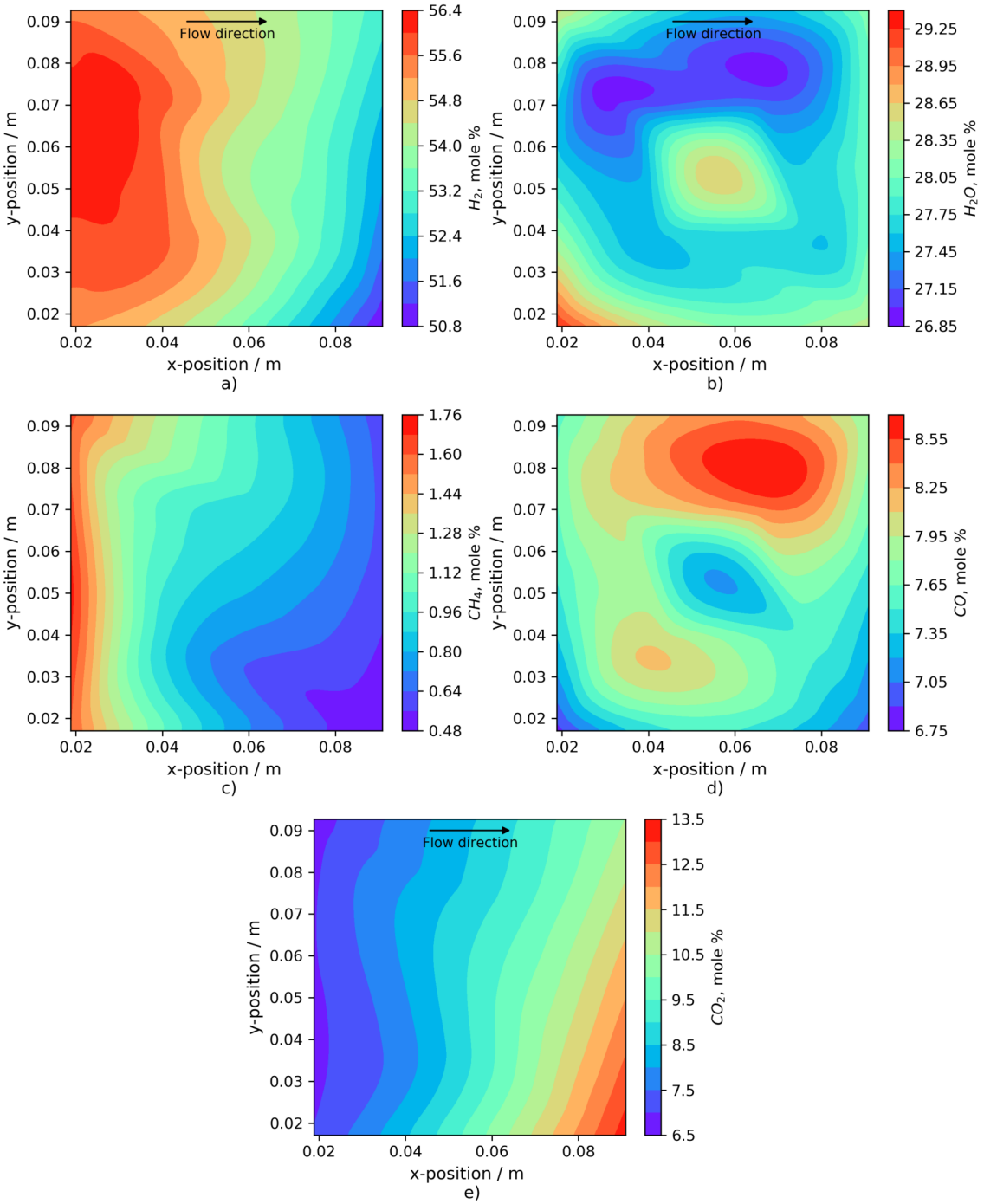

Figure 5.11. *Species distribution throughout the cell for LIR at 15 A and* 650 °C*: a)* H_2*, b)* H_2O*, c)* CH_4*, d) CO and e)* CO_2*.*

In the case of H_2, owed to the increase in the FU from 25% at 15 A to 50% at 30 A, it is justified a more pronounced difference in the species variation throughout the anode. Actually, the mole composition for hydrogen, along with that for methane, decreases in the flow direction. However, in spite of showing the expected qualitative trend, in both cases (15 A and 30 A), the

decrease in the measured amount of hydrogen does not agree with the expected one according to the FU of the set current. This is, from a rough calculation, the expected hydrogen decrease at a FU of 25% should be around 13%, while at 50% of FU it should be around 26%. These figures imply around 44% and 31% of H_2 at 15 A and 30 A, respectively, at the cell outlet. Nevertheless, these expected outlet compositions do not correspond with those obtained experimentally. They resulted to be 50.6% at 15 A and 37.8% at 30 A, around $\sim$6% higher than the expected ones, and representing a decrease from the inlet composition of only $\sim$6.4% at 15 A and $\sim$19.2% at 30 A.

One might think that this issue is owed to the non-considered participation of CO in the electrochemical reaction. However, by analyzing the inlet composition of CO, being 6%, and the possible CO increase by the SMR reaction, being maximum 2%, results a maximum available CO content of around 8%. As H_2 deviation resulted in around 6% in both cases, this results in a CO composition at the outlet of around 2% in both cases, to compensate the higher H_2 content. However, this is not either observed experimentally.

Therefore, because of several problems regarding water condensation during the GC analyses, it is more likely that some error during the measurements has occurred. Thus explaining also the huge increase in the CO_2.

Despite the above discussed issues, the clear and well defined CO decrease and CO_2 increase along the flow direction, appreciated in Fig. 5.12d and Fig. 5.12e, respectively, suggest a stronger occurrence of the WGS reaction at 30 A.

On the other hand, for comparative purposes, in the present work, the outlet equilibrium gas compositions under each analyzed condition were calculated using the chemical engineering simulation software CHEMCAD™ (quite the same as ASPEN PLUS™). In such a software, the inlet gas conditions and the reaction temperature need to be defined. Then, the program treats the cell as an "ideal chemical reactor" (so called Gibbs reactor) and the equilibrium compositions are just a result of minimizing the Gibbs enthalpy at the given temperature (isothermal model). Hence, the cell is considered as a black box that works like an "ideal" reactor.

For the cases studied here, it is well known that at OCV the anode catalyst serves as a reforming catalyst as well, and the anode gas composition changes because of the internal reforming reactions. However, if current is drawn, oxygen ions are transferred from the cathode to the anode. The flow rate of oxygen is then calculated from the current by Faraday's law. Therefore, under simulated loading conditions, oxygen is "added" to the anode feed gas and of course product gas composition will change because of oxidation reactions.

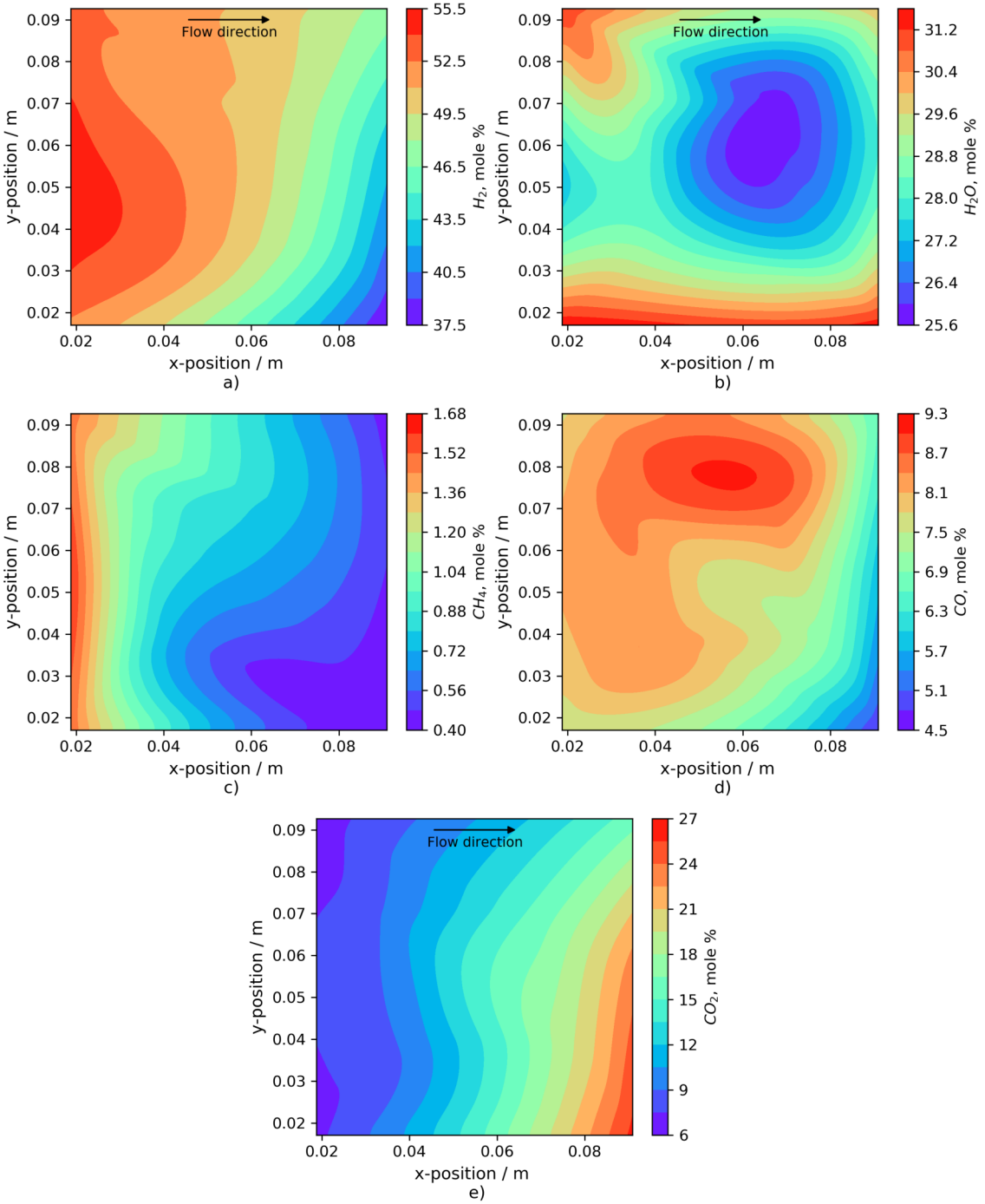

Figure 5.12. *Species distribution throughout the cell for LIR at 30 A and 650 °C: a) H_2, b) H_2O, c) CH_4, d) CO and e) CO_2.*

Accordingly, Table 5.2 shows a comparison of the theoretically calculated outlet compositions and the experimental ones under LIR at OCV, 15 A and 30 A. From here, it is observed that the measured inlet composition at OCV, 15 A and 30 A is quite similar to the theoretical one. These measurements were carried out in order to guarantee the same inlet composition and exclude pos-

sible errors of the flow meters. Regarding the outlet compositions, it is observed that in OCV condition the measured outlet composition and the calculated one are also quite comparable. However, the general change between the inlet and the outlet composition, for both, measured and calculated, is insignificant because of the low CH_4 content. In fact, as also illustrated in Fig. 5.8a and Fig. 5.9, the species variation in OCV respect to the inlet composition is not even noted because of the low reforming activity.

By contrast, under current, it is observed a major difference between the measured and the calculated outlet compositions. As already mentioned, the biggest differences correspond to H_2, CO_2 and H_2O. Nevertheless, these differences have been already related to some problems during the GC analyses, which will be further discussed in detail.

Table 5.2. Comparison of the measured and calculated inlet and outlet compositions for LIR at OCV, 15 A and 30 A.

LIR			H_2 [%]	CO_2 [%]	CH_4 [%]	CO [%]	H_2O [%]	T_{avg} [°C]	η_{WGS}	η_{ref}
	Inlet	Theoretical	57	8	2	6	27			
OCV	Inlet	Measured	57.0	7.6	2.4	4.6	28.4	652	-13.8%†	25%
	Outlet	Measured	54.4	7.1	1.0	8.1	29.4			
	Outlet	Calculated	56.5	7.0	1.8	7.4	27.3			
15 A	Inlet	Measured	54.9	7.2	2.3	4.8	30.8	656	27.5%	82.9%
	Outlet	Measured	50.6	12.7	0.5	7.1	29.1			
	Outlet	Calculated	44.6	9.7	0.4	5.6	39.7			
30 A	Inlet	Measured	54.9	7.2	2.3	4.8	30.8	666	54%	97.8%
	Outlet	Measured	37.8	26.7	0.4	4.8	30.3			
	Outlet	Calculated	30.6	12.0	0.1	3.7	53.6			

Theoretical: proposed inlet composition

Measured: obtained experimentally from GC measurements

Calculated: obtained from CHEMCAD™

T_{avg}: average cell temperature in steady state

η_{WGS}: WGS efficiency (CO mole percentage reacting)

η_{ref}: reformate efficiency (CH_4 mole percentage reacting)

†The negative sign means that CO is being produced owed to the occurrence of the reverse water-gas shift (r-WGS) reaction

Additionally, through the equilibrium compositions calculated at the outlet of the cell by means of CHEMCAD™, it has been also possible to theoretically determine which reactions occur under each condition and compare them with the experimentally determined ones. Accordingly, at OCV, with a negative percentage of CO reacting, it is assumed to occur the r-WGS reaction, since there

is a slight consumption of CO_2 and H_2 and a corresponding CO and H_2O increase. Under current, it is established that the WGS reaction occurs, according to a general balance of the corresponding species. In agreement with the experimental results, it is also obtained that the WGS reaction plays an important role mainly under high current densities.

In addition to the shifting reaction, it is presented the reforming efficiency, which, in all the three cases, i.e., OCV, 15 A and 30 A, suggests the occurrence of the SMR reaction. It can be observed that despite the low methane content, the amount that is reformed increases with current, which is reflected in the increase of the reforming efficiency.

It is noteworthy that the theoretical prediction of the above mentioned reactions is in complete agreement with the interpretation of the experimental results, so their occurrence is also concluded from the experimental species distribution.

Nevertheless, it is important to emphasize that it results compromising to ensure whether a reaction occurs or not only from such a simple analysis of the species distribution. And even more when some issues arise during the experimental campaign, thus increasing the uncertainty of the experimental measurements. Hence, in this case, the calculated compositions can be taken as a reference to compare the cell phenomena.

5.1.3.2. IIR

Operating under the intermediate internal reforming composition, Fig. 5.13a, Fig. 5.13b, and Fig. 5.13c show the respective species variation along the flow direction at OCV, 15 A and 30 A. It is illustrated the impact of increasing the reformate grade on the species variation owed to the simultaneous internal reforming reaction, water-gas shift reaction, and oxidation reaction of H_2 (when is the case). At the entrance of the anode, due to a higher methane content, the reforming reactions are much faster and methane is consumed quickly, Fig. 5.14c, while the production of H_2 and CO becomes evident, Fig. 5.14a and Fig. 5.14d, respectively.

As observed in OCV, Fig. 5.13a, most changes in the species compositions occur in the first 4 cm of the anode length, which is certainly owed to the SMR phenomenon. Meanwhile, along the rest of the anode length, an almost constant composition is appreciated for most species. The continuous CO increase, even after the first 4 cm, up to which it is supposed that the SMR almost ceased and thus it is not producing more CO, along with a corresponding CO_2 decay in the flow direction, indicate that the r-WGS reaction is taking place in OCV condition.

Under load, Fig. 5.13b and Fig. 5.13c, once that most of the methane is consumed, the H_2 electro-oxidation reaction becomes more evident through the consumption of H_2, which in fact can be seen more clearly at 30 A, Fig. 5.13c.

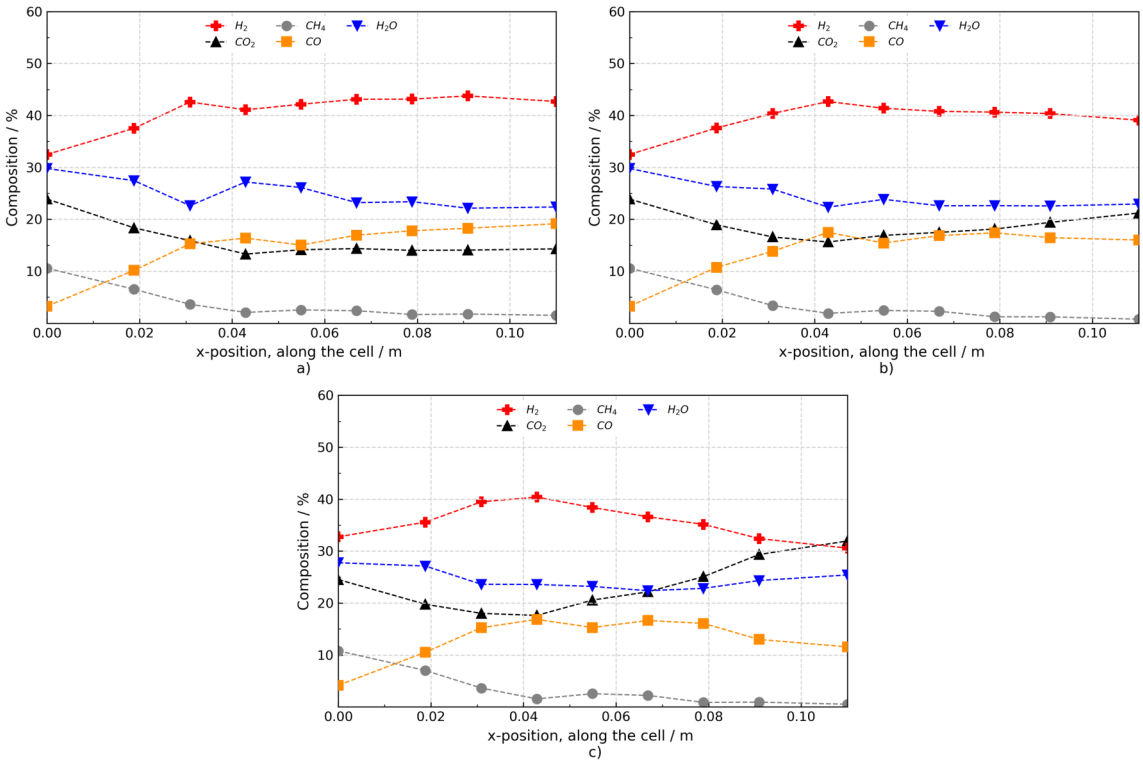

Figure 5.13. *Species variation along the cell for IIR at* 650 °C *and a) OCV, b) 15 A and c) 30 A.*

As observed from Fig. 5.13b and Fig. 5.13c, corresponding to the respective species variation at 15 A and 30 A, the initial content of CH_4 and H_2O decays, while the H_2 and CO mole composition increases, also in the very first 4 cm of the anode length. It indicates, qualitatively and quantitatively, the occurrence of the SMR. Additionally, it can be seen that the initial concentration of carbon dioxide declines about 10% along the same first 4 cm of the cell length for all the three cases, Fig. 5.14e. However, since the absolute amount of carbon dioxide is not directly affected by the occurrence of only the SMR and electrochemical reaction, the observed initial CO_2 decrease is explained because the number of gas molecules or the total volume of the new formed gas mixture increases due to the reforming reaction, resulting in a decline of the partial pressure or molar fraction of CO_2. This particular behavior of the CO_2, to initially decrease, was also observed in previous tests reported by Santoni et al. [74]. Hence, these issues suggest that, at steady state and under chemical equilibrium, SMR is the dominant reaction at the entrance of the cell, and until CH_4 starts getting depleted, the simultaneous H_2 electro-oxidation along with the WGS reaction occur along the rest of the anode length.

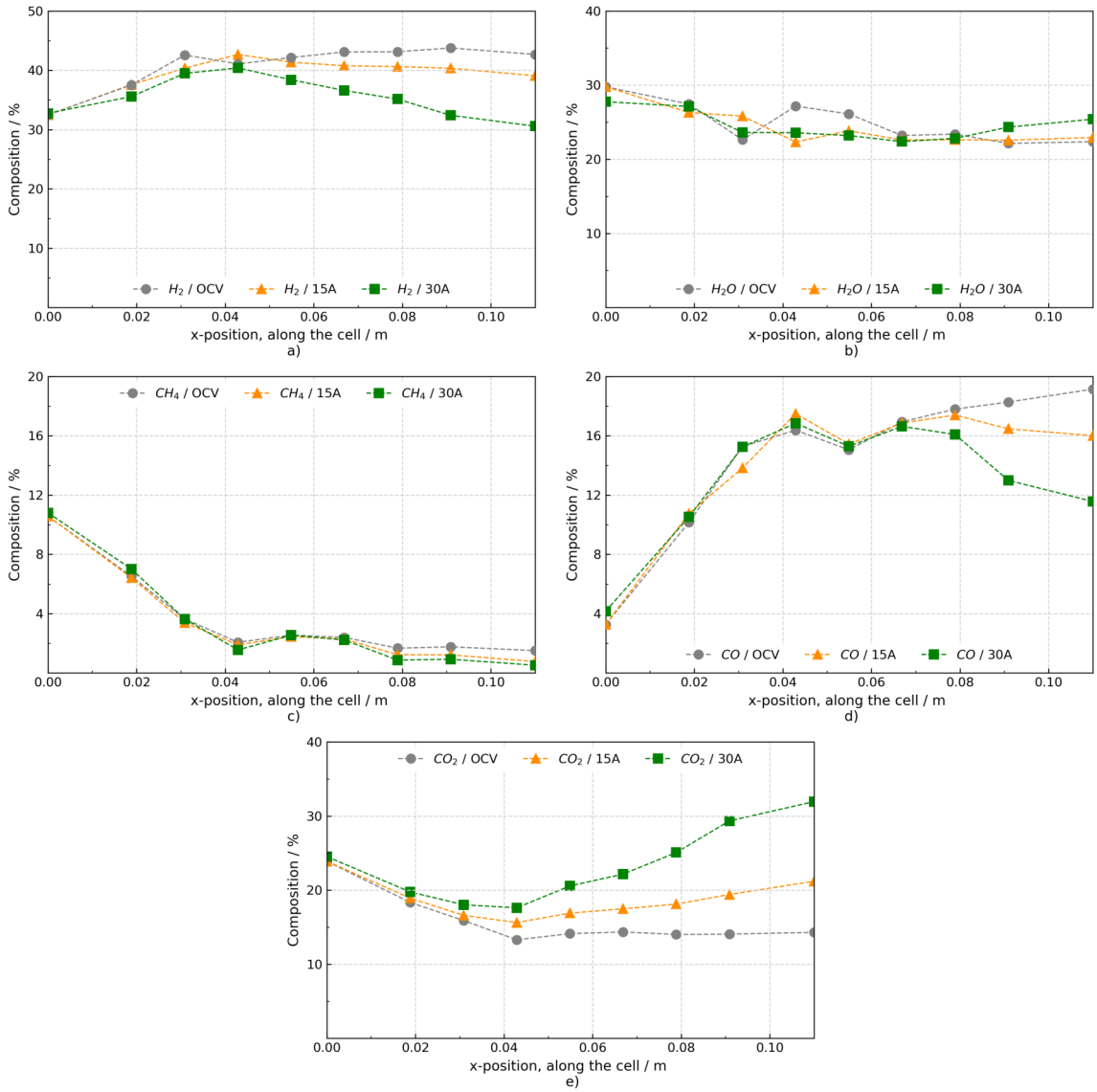

Figure 5.14. *Compositions comparison at OCV, 15 A and 30 A along the cell for IIR at* 650 °C *for a)* H_2*, b)* H_2O*, c)* CH_4*, d) CO and e)* CO_2*.*

It is known that, depending on the operating conditions, the equilibrium or kinetics approach must be valid or not. Particularly, as flow rates decrease the residence times increase. At sufficiently low flow rates, the kinetics can run sufficiently fast as to approach equilibrium behavior. Accordingly, in the present work, the fuel volume flow rates feed to the anode are considered very low for the size of the cell, which may explain why the equilibrium approach describes well the occurring cell phenomena. In addition to the above, Hecht et al. [160] also state that at relatively high cell voltages, where the current density is relatively low, being the case of the present study, the kinetics tends toward equilibrium behavior; while, at low cell voltages, where current densities are high, the reforming kinetics can be rate-limiting.

Hence, the above statements may support the validity of the chemical equilibrium approach considered in the present experimental analysis. Then, it is possible to move on the analysis of the species distribution over the anode. Accordingly, Fig. 5.15 shows the corresponding species contour plots obtained under OCV condition.

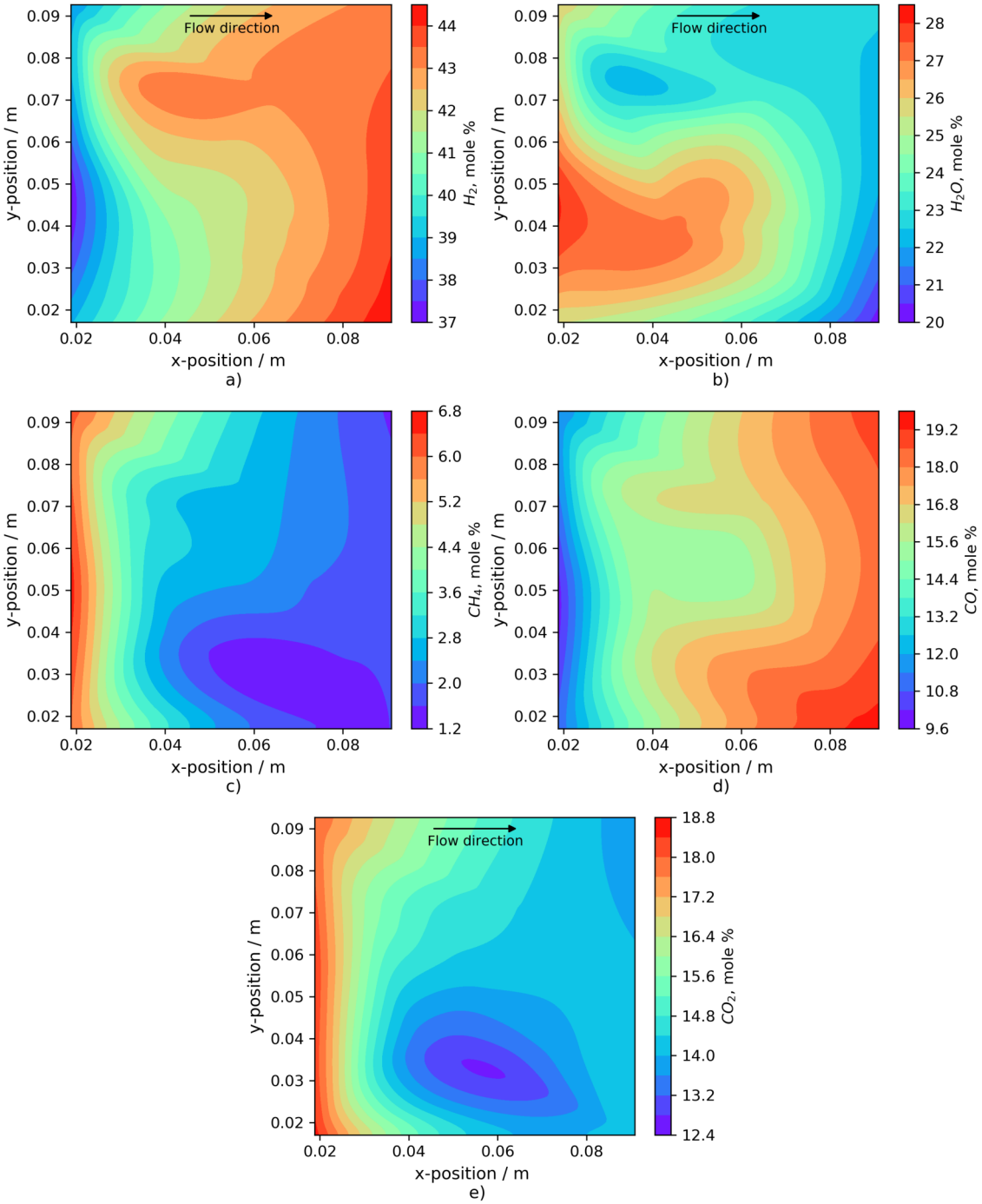

Figure 5.15. *Species distribution throughout the cell for IIR at OCV and* 650 °C*: a)* H_2*, b)* H_2O*, c)* CH_4*, d)* CO *and e)* CO_2*.*

As earlier described, not only hydrogen but also CO is produced as a result of direct steam methane reforming. Meanwhile, the CO_2 mole percentage may be decreased by the reverse water-gas shift reaction, in addition to the initial decrease because of the volume increase of the total mixture. Thus, since CO_2 has been detected to continuously decrease in OCV condition, and the CO production continuously increased, even after the CH_4 content was almost completely reformed, part of the CO can be seen to be converted from CO_2 by the r-WGS reaction.

Regarding the H_2O distribution, it was expected to decrease along the flow direction, as actually observed in Fig. 5.15b. The general H_2O consumption is owed to a stronger and dominant reforming activity over the subsequent r-WGS reaction.

Finally, according to Fig. 5.15a, it is observed that hydrogen can be produced steadily through SMR in the Ni-YSZ anodes, even at intermediate temperatures, resulting in an experimental efficiency of the direct steam reforming process of around 85%. Therefore, in the case of methane-rich fuels, methane is almost totally converted into hydrogen and carbon monoxide, shown the suitability of the DIR process.

On the other hand, from Fig. 5.16, corresponding to the cell operating under 15 A, it is observed that when current is drawn, the general phenomena occurring in the cell changes, which in turn is reflected in a different species distribution over the anode. Accordingly, H_2 increases in the first 4 centimeters of the cell length, while CH_4 decreases, both owed to the SMR reaction. The subsequent H_2 consumption and its uneven distribution along the flow direction is more related to the H_2 electro-oxidation. Such an uneven fuel distribution can give also an idea about the FU distribution throughout the anode, as will be later discussed.

Regarding CO_2, this species shows the particular trend to initially decrease and then subsequently increase along the anode, as already observed from Fig. 5.14e. The increase of CO_2, observed in the outlet region of the cell, more particularly close to the lower right corner, Fig. 5.16e, together with a barely perceptible decrease of CO in the same region, Fig. 5.16d, suggest that the water-gas shift reaction is scarcely taking place in this case. The apparent continuous CO increase in the flow direction is related to the reforming reaction, which increased the CO mole composition in the first part of the cell. From there, basically the same CO composition was dragged.

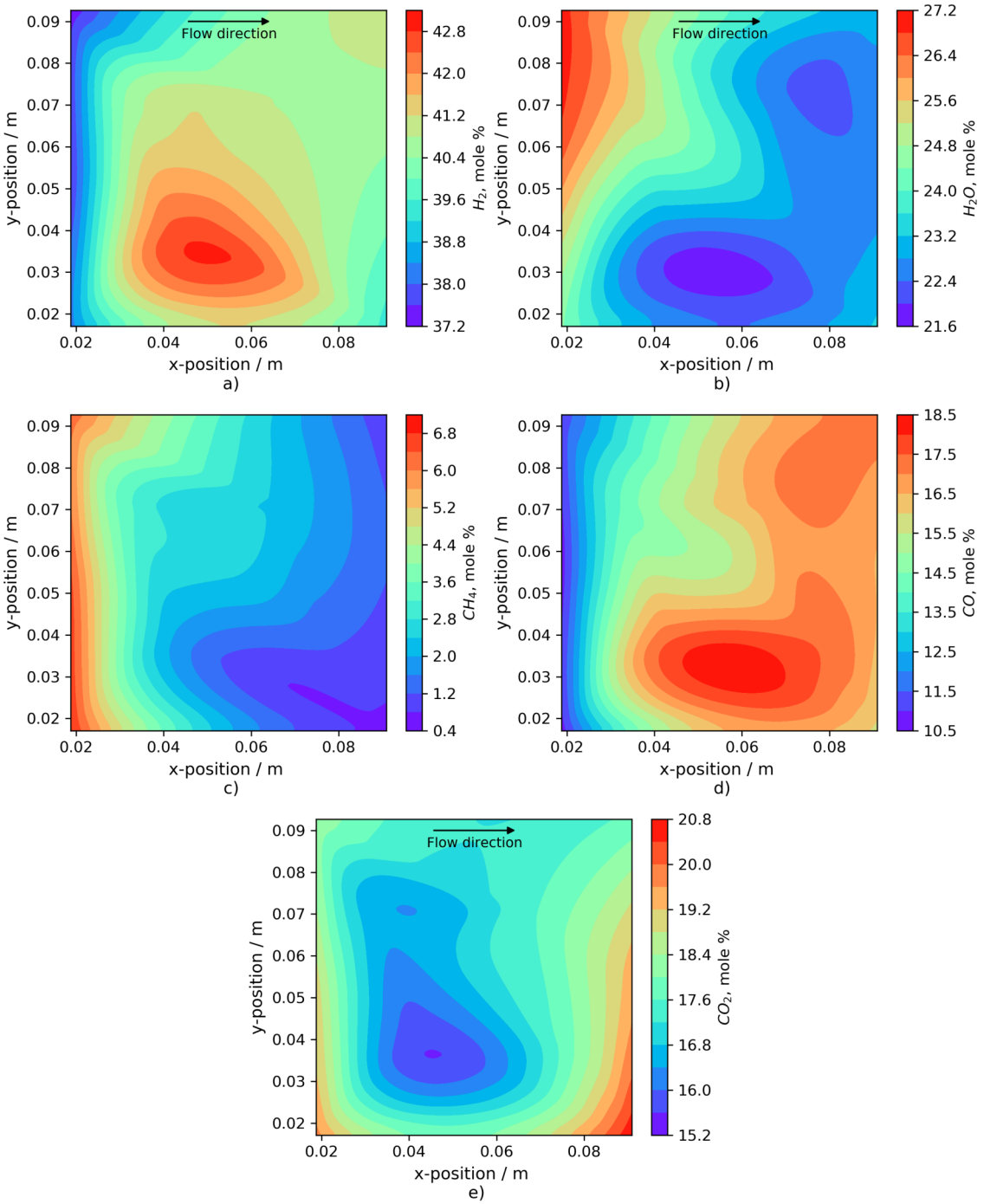

Figure 5.16. *Species distribution throughout the cell for IIR at 15 A and* 650 °C*: a)* H_2*, b)* H_2O*, c)* CH_4*, d) CO and e)* CO_2*.*

Finally, from the species distribution at 30 A, Fig. 5.17, it is observed a qualitatively similar distribution as in the case of 15 A. Close to the inlet of the fuel channel, a steep increase of the H_2 concentration can be observed. This is due to the rapid SMR reaction and is an indication that this occurs mainly close to the fuel inlet. After most CH_4 is depleted, the produced H_2 is then gradually

consumed along the length of the cell by the electrochemical reaction, Eq. (2.3), resulting in the decrease of its molar fraction after reaching a maximum value.

Fig. 5.17 illustrates the corresponding species distribution of the fuel gas in the anode at 30 A. The impact of the simultaneous occurrence of the SMR reaction, the WGS reaction and the electrochemical oxidation of H_2 at the anode catalyst layer is clearly shown. A rapid decrease in the CH_4 composition and a corresponding increase in the H_2 composition can be seen close to the inlet of the fuel channel, 5.17a and 5.17c, respectively. This is due to the very fast SMR reaction and partially because of the WGS reaction. A decrease in the H_2O composition can also be observed, which can also be attributed to the reforming and shifting reactions as steam plays the role of the reactant in these reactions. However, H_2 and H_2O are also participating in the H_2 electrochemical reaction, where they have an opposite role. When CH_4 starts getting depleted, H_2 composition begins to decrease, as now the effect of the electrochemical reaction is dominating. Consequently, the H_2 composition exhibits a maximum close to the point where CH_4 is depleted. Similarly to H_2, at the inlet region there is an increase in the CO composition due to the SMR reaction, which starts decreasing as soon as CH_4 is consumed and the WGS reaction dominate. These trends, presented in Fig. 5.13c, are in qualitative agreement with results from [77, 202, 235, 265], but vary quantitatively due to the use of different operating parameters.

Additionally, as observed from Fig. 5.17d and Fig. 5.17e, the stronger occurrence of the WGS reaction is reflected in a more marked and clearer trend of some of the involved species. Unlike 15 A, at 30 A it is evident a clearer CO_2 increase in the flow direction and a CO decrease, this latter observed from the middle of the anode to the outlet. This issue suggests that the WGS reaction becomes more important under high current densities. Hence, there is a clear difference between the distribution of CO_2 in OCV and under load. Fig. 5.15e clearly shows the occurrence of the shifting reaction towards the left direction (r-WGS reaction) through a constant CO_2 consumption. Meanwhile, Fig. 5.17e, shows the production of CO_2 owed to a stronger WGS reaction.

Nevertheless, as in the case of LIR, under loading conditions it is obtained an unexpected H_2O behavior. Since H_2O is produced as the electro-oxidation reaction of hydrogen proceeds along the flow direction, it should be expected that the H_2O concentration increases in the flow direction. Nonetheless, this is not observed. As mentioned in the previous analysis, this fact may be related to some issues with the species quantification.

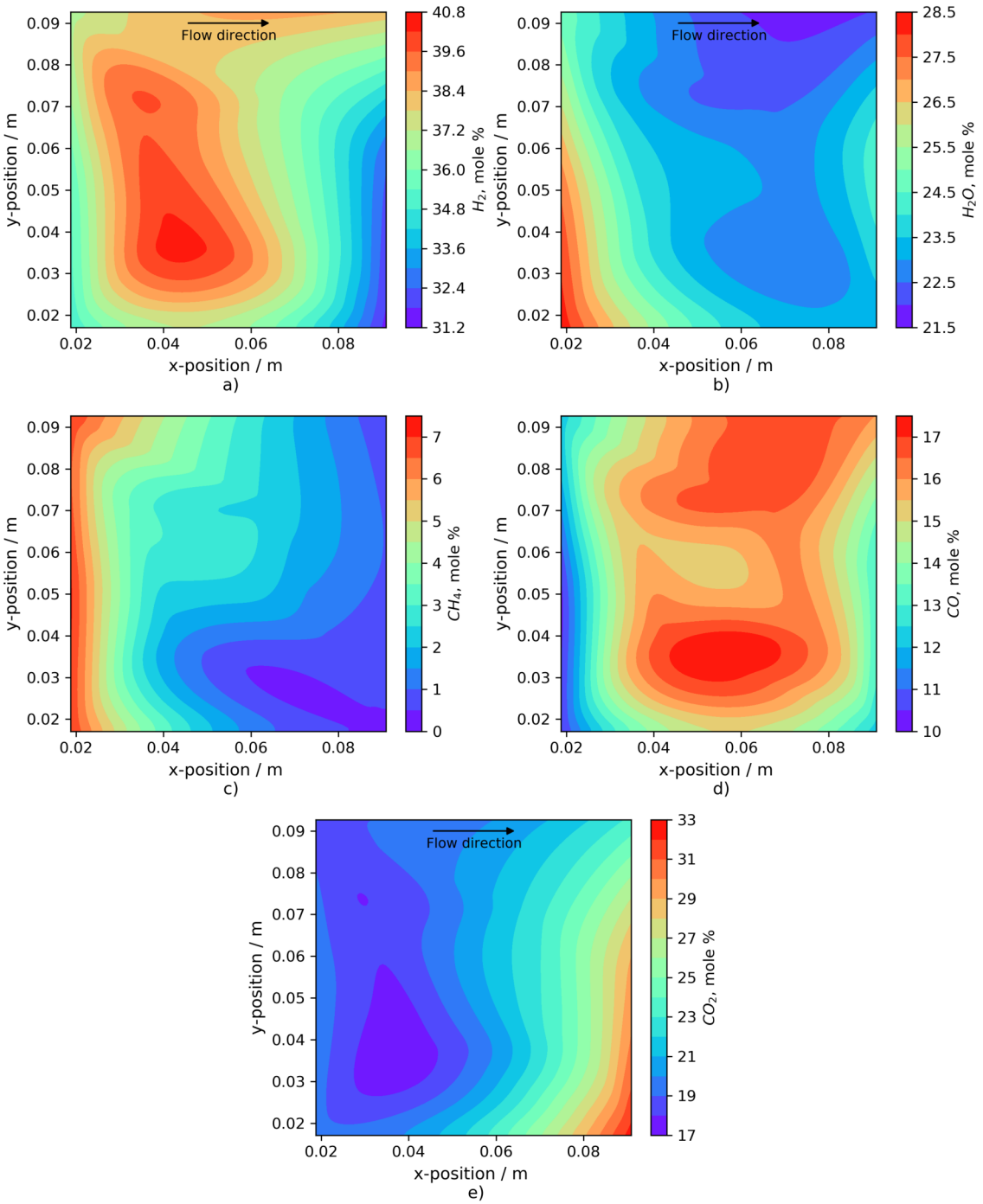

Figure 5.17. *Species distribution throughout the cell for IIR at 30 A and* 650 °C*: a)* H_2*, b)* H_2O*, c)* CH_4*, d) CO and e)* CO_2*.*

In Table 5.3 it is presented the comparison of the experimental outlet compositions and the calculated ones. Under OCV condition it is observed, in general, a quite good agreement between the different species, while under load larger differences can be identified for some species. Nevertheless, as both measured and calculated results are roughly comparable, once more, it may show

that the physicochemical processes experimentally identified, i.e. the reactions occurring in the cell and the phenomena qualitatively described, are not far from the chemical equilibrium approach considered in the theoretical estimations.

Table 5.3. Comparison of the measured and calculated inlet and outlet compositions for IIR at OCV, 15 A and 30 A.

IIR			H_2 [%]	CO_2 [%]	CH_4 [%]	CO [%]	H_2O [%]	T_{avg} [°C]	η_{WGS}	η_{ref}
	Inlet	Theoretical	31	23	12	4	30			
	Inlet	Measured	32.5	23.9	10.5	3.3	29.8			
OCV	Outlet	Measured	42.7	14.3	1.5	19.1	22.4	647		85.7%
	Outlet	Calculated	44.7	15.3	2.8	15.6	21.6		∼-36.5%†	72.8%
	Inlet	Measured	32.4	23.9	10.6	3.3	29.8			
15 A	Outlet	Measured	39.1	21.2	0.8	16.0	22.9	650		92.7%
	Outlet	Calculated	38.0	19.1	0.9	12.2	29.8		∼3.5%	91%
	Inlet	Measured	32.7	24.5	10.8	4.2	27.8			
30 A	Outlet	Measured	30.6	31.9	0.5	11.6	25.4	660		95.1%
	Outlet	Calculated	29.0	22.8	0.2	8.8	39.2		∼34%	98.3%

Theoretical: proposed inlet composition

Measured: obtained from GC measurements

Calculated: obtained from CHEMCAD™

T_{avg}: average cell temperature in steady state

η_{WGS}: WGS efficiency (CO mole percentage reacting)

η_{ref}: reformate efficiency (CH_4 mole percentage reacting)

†The negative sign means that CO is being produced owed to the occurrence of the r-WGS reaction

It has been previously pointed out that under load greater differences between the measured and calculated compositions can be discerned. Excluding the H_2O from this analysis, at 15 A, the largest deviation is observed for CO, which is reflected in a lower H_2O content than the expected. At 30 A, the greatest difference resulted for CO_2 and relatively minor for CO, which again, have been reflected in the water quantification, making it to seem that the H_2O content does not increase with current.

As already discussed in the LIR analysis, in this case it is not either possible that such differences are owed to the occurrence of different reactions than the ones considered here, because some of the measured species are quantitatively similar to those calculated theoretically. As an example, by comparing the measured and calculated CH_4 and CO compositions at 30 A, it is observed that both are quite similar. Not so for CO_2 and H_2O, which mainly show a huge difference. However,

there is no way or possible reaction that causes such an increase in CO_2 without any effect on the CO. Besides, it is observed that such differences are mainly evident under load. As it is well known, under load there is more water being produced, meanwhile in OCV it is usually being consumed. In effect, during the gas analyses there was water condensation that caused water clogging of the system in several times. For such a reason the GC equipment had to be cleaned frequently with air while performing the composition analyses. Furthermore, the gas analyses were performed at least twice in each single point in order to assure the validity of the results obtained after each measurement. Usually, when water clogging occurred, the intensity of the peaks related to a particular or some species used to change. Thus, it was the way in which it was realized when there was condensate water in the GC system and thus it needed to be removed by means of air usage.

Actually, this issue really makes sense when the operating principle of the GC system is analyzed. In section 3.3 it was mentioned that the rate at which the molecules from a gas mixture progress along the column depends on the strength of adsorption, which in turn depends on the type of molecule and on the stationary phase (solid phase) materials. Since each type of molecule (analyte) has a different rate of progression, the various components of the sample mixture (H_2, CO, CO_2, CH_4) are separated as they progress along the column and reach the end of the column at different times (retention time). Hence, when water condensation occurred in the GC system, it caused a plug that could make that the mixture composition changes completely.

Accordingly, it is reported that in a wet mixture, water normally elutes much after the CO_2 peak on a Q column (type of column used in the present analysis), which may explain why in most cases the CO_2 peak resulted with a much higher intensity than the real one and thus overestimating its composition. Additionally, it is clearly reported [266] that if sample gas stream is saturated with moisture, then condensation can occur on cold internal tubing surfaces, causing loss of analytes and other more serious problems, e.g., vapor can back-flush into the gas supply lines which are not heated and cause persistent sample carryover. Therefore, it is usually suggested to keep the oven temperature above 80 °C, which until then was avoided in order to prevent possible damages to the adapted column. Hence, in addition to the inadequate temperature set in the GC oven; the non-well heated sampling lines and their capillary diameter are also considered as other potential causes of the experienced water condensation that could have affected the intensity of some peaks.

It is not either discarded the possibility of some compositions deviations because of the calibration curves. However, since these were done twice, its contribution to the composition differences is expected to be low. It is rater related, as just mentioned, to the stability of the sample because of insulation problems and an inappropriate GC method for the analyzed mixture, which in fact contains H_2O in a very high content. For that reason, all the scientific publications reviewed so far that include GC analyses, always remove the steam from the gas mixture before entering to the GC system [11, 51, 77, 78], in order to avoid dealing with all these issues. However, it is clear that the

feature that makes this multisampling set-up a particular system in the world is the possibility of quantifying water directly from *in-operando* analyses. This is what makes it worthwhile to seek for an adequate method to carry out the composition analyses.

Therefore, once clarified the reason of the observed differences between the measured and the calculated compositions, it is possible to highlight the general agreement between the theoretical and the experimental outlet compositions for IIR. In accordance with the species analysis, from the calculated outlet compositions it was determined the occurrence of the r-WGS reaction in OCV and the WGS reaction under current, increasing its efficiency proportionally to the applied current. Regarding the reforming efficiency, it was obtained in both cases, experimentally and theoretically, high reforming efficiencies, thus suggesting an almost total methane conversion over the whole cell.

5.1.3.3. CIR

For the analysis of the complete internal reforming composition, it should be pointed out that in this case, the tested currents were 15 A and 25 A, the latter instead of 30 A.

As observed from Fig. 5.18, under the actual composition, the characterization at 30 A was not possible owed to a voltage instability at such current value. In fact, it is clearly seen the magnitude of the voltage fluctuations at 30 A and how they are, compared with those at 15 A. Although it was certainly possible to reach 30 A during the I-V curve recording under this composition, during the attempt to carry out the GC analysis was when such voltage instability was observed. Even after waiting enough time for the cell stabilization, the high voltage fluctuations were still present. Therefore, this issue just highlights the lack of SOFCs stability under DIR of wet methane when high current densities are drawn.

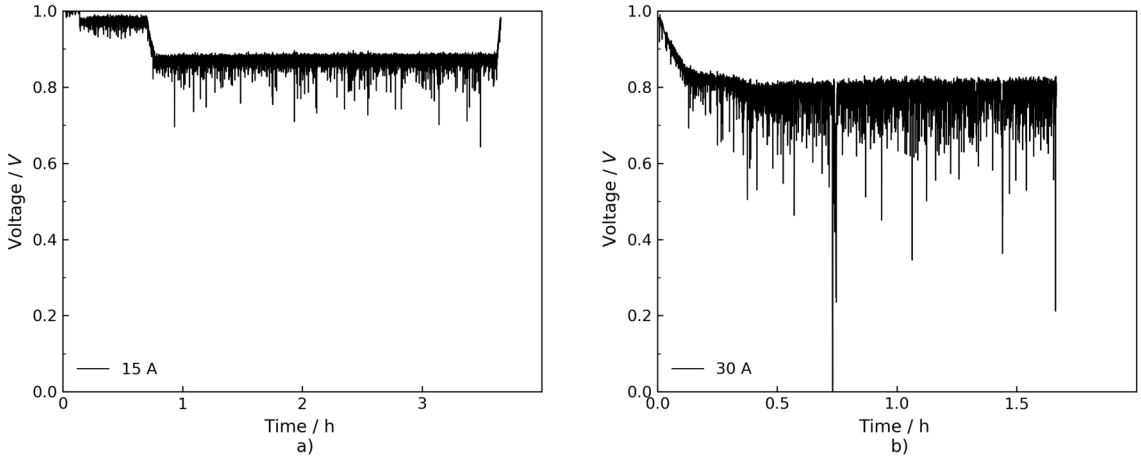

Figure 5.18. *Voltage fluctuations comparison during time for CIR at* 650 °C *and a) 15 A and b) 30 A.*

Thus, by decreasing the current little by little and monitoring the cell stability over time, it was

reached 25 A. This value of current was the maximum current under which it has been possible to carry out a complete characterization with a better voltage stability than that observed at 30 A.

Accordingly, in Fig. 5.19 it is presented the species variation along the anode under OCV, 15 A and 25 A, respectively. Meanwhile, in Fig. 5.20 it is presented the comparison of each species under the corresponding three different values of current.

From the analysis of Fig. 5.19 and Fig. 5.20, it is observed that with a higher inlet concentration of methane, the direct conversion of CH_4 is more favored. In fact, the plots show an almost total methane conversion along the whole cell. The almost total methane conversion, Fig. 5.20c, results in a steep rising of hydrogen concentration, Fig. 5.20a, and a gradual CO and CO_2 concentration increase. The small drop of CO, Fig. 5.20d, and the corresponding peak of CO_2, Fig. 5.20e, after the first 6 cm of the cell length are caused by the fast shift-reaction.

Reactions presented in Eq. (2.18) and Eq. (2.19) are reversible and they proceed fast over active catalyst, including Ni/YSZ anodes, at temperatures above 600 °C. For SOFC systems with DIR, it can hence be assumed that the reactions from Eq. (2.18) and Eq. (2.19) are in equilibrium, with the product gases governed by the thermodynamic equilibrium set up between both reactions.

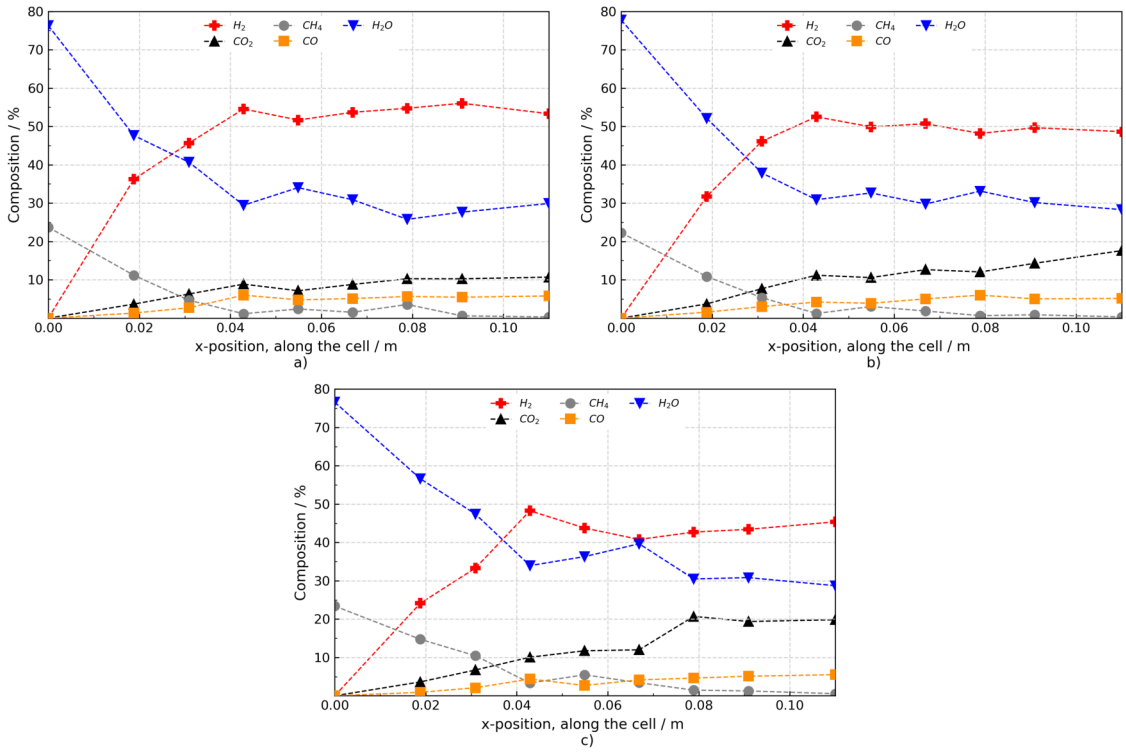

Figure 5.19. *Species variation along the cell for CIR at* 650 °C *and a) OCV, b) 15 A and c) 25 A.*

Excess addition of steam moves the equilibrium towards more hydrogen, implicating a higher utilization of the fuel already in the processing step. Additionally, at higher S/C ratios the methane

is completely reformed even at intermediate temperatures and carbon deposition is avoided. This is, the steam content in the gas mixture can be increased to suppress carbon deposition. By doing this, and according to Le Chateliers principle, the equilibrium of the reforming reaction is shifted towards the products. Nevertheless, this dilutes the fuel and significantly reduces the cell performance and the overall cell efficiency, as actually observed from Fig. 5.18.

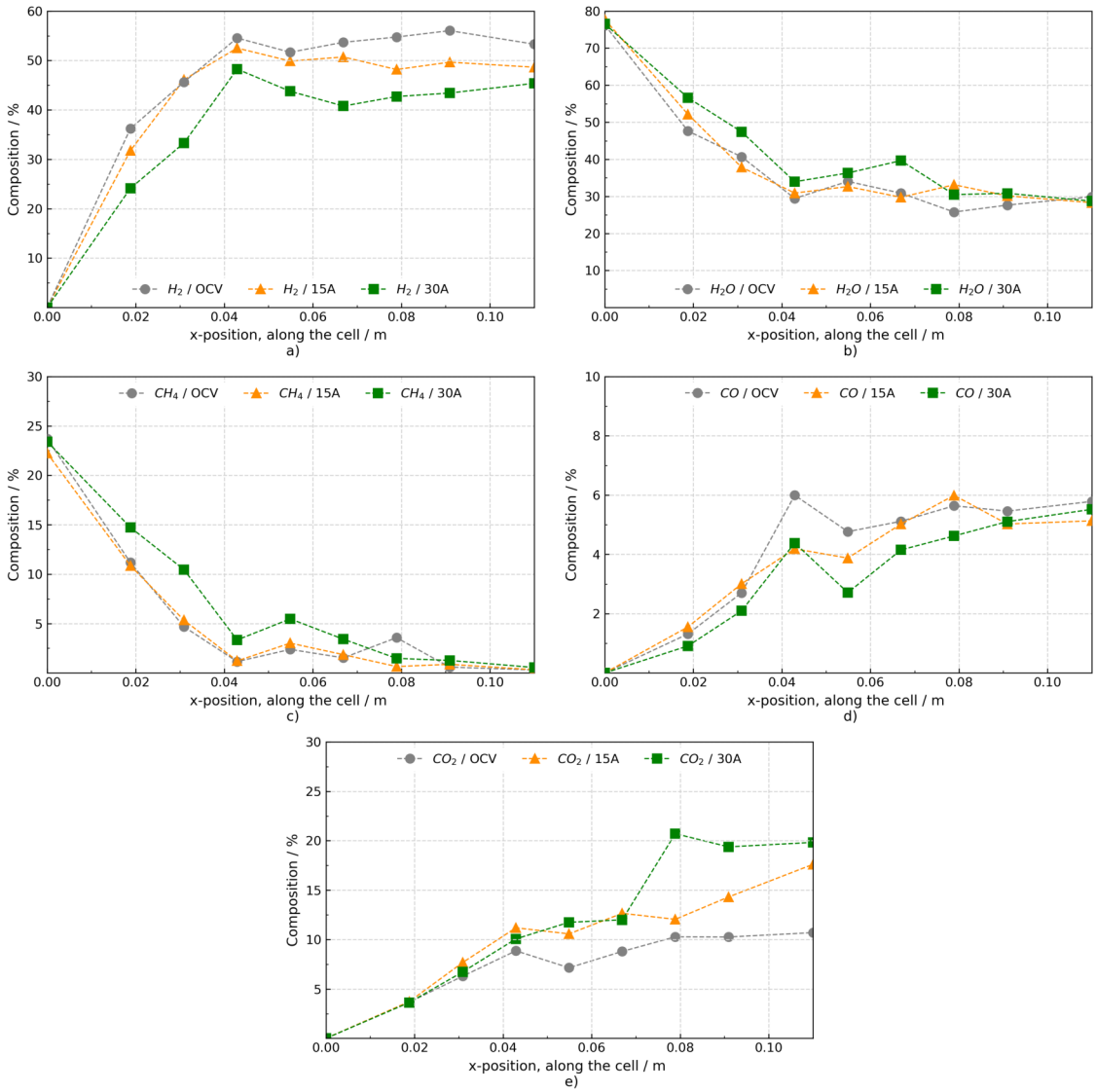

Figure 5.20. *Compositions comparison at OCV, 15 A and 25 A along the cell for CIR at* 650 °C *for a)* H_2*, b)* H_2O*, c)* CH_4*, d) CO and e)* CO_2*.*

From the analysis of the species variation along the anode, Fig. 5.20, a clear picture of the way in which the different reactions occur under this composition can be given. Accordingly, from a simple analysis of the species trend under OCV, 15 A and 25 A, it is observed that for all the three cases the species variation is qualitatively the same. Near to the inlet of the cell, an abrupt increase of the H_2 concentration is observed, due to the fast SMR reaction. After most CH_4 is reformed,

along the first 4 centimeters of the cell length, the produced H_2 is then gradually consumed along the length of the cell by the oxidation reaction (when is the case), resulting in the decrease of its mole composition after reaching a maximum value. Simultaneously, the WGS reaction, under the three loading conditions, becomes evident from the first centimeters of the cell length until the outlet.

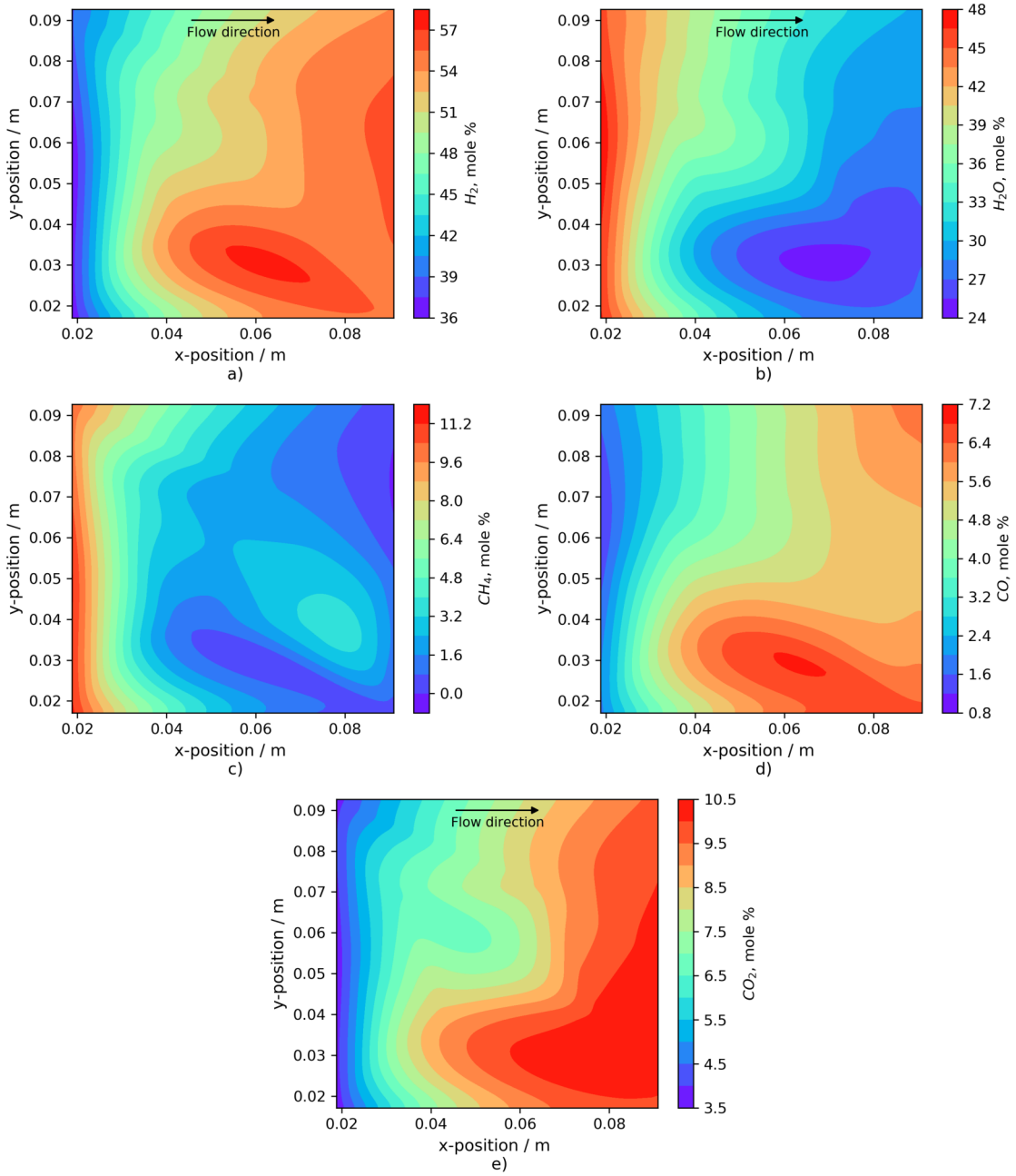

Figure 5.21. *Species distribution throughout the cell for CIR at OCV and* 650 °C*: a)* H_2*, b)* H_2O*, c)* CH_4*, d) CO and e)* CO_2*.*

Fig. 5.21 shows the resulting steady state species distribution over the anode in OCV condition.

It is observed that at the inlet, due to the high methane content, the reforming reaction proceeds much faster, consuming methane quickly and at the same time producing large amounts of H_2. As also observed, from the entrance of the anode there is a gradual production of CO and CO_2. CO has been certainly produced through the SMR reaction, but at the same time consumed since the beginning by the WGS reaction, to consequently increase the CO_2 concentration.

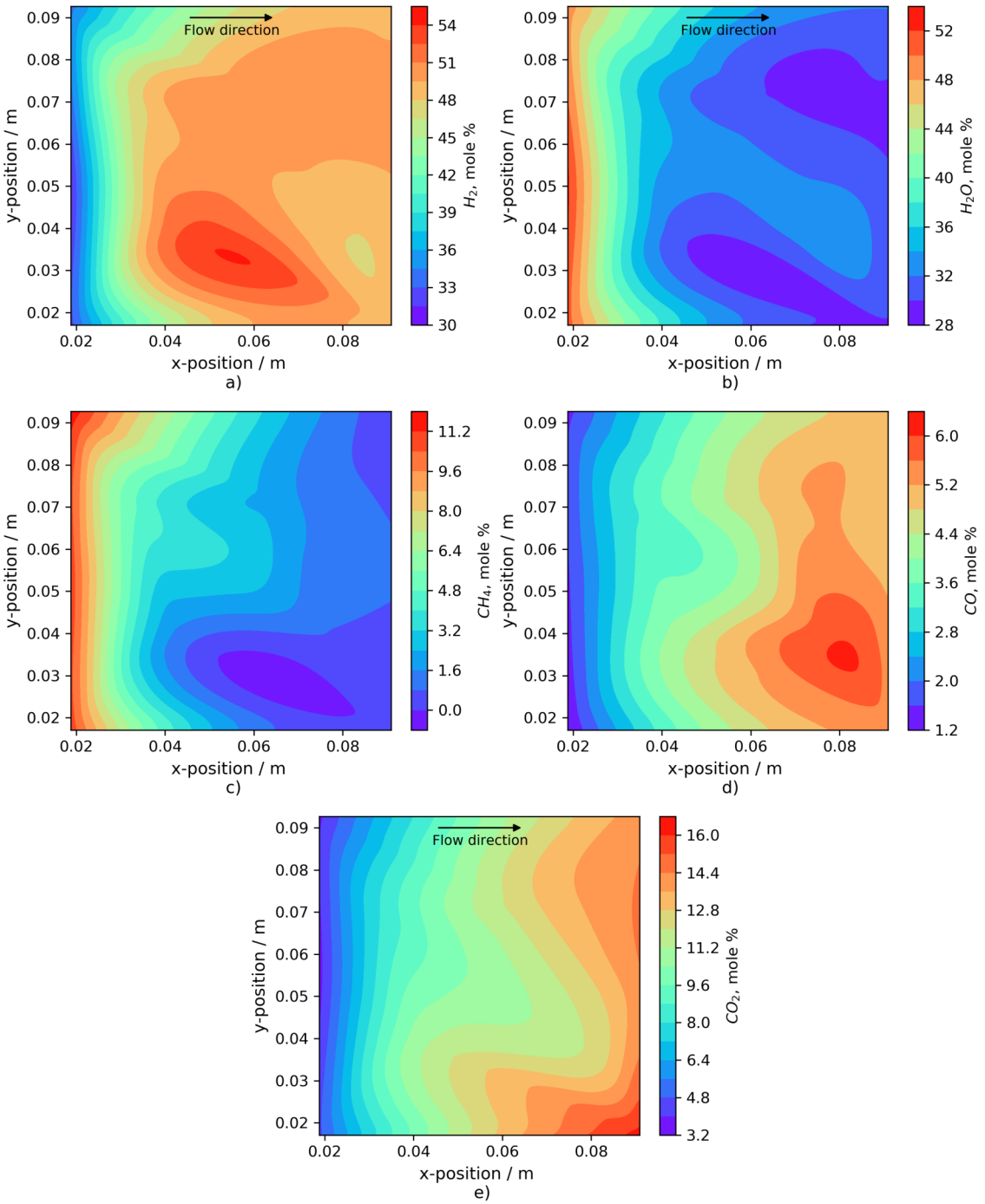

Figure 5.22. *Species distribution throughout the cell for CIR at 15 A and 650 °C: a) H_2, b) H_2O, c) CH_4, d) CO and e) CO_2.*

At 15 A, in spite of corresponding to the species distribution under load, the hydrogen content observed in Fig. 5.22a does not decrease in the flow direction as it could be expected. Accordingly, as already showed in the previous analyses, i.e., LIR and IIR at 15 A, the resulting H_2 distribution tended to decrease in the flow direction because of the evolution of the electrochemical reaction. By contrast, in this case, an apparent hydrogen increase in the flow direction despite the current is observed. This is rather owed to the huge and sudden H_2 production from the very first centimeters of the cell due to the strong SMR reaction. Hence, the reforming and shifting reactions coupled to the oxidation reaction result in basically the same species distribution as in OCV, but with its obvious quantitative differences.

Regarding CO_2 and CO, it is still observed a slight CO decrease respect its content under OCV condition, and at the same time a continuous CO_2 increase under load. This issue suggests the CO_2 production still by means of the WGS reaction, but with a stronger contribution than in OCV.

At 25 A, Fig. 5.23, methane is still converted into hydrogen and carbon monoxide mainly in the first 4 cm of the cell length, thus resulting in a similar hydrogen distribution as in the case of OCV. However, a clear decrease in the concentration of hydrogen is observed from the scale of the corresponding contour, as expected because of the increase in the FU. Additionally, all the other species also show a very similar distribution as in OCV and 15 A. Accordingly, the continuous CO_2 increase still suggests the occurrence of a more dominant WGS reaction.

Hence, from Fig.5.23e, it is observed that the fuel utilization is one of the major parameters which may affect the exhaust gas composition, and particularly the CO_2 production. Increasing the FU results in a high increase of the CO_2 content, as in effect is shown by the ChemCad results.

In Table 5.4 it is finally presented the comparison of the measured and calculated outlet compositions. Again, it is observed a good agreement mainly in OCV condition, while under load, the major differences resulted for H_2, CO_2, and consequently for H_2O. These differences have been already explained, allowing to state that also in this case the approach of chemical equilibrium may be valid.

As it is observed from the WGS efficiency, and according to the obtained species distribution, under CIR a positive quantity of CO reacts even in OCV. This fact suggests that the WGS reaction takes place even in open-circuit voltage condition, in contrast to what has been observed under LIR and IIR at OCV. Under these latter, a negative quantity of CO apparently reacted, which rather meant, that instead of being reacting, CO was being produced through the r-WGS reaction.

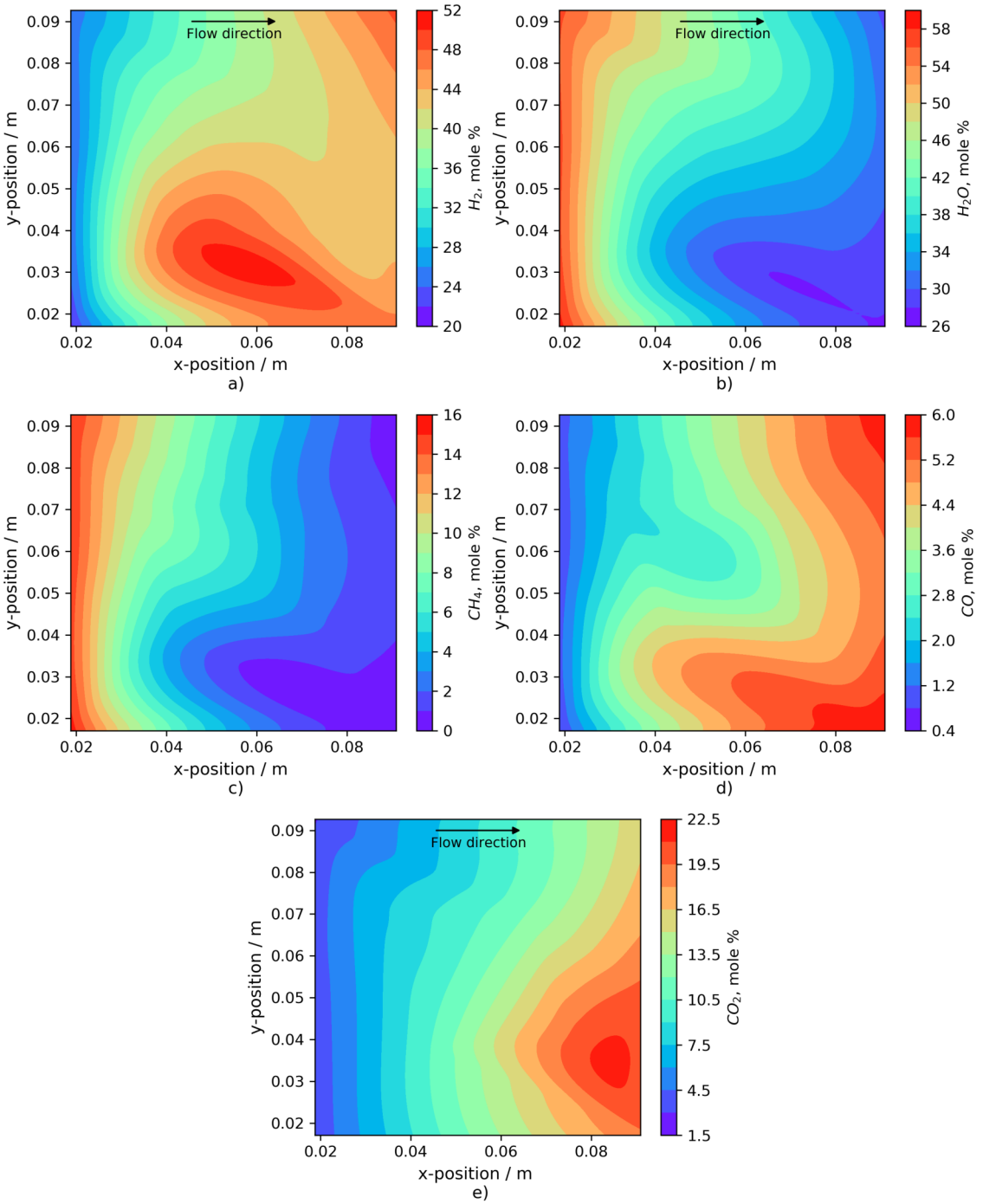

Figure 5.23. *Species distribution throughout the cell for CIR at 25 A and* 650 °C*: a)* H_2*, b)* H_2O*, c)* CH_4*, d) CO and e)* CO_2*.*

Regarding the experimental reforming efficiency, on the basis of ∼0.3% and ∼0.6% of residual CH_4, a methane conversion efficiency of ∼98.7%, ∼98.5% and ∼97.6% results at OCV, 15 A and 25 A, respectively. Accordingly, as earlier stated, H_2 can be produced stably through DIR of methane over SOFC anodes with a Ni catalyst, even at intermediate operating temperatures.

Finally, one important advantage of DIR fueling with similar compositions to the actual one, CIR, or with a methane-reach fuel, is the low CO_2 content in the exhaust gas.

Table 5.4. Comparison of the measured and calculated inlet and outlet compositions for CIR at OCV, 15 A and 25 A.

CIR			H_2 [%]	CO_2 [%]	CH_4 [%]	CO [%]	H_2O [%]	T_{avg} [°C]	η_{WGS}	η_{ref}
	Inlet	Theoretical	0.0	0.0	22.4	0.0	77.6			
	Inlet	Experimental	0.0	0.0	23.7	0.0	76.3			
OCV	Outlet	Experimental	53.3	10.7	0.3	5.8	29.9	645		98.7%
	Outlet	Calculated	52.0	8.2	1.3	6.4	32.1		56%	91.9%
	Inlet	Experimental	0.0	0.0	22.2	0.0	77.8			
15 A	Outlet	Experimental	48.6	17.6	0.3	5.1	28.3	650		98.5%
	Outlet	Calculated	42.4	10.1	0.4	5.1	42.0		66.5%	97.6%
	Inlet	Experimental	0.0	0.0	23.4	0.0	76.6			
25 A	Outlet	Experimental	45.4	19.8	0.6	5.5	28.7	656		97.6%
	Outlet	Calculated	35.3	11.2	0.1	4.2	49.2		73%	99.2%

Theoretical: proposed inlet composition

Measured: obtained from GC measurements

Calculated: obtained from CHEMCAD™

T_{avg}: average cell temperature in steady state

η_{WGS}: WGS efficiency (CO mole percentage reacting)

η_{ref}: reformate efficiency (CH_4 mole percentage reacting)

The analysis here presented is just a general picture of how the reforming reactions occur, based on the species distribution. However, the actual reaction pathways are still far from being well understood, and more research is needed to obtain a clearer picture and a more in-depth understanding of the different electrode reactions.

5.1.4. Thermal analysis

Real time surface temperature distribution monitoring of SOFC systems is important to identify temperature related degradation and understand cell performance. Usually, this type of monitoring is limited owed to the harsh operating environment of SOFCs. Therefore, the temperature variation of an operating SOFC is generally predicted by applying modeling tools [34, 202], while other few studies opt to monitor the cathode surface temperature [51, 208].

However, SOFCs operation is highly dependent upon the application requirements and system

configuration, but generally thermal response should be damped to the possible extent [132]. Therefore, in this study, the temperature distribution of the SOFCs is *in-situ* and *in-operando* monitored simultaneously throughout the anode, under both OCV and loading conditions, by means of 11 thermocouples strategically inserted in order to detect possible hot-spots.

5.1.4.1. LIR

Fig. 5.24 shows the temperature profiles of the 11 sampling points corresponding to the LIR composition under OCV, 15 A and 30 A, at 650 °C and OCV at 700 °C.

From the OCV profiles at both temperatures, it is observed how the steady state is reached quickly. Additionally, as expected, there is no an evident cooling effect because of the low reforming activity. It is noteworthy that even when the steady state is reached quickly under predetermined conditions, it does not necessarily imply that chemical equilibrium does so. However, the opposite does apply, i.e. reaching chemical equilibrium implies reaching the steady state firstly. Consequently, and just to clarify, in the present study the composition analyses were generally performed after at least 3 hours of setting the condition of interest and according to a monitoring of the voltage and temperature changes over time, seeking to approach as much as possible to the chemical equilibrium but always assuring the steady state.

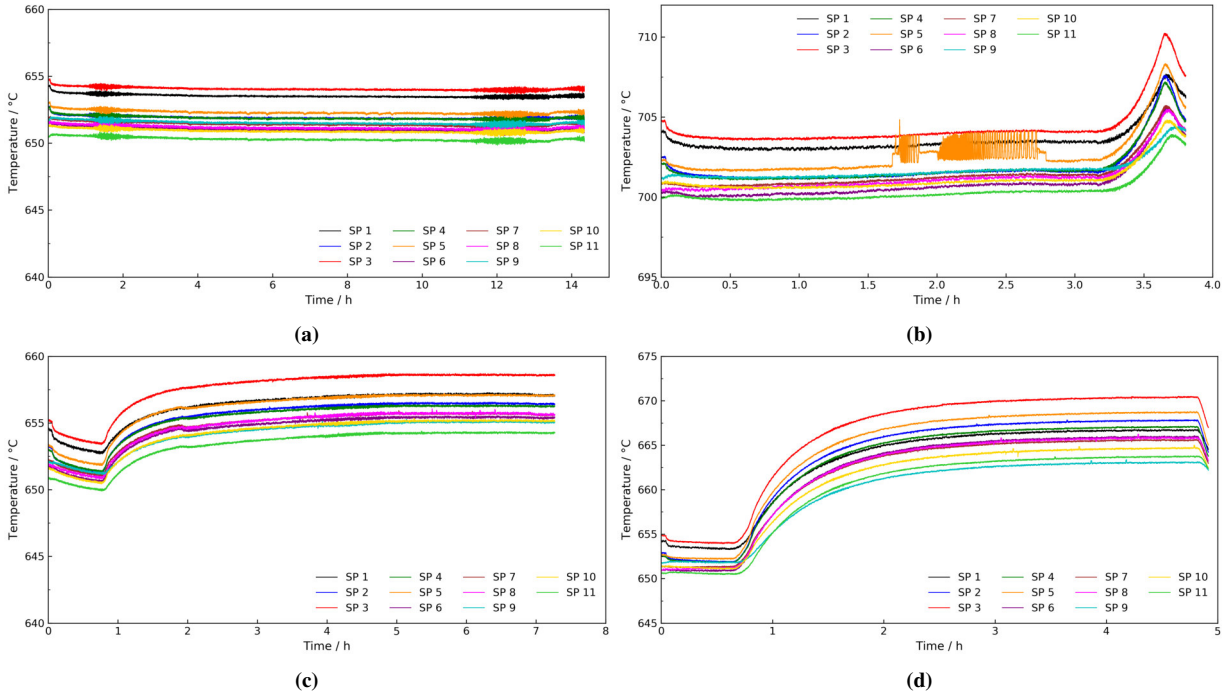

Figure 5.24. *LIR temperature profiles comparison at a) OCV-650 °C, b) OCV-700 °C, c) 15 A-650 °C and d) 30 A-650 °C.*

In Fig. 5.24b, corresponding to OCV condition at 700 °C, there is a noise observed in thermocouple 5, which comes from the EIS measurements. The frequency at which the spectrum was recorded caused some interference with the frequency at which the temperature of that particular sampling point was recorded. In addition, the temperature peaks observed in all the thermocouples right after 3 hours are owed to the I-V curve recording while the characterization.

From the temperature profiles under load, Fig. 5.24c and Fig. 5.24d, it is observed that the cell takes longer than in OCV to reach the steady state. Additionally, unlike 30 A, Fig. 5.24d, in the case of 15 A there is a cooling effect observed at the beginning of the test, Fig. 5.24c. However, it should be clarified that owed to the low methane content in the mixture such an effect was not caused by the endothermic SMR reaction, as it could be thought. It is just a temperature drop caused because, the night before to the corresponding test, the cell experienced a depletion of N_2 under the reference condition (from which each test used to begin), causing the cell to become warmer respect to its normal temperature. Thus, when the reference composition was switched to the LIR one the cell experienced the observed cooling effect. In fact, this false cooling effect is no longer observed in the plot at 30 A. It is also seen from these plots that after the composition under analysis is set and kept in OCV condition for around 1 hour, there is a sudden temperature increase owed to the applied current, as observed at 15 A and 30 A in Fig. 5.24c and Fig. 5.24d, respectively. Such a temperature increase is mainly owed to the Joule heating effect, the exothermic oxidation reaction and all the other cell irreversibilities, which in fact are dependent on the applied current.

On the other hand, Fig. 5.25 shows the steady state temperature contour plots in OCV, 15 A and 30 A under LIR composition. In agreement with the gas analyses, the temperature distributions do not show any cooling effect at the inlet region of the cell, which is owed, as already mentioned, to the insignificant reforming activity because of the gas composition. Rather, these three conditions show a temperature drop in the flow direction. Even under load, where the temperature was expected to increase due to the dominance of the exothermic electrochemical reaction, this tendency to decrease from the inlet to the outlet is also observed. Besides, it is also noticeable the hotter zone in the lower left corner of the anode for all the three conditions. This can be explained by the uneven inlet flow distribution due to the design of the flow distributors, which make likely that fuel reaches first that region of the cell and causing it to react first in that zone, thus explaining the hot spot in that region.

Regarding the unexpected behavior of the temperature to decrease from the inlet to the outlet under loading conditions, two possible explanations for this tendency are considered: 1) an insufficient insulation causing heat losses directly to the environment, and 2) a non-uniform heating of the system caused by a problem with the front resistance which was broken and then repaired seeming to heat more than the other ones. Either way, both possibilities suggest an uneven or non-uniform heating of the enclosure or the system in general.

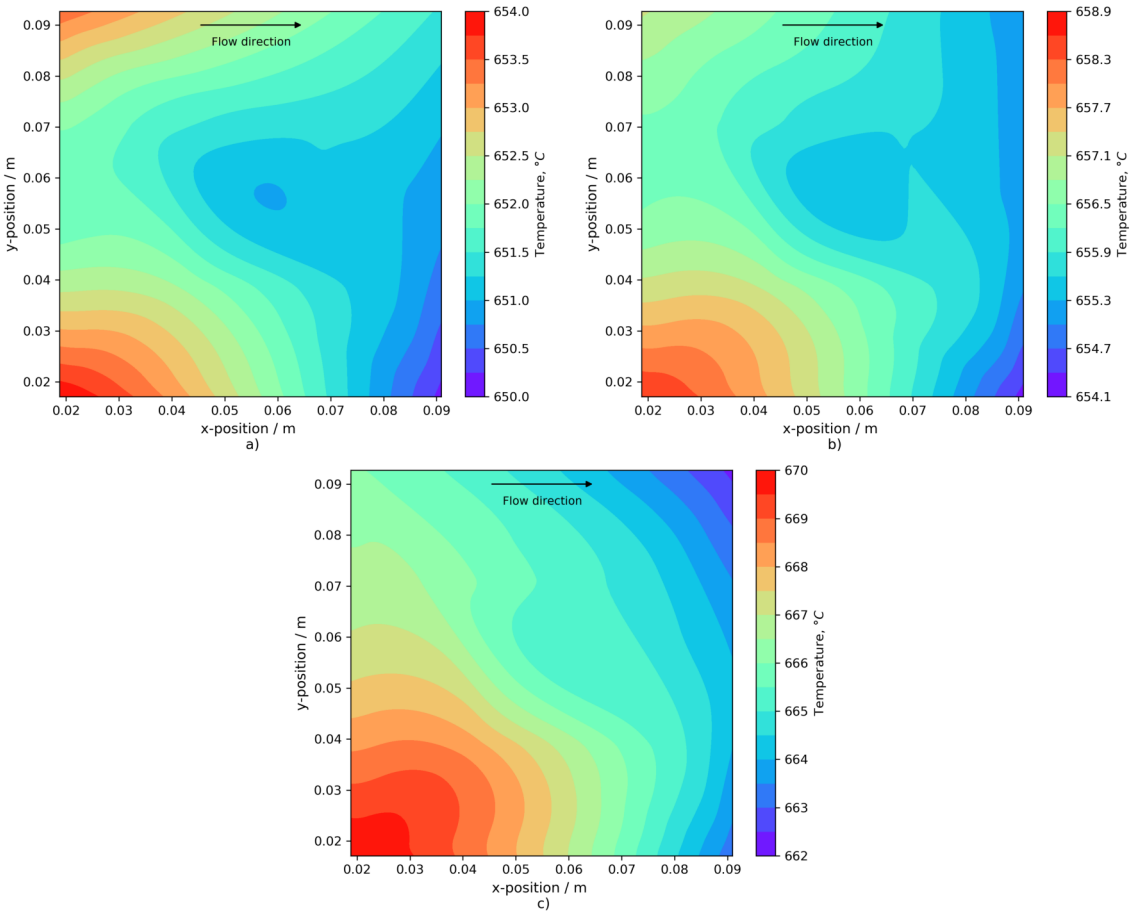

Figure 5.25. *LIR contour-plot comparison at* 650 °C *and a) OCV, b) 15 A and c) 30 A.*

On the other hand, it would be expected that due to the geometry and relatively large size of the tested cell, notable current variations develop along the cell and cause significant temperature variations. Nonetheless, from Fig. 5.25, it can be observed that the weak endothermic cooling effect reduces the maximum temperature difference throughout the anode at OCV from ∼4.2 °C (under the reference condition) to only ∼3.8 °C (under LIR). Under current, this maximum temperature difference increases to ∼4.3 °C at 15 A and ∼7.6 °C at 30 A due to the strong exothermic electrochemical reaction. Actually, the average temperature of the anode increases from 651.7 °C in OCV, to 656.1 °C at 15 A and 665.7 °C at 30 A. As observed, the average temperature increment from OCV to 15 A is about 4.4 °C while from OCV to 30 A is about 14 °C. These figures strongly agree with the fact that the heat released by the balance between the different reactions and by the overpotentials of the cell is directly proportional to the square of the current, which may explain a more pronounced temperature increase at 30 A than at 15 A.

5.1.4.2. IIR

At both OCV and loading conditions, Fig. 5.26 shows the temperature evolution profiles under IIR composition. Fig. 5.26a and Fig. 5.26b correspond to the OCV condition at 650 °C and 700 °C, respectively, while Fig. 5.26c and Fig. 5.26d correspond to 15 A and 30 A at 650 °C.

In Fig. 5.26b, corresponding to OCV condition at 700 °C, it is again observed an external noise in thermocouple 5, whose cause, along with that of the temperature peaks observed after the third hour, have been previously explained. Besides, in this same figure, it is observed a very slight but still noticeable slope that continues until the end of the recording. This slight slope is just owed to a change in the furnace temperature, since the previous analysis was carried out at 650 °C and the furnace temperature was then adjusted to reach the final cell temperature of 700 °C. Hence, for this particular case, it seems that the waiting time before to start the characterization was not enough as to let the cell to reach totally the steady state.

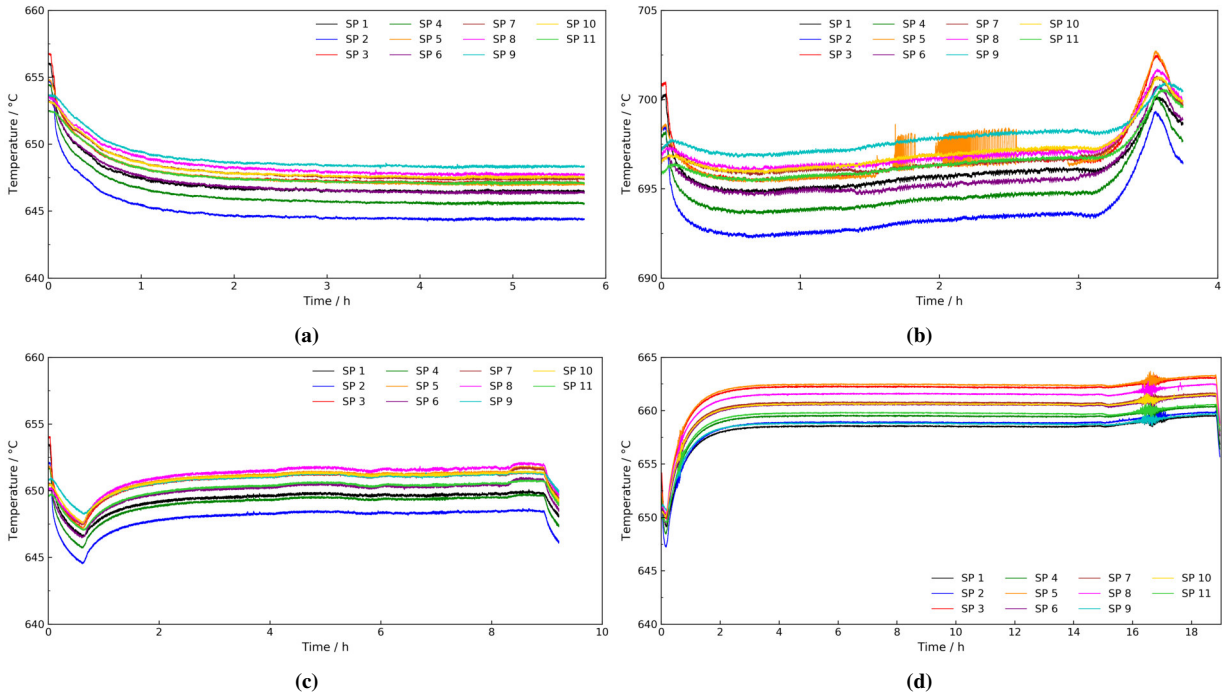

Figure 5.26. *IIR temperature profiles comparison at a) OCV-650 °C, b) OCV-700 °C, c) 15 A-650 °C and d) 30 A-650 °C.*

Furthermore, unlike LIR, from the temperature evolution profiles of IIR composition it is perceived a temperature drop at the beginning of the recording, i.e., when switching from the reference composition to the IIR one. The resulting temperature drop is about 5.2 °C, that compared to that under LIR, which was only about 0.5 °C, is relatively considerable but still not so big when considering the size of the cell. Additionally, regarding the profiles at 650 °C in OCV, 15 A and 30 A, it is again confirmed that the lower the fuel utilization the faster the steady state is reached, as illustrated

by the curve plateau from the three conditions. Accordingly, at OCV, the plateau has been reached after about two hours, at 15 A between 2.5 and 3 hours, and at 30 A between 3.5 and 4 hours.

At steady state, the resulting temperature distribution under the three loading conditions (OCV, 15 A and 30 A) is quite homogeneous, contour plots from Fig. 5.27. The contour plots show a maximum temperature difference throughout the anode of ∼3.4 °C in OCV, ∼3.2 °C at 15 A and ∼3.9 °C at 30 A. These figures suggest that, when the steady state is achieved, the contributions of the exothermic and endothermic reactions are quite similar, leading to a general heat balance. Hence, these findings suggest that the problem of large temperature gradients, caused by internal reforming, is almost avoided under direct internal reforming.

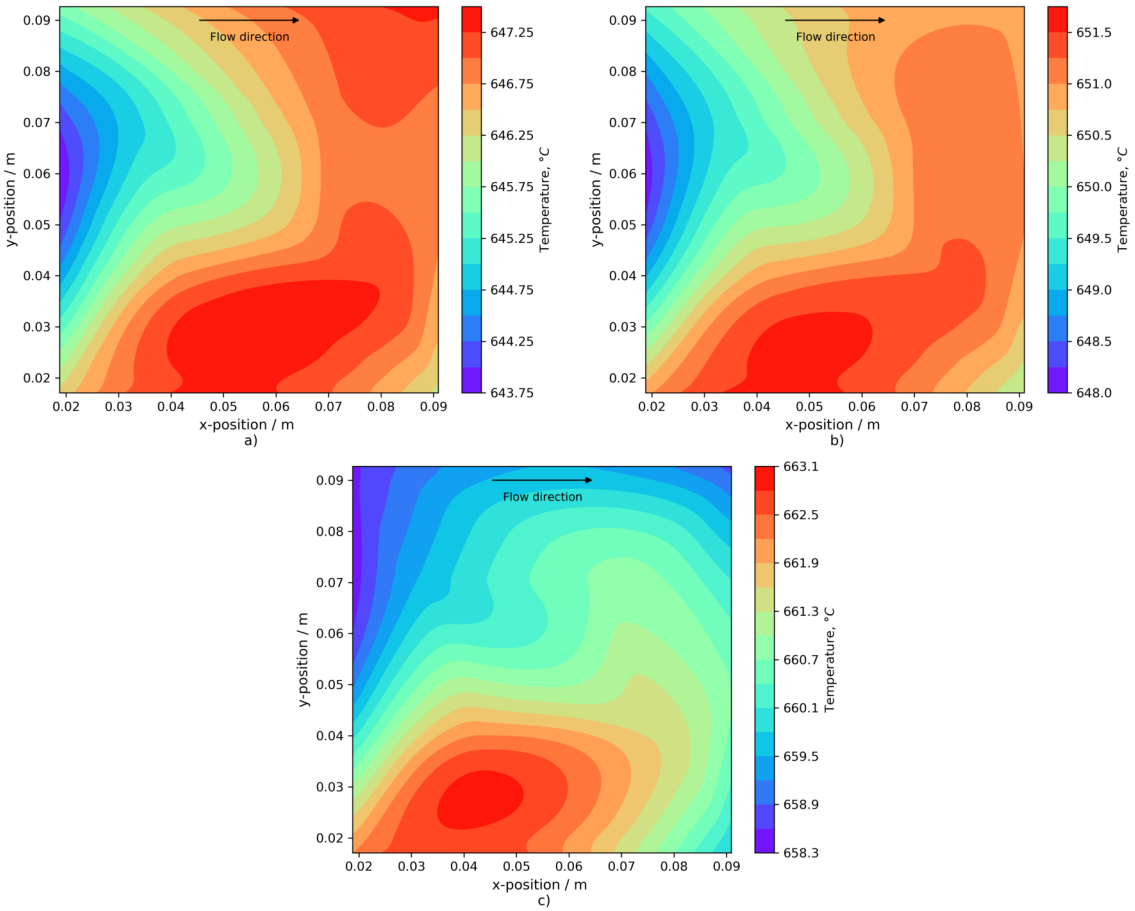

Figure 5.27. *IIR contour-plot comparison at* 650 °C *and a) OCV, b) 15 A and c) 30 A.*

Furthermore, the temperature contours under IIR composition, which has a higher methane content in comparison to LIR composition, show an evident cooling effect at the inlet region of the cell followed by a subsequent temperature increase in the flow direction. Particularly, at OCV condition and 15 A, it is observed a well-defined zone at the entrance of the cell that corresponds with the coldest region of the anode. In accordance with the gas analysis, this behavior confirms

the dominance of the SMR in the inlet region of the cell. Meanwhile, the subsequent and gradual temperature increase in the flow direction, suggests in OCV a methane depletion owed to the quick methane consumption by the reforming reaction and at 15 A, Fig. 5.27b, the dominance of the exothermic oxidation reaction over the reforming and shifting reactions.

Nonetheless, at 30 A and despite the increase in the fuel utilization, the temperature distribution changed almost totally its pattern. Still, the coldest region of the anode remains at the entrance of the cell but it extends through the upper half, i.e., mainly in the upper left corner, while the hotter region is only observed at the front part of the anode, almost in the same region as in the case of LIR at 30 A. Since there is no direct relation with the H_2 species distribution at this condition that suggests a higher electrochemical activity or FU in that region, this temperature behavior is explained because of an insufficient insulation and non-uniform heating of the system, as previously pointed out in the case of LIR composition. In fact, it does make sense that heat losses are more noticeable at higher current densities, causing higher temperatures, since a higher temperature difference between the system and the environment eases heat transfer, or in this case, the heat losses to the environment.

As also observed, the average temperature at steady state resulted to be ∼646.2 °C in OCV (∼5.2 °C below the reference condition), ∼650.3 °C at 15 A (∼4.2 °C above OCV) and ∼660.3 °C at 30 A (∼14.1 °C above OCV). As earlier mentioned, the temperature rise under current is a result of the ohmic heating or cell irreversibilities and the surplus of heat (that could not be removed with the excess of air from the cathode) coming from the balance between the exothermic reactions of electro-oxidation and WGS, and the endothermic SMR reaction.

5.1.4.3. CIR

As a last case, Fig. 5.28 shows the respective temperature profiles evolution corresponding to the CIR composition in OCV at 650 °C and 700 °C, Fig. 5.28a and Fig. 5.28b, and at 15 A and 25 A, Fig. 5.28c and Fig. 5.28d.

From these temperature profiles it is clearly observed the cooling effect that the cell experiences under this composition owed to the methane reforming reaction. Accordingly, the average temperature drop over the anode, measured respect to the reference condition, was about 7.3 °C, which implies a temperature drop ∼28.7% higher than that obtained under IIR. This clear difference is because of the higher methane content under CIR, which in turns means a stronger cooling effect.

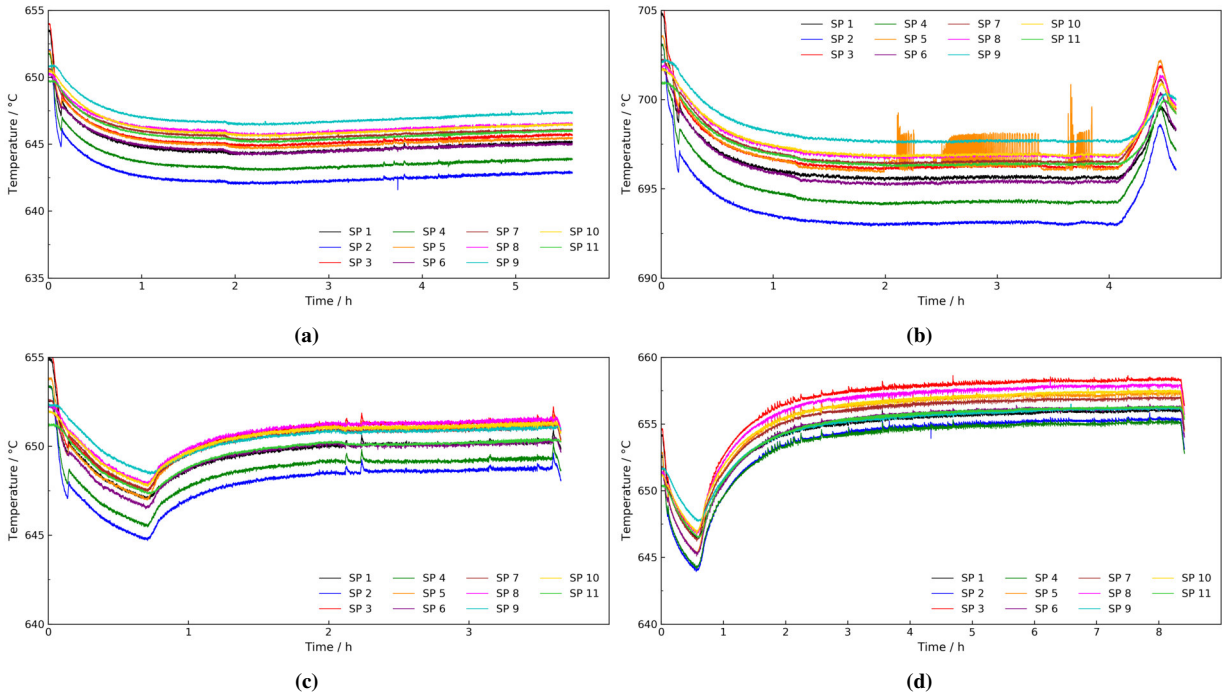

Figure 5.28. *CIR temperature profiles comparison at a) OCV-*650 °C*, b) OCV-*700 °C*, c) 15 A-*650 °C *and d) 25 A-*650 °C*.*

Regarding the time that took the cell to reach the steady state under each condition, i.e. OCV, 15 and 25 A, from the curve plateau it is observed that in OCV it took around 2 hours, at 15 A a bit more than two hours and at 25 A around 4 hours. There is a clear difference between the stabilization time at 15 A and 25 A, which may be owed to the stabilization problem at higher current densities (already described in section 5.1.3) under this kind of compositions consisting of only CH_4 and H_2O.

On the other hand, from the contour plots of the temperature distribution at steady state, Fig. 5.29, it is observed that the stronger endothermic cooling effect increased the maximum temperature difference at OCV from ∼3.4 °C under IIR, to ∼4.8 °C under CIR. This maximum temperature difference became smaller with increasing the current: ∼3.5 °C at 15 A and ∼3.2 °C at 25 A. Additionally, the average steady state temperature increased from ∼644.9 °C in OCV to ∼650.5 °C at 15 A and ∼656.6 °C at 25 A. This implies that the heat production rate by the overpotentials or ohmic heating, the exothermic WGS and oxidation reaction is higher than the heat absorbed by the SMR reaction and the heat eliminated by the air stream from the cathode.

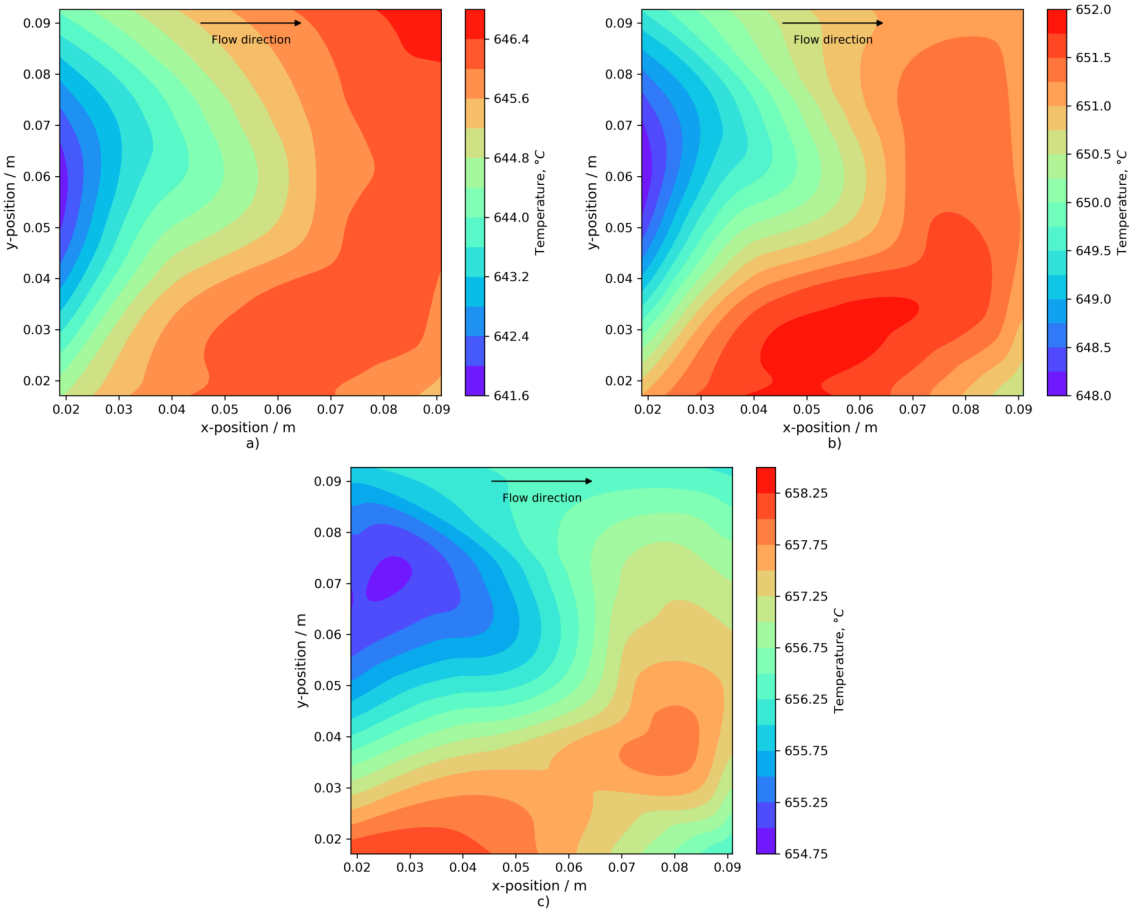

Figure 5.29. *CIR contour-plot comparison at* 650 °C *and a) OCV, b) 15 A and c) 25 A.*

The qualitative temperature distribution in this case is closely the same as the observed under IIR, i.e. a noticeable cooling effect at the inlet of the cell followed by a gradual temperature increase in the flow direction. It can be noticed again that at the highest tested current, in this case at 25 A, the temperature does not increase uniformly along the flow direction. In fact, a higher temperature or hotter zone is localized mainly at the front part of the cell, as observed in Fig. 5.29c. As already mentioned, it may be owed to the non-uniform furnace insulation and heat losses to the environment, among others. However, under this composition, in all the three cases (OCV, 15 A and 25 A) the coldest region is clearly defined at the inlet of the cell.

5.1.4.4. Fuel, current and temperature comparison

In the following temperature contour plots it is presented just a comparison of the three compositions under each loading condition. Fig. 5.30 shows the comparison at 650 °C and OCV, Fig. 5.31 shows the same comparison but at 700 °C, Fig. 5.32 shows the comparison at 650 °C and 15 A, and finally, Fig. 5.33 presents the comparison at 650 °C and 30 A, in all the cases for a) LIR, b)

IIR and c) CIR.

From the comparison of the temperature distribution at 650 °C under OCV, Fig. 5.30, it is clearly observed the effect of the different analyzed compositions on the final temperature distribution, which is actually related to the chemical phenomena occurring in there.

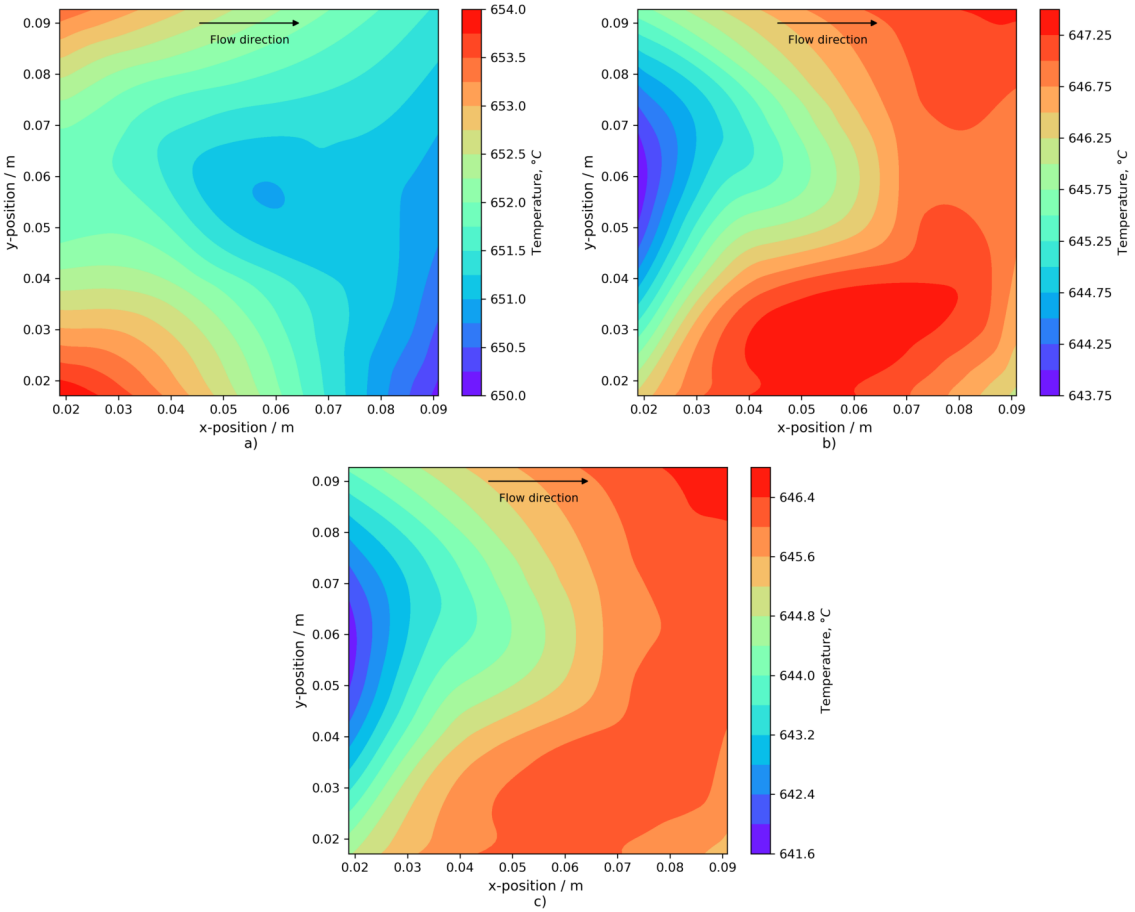

Figure 5.30. *Contour-plot comparison at* 650 °C *and OCV for a) LIR, b) IIR and c) CIR.*

In Fig. 5.31, it is also shown the temperature distribution under OCV but at 700 °C. Comparing with the temperature distribution at 650 °C, Fig. 5.30, it is observed basically the same temperature distribution and the same temperature gradients throughout the anode, suggesting then the same thermo-chemical phenomena at a higher temperature. Additionally, as mentioned at the beginning of the current section, real time surface temperature distribution monitoring of SOFC systems may also help to identify temperature related degradation. Remembering the electrochemical analysis at 700 °C, it was stated that when the electrochemical characterization and thermal analysis under LIR and CIR were carried out at this temperature, the cell showed some signs of degradation, which up to that point, were mainly reflected as an increase in the internal resistance of the cell. Nonetheless, as observed from these contours of temperature, the cell degradation experienced is not temperature

related since all the thermal changes for all the three compositions at this temperature are quite comparable to those observed at 650 °C. It results a bit strange that the cell temperature under LIR and CIR has not being affected because of the cell degradation, since it was related to an increase of the cell resistance, which in turn is usually reflected in a temperature increase. However, such an investigation is outside the scope of this study.

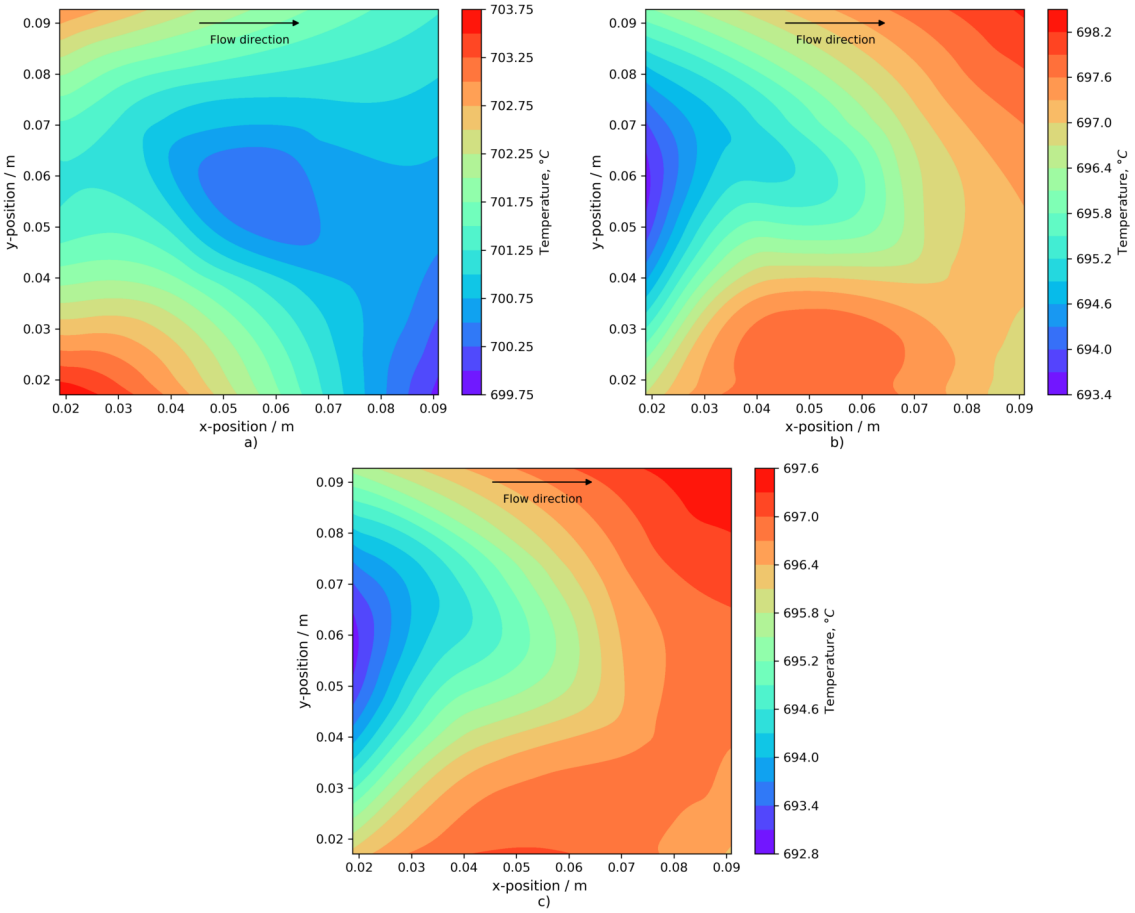

Figure 5.31. *Contour-plot comparison at* 700 °C *and OCV for a) LIR, b) IIR and c) CIR.*

On the other hand, in Fig. 5.32 it is just summarized the earlier discussed results regarding the temperature distribution at 15 A under the three analyzed composition. Accordingly, under IIR and CIR, the temperature of the anode, as expected, increases from the inlet to the outlet because of the co-flow feeding configuration of the test facility. Nevertheless, under LIR composition, with a very low methane content, this tendency is not observed. This issue has been potentially attributed to the non-uniform heating of the enclosure owed to an insufficient insulation of the system and possible heat losses to the environment.

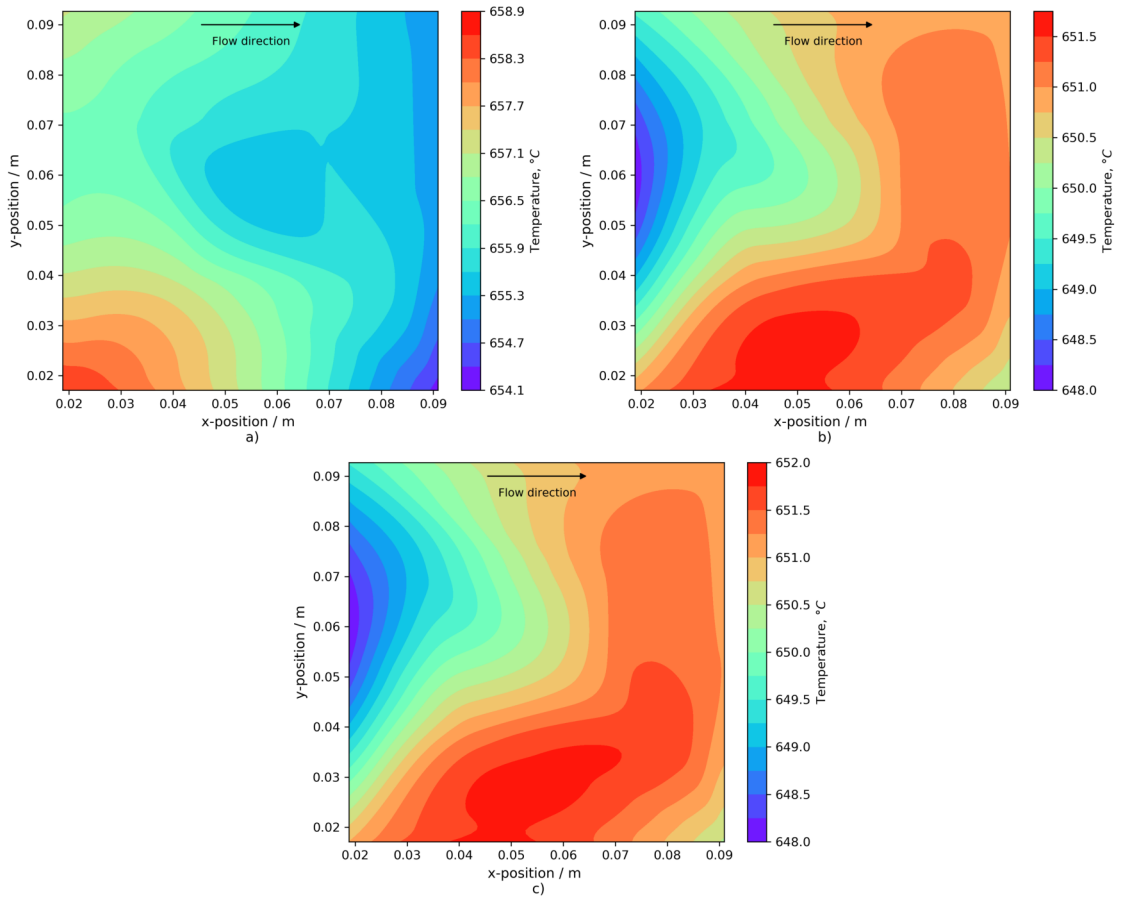

Figure 5.32. *Contour-plot comparison at* 650 °C *and 15 A for a) LIR, b) IIR and c) CIR.*

Fig. 5.33, shows the comparison of the temperature distribution at 30 A and 650 °C. Although under CIR composition this analysis was not formally carried out because of cell stabilization issues at this loading condition, the temperature contour plot here presented was obtained while the attempt to carry out the composition analysis. However, the temperature contour plot at 30 A is just presented for illustrative purposes because owed to the cell instability and high voltage fluctuations under such loading condition, it does not correspond to a temperature distribution at steady state as the cell could not even reach the steady state condition.

Nevertheless, the main characteristic of this comparison corresponds to the location of the hotter zone, which in all the three cases it is found in closely the same region. There is no doubt that this unexpected distribution, which has no relation with the fuel distribution, only suggests an uneven heating of the cell because of possible heat losses to the environment. However, when considering the maximum temperature difference throughout the anode, such "hot spots" do not even make sense to the name because in general the temperature distribution is very uniform.

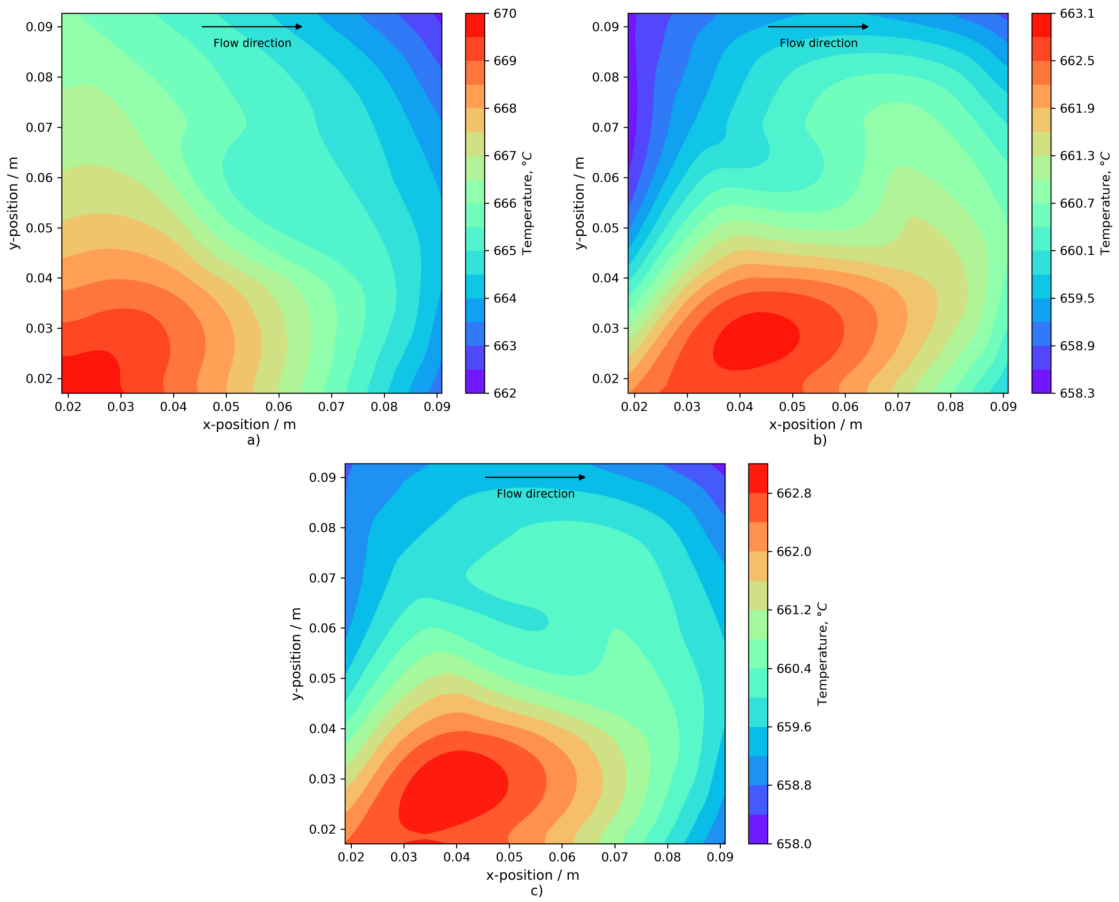

Figure 5.33. *Contour-plot comparison at* 650 °C *and 30 A for a) LIR, b) IIR and c) CIR.*

Finally, in Table 5.5 it is presented a summary of the thermal analysis, in which a clear comparison of the temperature differences and steady state temperatures can be found.

It is noteworthy that the values of the cell temperature differences obtained in this study (from ∼4 to ∼10 °C) are much lower than those usually reported from numerical simulations of direct internal reforming under similar conditions (from ∼40 to ∼250 °C). Such numerical temperature discrepancies are usually attributed to the different thermal boundary conditions (adiabatic vs. radiation heat exchange) used in the models [51]. Only a few works have been found in the literature, a couple of experimental analyses [51, 208] and some numerical works [16, 258, 267], that report temperature differences similar to those obtained experimentally in the present work.

It is observed from the comparison of the temperature at 15 A that, at steady state, the average temperature and the maximum temperature difference under IIR and CIR are closely the same, despite the differences in their composition. However, not so for the composition with the lowest methane and highest hydrogen content, LIR composition, which experienced the highest temperature differences under load as well as the highest average temperatures under the three analyzed conditions, i.e., OCV, 15 A and 30 A. From the comparison at 30 A for IIR and 25 A under CIR,

is highly probable that analogous results had been obtained at 30 A under both compositions if the analysis at 30 A under CIR had been possible.

Table 5.5. Summary of the thermal analysis for the three analyzed compositions at the three loading conditions.

	LIR @ 650 °C				**LIR** @ 700 °C	
	Ref. condition	**OCV**	**15 A**	**30 A**	**Ref. condition**	**OCV**
T_{avg} [°C]	652.2	651.7	656.1	665.7	701.7	701.3
ΔT_{cell} [°C]	4.2	3.8	4.3	7.6	4.8	3.8
ΔT_{ref} [°C]		-0.5	3.9	13.5		-0.4
T_{max} [°C]		654 / T_3	658.61 / T_3	670.0 / T_3		703.7 / T_3
T_{min} [°C]		650.2 / T_{11}	654.3 / T_{11}	662.4 / T_9		699.9 / T_{11}
	IIR @ 650 °C				**IIR** @ 700 °C	
	Ref. condition	**OCV**	**15 A**	**30 A**	**Ref. condition**	**OCV**
T_{avg} [°C]	651.3	646.2	650.3	660.3	701.7	696.4
ΔT_{cell} [°C]	4.4	3.4	3.2	3.9	4.9	4.6
ΔT_{ref} [°C]		-5.2	-1.0	9.0		-5.4
T_{max} [°C]		647.3 / T_9	651.3 / T_8	662.4 / T_5		698.3 / T_9
T_{min} [°C]		643.9 / T_2	648.2 / T_2	658.8 / T_2		693.6 / T_2
	CIR @ 650 °C				**CIR** @ 700 °C	
	Ref. condition	**OCV**	**15 A**	**25 A**	**Ref. condition**	**OCV**
T_{avg} [°C]	652.2	644.9	650.5	656.6	702.8	695.9
ΔT_{cell} [°C]	4.2	4.8	3.5	3.2	4.6	4.7
ΔT_{ref} [°C]		-7.3	-1.7	4.3		-6.9
T_{max} [°C]		646.6 / T_9	651.7 / T_8	658.2 / T_3		697.7 / T_9
T_{min} [°C]		641.8 / T_2	648.1 / T_2	655.0 / T_4		693.0 / T_2

Ref. condition: Reference condition specified in Table 4.3

T_{avg}: average temperature in steady state, calculated from the 11 sampling points

ΔT_{cell}: maximum temperature difference throughout the anode, calculated as $\Delta T_{cell} = T_{max} - T_{min}$

ΔT_{ref}: temperature difference respect to the average reference condition, calculated as $\Delta T_{ref} = T_{avg} - T_{avg,ref}$

T_{max}: maximum measured temperature over the anode at the given condition / corresponding sampling point

T_{min}: minimum measured temperature over the anode at the given condition / corresponding sampling point

Therefore, DIR should be rather considered as an advantage due to the cooling effect caused by the endothermic reaction. It has been observed experimentally that far from harming, DIR helps to regulate the cell temperature avoiding the widely reported hot spots and their consequent thermal stresses. In other words, it has been observed that the direct internal reforming phenomenon far from creating hot spots, it helps to regulate or compensate the temperature rise caused by the cell irreversibilities and the electrochemical and WGS reaction. Accordingly, at higher currents, under

LIR composition it has been observed a greater temperature difference owed to the low reforming activity and to the dominance of the oxidation reaction. In contrast, under the other two cases, being methane-rich fuels, the corresponding temperature difference was much lower.

5.2. Numerical and experimental comparison of the three internal reforming grades

In this section, the results from a simple zero-dimensional model for the current-voltage characteristics of anode-supported SOFCs and from a simple 2D model based on finite differences for the local prediction of the current density distribution are presented. Like some modeling approaches cited above, the procedures include modeling of the activation losses by the Butler-Volmer equation, the ohmic losses by the Ohm's law, and the calculation of the gas diffusion losses from Fick's model. However, most of the modeling parameters have been taken from an experimental work based on ASCs [42], while some others have been calculated or directly used from the obtained experimental data, in order to get a better fit of the models with the experimental results.

The electrochemical 0D model has been implemented in the Engineering Equation Solver (EES), according to the algorithm shown in Fig. 5.34, while the model based on finite differences was implemented in Matlab as summarized by the algorithm presented in Fig. 5.42 and Fig. 5.43. Although each model has its own particularities, both of them are essentially based in the same assumptions, thereby taking into consideration the following issues:

1. Steady state.
2. Constant properties.
3. Electro-oxidation, SMR and WGS reaction are the only reactions that occur.
4. H_2 electro-oxidation responsible for the electrical flow.
5. CH_4 only participates in the steam reforming reaction and CO exclusively in the WGS reaction.
6. SMR and WGS occur in chemical equilibrium.
7. Ohmic, activation and concentration overpotentials are responsible for the cell voltage losses.

For a more detailed description of the implemented models, please refer to Appendix A.

5.2.1. Comparison with the electrochemical 0D model

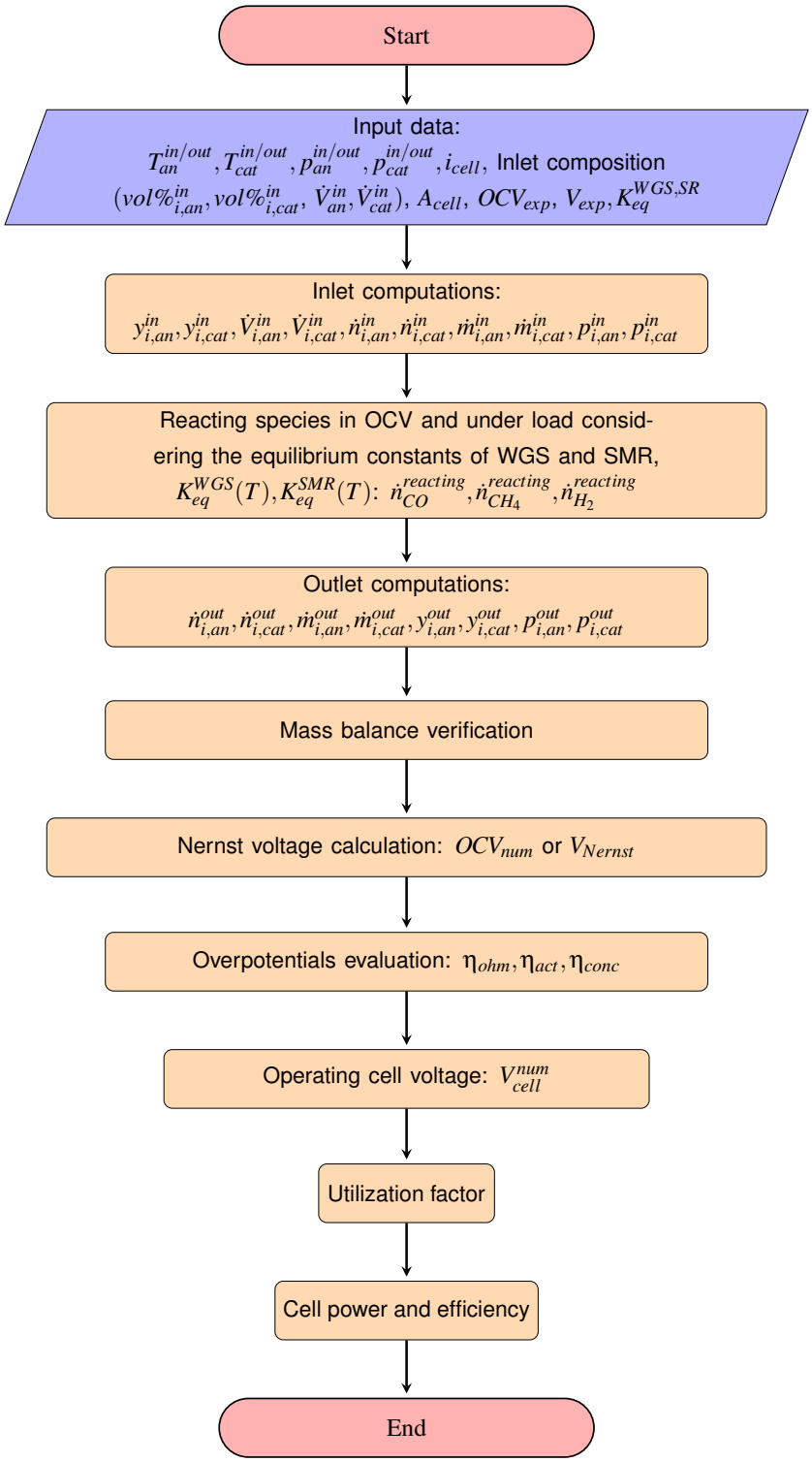

Figure 5.34. *Zero dimensional algorithm.*

5.2.1.1. Polarization curves

Fig. 5.35 shows the comparison of the resulting experimental and numerical polarization curves for the three tested compositions at 650 °C, which in general show a good agreement along the entire corresponding experimental I-V curve. Accordingly, the numerical OCV or Nernst voltage shows a slight numerical overestimation of 7 mV for LIR, Fig. 5.35a, and 3.5 mV for CIR, Fig. 5.35c, whilst for IIR, Fig. 5.35b, there is an underestimation of only 2 mV. The average voltage difference between the numerical and experimental I-V curve corresponds to ∼5.8 mV (∼0.65%) under LIR, ∼11.1 mV (∼1.23%) under IIR and ∼1.3 mV (∼0.14%) under CIR.

As observed, the major deviation between the numerical and experimental polarization curves was obtained for IIR composition. This deviation seems to increase with the current density, Fig. 5.35b, which can be attributed to some parameters of the diffusion model for the computation of the concentration overpotentials. It is noteworthy that, in effect, this kind of overpotentials are more important at higher current densities. Nonetheless, it is not either discarded the activation energy used in the model as another significant factor.

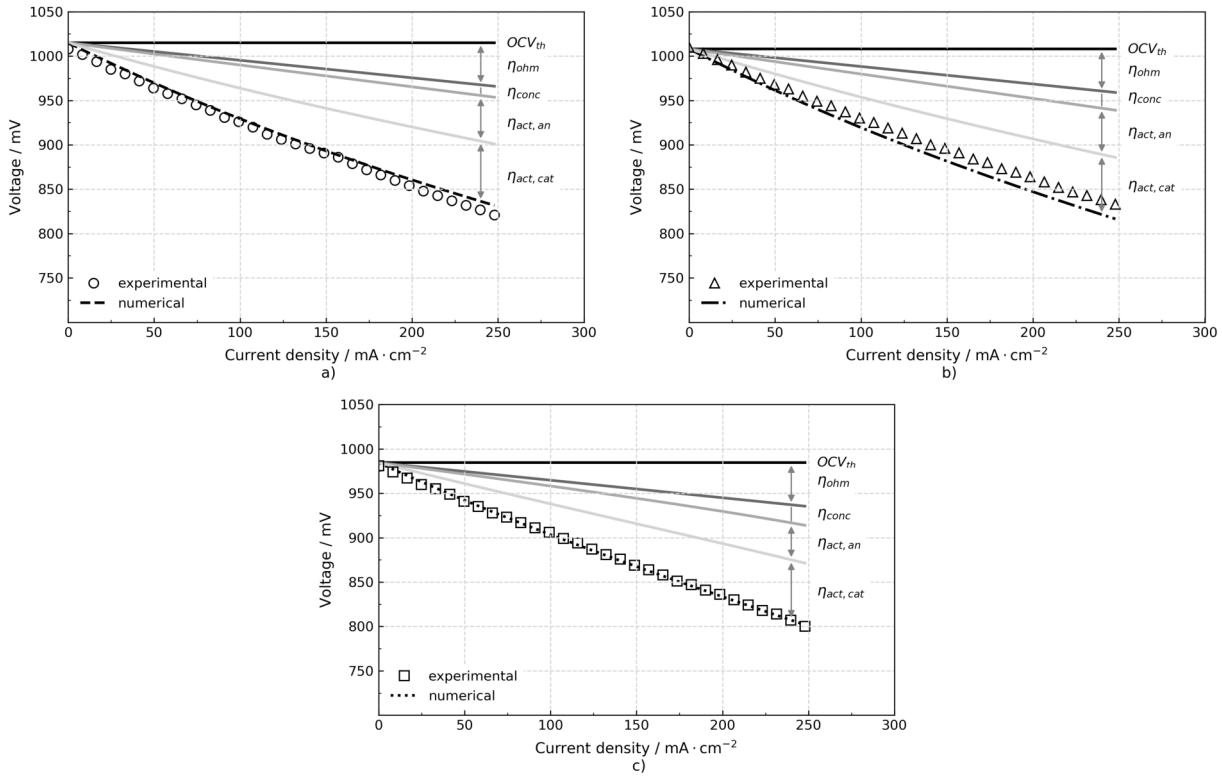

Figure 5.35. *Numerical and experimental comparison of the polarization curves at* 650 °C *for a) LIR, b) IIR, and c) CIR.*

Additionally, in the same plots are also illustrated the individual numerical contribution of the different overpotentials. In accordance with Aguiar et al. [202], for the three analyzed cases, and

although the cell under study is an anode-supported one, it is found that cathode activation overpotentials represent the major source of voltage losses, followed by anode activation and ohmic losses. Regarding the concentration overpotentials, these are relatively small in comparison with the other contributions. However, anode concentration overpotentials are considerably much higher than those at the cathode, around 400 times greater. Hence, the concentration overpotentials observed in the plots are basically an anode contribution.

In Fig. 5.36, the numerical and experimental comparison of the polarization (activation + concentration), ohmic, and total losses at 650 °C are presented as a function of the current density. The way in which they were experimentally obtained will be later described in section 5.3.

In accordance with the I-V curves comparison, the major differences in this overpotentials comparison are also observed for the IIR case, Fig. 5.36b, while in the case of LIR and CIR compositions, Fig. 5.36a and Fig. 5.36c, there is a quite good agreement between the numerical and experimental overpotentials. In the case of IIR composition, there is an average numerical over-prediction of ∼9.3 mV observed in the polarization losses, and consequently, in the total overpotentials. Meanwhile, for both LIR and CIR compositions, it just resulted in an average over-prediction of ∼2.1 mV and ∼4.8 mV, respectively.

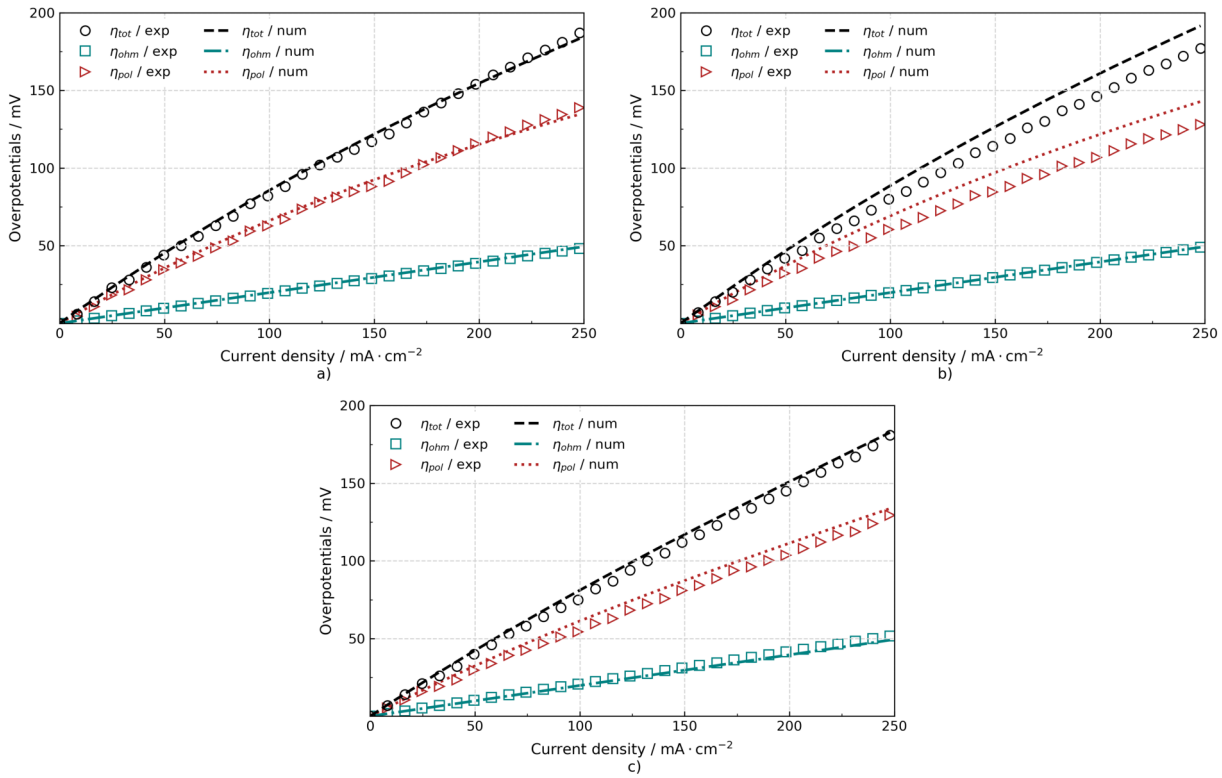

Figure 5.36. *Numerical and experimental comparison of the different overpotentials at* 650 °C *for a) LIR, b) IIR, and c) CIR.*

As earlier mentioned, activation losses are the main cause of voltage drop for anode supported SOFCs operated in the low- and intermediate-temperature range. Hence, such overpotentials are the main contribution to the polarization resistance here observed. Therefore, polarization losses are predominant due to activation and, to a lesser extent, to concentration losses, although occasionally, they can also have significant contributions owed to crossover.

On the other hand, Fig. 5.37 shows the experimental and numerical comparison of the I-V curves, with their corresponding individual contribution of the different overpotentials at 700 °C for the three tested compositions. Whereas Fig. 5.38 illustrates the comparison of the different overpotentials experimentally and numerically at the same operating temperature.

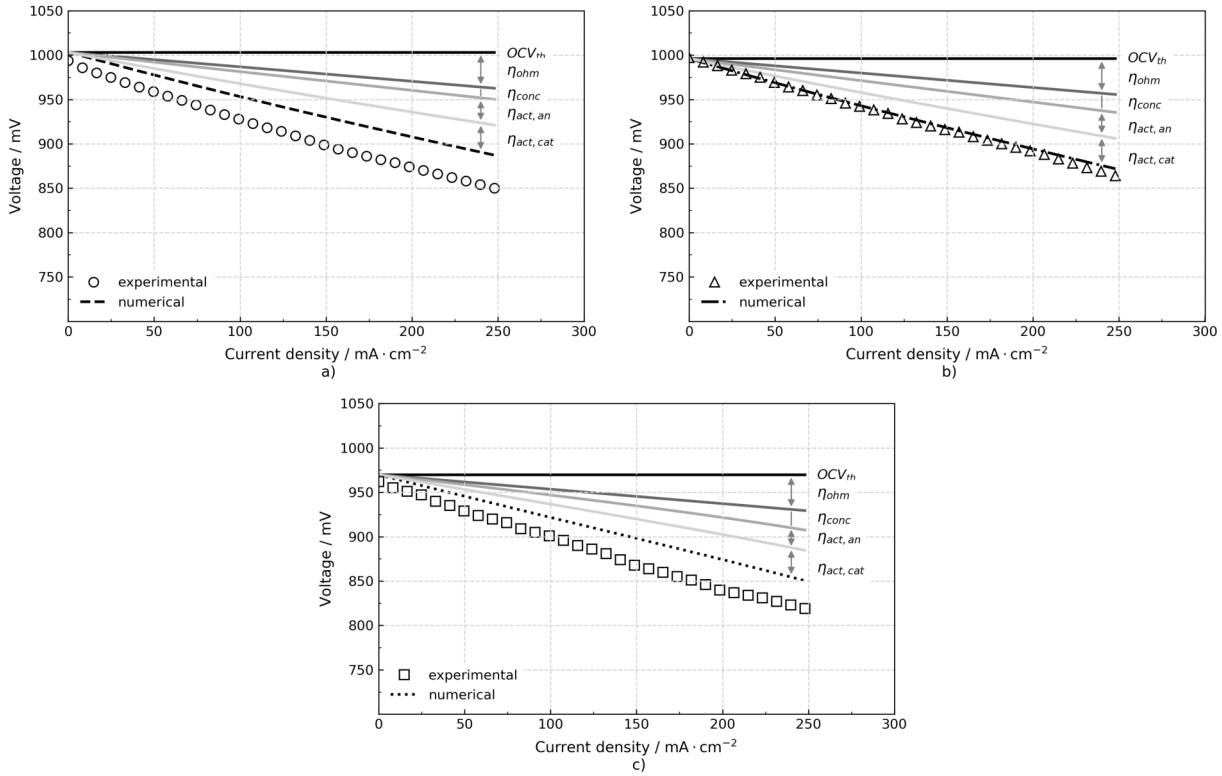

Figure 5.37. *Numerical and experimental comparison of the polarization curves at* 700 °C *for a) LIR, b) IIR, and c) CIR.*

First of all, from the experimental and numerical comparison of the I-V curves, it is confirmed the experienced cell degradation when the analysis under LIR and CIR compositions was carried out. This affair has been already pointed out in the analysis of the experimental results. Actually, only for both compositions, Fig. 5.37a and Fig. 5.37c, it is observed a substantial or significant deviation between the numerical and the experimental results. Accordingly, the average voltage difference between the experimental and numerical I-V curve is ∼26.8 mV and ∼24 mV for LIR and CIR, respectively, while for IIR composition it just resulted in a minor average difference of

~2.4 mV. As can be seen, the average differences under LIR and CIR are almost in the same order of magnitude, which as just mentioned, is attributed to the cell degradation. Meanwhile, the good agreement for IIR composition shows the good prediction and validity of this simple zero-dimensional model.

Then, from the individual contribution of the numerical voltage losses at 700 °C, shown in Fig. 5.37, it is observed a decrease with the operating temperature in most of the different overpotentials, as expected. However, it is mainly reflected in the cathode and anode activation overpotentials, with an average improvement of around 56% and 48.5%, respectively. Meanwhile, the ohmic ovepotentials show an enhancement of around 17.5%. In fact, at 700 °C the major contribution to the voltage losses are now the ohmic overpotentials, followed by the cathode and the anode activation losses. Additionally, owed to the reduction in the magnitude of such losses, the concentration overpotentials are almost comparable to the anode activation ones.

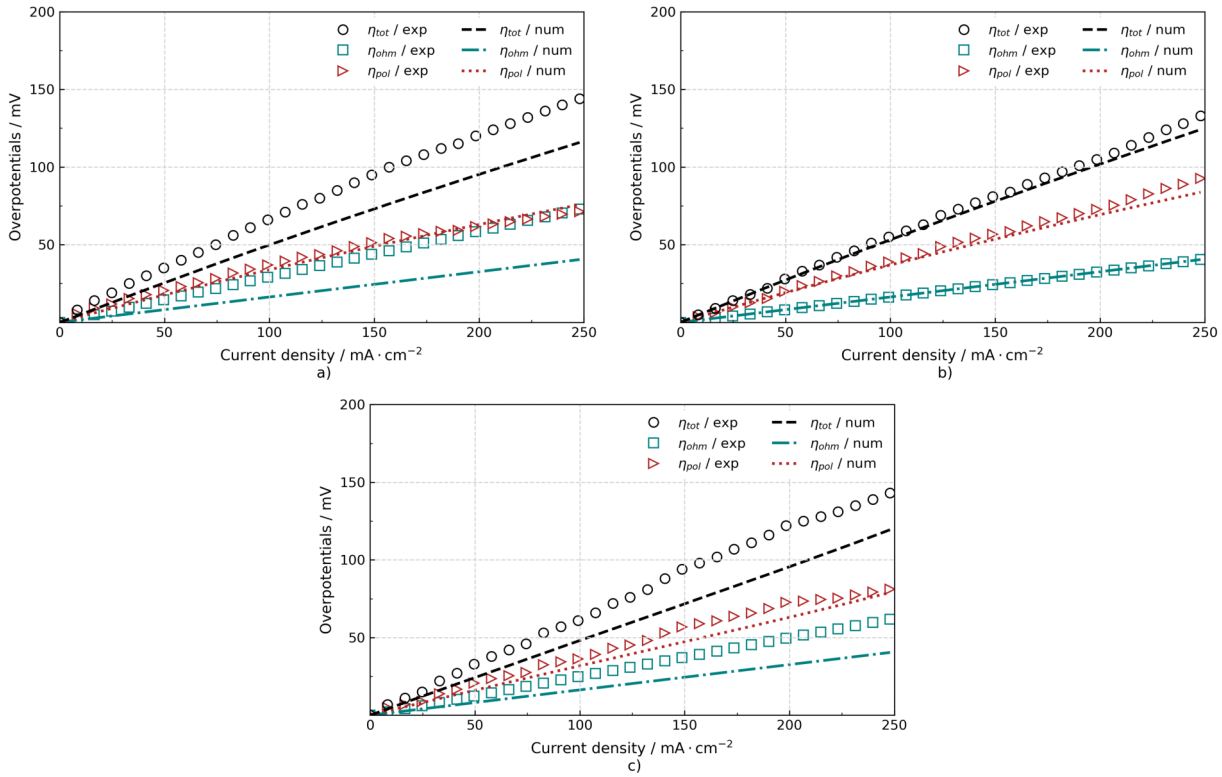

Figure 5.38. *Numerical and experimental comparison of the different overpotentials at* 700 °C *for a) LIR, b) IIR, and c) CIR.*

Regarding the numerical and experimental comparison of the overpotentials at 700 °C, Fig. 5.38, it is observed that the major differences between the numerical and experimental results correspond to LIR and CIR compositions. In both cases, these differences are mainly perceived for the ohmic contributions, and thus, for the corresponding total overpotentials, followed by a relatively

lower change in the polarization losses. In the case of LIR and CIR, the average difference between the numerical and experimental ohmic overpotentials correspond to 16.2 mV and 10.7 mV, respectively. In contrast, for the polarization losses, this difference corresponds to only 2.6 mV and 5.5 mV for LIR and CIR, respectively. These figures result in an average deviation of the total overpotentials of 17.5 mV for LIR and 16.2 mV for CIR. Hence, the observed deviation in the ohmic overpotentials under LIR and CIR compositions, rather than being an under-prediction of the model, they are just an effect of the cell degradation that it experienced until the moment that those experimental conditions were tested. Meanwhile, the results for the numerical and experimental comparison for IIR composition evidence the good agreement of this simple 0D model.

5.2.1.2. Reacting species

In Fig. 5.39 and Fig. 5.40 it is presented the molar rate of CH_4 and CO reacting (through the reforming and shifting reactions, respectively) as a function of the current density for the three analyzed compositions and at both analyzed operating temperatures.

From the molar rate of CH_4 reacting , Fig. 5.39, it is observed that at 650 °C, Fig. 5.39a, the methane conversion is promoted when increasing the current density, regardless the methane content, since the same trend is observed for all the three compositions. This methane conversion enhancement with current density can be explained because of the increase in the H_2 demand (direct product of the SMR reaction) while increasing the fuel utilization, and because of the temperature rise when increasing the current. Nonetheless, the later cannot be considered in this case, owed to the isothermal considerations for the present model.

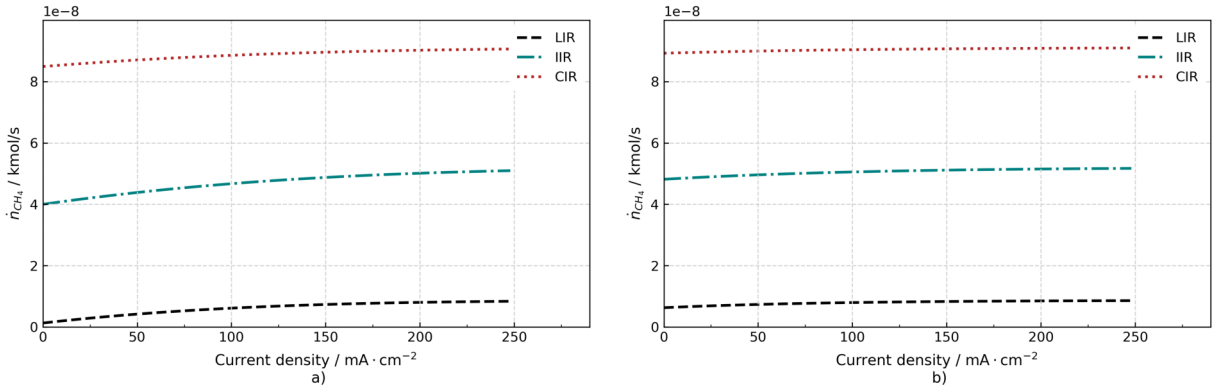

Figure 5.39. *Molar rate of CH_4 reacting as a function of current density at a)* 650 °C *and b)* 700 °C *according to the equilibrium constant of the internal reforming reaction.*

At 700 °C, Fig. 5.39b, it is noted that owed to the thermodynamics and equilibrium of the steam methane reforming reaction at this temperature, the methane consumption rate for all the three compositions seems to be less influenced by the current density, as comparing at 650 °C.

This issue implies that at higher operating temperatures, methane conversion can not be much or significantly improved from that resulting in OCV when the current density is increased. This is because, regardless the fuel composition, even in OCV condition a very high methane conversion is achieved, remaining apparently constant as the current density increases. This trend, along with the previous one at 650 °C, totally agree with the results obtained from the experimental composition analyses, suggesting a potential feasibility/applicability of these commercial cells to be also used as very efficient reformer devices.

Regarding the CO reacting, Fig. 5.40, it can be seen that in the case of LIR and IIR compositions "a negative quantity" of this species resulted to react at low current densities. However, a negative molar rate of CO rather implies that instead of being reacting, CO is being formed through the r-WGS reaction. That is, the WGS reaction is being pushed towards the left direction under the observed operating conditions. Therefore, in accordance with the gas analyses and CHEMCAD results, it is also numerically obtained through this simple model, that at OCV under LIR and IIR compositions and at both analyzed temperatures, the r-WGS reaction is proceeding. Meanwhile at 650 °C when the cell supports 15 A and 30 A, corresponding to 125 mA cm^{-2} and 250 mA cm^{-2}, respectively, the WGS reaction is taking place for all the three analyzed compositions. In particular, for IIR at 15 A, it is predicted a barely noticeable or weak CO conversion through the WGS reaction, as actually pointed out from the experimental results.

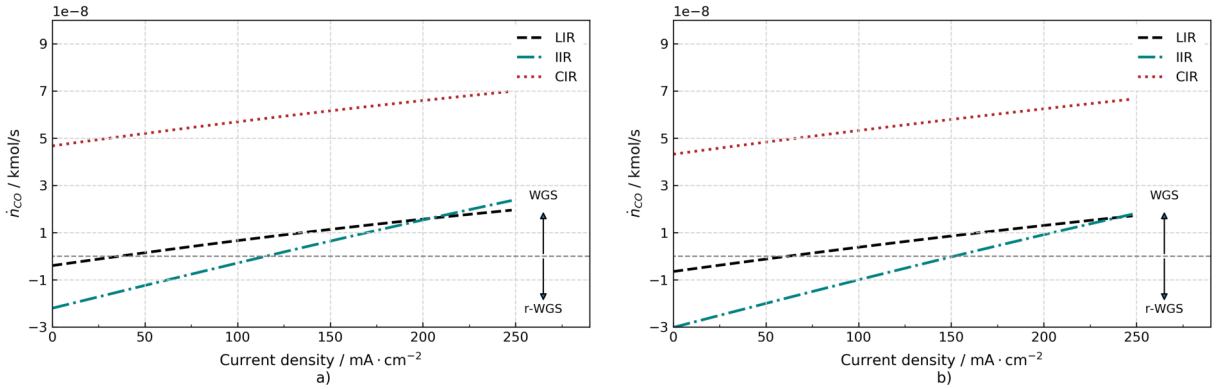

Figure 5.40. *Molar rate of CO reacting as a function of current density at a) 650 °C and b) 700 °C according to the equilibrium constant of the water-gas shift reaction.*

It can be also observed that the intersection of the CO reacting lines with the horizontal axis represents the point where the WGS reaction changes the direction in which it is proceeding, i.e. from backward to forward. Then, under both compositions, LIR and IIR, such a change occurs at lower current density values at 650 °C compared to 700 °C. This issue can be actually illustrated since the chemical equilibrium of the WGS reaction is shifted towards the products at a lower current density, ∼36 mA cm^{-2} for the case of LIR and ∼115.3 mA cm^{-2} for IIR, when the cell is running at 650 °C in both cases. Meanwhile, at 700 °C the WGS reaction proceeds at a bit higher

current density: $\sim$61.7 mA cm^{-2} and $\sim$151.4 mA cm^{-2}, for LIR and IIR, respectively.

In the case of IIR, it is also observed that at both temperatures, the equilibrium towards the products is reached at higher current densities than in the case of LIR. This issue can be explained owed to the higher CO_2 content in the IIR gas mixture compared to the LIR one. Thus, the occurrence of the r-WGS reaction instead of the WGS reaction in a more extensive current density region is also favored by the CO_2 content, which pushes the equilibrium towards the left direction. Meanwhile, in the case of CIR, it is always evident the occurrence of the WGS reaction, as also shown from the gas analyses.

Finally, as an example, Table 5.6 shows a comparison of the outlet gas compositions at 15 A and 650 °C for LIR, IIR and CIR, obtained from this numerical model and compared with those calculated using Chemcad and with the experimental ones.

It is observed that, for all the three cases and for all the species, the composition differences between the present model and Chemcad are lower than 0.5%. The existing differences are related to the temperature used for the computations. That is, while for the present model it was always used the corresponding operating temperature of 650 °C, in Chemcad it was used the corresponding average temperature presented in Table 5.2, Table 5.3 and Table 5.4 for LIR, IIR and CIR, respectively.

The issues related to the differences with the experimental outlet compositions have been already discussed in section 5.1.2.

Table 5.6. Comparison of the outlet gas compositions for the three analyzed compositions at 15 A and 650 °C.

		H_2	CO_2	CH_4	CO	H_2O
LIR	0D Model	44.48	9.75	0.42	5.34	40.01
	Chemcad	44.58	9.71	0.41	5.62	39.68
	Experimental	50.55	12.72	0.51	7.07	29.14
IIR	0D Model	38.12	19.14	0.79	12.01	29.94
	Chemcad	38.03	19.11	0.88	12.20	29.78
	Experimental	39.08	21.20	0.77	16.01	22.94
CIR	0D Model	42.67	10.16	0.34	5.12	41.71
	Chemcad	42.44	10.11	0.37	5.11	41.97
	Experimental	48.64	17.61	0.32	5.13	28.30

Very similar differences (below 0.6%) between the outlet compositions calculated with the present model and with Chemcad were also obtained under the other two loading conditions and for all the three cases. Therefore, the present 0D model is able to predict in a very simple way the outlet compositions under complex mixtures with a quite good accuracy level.

5.2.1.3. *Cell power and efficiency*

Finally, from this simple zero-dimensional model, the electrical power and efficiency of the cell at 650 °C and 700 °C are also numerically and experimentally compared. The resulting comparisons are depicted in Fig. 5.41.

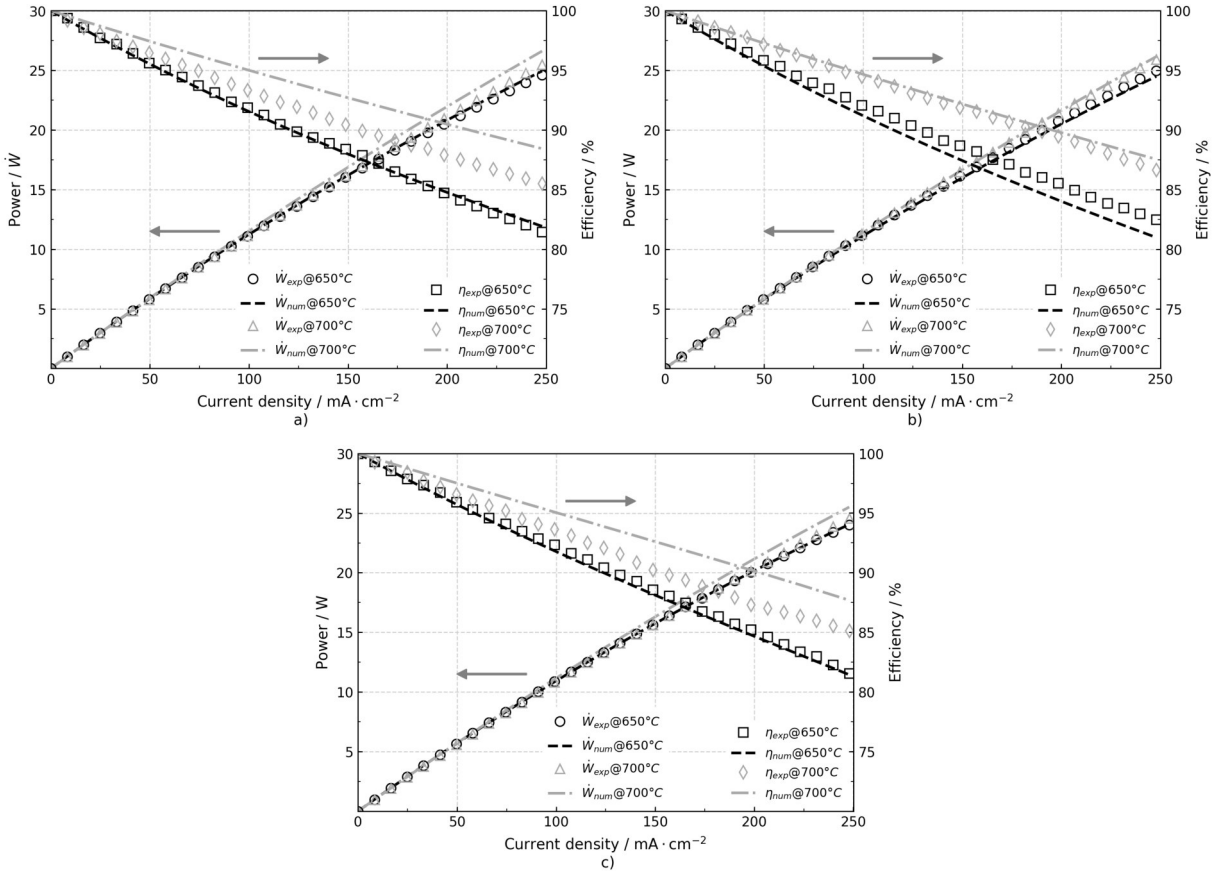

Figure 5.41. *Numerical and experimental comparison of the cell electrical power, and efficiency at 650 and 700 °C for a) LIR, b) IIR and c) CIR.*

It is roughly observed, that except for the cell degradation issues, in general these experimental and numerical results are quite similar. They show an insignificant average deviation of less than 3% in all the three cases for both, power and efficiency. Additionally, the electrical power delivered under these three conditions are quite comparable to those reported in the literature under similar compositions and even for SOFCs running under hydrogen fuel [51, 117, 202, 257, 268].

About the comparison and magnitude of the cell electrical power yield under the three analyzed compositions at both temperatures, they have been already discussed in the experimental section. Nonetheless, regarding the cell efficiency, relatively high efficiencies ranging from ∼82% to ∼100%, are observed for all the three cases. Accordingly, under LIR the respective and corresponding experimental efficiencies at 15 A and 30 A are 89.8% and 81.4% at 650 °C and 91.9%

and 85.5% at 700 °C. Under IIR composition the experimental efficiencies are 90.4% and 82.4% at 650 °C and 93.1% and 86.6% at 700 °C for 15 A and 30 A, respectively. And finally, under CIR the experimental efficiencies at 15 A and 30 A are 90.4% and 81.5% at 650 °C and 92.1% and 85.1% at 700 °C, respectively. Therefore, as observed, also in terms of cell efficiency, the IIR composition seems to give the best trade-off from the three analyzed compositions.

5.2.2. Current density distribution through the model based on finite differences

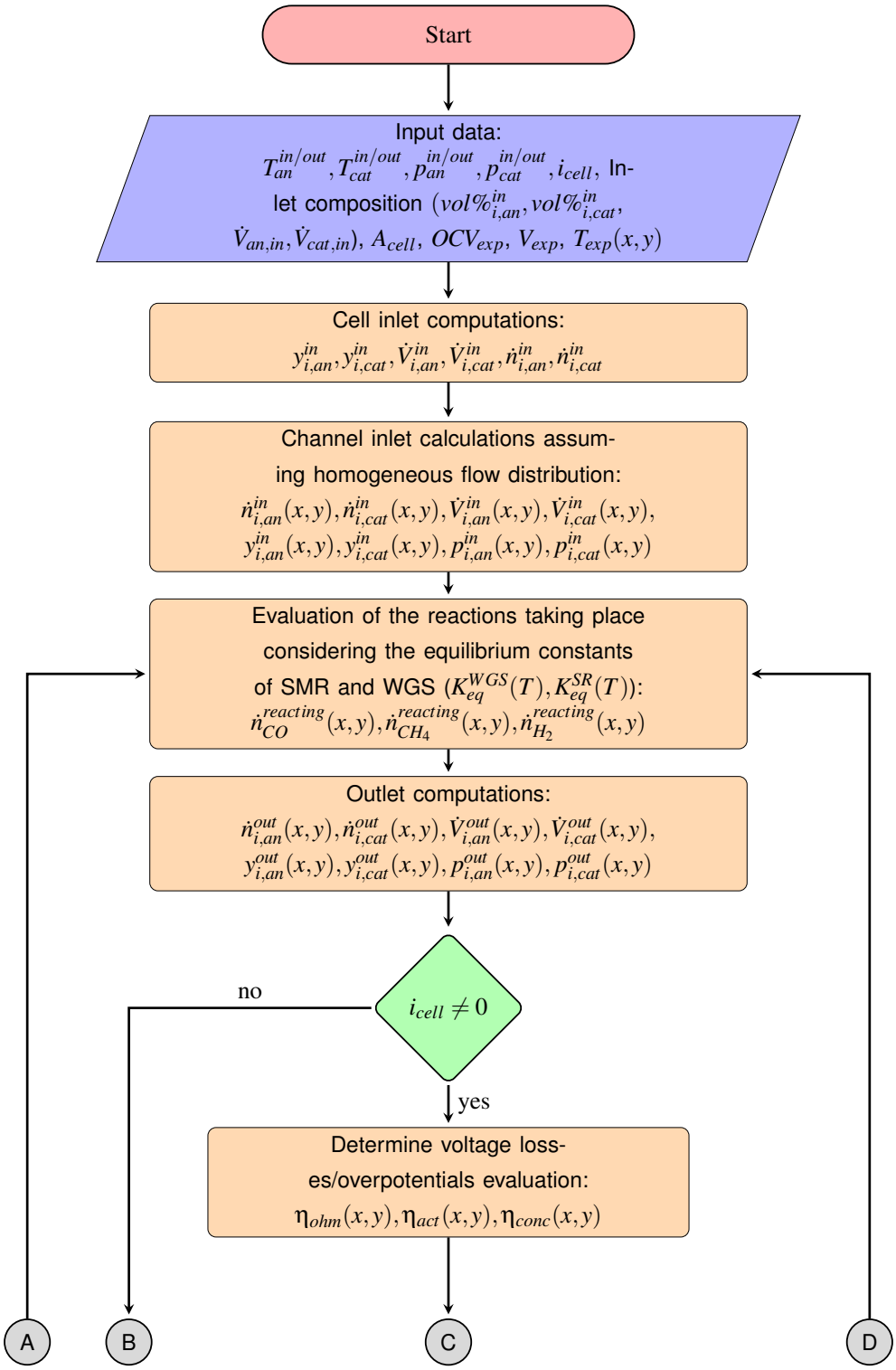

Figure 5.42. *MATLAB algorithm, part 1.*

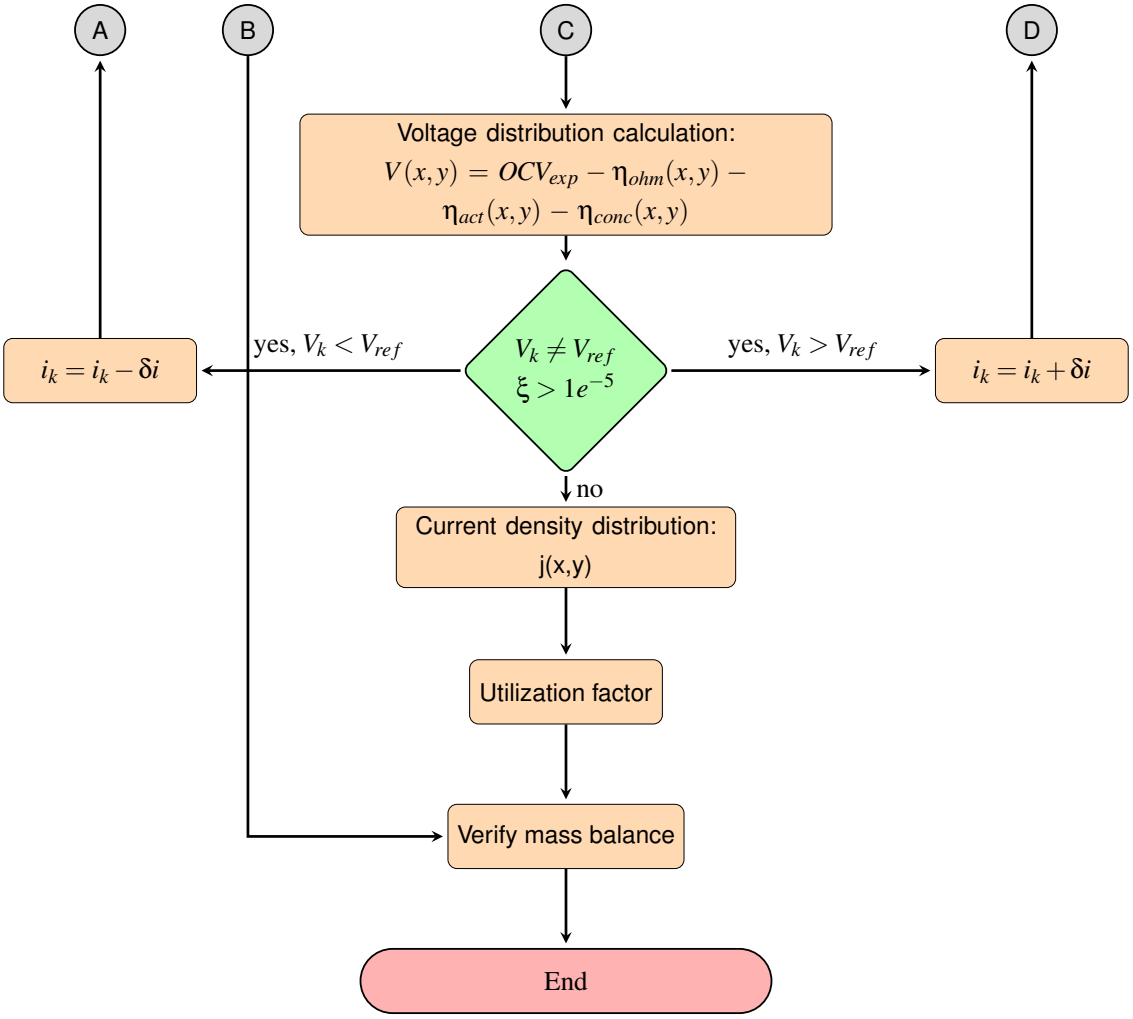

Figure 5.43. *MATLAB algorithm, part 2.*

5.2.2.1. Current density distribution

From the numerical model developed using Matlab, according to the algorithm shown in Fig. 5.42 and Fig. 5.43, the current density distribution throughout the whole anode has been obtained for the analyzed compositions. It is pointed out that the different experimental temperature data are introduced (as an input) in the current model as a temperature mapping coming from a paraboloid fitting of the corresponding temperature data. However, for a more detailed description of the model, the reader is referred to section A.2.

Hence, Fig. 5.44 respectively illustrates the resulting current density distribution at 15 A and 30 A for LIR composition at 650 °C. It is observed that at both values of electrical current the correlation between temperature distribution and current density seems to mostly be governed by the input data rather than by the H_2 distribution, Fig. 5.11a and Fig. 5.12a . Accordingly, the zone of the highest current density is found in the front part of the cell/anode, region where the

highest temperatures in the corresponding thermal analyses, Fig. 5.25b and Fig. 5.25c, have been also observed. Despite the previous characteristic, it is observed a relatively uniform current density distribution, mainly at 15 A, which can be attributed to the hydrogen distribution in the cell owed to the lack of reforming activity under this composition and which is clearly governed by the temperature differences over the anode.

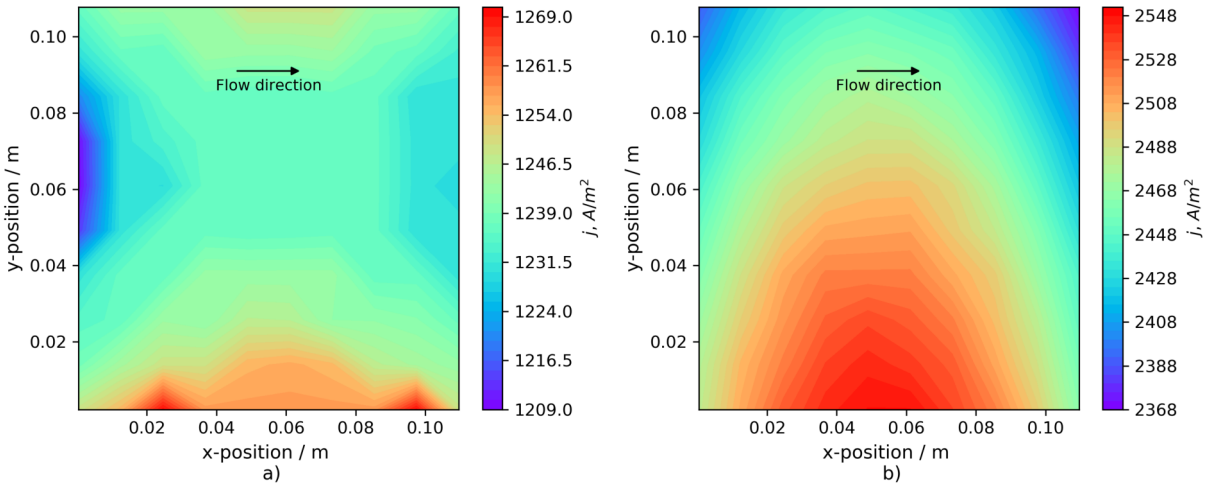

Figure 5.44. *Numerical current density distribution throughout the cell for LIR at* 650 °C *and a) 15 A and b) 30 A.*

Then, Fig. 5.45 illustrates the resulting current density distribution condition at 15 A and 30 A for IIR composition at 650 °C. It is more clearly shown that in this case the correlation between temperature and current density is (more) clearly governed by the input (experimental) data. Therefore, in agreement with Andersson et al. [269], in this case there is a clear coupling between the local current density and the local temperature. Actually, the current density distribution shows quite the same trend, mainly at 15 A, as that observed in the corresponding thermal analyses, Fig. 5.27b and Fig. 5.27c. Hence, it can be observed that the current density increases along the main flow direction, due to the temperature rise from the electrochemical reactions. However, this increase is limited owed to the consumption of electrochemical reactants within the cell. Therefore, it can be said that the increase in current density is accelerated from an increase in temperature along the main flow direction, as also Andersson et al. [170, 269] pointed out.

Hence, the current density distribution should not only show a relation with the input experimental data. In fact, it is observed that it also shows a strong and consistent correlation with H_2 distribution at the corresponding conditions, Fig. 5.16a and Fig. 5.17a, i.e., to decrease where current density increases, which is clearly owed to the electrochemical reaction progress. Therefore, it can be observed that in both cases the numerical current density distribution is also in agreement with the qualitative experimental species distribution.

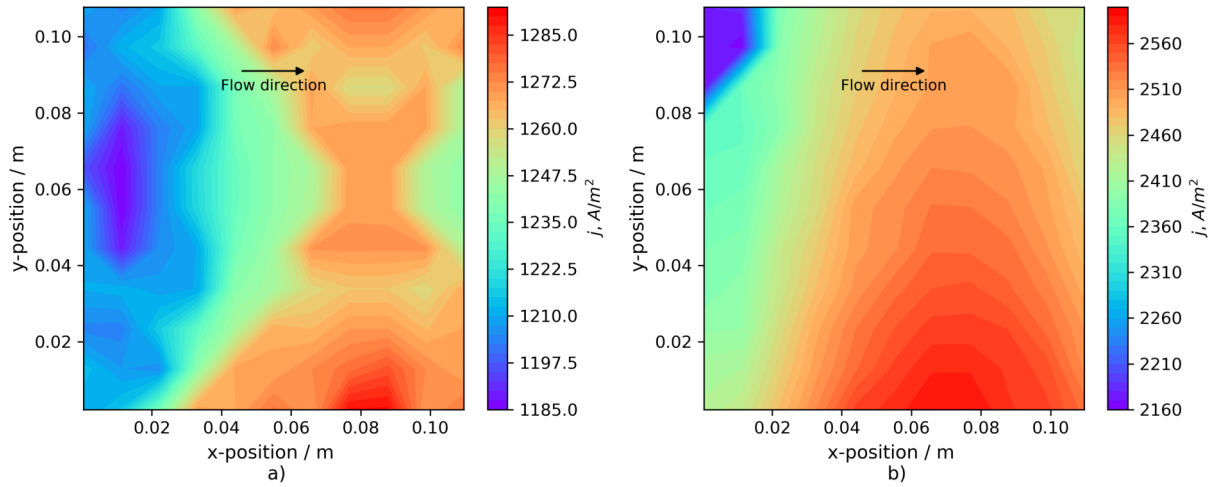

Figure 5.45. *Numerical current density distribution throughout the cell for IIR at* 650 °C *and a) 15 A and b) 30 A.*

On the other hand, comparing the current density distribution with the previous case (LIR), Fig. 5.44, it is observed that at 30 A, the zone of the highest current density seems to shift towards the cell outlet and at the same time expands across the cell. This could be explained because of the increased hydrogen production as the reforming reaction is progressing in the flow direction, which increases the hydrogen availability and thus the electrochemical activity. At 15 A, however, seems that this zone only expands across the cell. Hence, in general terms, it is observed that the electrochemical activity of the cell enhances under IIR since the local current density value is higher in most parts of the cell, resulting in a more homogeneous current density distribution with the highest value of current density.

Finally, Fig. 5.46 shows the current density distribution at 15 A and 25 A for the CIR composition at 650 °C. In both cases, it is also observed an increase of the current density along the flow direction, resulting as in the previous case, from the coupling with the experimental temperature distribution, Fig. 5.29b and Fig. 5.29c.

As initially pointed out, since the current density distribution has been obtained using the corresponding experimental temperature distribution, it is clearly observed, in some cases, the strong coupling between temperature and current density distribution. Nonetheless, there is also a clear relation with the experimental H_2 distribution. For example, in this case (CIR), since the methane content gives rise to a higher H_2 production in the flow direction, the current density distribution increases with the H_2 production in the same direction.

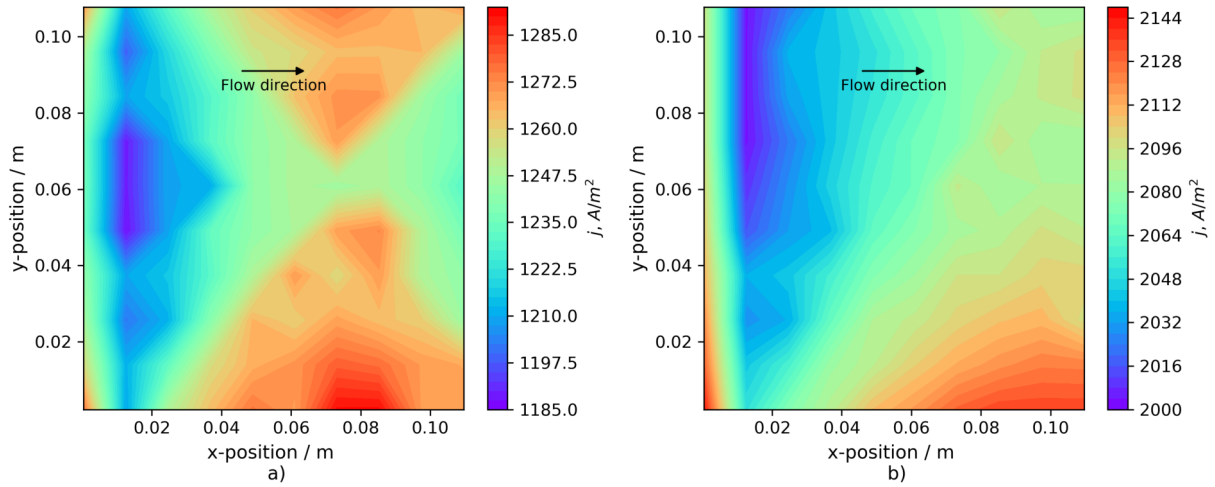

Figure 5.46. *Numerical current density distribution throughout the cell for CIR at* 650 °C *and a) 15 A and b) 25 A.*

Therefore, the current density distribution for most cases shows a similar behavior from the inlet to the outlet, because the decrease of ideal voltage due to the temperature increase and the consumption of fuel and oxygen is compensated by an increase of the current density related to an increased cell temperature. In effect, the contour plots of current density distribution are consistent with the corresponding H_2 distribution, reflecting and confirming the assumption that the electrochemical process occurs by only hydrogen oxidation, while CO consumption is according to WGS equilibrium [270].

5.3. Single cell long-term operation under internal reforming

In the last part of this analysis, the results of an endurance performance investigation towards methane reforming stability are presented. Long-term steam methane reforming has been investigated from the perspective of methane conversion, hydrogen yield and, overall, cell stability. Therefore, according to the above results, in general, under IIR composition it has been achieved the best trade-off in terms of H_2 production and electrical power generation, yielding the highest electrochemical performance from the three studied gas mixtures. Hence, in the following, the corresponding results are presented.

During the period in which the cell was operated (∼500 h) several unexpected events were experienced. The time evolution of the operating cell voltage, some representative events, and their impact on the cell performance are shown in Fig. 5.47.

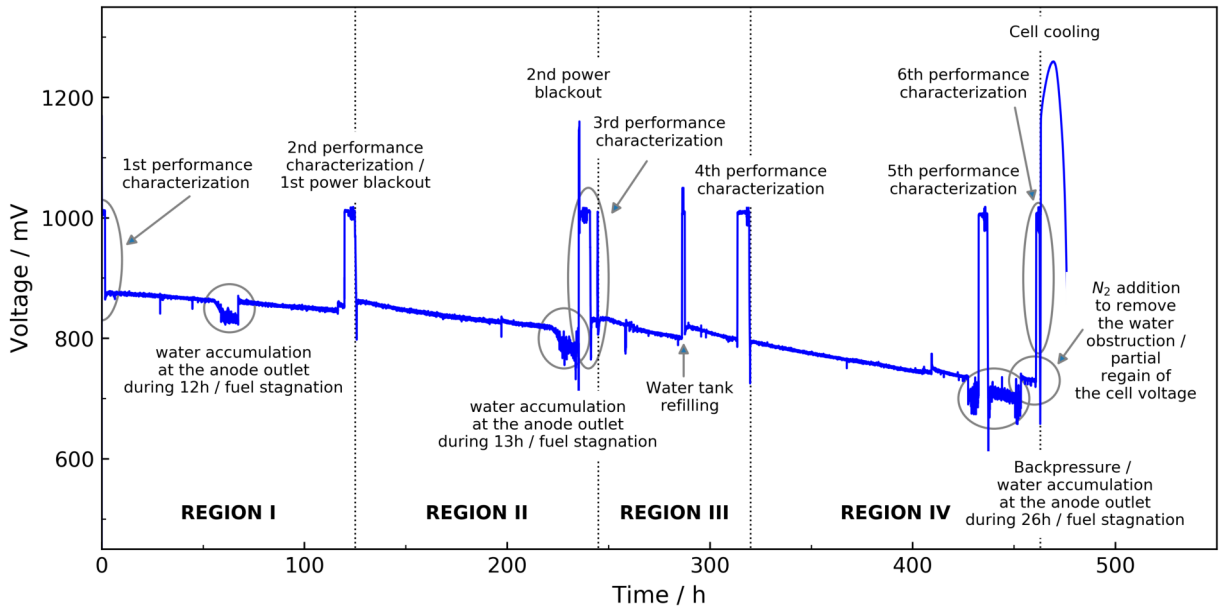

Figure 5.47. *Cell voltage variation with some representative events during its operation at* $248\,\mathrm{mA\cdot cm^{-2}}$ $(FU = 43\%)$ *and* $650\,^{\circ}\mathrm{C}$.

From Fig. 5.47, four different regions are distinguished. Each of them corresponds to the period in which the cell is running under current before taking it to OCV to later perform the corresponding characterization.

The degradation rates in these regions are bounded by sudden voltage drops owing to severe accumulation of water downstream, which was generated as a result of the large cell area, the high water content in the fuel, and the involved electrochemical and internal reforming reactions, Eq. (2.3), Eq. (2.18) and Eq. (2.19). This phenomenon has been recently reported in the literature as a particular problem when testing large-area fuel cells [51,80,81] or when the dilution of the fuel with water is high [52, 175], resulting in lower overall efficiency [4, 5, 159] and detrimentally affecting the operational stability of the cells [7].

In the case of regions I and II, this phenomenon was present mainly due to the inappropriate management of the high production rate of water in the relatively small discharge tank. For the subsequent two regions, i.e. regions III and IV, the small discharge tank was replaced for a bigger one. Nevertheless, the sudden voltage drops were still present, which were rather attributed to a possible back-pressure at the fuel outlet, which in turn might be due to the configuration of the water discharge system.

Hence, a back-flow, a momentary fuel stagnation and partial fuel depletion in the downstream region would have taken place. Moreover, during the second and third characterization, sudden power blackouts occurred. The hypothesis of a possible back-pressure arises since there was a high content of water at the outlet region of the cell, thus a high partial pressure of water. The latter,

in addition to the experienced power blackouts, could have led to thermal stresses and therefore to mechanical damage, creating cracks. Then, having a flow almost 4 times greater at the cathode and flow stagnation at the outlet region of the anode, it could have induced a pressure difference by dragging part of the anode flow towards the cathode side through the formed cracks.

It is clearly seen from Fig. 5.47 that as the running time increased and the different incidents were taking place, the cell voltage abruptly drops, increasing the degradation rate in each region, with some partial voltage regain after the cell was taken to OCV condition. This small voltage regain occurs because the water obstructions generated under current are removed in OCV, since the production of water through the electrochemical reactions ceases in this latter condition. This is consistent with the literature, since it has been extensively reported that the voltage is reversible when cathode gas is changed from humid to dry [86]. This statement makes even more sense if the high partial pressure of water and its accumulation is considered to influence the cathode side. This phenomenon will be discussed later.

Accordingly, since the beginning, the cell underperformed with an unstable voltage trend coupled to a visible performance decay. The experienced degradation rates were calculated according to [80], using the following equation:

$$DR(\%/h) = \frac{V_f - V_i}{V_i} \times \frac{1}{t} \times 100 \tag{5.1}$$

Where V_f, V_i and t are the final cell voltage, the initial cell voltage, and the corresponding operating time in each region, respectively. Thus, the degradation rate in region I was $\sim$3.54% during the first 120 h, $\sim$6.32% for the consequent 120 h in region II, $\sim$7.54% in the next 75 h corresponding to region III, and $\sim$11.03% for the following 145 h in region IV. These values correspond to a degradation of 258.96, 453.38, 838 and 604.82 $\mu V/h$ for regions I, II, III and IV, respectively. In this case, a relative approach was used to calculate the degradation rates, since it is clearly seen that the slope for each region is different. However, it is also possible to give the absolute approach, by keeping the initial voltage fixed instead of using the initial one in each region, thus obtaining: $\sim$3.54%/120 h, $\sim$8%/120 h, $\sim$12.06%/75 h and $\sim$19.24%/145 h, respectively.

In general, the degradation rate did not decrease, but rather accelerated even more. Up to region III an increase of almost twice the corresponding previous degradation rate was experienced. However, for region IV a decrease in the degradation rate of around 25% was obtained compared to that from region III. Nevertheless, the voltage became too unstable, having decreased too much from the beginning to be recovered as cell operation continued.

This phenomenon could be explained in such a way that during the first phase in a long-term operation, where a time-related degradation is experienced, a reorganization in the microstructure

of the electrodes in the cell occurs, leading to an increase or decrease of the performance. Then, the second phase shows a continuous degradation rate, followed by a fast decrease in the performance during the third phase. However, since the beginning, the degradation rate was very high for it to be considered time-related only. Rather, a thermal-cycling related degradation mechanism seemed to occur, which always shows an accelerated degradation and sometimes, a fast decrease of the performance, in combination with a time-related degradation mechanism. However, there is no published consensus in this field [126, 163, 169, 174]: some authors reported massive degradation [6, 86, 98, 172, 174], while some others reported no significant degradation [80, 81, 176].

5.3.1. Polarization curves and electrochemical analysis

The characterization tests were conducted six times during cell operation. Nevertheless, since the conditions in which the fifth set of tests was carried out were not appropriate because the cell was flooded, as in fact it is observed in the I-V curve at 430 hours from Fig. 5.48, these results are excluded from this analysis.

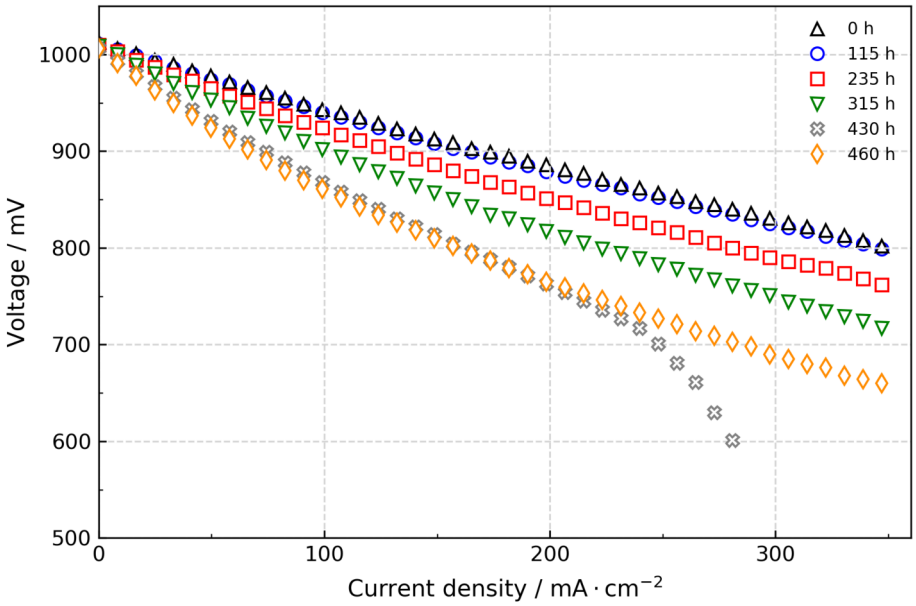

Figure 5.48. *Polarization curves recorded during the test and corresponding to the fuel flow composition specified in Table 4.10.*

The I-V measurements were mainly recorded in the low-current-density region (0-350 mA/cm^2), and the corresponding I-V curves are plotted in Fig. 5.48. The polarization curves were recorded in this region to avoid the stress of taking the cell to high current density values, thus keeping the cell running under safe operating conditions. However, before the last characterization and after all the incidents, a high degradation was observed, the operating voltage was very low, and the cell was

not able to continue over 460 h because of a drastic increase in the polarization losses.

From the polarization curves, is evident that the slopes increase over time, reaching at the end up to twice their initial value. Although this current density region is theoretically mostly dominated by activation overpotentials [81], to determine the contribution of these, or to separate them from the other overpotentials, a more detailed analysis is necessary, since SOFC operation involves a complex interplay of different processes, and even more under internal reforming.

Thus, the obtained polarization curves also confirmed that the characteristics of the cell quickly and significantly degraded over time. Moreover, it can be seen that just after the first power blackout took place (region II), the voltage decay became more evident, in fact the I-V characteristics (from the third characterization, at the end of region II) drastically degraded, and even more after the consequent sudden shutdown cycles that the cell experienced, thus suggesting that thermal-cycling is critical when SOFCs are operated for long periods and under a transient mode operation, especially when their regular operating performance is already compromised.

Nevertheless, the recorded polarization curves and measured cell voltages only reveal the total loss in performance and provide no accurate information with respect to losses and changes due to ohmic resistance and/or polarization resistances during the testing period. Hence, electrochemical impedance spectroscopy analysis was adopted, in order to establish which electrode is responsible for the observed cell degradation, and the corresponding recorded spectra are shown in Fig. 5.49.

From the Nyquist plots (EIS spectra), and as earlier pointed out, three arcs can be distinguished, namely: high, intermediate and low frequency arcs. As presented in the EIS analysis of the IIR composition, the low-intermediate frequency region of the measured spectra is characterized by two distinctive impedance arcs. In addition to the semicircle at ca. 50 Hz, the semicircle at characteristic frequencies below 1 Hz is also observed, which is characteristic in the operation of reformate-fueled cells [30, 84].

It is evident that the ohmic resistance (high-frequency intersection with the real axis) of the cell has increased. However, the high-frequency arcs of the EIS spectra are similar and they just change their size over time a little. Nevertheless, the intermediate-frequency arc shows considerable differences.

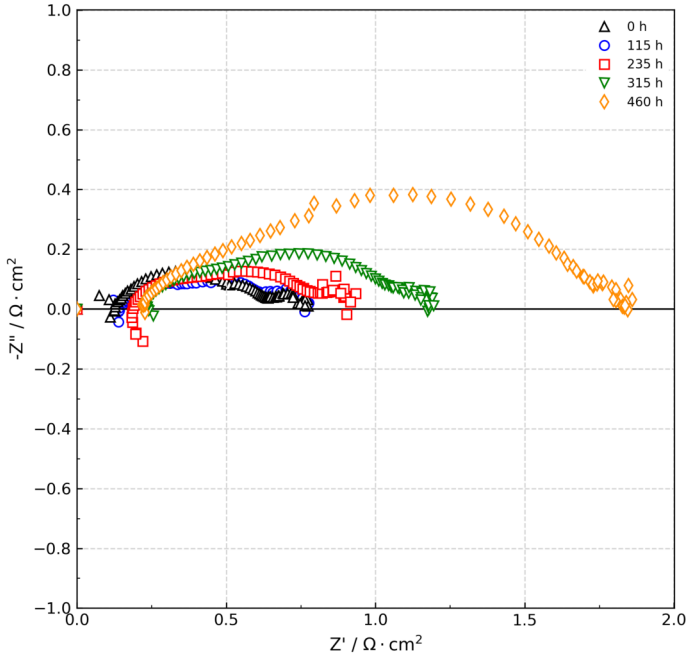

Figure 5.49. *Nyquist plots or EIS at OCV condition recorded during all the characterizations, showing mainly a big increase in the intermediate frequency arc.*

Hence, based on the electrochemical spectra, the degradation of the cell has been reflected in a simultaneous increase of the internal but predominantly of the polarization resistance, the latter reaching up to 2.5 times its initial value, while the internal resistance almost doubled its initial value. Thus, mainly the medium frequency region increased significantly during the time that the cell was tested. In this case, where large degradation rates have been observed, large changes in the individual arcs of the impedance spectra were also observed.

It should be remembered that below 10 Hz the impedance spectra are influenced by diffusion and fuel conversion, whereas the cathode influences the medium frequency region (1 to 200 Hz) and the anode mainly influences the high frequency region (above 200 Hz) for anode-supported cells [58, 83, 123, 124, 126, 271].

Although the largest difference of the impedance spectra measured on the reformate-fueled cell is mainly observed at intermediate frequencies (between 10 and 200 Hz); the changes in the imaginary part of the spectra contain contributions from both cathode and anode.

However, the region assigned to anode processes changed relatively little, compared to the region corresponding to cathode processes, implying that the anode was affected to a smaller extent resulting just in a slight increase in the activation and concentration resistances. This suggests that cathode degradation was the main contribution to the performance deterioration of the cell, since the observed characteristics of the impedance spectra are ascribed to process-related microstructural

changes in the cathode when thermal-cycling occurs [65, 271].

During the first 115 h of operation, both the internal and polarization resistances remained almost unchanged. For the next 120 h both increased relatively little, whereas for the last 230 h the internal resistance continued increasing but again relatively little, reaching twice its initial value and then remaining constant; unlike the polarization resistance, which seemed to increase exponentially over time, as shown in Fig. 5.50 where internal and polarization electrical resistances are plotted as a function of time.

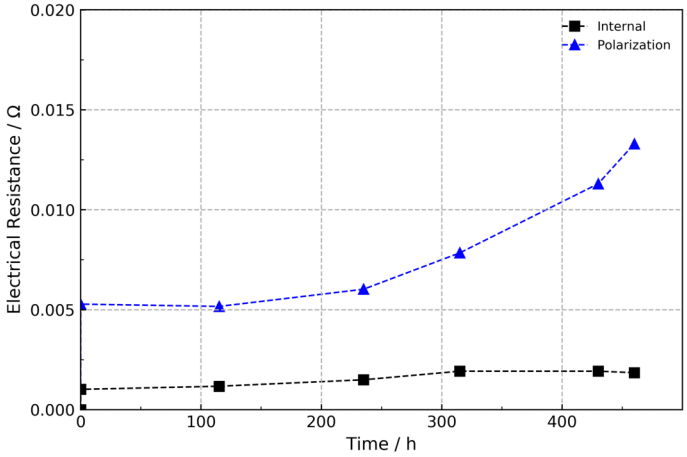

Figure 5.50. *Increase of the internal and polarization electrical resistance over time, obtained from the impedance spectra.*

In addition to the electrochemical analysis, the total overpotentials of the cell were separated into ohmic and polarization resistances, and plotted as a function of the current density, as shown in Fig. 5.51. This plot was obtained from the polarization curves and impedance spectra, as follows: 1) the time-related internal resistances of the cell were calculated from the EIS spectra obtained in OCV condition during the different characterizations, 2) with the corresponding time-related internal resistance, the ohmic losses were calculated from Ohm's law as a function of current; 3) then, from the polarization curves a total voltage loss for each value of current was determined as the difference between the open-circuit voltage and the closed-circuit voltage at the corresponding current value, as represented by Eq. (5.2), and finally, 4) with the ohmic loss and total voltage loss calculated for each value of current, the polarization overpotentials were estimated as the difference between the total loss and the ohmic overpotential, Eq. (5.3).

$$\Delta V_{Total,loss} = OCV - V(i) \tag{5.2}$$

$$V_{pol} = \Delta V_{Total,loss} - V_{ohm} \tag{5.3}$$

It is important to clarify that for the estimates of these overpotentials, it was considered that the cell temperature remained constant while the I-V curves were obtained, i.e. that the cell remained at the same temperature when increasing the current, which is an assumption since the cell temperature normally does increase with current as an effect of the Ohmic heating or Joule heating effect, which in turn is reflected in a decrease of the internal resistance. However, the fitting of the internal resistance variation with temperature was not considered since the temperature increase at 30 A respect to the OCV condition for the tested cell was not very significant (∼12 °C and ∼14 °C at 0 h and 460 h, respectively), as it is further discussed in the thermal analysis, representing only a slight difference to the internal resistance, ∼4.7% and ∼5.5% at 0 h and 460 h, respectively.

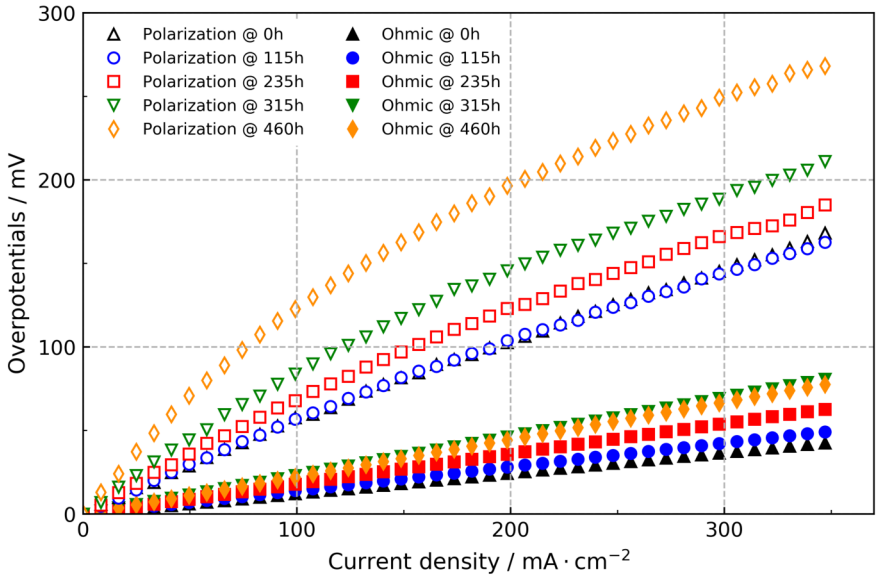

Figure 5.51. *Individual increase of the overpotentials with time.*

The resulting plots show in a clearer way how the overpotentials change with time and current density, where the contribution of the polarization resistance to the cell degradation and voltage drop is evidently larger.

Although many studies have been conducted to identify the degradation mechanisms that lead to cell failure, the progress for a further improvement of these cells is partly constrained by an incomplete understanding of the physicochemical origin of the individual polarization processes controlling the cell performance. In this task DRT analysis is proving to be a useful technique in degradation and stability analysis [61, 90, 98]. Therefore, the recorded EIS spectra were subsequently analyzed with the DRT method.

The DRT is supportive in deconvoluting complex impedance spectra, since the output signal of an electrochemical cell is correlated to diverse physicochemical processes occurring at distinctive relaxation times and with different strengths [42].

To obtain the DRT distribution functions, it was indicated that in the present work the Tikhonov regularization algorithm and the optimum value of the regularization parameter (λ), applying the L-curve method for the latter, have been solved using an in-house program run in MATLAB® (for a more detailed description of the DRT method employed in this work, please refer to section 3.2.3 or to [43, 85]). The imaginary part (Z'') of the impedance data has been employed and the used optimum value of the regularization parameter was 0.25 ($\lambda = 0.25$). The DRT spectra obtained are depicted in Fig. 5.52, which gives a comparison of DRTs under reformate operation at the beginning and at the end of the test.

Comparison of the initial and final DRT confirm that the changes in the imaginary part span a large frequency region (~1 to 1000 Hz), with the largest increase around a frequency of ca. 35 Hz, which to a great extent coincides with the frequency range affected by oxygen partial pressure, i.e., the frequency range where cathode processes dominate [30, 123, 177].

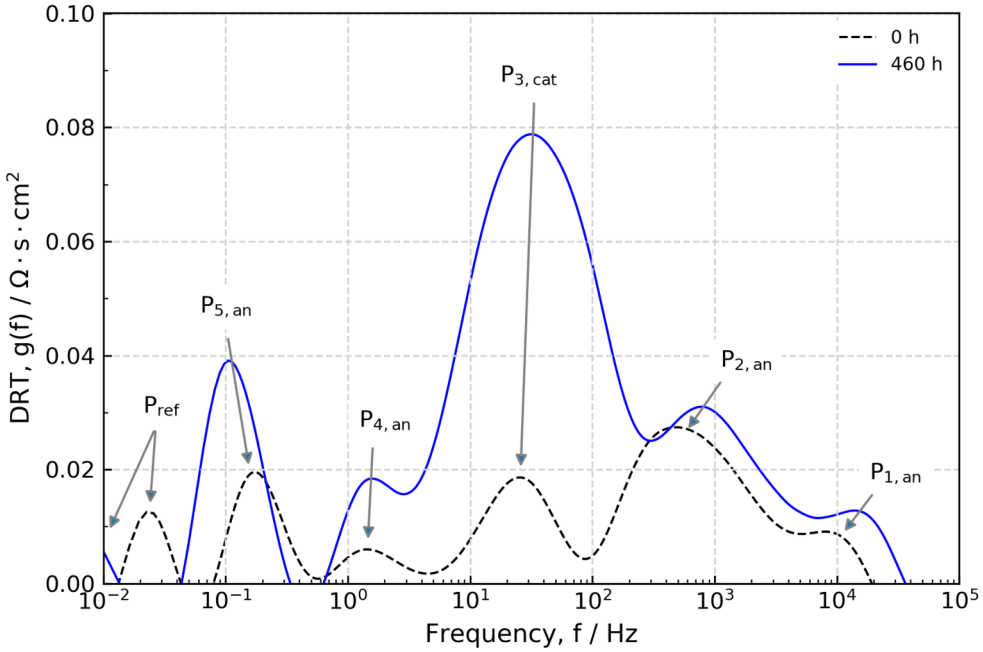

Figure 5.52. *DRT identification processes according to [30, 90, 94], where the most significant difference is found for the cathode-related processes.*

Furthermore, DRT analysis reveals the individual polarization processes which form the measured spectra, Fig. 5.49. In this case at least six processes can be clearly distinguished in the calculated DRT as well.

It is visible how the two high-frequency processes evolve above 100 Hz, $P_{1,an}$ and $P_{2,an}$. At the same time the third process, denoted as $P_{3,cat}$, becomes also visible between 100 and 10 Hz, partly overlapping the low-frequency peaks, $P_{4,an}$ and $P_{5,an}$.

As already refered in section 5.1.2, the two high-frequency processes $P_{1,an}$ and $P_{2,an}$ have been ascribed to the electro-oxidation mechanism, i.e., ionic transport in the Ni/YSZ anode structure and charge-transfer, respectively, in agreement with other reported works [30, 58, 84, 94]. The process $P_{3,cat}$ is reported to show a dependency on changes in the oxygen partial pressure of the cathode gas and the operating temperature, and thus associated to the oxygen reduction within the cathode layer, i.e., the oxygen surface exchange kinetics of the LSC as well as the diffusivity of oxygen ions within the LSC bulk. In the low frequency region, the two distinct features, one falling at ca. 1 Hz and the other one around 10^{-1} Hz (process $P_{4,an}$ and $P_{5,an}$), have been both ascribed to the mass-transfer process caused by the gas-phase diffusion in the pores of the Ni/YSZ anode-substrate.

The additional polarization process, P_{ref}, detected for operation on reformate or on hydrocarbon fuels [30, 84], has been already attributed to the internal reforming phenomenon.

It should be noticed that the characteristic frequencies of the above-mentioned anodic and cathodic processes for this cell are also shifted to lower frequencies compared to those reported by Leonide et al. [94] and Kromp et al. [30]. However, it was clarified that this difference is because they have tested cells with different cathode materials, at higher temperatures and under different operating conditions. The characteristic frequencies of the different processes are usually shifted to lower or higher frequencies depending on the cell and operating conditions. Nonetheless, the process $P_{3,cat}$ is always observed at an intermediate frequency range between 10 Hz and 100 Hz [58], and even when having different cathode materials such as $La_{0.58}Sr_{0.4}Co_{0.2}Fe_{0.8}O_{3-\delta}$ (LSCF) [84, 94].

Therefore, the DRT analysis also confirm the results obtained from I-V curves, Nyquist and Bode diagrams, where the most significant difference was found for the cathode-related processes.

5.3.2. Thermal analysis

Real time surface temperature distribution monitoring of SOFC systems can help to identify and dismiss temperature-related degradation as well as to understand the cell performance. Accordingly, from the thermal analysis, Fig. 5.53, it can be observed that the overall anode temperature did not change so much over time, remaining almost constant during cell operation. This could be explained because the temperature variation over (long) time for a cell in a temperature-controlled furnace is expected to be always low, because of the isothermal conditions. However, in this case, the slight increase in the temperature is well correlated with EIS results, but no with the experienced degradation rate. The effect of the cell degradation on the changes of the cell temperature over time was not significant as it could be expected. This fact is explained since the main contribution to the cell degradation was an increase in the polarization resistance rather than the ohmic resistance,

which mainly causes temperature increment in the cell because of the ohmic heating or Joule heating effect. In fact, an increase under constant load at the end of the test of just 3 °C on the average anode temperature was obtained.

Regarding the effect of the different incidents on the anode temperature, an evident heating of the cell was recorded when these took place.

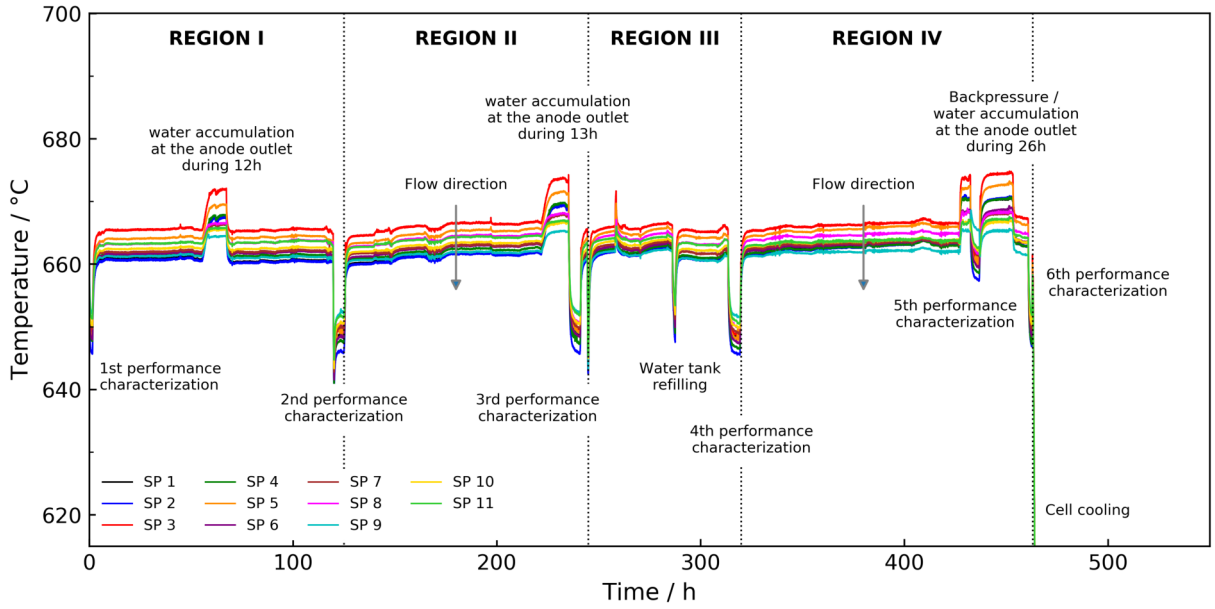

Figure 5.53. *Temperature profiles of the 11 sampling points in the anode during the stability test. For the distribution of the sampling points throughout the anode, please refer to Fig. 4.4.*

From Fig. 5.54, it can be more clearly seen that the effect of the high cell degradation did not have a significant effect on the temperature of the fuel electrode and thus on the cell temperature, as previously said, neither in OCV, nor under closed-circuit conditions.

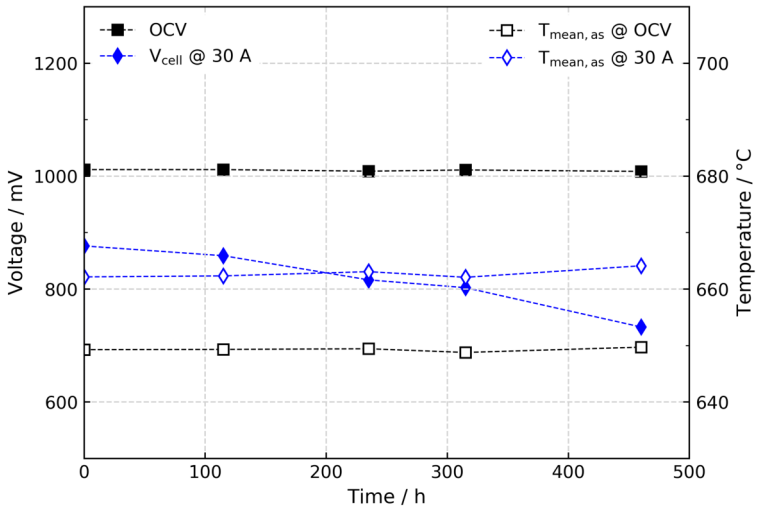

Figure 5.54. *Cell voltage and average anode temperature during the test in OCV and at* 248 $\mathrm{mA/cm^2}$.

Therefore, it was found that just small temperature gradients existed along and across the cell. In OCV condition the maximum temperature was found at the outlet, as it was expected, since the endothermic steam reforming reaction, Eq. (2.18), is dominant at the inlet region [51]. Unlike OCV, under load the maximum temperature was identified in the front part, creating a temperature gradient across the cell. This region where the hot spot was found, corresponds with the area where the fuel gas enters and thus first reacts. Hence, this temperature distribution may be owed to the design of the flow distributors, the non-uniform furnace insulation and heat losses (transferred partially to the environment through the furnace side wall and partially through the hotter outlet gases).

In open-circuit condition, i.e. under only internal reforming, the inherent temperature difference between the hottest and the coldest region of the anode was established to be ∼6.2 °C at the beginning and ∼5 °C after 460 h of operation. Under 30 A, the maximum temperature difference at 0 h was ∼4.5 °C and ∼5.7 °C at the end of the test, showing in both cases (OCV and 30 A) a slight heating of the cell, Fig. 5.55. These very similar differences under load and in OCV are because direct internal reforming promotes intrinsic thermal coupling between endothermic and exothermic reactions within the cell, representing an effective method to remove the excess heat generated in the cell. Furthermore, both exothermic and endothermic effects are not significant in this experimental campaign because of the set low current density and low methane flow rate, since the exothermic effect by the electrochemical reaction is expected to decrease when the cell is operated under low current density and the endothermic effect reduced when the amount of methane is smaller.

The temperature contours from Fig. 5.55a and Fig. 5.55b show the steady state temperature in OCV at 0 h and 460 h, whereas Fig. 5.55c and Fig. 5.55d show it under load at 0 h and 460 h, respectively. In OCV, respect to the reference condition (pure H_2 in OCV and at an average temperature of 660 °C), the outlet temperature at the beginning and at the end of the test only lowered ∼8.7 °C and ∼8.6 °C, respectively, whereas the inlet temperature lowered ∼12 °C and ∼10.8 °C at 0 h and 460 h, respectively, as an effect of the internal reforming reactions. This indicates that most of the cooling effect occurred at the inlet region, and the cooling effect was gradually decreased from the gas inlet to the gas outlet region.

The temperature distribution obviously changed when the fuel cell was under load because of the global effect of the internal reforming, WGS and the electrochemical reactions. The average temperature of the anode was 662.1 °C at 0 h and 664.1 °C at 460 h, which represent an average increase of ∼12.1 °C and ∼14.1 °C respect to the OCV condition.

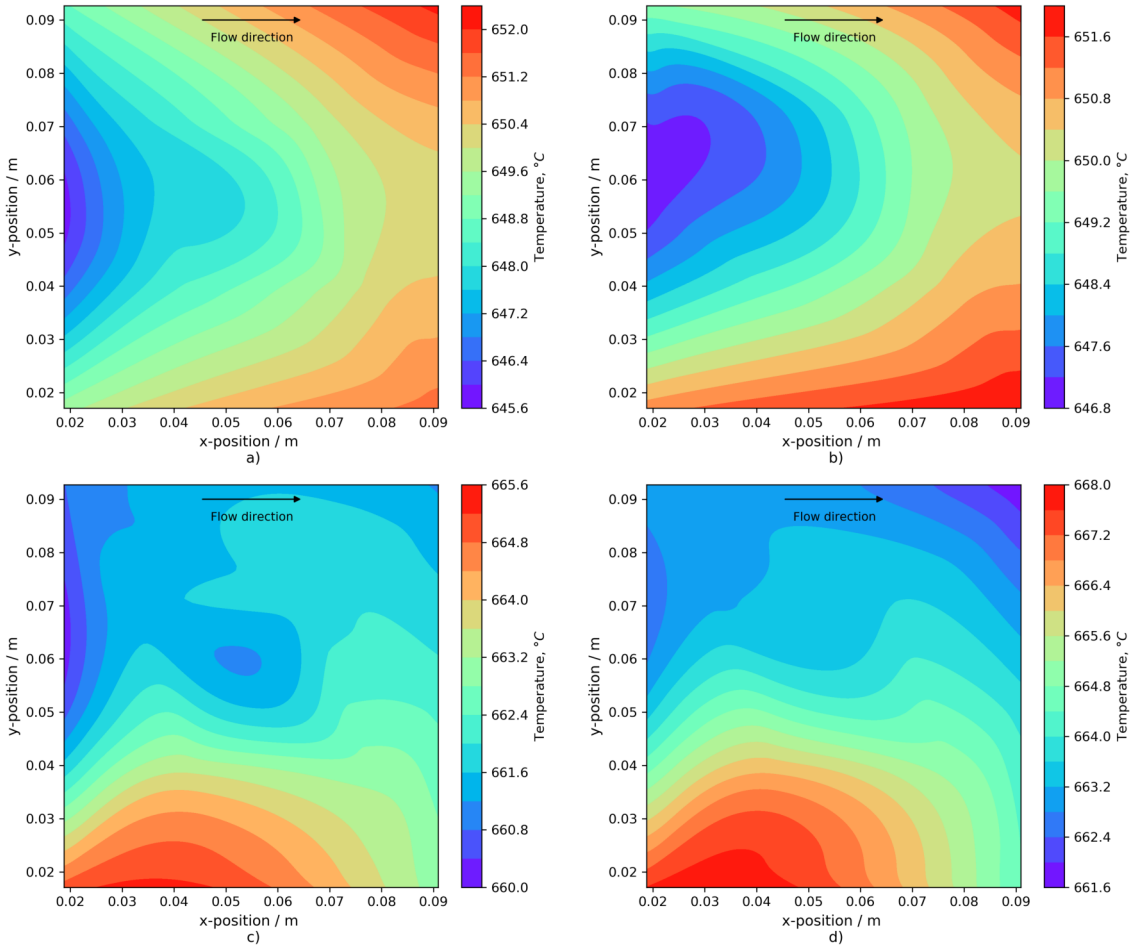

Figure 5.55. *Experimental temperature contours at a) OCV-0h, b) OCV-460h, c) 30A-0h, and d) 30A-460h.*

Therefore, even under continuous operation, the composition tested for the long-term study on the planar-type anode-supported cell showed moderate thermal differences, both in OCV and under load. In addition to the intrinsic thermal-coupling between the endothermic (steam reforming) and exothermic (WGS and electrochemical) reactions, this may also result because of the tested condition (low current density and low methane flow rate).

5.3.3. Gas analyses

Addressing the fuel distribution by the internal reforming and electrochemical reactions, gas-fuel variations have been monitored *in-situ* and *in-operando*. The electrochemical performance of SOFCs is highly dependent on the spatial distribution of the reactant and product species. The structural degradation processes are associated with the spatial compositions as well. Hence, in-situ gas analysis may provide profound information about the local processes occurring. Accordingly, the fifth gas analysis at 435 h (not included in the plots but as suggested by the early limiting current

density in the corresponding I-V curve) has revealed that fuel depletion is worsen downstream during internal reforming operation, resulting in a declining cell voltage and larger performance degradation. In some cases, water accumulation in the cell is such that hydrogen transport to the reaction sites is extremely limited. As a result, very small limiting current densities are obtained, as in effect is shown in Fig. 5.48.

From the inlet to the outlet of the cell and under load, the fuel composition and thus the current are expected to decrease because of the fuel consumption, i.e. the hydrogen produced at the anode side through the internal reforming reaction is consumed by the fuel cell electrochemical reaction; while product water should increase. However, the hydrogen concentration depends on the transport within the porous anode and the chemistry of the heterogeneous reforming reaction, i.e. due to the presence of the internal reforming phenomenon occurring contemporaneously with the electrochemical reaction and depending on the fuel composition and operating conditions, the compositions at steady state may show different trends due to the complexity and simultaneity of all these processes, because in some cases some compounds are being produced from various reactions and consumed at the same time by some others.

The gas chromatography analyses were conducted under real steam contents at the 11 sampling points and at the inlet and outlet gas lines as well. The corresponding results under load for five different characterizations performed during the test and in OCV at the beginning of the test, are shown in Fig. 5.56.

Fig. 5.56 a), b), and c) show the composition (mole fraction) profiles for H_2, H_2O and CH_4, respectively. During the first hours of operation, the measured outlet gas compositions, both in OCV and under load, were very close to the calculated compositions considering chemical equilibrium. At OCV, the species profiles proceed predominantly through the equilibrium between the reactions. The decrease in CH_4 and H_2O concentration is attributed to the steam reforming that leads to the production of H_2 and CO. Subsequently, the CO generates CO_2 and adds more H_2 via the WGS reaction.

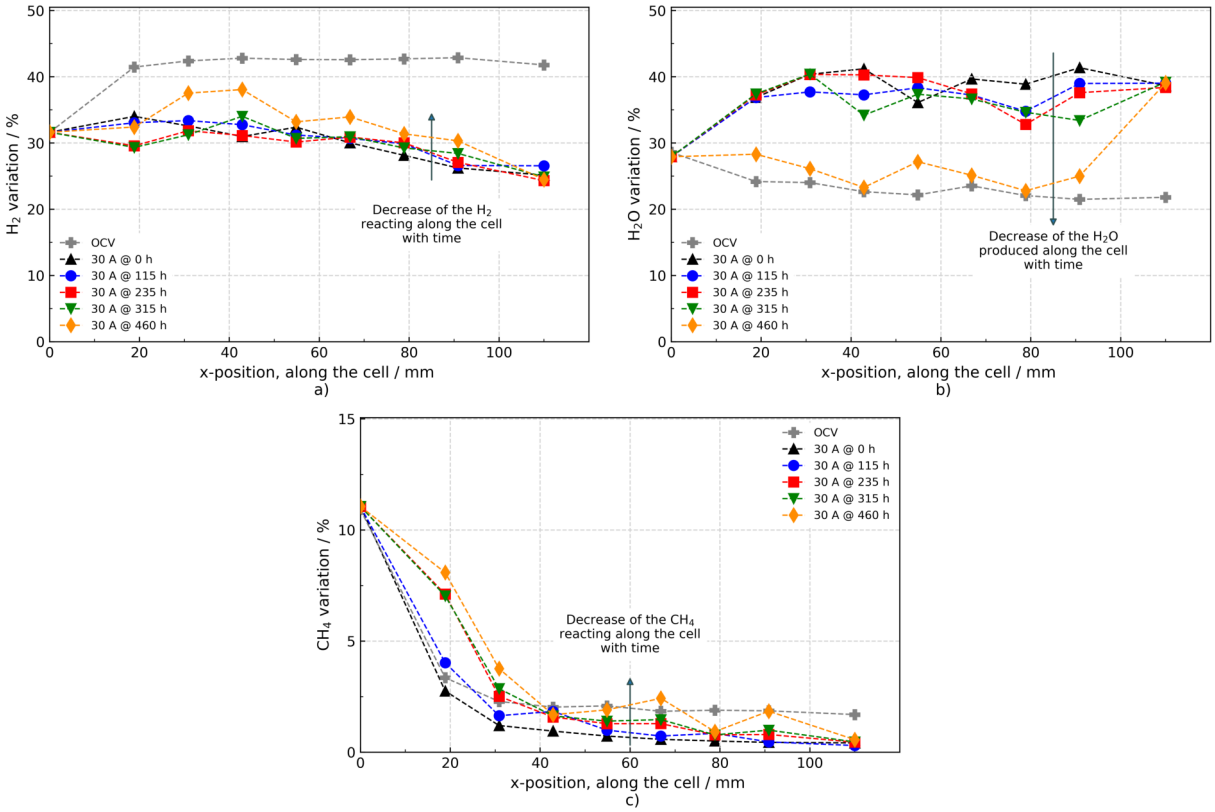

Figure 5.56. *Concentration temporal and spatial variation under load and at OCV; a) H_2 variation, b) H_2O variation, c) CH_4 variation.*

It can be observed, that the conversion of methane increases with the current at the beginning of the test, Fig. 5.56c, gray line vs. black line. However, a proper amount of H_2 is formed in both OCV and under load. Accordingly, it was found that most of the methane in the mixed gases was converted into H_2, CO, and CO_2. The conversion efficiency (calculated as in [6, 166]) was ∼99.9% during the first hours of operation. Similar conversion efficiencies, ∼98% at 720 °C, 1 bar and S/C=2, are reported by Papurello et al. [117]. The conversion efficiency gradually decreased with time, indicating a non-significant or gradual degradation in the catalytic activity of the anode. The same trend is observed for the H_2 composition owed to a possible reduction or blocking of the active sites. As the quantity of H_2 that reacts decreases with time, the quantity of H_2O that is produced also decreases over time.

The methane conversion efficiency may result very high because the flow rate used was low, because otherwise, when the flow rate of methane is higher respect to the surface area, some methane may pass through the gas channels without reforming, resulting in a lower conversion efficiency.

Therefore, in general the cell degradation did not seem to be related to the anode activity as to show an effect on the chemical and electrochemical fuel cell reactions, as it could be thought according to the rates of degradation. Mainly because the methane conversion efficiencies remained

highly acceptable even at the end of the test. Hence, the gas analysis suggests that the anode was not the main responsible of the observed degradation.

However, the actual reaction pathways and their correlation with the degradation phenomenon are still far from being well understood, and more research is needed to obtain a clearer picture.

5.3.4. Post-mortem analysis

Once established which electrode was responsible for the observed cell degradation, the cause was investigated. Therefore, a post-test SEM analysis was performed on the tested cell in order to identify degradation processes on the cell components. In addition, it was expected to verify the conclusions drawn based on the detailed impedance analysis regarding participation of both anode and cathode. Then, both cathode and anode were analyzed.

Although the major causes of anode degradation are attributed to the agglomeration of Ni particles [20] and carbon deposition [7, 8], in this case no significant changes developed in the anode microstructure after the test. That is, neither visible nickel agglomeration from the SEM analysis of the anode was observed, Fig. 5.57, nor carbon deposition. Hence, once again, these results confirm that the anode was not the main contribution to the cell degradation.

However, since the microstructure analysis of the anode was made on a random position, it could be that analyzing this element in the gas outlet region some microstructural changes may appear, due to the conditions to which this section of the cell was subjected to.

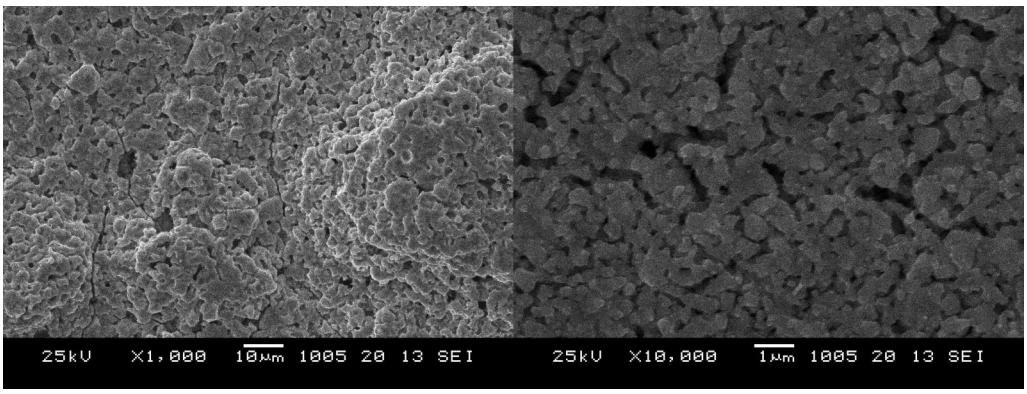

Figure 5.57. *SEM micrographs of the anode functional layer after the test. Note that no significant microstructural changes developed during the test.*

The EDS analysis to investigate chromium poisoning and strontium diffusion in the cathode side was conducted using a line scan or mapping over three different regions of the cathode surface: inlet, central and outlet region.

It was very tempting to interpret the fast performance degradation in the sense of a traditional catalysis poisoning effect. Nevertheless, as no significant change was observed in the OCV and a very small amount of chromium was detected by EDS, Fig. 5.58, which is within the error range [80,81,272], such phenomenon was discarded. Cathode delamination could not be associated to the perceived degradation either, because SEM results did not show evidence of this phenomenon, which, in fact, would have caused an increase mainly in the ohmic resistance.

Since the SEM analysis of the anode and cathode showed no clear evidence of Ni agglomeration, nor cathode delamination or poisoning, this suggested a more complex nature of the main degradation mechanism.

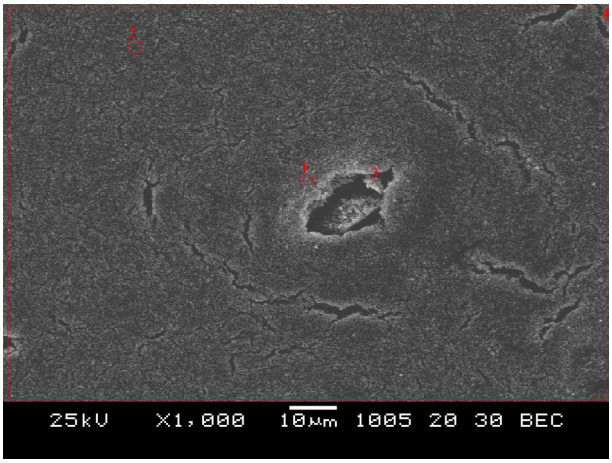

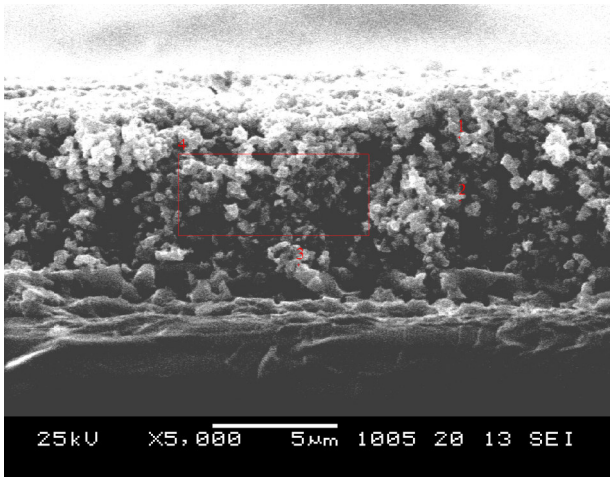

a)

Element	Weight %	Atomic %
Cr	**0.215**	**0.197**
O	20.416	60.667
Co	17.825	14.380
Sr	18.433	10.001
La	43.111	14.756

b)

Element	Weight %	Atomic %
Cr	**0.00**	**0.00**
O	39.967	79.536
Co	13.064	7.058
Sr	19.677	7.15
La	27.292	6.256

Figure 5.58. *EDS results after the test of Sr segregation/diffusion and chromium poisoning, corresponding to the central section of the a) LSC cathode surface, and b) cross-section, both corresponding to the region 4 indicated in the images.*

Referring to Fig. 5.59, it can be observed that mainly Strontium (Sr), which is initially only present in the cathode (top part), diffuses towards the other components of the cell (barrier, electrolyte and anode). Thus, it is deduced that this diffusion progression occurred during cell operation, even though there is no direct proof that this phenomenon did not occur during the sintering process. The initial electrochemical performance of the cell, along with the results from the stability test, support this inference. In addition, the strontium compositions (Sr/(Sr+La)) over the cathode surface were ∼0.312, ∼0.403 and ∼0.292, calculated at the inlet, central and outlet region, respec-

tively. As it can be seen, the Sr composition in the central region, Fig. 5.58a, maintained almost the stoichiometric composition of the LSC ($La_{0.6}Sr_{0.4}CoO_{3-\delta}$) cathode used for the present work. However, for the inlet and for the outlet region there is an obvious difference from the stoichiometric composition, suggesting the depletion or mobility of this element from the surface. Besides, making the corresponding computation for the cross-section in the central region, Fig. 5.58b, a Sr composition of ∼0.533 is obtained. This increase respect to its stoichiometric composition, and in a region below the surface, confirm the Sr mobility from the cathode towards the other components of the cell.

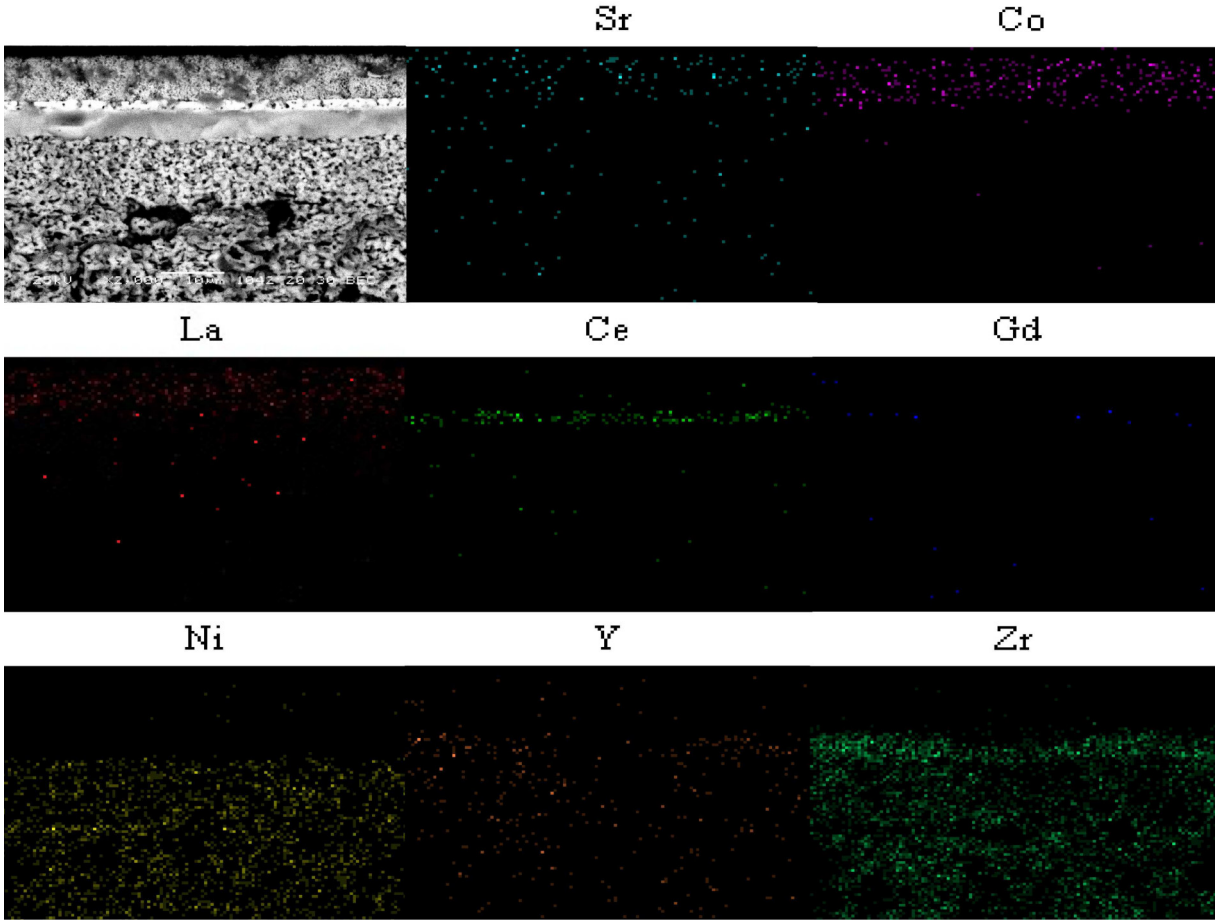

Figure 5.59. *EDS results after the long-term test corresponding to the outlet cross-section.*

Additionally, traces of Lanthanum, Ceria and Gadolinium can also be observed in the anode and electrolyte, while traces of Yttria are also observed in the cathode, suggesting a depletion of these elements in the corresponding cell component and leaving the cathode in direct contact with the anode, as well as enabling the reaction between these elements. It is well documented the ease of LSC cathodes, with or without GDC barrier layers [103], to form secondary phases such as strontium hydroxides [95] which are formed in presence of water; or zirconate phases, because of strontium mobility during the sintering process [100] or during the operation [103], resulting in any

case in fast performance degradation.

However, to avoid any doubts about whether the mobility occurred during the operation or during the fabrication of the cell, further stability tests are suggested in order to analyze the cell before and after the test.

Then, regarding the relatively low anode degradation, according to the DRT results, it could be explained by the cracks, visible to the naked eye, suggesting a thermomechanical mechanism that may have arisen from thermo-cycling or thermal stresses owing to the experienced blackouts and shutdown cycles in addition to the high partial pressure of water because of the backflow phenomenon at the outlet region, where cracks, Fig. 5.60, and rusty zones, Fig. 5.61, were observed. The fact that OCV remained constant despite the cracks could be explained by the region in which the cracks were formed, since they were in the corners of the cell at the outlet region, their contribution seemed not to be enough as to have a notable effect on the global OCV. This behavior of the cracks present in the anode layer, without effects on the OCV, has been also observed by Wang et al. [7], where it has been explained that the micro-cracks in the anode layer were the initial damage caused by partial redox cycling during electrochemical oxidation.

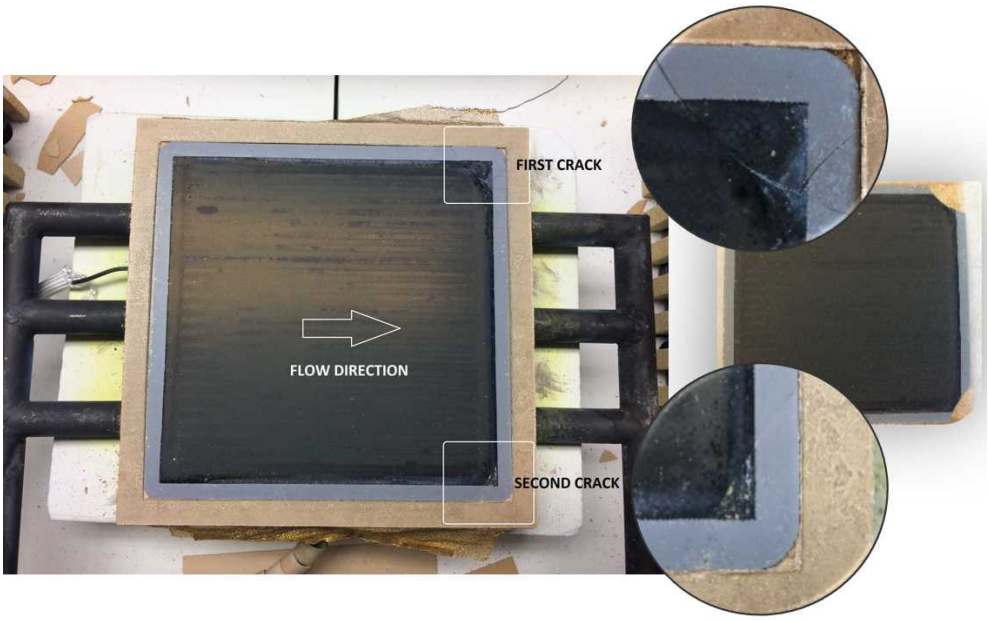

Figure 5.60. *Cell cracks at the outlet corners showing a particular pattern on the failure mode.*

Additionally, some changes in the microstructure could have occurred when the sudden blackouts took place.

In the literature, cracking of the anode and electrolyte is reported as the major draw-back for anode supported cells under redox cycling conditions. This phenomenon is associated with an

irreversible and serious volume change, leading to a decrement of the cell performance [60, 163], which is in accordance with the observed cracks in both corners of the downstream region.

A redox cycle can occur for several reasons such as: thermal cycle of a SOFC system during shut down and start-up operations, cutting-off gas supply in the case of an emergency, oxidation from steam in the SOFC system with steam reforming, leakage through a sealing, and high fuel dilution or local fuel starvation. It must be underlined that fuel starvation process is one of the most dangerous factors of anode degradation due to microstructure changes [175].

Therefore, cathode gas humidification could have taken place through the cracks and owed to the above-mentioned water accumulation, according to the gas analyses performed. The presence of water at the cathode is not from a fundamental point of view expected to have an influence on SOFC performance. However, several studies have shown that humidity can have a negative effect resulting in a severe voltage drop [65, 82, 86, 105, 174], as was experienced in this case.

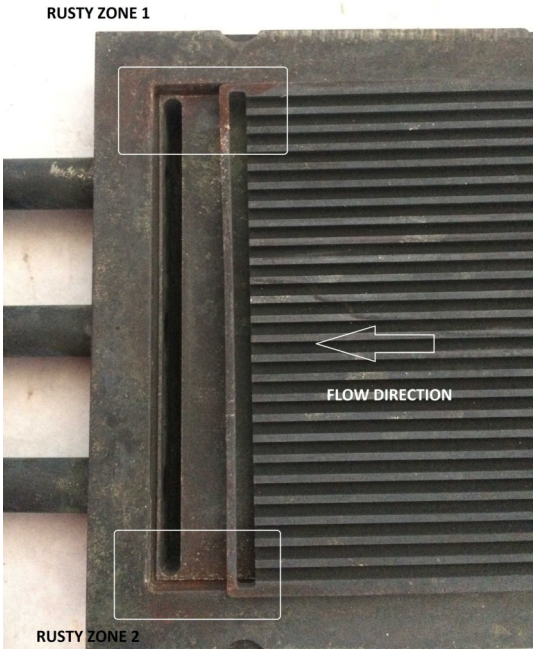

Figure 5.61. *Cathode gas diffusion plate (GDP) after the test showing the same two corresponding rusty zones to those with the zone failure/cracks.*

The above-mentioned phenomenon of water accumulation at the anode outlet region could have taken place since the electrochemical reaction sites are more active at the gas inlet region while partial pressure of water is mainly concentrated at the gas outlet region. Additionally, the extensive dilution of hydrocarbon fuel with water may lead to extremely high water concentrations in the downstream region of the fuel cell under discharge condition [52].

As high water content damages the Ni surface and catalytic activity by strong adsorption of

water, the product gas (water vapor) management is an important factor for long-term performance and stability, especially in the case of a large-area anode supported SOFC.

The presence of water at the cathode side has been proved with the observed rusty zones on the gas diffusion plates (GDPs), anode and cathode cases, Fig. 5.61; and confirmed with the presence of Magnesium and Potassium deposits found in the outlet region of the cathode, which concurred with the crack locations. This strongly indicates that the observed cracks have appeared during test and not during the cooling of the cell.

SEM/EDS analysis showed no clear evidence of any specific degradation phenomenon on the electrodes, apart from the mobility of certain elements. On the basis of the experimental results along with an extensive literature review, the cathode/electrolyte interface interactions are suspected to be the most probable cause of cathode degradation mechanism, as cathode humidification is known to make specific elements more mobile and catalyze certain processes, forming non-conductive nano-sized secondary phases and acting as a barrier to the ion conduction [65, 86, 124, 176]. Additionally, such degradation mechanism is reported to become more evident when testing in air at the cathode side instead of pure oxygen, being strongly dependent on the oxygen partial pressure as well [124], and perfectly correlating with the EIS findings. However, as direct identification of such phases requires more advanced techniques than just SEM/EDS [65, 124], a more appropriate analysis such as XRD and/or TEM is suggested for further tested cells.

The hypothesis was therefore to relate the degradation effect partly to cathode humidification because of high water partial pressure at the downstream region. In steam and under polarization, some phases in the materials may become more mobile due to decreased viscosity and enhanced wettability. They may change their shape from blocks into thin films affecting a larger area of the interface and could segregate around the three-phase boundary points, thereby decreasing the performance [163], and leading to irreversible cell voltage drop [106].

5.3.5. Effect of the testing procedure on the cell performance

In order to discuss the effect of the test procedure and geometry on the performance of this kind of cells, a comparison with a previous published work using the same commercial cells and different test procedure is carried out.

As already mentioned, the used testing procedure in this stability test has been specified by the cells manufacturer. However, in previous tested cells [74] a different test procedure was followed. Particularly step 1 corresponding to the heating step in which the cell was only heated to 650 °C instead of 700 °C (as the manufacturer suggested). Besides, the first activation step (pure H_2 supplied at 500 Nml/min) was omitted, and consequently the cooling from 700 °C to 650 °C as well.

As a result of the test procedure described above, the internal and polarization resistances were greater for such cell. Hence, it has been observed and even proved [161] that any differences in test procedure, such as the reducing temperature and time, do have an effect on the value of the internal resistance.

Regarding the anode activity (followed through the gas analyses), it was improved when following the suggested procedure. Actually, comparing the methane conversion efficiencies in OCV condition, from this study the methane was almost totally converted in the first 4 cm of the cell length, while for the cell reduced at a lower temperature, it takes almost twice that length (i.e. $\sim$8 cm) to reach the same methane conversion efficiency. The same trend is observed when comparing the other fuel compounds. Therefore, an improvement in the chemical and catalytic activity of the anode has been observed when increasing the reduction temperature. Therefore, a difference in the results obtained will be present when differences in the test procedure exist.

Concerning thermal differences, comparing the temperature distribution over the anode (contour plots) in OCV condition, i.e. under the effect of only internal reforming, for the present analysis a temperature distribution that ranges from $\sim$646 °C to 652 °C was obtained, resulting in a very uniform temperature distribution along and across the cell, with a temperature difference of only $\sim$6 °C (as already mentioned in the thermal analysis), while for the cell reduced at a lower temperature, a higher temperature difference was obtained ($\sim$11 °C), ranging from 651 °C to 662 °C. Even though the differences are not very large, they are still significant.

Regarding the cell geometry, and although direct internal reforming promotes intrinsic thermal-coupling between endothermic and exothermic reactions within the cell, it is expected that increasing the length of the cell causes further increase in the temperature differences, along and across the cell (hot spots), along with an uneven fuel gas distribution. The dependence of temperature distribution on the cell geometry has been already indicated [168]. In addition, a higher water content is expected for larger-area cells, adding more complexity to the system and making more challenging the water management, as has been already discussed in this analysis. Therefore, special attention should be given to this issue.

Chapter 6

CONCLUSIONS AND RECOMMENDATIONS FOR FUTURE WORK

6.1. Conclusions

In this work, a combined experimental and numerical investigation towards methane reforming in commercial anode-supported single SOFCs operating at intermediate temperatures has been presented. Steam methane reforming has been investigated from the perspective of methane conversion, hydrogen yield, power delivered, and cell stability. Three different ratios between methane, steam, carbon dioxide, carbon monoxide and hydrogen were used in order to simulate different grades of methane internal reforming, namely, LIR, IIR and CIR.

The experimental work consisted in two main parts: the experimental campaign itself, where the cell was evaluated under the three different compositions; and the endurance performance test, where the cell stability and degradation phenomena were evaluated under IIR composition. In both parts of the experimental work, the cell was extensively characterized by means of EIS and DRT, I-V curves and simultaneous gas and temperature analyses in OCV and under loading conditions.

Prior carrying out the experimental campaign, one of the main achievements during this experimental work has been the validation of the novel and very particular in-house built multisampling set-up. The validation has been achieved after several improvements to the test bench. It consisted in testing a single cell at 650 °C and 700 °C in pure hydrogen (CUTEC composition). Then, the corresponding polarization curves were compared with those obtained by CUTEC Lab under the same operating conditions, where these later were considered as the reference. At 650 °C the re-

sults showed an OCV deviation of ca. 38 mV below the reference, representing a difference of only 3.1%, and an average voltage difference of 10.7 mV along the I-V curve. Correspondingly, at 700 °C it was obtained an OCV deviation of ca. 28.5 mV, also below the reference, representing a difference of 2.4%, and an average voltage difference of 12.5 mV along the curve. Although an OCV mismatch was still present, very similar polarization curves were obtained, which to a greater extent validated the multisampling set-up.

Then, from the experimental campaign, examining the power densities, I-V curves and impedance data, it was found that the initial performance of the cell, mainly at low current densities, was very similar regardless the fuel employed. Nonetheless, in general, it was obtained that the voltage dropped more slowly with increasing current density under IIR composition. Hence, the composition that showed the best electrochemical performance in terms of power delivered, although its polarization resistance was not the lowest one, corresponds to the IIR, followed by the LIR and CIR compositions. By comparing their performance at the same FU (43%), it was obtained a respective difference in the total yielded power of 12.2% and 3.9% when operating with LIR and CIR, below the total power delivered with IIR composition at 650 °C. At 700 °C, these differences were 13.1% with LIR and 5.1% with CIR, in both cases below the power delivered under IIR. Since IIR composition represents an anode off-gas recirculation mixture, the obtained results from the electrochemical analysis are found very promising in terms of technical applications, where the main drivers for anode recirculation are the increased fuel efficiency and the independence of the external water supply for the fuel pre-reforming process.

Therefore, in terms of fuel composition, results indicated that adding more methane to the fuel mixture and as long as it contains hydrogen, the resulting cell performance improves even more than that obtained under an inlet mixture with a higher hydrogen content. This fact is attributed to the huge hydrogen production and availability through the promotion of the reforming and shifting reactions. Meanwhile, employing only wet methane or high methane containing atmospheres, like the CIR case, can lower the cell performance by the fact that increasing the concentration of methane implies increasing also the quantity of steam in order to avoid carbon deposition. Consequently, operating under high water contents is a big deal since it makes difficult the analysis and the cell operation, and in the worst of the cases, being a rate-determining step of the overall processes owed to water clogging effects in the system.

On the other hand, processes identification was accomplished using the DRT method applied to EIS measurements, allowing the recognition of the single physicochemical processes, their contribution to the overall performances, and the evaluation of degradation effects. From the variation of a single operating parameter at a time, the observed response of DRT peaks was ascribed to different electrochemical processes occurring at the anode or at the cathode side.

Up to six different processes were identified. The two high-frequency processes $P_{1,an}$ and $P_{2,an}$ were both ascribed to the electrochemical oxidation process occurring at the anode side owed to their pronounced dependency on the operating temperature and slight modification with the fuel composition. Particularly, $P_{1,an}$ has been related to the ionic transport phenomenon, while the process $P_{2,an}$ has been ascribed to the charge transfer process in the oxidation reaction. On the other hand, due to its pronounced thermal activation and relatively low dependence on the variation of the fuel composition observed at both operating temperatures, the high-frequency process of the cathode, $P_{3,cat}$, was associated to the oxygen surface exchange kinetics of LSC as well as the diffusivity of oxygen ions within the LSC bulk.

Regardless the cell degradation during the experimental campaign, processes $P_{4,an}$ and $P_{5,an}$ showed a negligible dependency on the operating temperature and exhibited continuous shifts and amplitude changes for the variation of the fuel gas composition. These two peaks identified at lower frequencies have been associated to a single mass transfer processes caused by a gas-phase diffusion through the open porosity of the anode substrate. In fact, in the case of CIR the process $P_{5,an}$ resulted convoluted with the process $P_{4,an}$, showing that in effect, it is a single process.

And finally, the sixth process, P_{ref}, scarcely reported in literature, was identified at frequencies below 0.1 Hz. Due to its clear occurrence under reformate operation, it has been associated to the reformate process. The significant and clear dependency of the reforming process, P_{ref}, on the reformate gas mixture and temperature, mainly reflected in a frequency shift, allowed to ascribe this physicochemical process to both the steam methane reforming and the WGS reactions. The impact of P_{ref} on the overall polarization resistance of the cell was less significant at higher temperatures and became more relevant for lower temperatures. Additionally, it resulted interesting how P_{ref} was not visible under LIR composition, which was attributed to the very low internal reforming activity because of the relatively low methane content in the fuel mixture.

Furthermore, the DRT method showed its feasibility as a tool for the analysis of degradation. Accordingly, concerning the above-mentioned cell degradation, it was suggested from the DRT analysis that mainly the anode was the electrode responsible of the cell degradation since the phenomena that worsen when increasing the cell temperature were identified at the characteristic frequencies where anode processes take place.

Nonetheless, although DRT is playing an important role in AC impedance data interpretation, a single EIS plot can have several DRT interpretations depending on the regularization parameter selected, whose selection is, in turn, very subjective. Hence, the uniqueness of the data treatment becomes a problem, and even more when larger cells under complex mixtures with high water contents and a strong coupling of different phenomena are analyzed. Actually, even in button cells, the physicochemical phenomena of DRT are not completely clear. Thus, in order to clarify and to

achieve a better and deeper comprehension of the individual physicochemical processes, complementary analysis such as complex non-linear least squares fitting or an analysis of differences in impedance spectra can be used.

Regarding the gas composition and temperature analyses, the implementation of novel analysis tools was specifically carried out to study the chemical and thermal gradients along the anode caused by the evolution of the multiple reactions at the different operating conditions. The novel multisampling set-up proved that, in spite of its remaining issues, reliable characterizations of single SOFCs *in-operando* are possible. In fact, with only 11 sampling points throughout the anode, it allowed for a reasonable chemical and thermal mapping of the anode under different operating conditions, highlighting the evolution, competition and impact of the different reactions with a good spatial resolution.

That is, by means of the local sampling of both gas concentrations and temperature it was possible to follow and correlate local changes with the possible reactions occurring. Accordingly, combined experimental and theoretical results indicated that for all the three studied reformate gas mixtures, depending on the current drawn, three main reactions occur: the electrochemical oxidation of hydrogen, the steam methane reforming reaction, and either the water-gas shift or the reverse water gas-shift reaction.

In agreement with the DRT results, for LIR it was obtained that the species variation in OCV respect to the inlet composition was not significant because of the low reforming activity. However, the slight changes allowed to determine that a weak SMR and r-WGSR were taking place in OCV condition. Meanwhile at 15 A and 30 A, it was determined that a bit stronger SMR and WGS reactions along with a dominant oxidation reaction of hydrogen were occurring.

For IIR composition, the local changes in the species concentrations were more evident owed to a higher methane and carbon dioxide content. In fact, most changes in the species compositions occurred in the first 4 cm of the cell length, which was certainly attributed to the dominance of the SMR phenomenon at the inlet region of the cell under the three loading conditions. At 15 A and 30 A, once methane was depleted, the effect of the electrochemical reaction became dominant, exhibiting a maximum close to the point where methane was depleted. Furthermore, in OCV condition it was clearly indicated that a stronger r-WGS reaction, compared to that under LIR in OCV, was taking place. Meanwhile, owed to the occurrence of the WGS reaction under load and its increasingly noticeable dominance when increasing the electrical current, it has been indicated that the WGS reaction plays an important role mainly under high current densities. Furthermore, from this composition analysis, it was clearly observed that hydrogen was produced steadily through SMR in the Ni-YSZ anodes, even at intermediate temperatures, resulting in an almost total methane conversion over the whole cell.

Regarding CIR gas composition analyses, the fast SMR reaction resulted in an steep increase of the hydrogen concentration near to the inlet of the cell. Once that most methane was reformed, along the first 4 centimeters of the cell length, the produced hydrogen was then gradually consumed along the length of the cell by the oxidation reaction (when was the case). Simultaneously, the WGS reaction, under the three loading conditions, became evident from the first centimeters of the cell length until the outlet. Thus, in this case, the WGS reaction took place even in OCV condition, unlike under LIR and IIR, where the r-WGS reaction proceeded at OCV. An observed important advantage of DIR fueling with methane-reach fuels is the low carbon dioxide content in the exhaust gas. However, it has been observed that excess addition of steam, necessary to avoid carbon deposition, dilutes the fuel and significantly reduces the cell performance and cell stability. Thus, it has been highlighted the lack of SOFCs stability under DIR of wet methane when high current densities are drawn.

On the other hand, the obtained results from the three studied cases under loading conditions confirm that in the case of reformate fuels, hydrogen is preferred for the electrochemical oxidation, and thus carbon monoxide is only involved in the WGS, producing more hydrogen to be further oxidized. Nonetheless, in order to clearly prove this statement, further and more specific experimental testing is necessary.

Furthermore, it has been discussed the validity of the equilibrium approach for the present experimental analysis. From a comparison of the measured outlet species with the calculated ones by means of CHEMCAD, it was obtained, in general, a good agreement between the different species, mainly under OCV condition. This issue supports the fact that the physicochemical processes here claimed to occur, i.e. the reactions occurring in the cell, are not far from the equilibrium approach.

From the thermal analysis, it was obtained in all the cases very slight temperature gradients all over the anode. In fact, the cell temperature differences were much lower than those usually reported for simulated direct internal reforming under similar conditions. It was also possible to correlate the effect of the different identified reactions, from the gas analyses, with the final temperature distribution. However, in some cases it was found that the temperature decreased from the inlet to the outlet under loading conditions. For this behavior two possible explanations were given: an insufficient insulation that caused heat losses directly to the environment, and a non-uniform heating of the system caused by a problem with a resistance that was broken and then repaired seeming to heat more than the other ones. As observed, both of them suggested an uneven or non-uniform heating of the enclosure.

Nevertheless, owed to the slight temperature differences obtained in all the cases, DIR can be therefore considered as an advantage due to the cooling effect caused by the endothermic reaction. It has been observed experimentally that far from harming, DIR helps to regulate the temperature

of the cell avoiding the widely reported hot spots and their consequent thermal stresses. In other words, it has been observed that the direct internal reforming phenomenon far from creating hot spots, it helps to regulate or compensate the temperature rise caused by the cell irreversibilities and the electrochemical and WGS reactions. Consequently, at higher currents, under LIR composition it has been observed a major temperature difference because of the low reforming activity and owed to the dominance of the oxidation reaction. In contrast, under the other two cases, being methane-rich fuels, the temperature difference throughout the anode was much lower. These findings have suggested that the problem of large temperature gradients is almost avoided under direct internal reforming.

Regarding modeling, a comprehensive zero-dimensional model of the tested samples, incorporating thermodynamic equilibrium and some experimental parameters, has been validated by confronting the simulated polarization curves with the experimental ones. Thermodynamic equilibrium modeling was employed to determine the concentrations of each gas species in the equilibrium state. This model has demonstrated to be a compelling tool to characterize the performance of the cells while establishing the bases to follow and analyze the effects of potential degradation phenomena and predict the electrical output of the cell under pre-determined operating conditions. This combined experimental and numerical study also elucidated the thermochemical phenomena for a better comprehension of the most important reaction processes that determine the performance of the cell.

Additionally, a 2D model, based on finite differences and combined with some experimental results, has been also implemented for a mapping of the current density distribution over the anode. Therefore, in this way, modeling allowed to determine some cell characteristics, such as the individual cell overpotentials and the local current density, that will not be possible through only experimental testing.

The modeling and experimental results, both, showed that at 650 °C, above 90% of methane conversion is achieved in most of the cases. Furthermore, the experimental data and modeling results are also consistent in the equilibrium approach and the reactions and physicochemical phenomena that occur in the cell under the analyzed conditions.

It was also obtained that the cell polarization resistance, mainly caused by activation in both electrodes, is the major limiting factor of single cell performance, especially at low and intermediate temperature.

Thus, a systematic synergistic approach between the experimental measurements, the use of novel analysis tools and techniques –as the deconvolution of impedance spectra by means of the DRT method and *in-operando* gas and temperature analyses by means of a validated in-house built spot-sampling set-up –and modeling theory has proved to be instrumental for the estimation of parameters describing the electrochemical properties of planar SOFCs.

On the other hand, since in general, under IIR composition it has been achieved the best trade-off in terms of hydrogen production and electrical power generation, yielding the highest electrochemical performance from the three studied gas mixtures, the endurance performance investigation towards methane reforming stability has been investigated under this composition.

Accordingly, more than 450 h of operation at 650 °C were reached, under constant flow and current conditions. During cell operation, the test bench failed to operate as intended. However, the performance of the tested cell was, in general, satisfactory since the large-area SOFC showed stable operation towards several shut down situations, even with the cell in short-circuit.

During the first hours of operation, the measured outlet gas compositions were very close to the calculated compositions in equilibrium. Despite a decline in the voltage, the activity of the anode and temperature changes seemed to be almost the same, discarding the anode as the main contribution to the cell degradation, and suggesting that internal reforming does not affect the long-term stability of this kind of cells.

Although in effect, the single cell performed certainly poorly with an unstable voltage coupled to a visible performance decay, the innovative characterization techniques have been assessed under constant operation. The use of these in-situ and in-operando techniques have helped to understand the origin of the experienced decline in the cell performance and coupled to complementary techniques they have demonstrated that several degradation mechanisms occur at the same time or at different stages in the lifetime of the electrochemical device. However, since the electrochemical analysis showed that the main contribution was the cathode, and the set-up is equipped to follow the phenomena on the anode side, it was not possible to certainly correlate and follow the cathode degradation phenomena.

From the post-mortem analysis, the diffusion of strontium and other elements has been observed, mainly from the cathode towards the other components of the cell, in addition to the presence of water at the cathode side that has been proved and confirmed with the existence of some deposits of magnesium and potassium found in the outlet region of the cathode, along with the observed rusty zones on the gas diffusion plates and on the anode and cathode cases, which concurred with the crack locations. Thus, based on all the experimental results along with an extensive literature review, it was possible to conclude that the main source of degradation was the presence of water at the cathode side and that the cracks were the less prominent effects on the cell, corresponding with the observed changes in the impedance spectra. Hence, owing to the proven cathode humidification, it is suspected the formation of some secondary isolating phases that arose from the several incidents of the real mode operation of large-area solid oxide fuel cells, greatly increasing the overall cell resistance, and causing low cell performance and durability. It cannot be excluded, and it is certainly probable, that other than the one discussed, degradation processes

occur in the cathode and anode simultaneously. These could include effects such as local changes of the microstructure or, as previously said, the formation of foreign phases.

This experimental work can be considered as one of the first steps towards understanding the interplay and evolution between various physicochemical phenomena occurring in relatively large-area cells, and although these *in-situ* and *in-operando* techniques can help to clarify the discrepancy found in the literature regarding the temperature and composition studies, these techniques are still at its early stage, and several testing and technical challenges remain, especially concerning the design. Therefore, some modeling investigations on the system design and thermo-fluids, as well as more experimental testing need to be carried out.

6.2. Future work and recommendations

From the validation of the multisampling set-up it was observed that an OCV mismatch with the reference was still present. Thus, in order to decrease this still existing OCV mismatch, it would be interesting to implement a controlled mechanical load in the system to reduce as much as possible the actual mismatch that may be caused by existing gaps in the assembly owed to a non-uniform pressure/contact over the cell components.

On the other hand, from the experimental results, it has been shown that higher water contents are expected for large-area cells, making more challenging the water management and adding more complexity to systems that allow for in-situ and *in-operando* analyses. Therefore, special attention should be given to this issue.

Accordingly, from the gas analysis in the main experimental campaign, it was discussed the negative effect on the GC quantification of some species caused by water condensation in the system lines. The presented potential causes of the experienced water condensation that affected the quantification of some species were: the high-water content in the tested gas mixtures, the relatively low temperature of the GC oven, the non-uniform heating and insulation of the sampling lines as well as the capillary diameter of these latter. Therefore, it is still necessary to improve the heating and insulation of the system, as well as to seek an adequate method for the GC system. In the latter case, seeking the adequate operative conditions for the GC system is particularly important in order to avoid the problem of water condensation but at the same time preventing possible damages to the adapted column. In this sense, it is strongly suggested to modify the method keeping the GC oven temperature above 80 °C. Alternatively, the split ratio could be increased, or the injection volume decreased. However, any of these options implies a substantial modification of the method. Another option could be removing the steam from the gas mixtures before entering to the GC system. However, it is clear that the feature that makes this multisampling set-up a particular system in the

world is the possibility of quantifying all the species directly from *in-operando* conditions.

From the endurance performance analysis, it was suspected on the formation of some secondary isolating phases, that might have arisen from the several incidents during the cell operation, as the main source of degradation which caused low cell performance and durability. However, since direct identification of such phases requires more advanced techniques than those used in the present study, a more appropriate analysis, such as TEM, is suggested. Additionally, in order to certainly follow micro structural changes, it is suggested to cover the entire length of the cathode and anode and perform this kind of analysis before and after testing.

Finally, the synergistic approach presented in this work allowed to obtain qualitative and quantitative data on individual processes as well as on the chemical and electrochemical reactions that occur throughout the electrode surface under different operating conditions. This work has been therefore the foundation of on-going studies where the assessed tools will be now used to study high-temperature SOFCs operated in reversible mode, i.e. solid oxide electrolysis cells (SOECs), in-operando conditions, which is particularly important in view of the growing needs of energy storage.

Appendices

Appendix A

MODELS DESCRIPTION

A.1. Electrochemical zero-dimensional model

In order to investigate the performance of commercial anode-supported cells under internal reforming, a simple 0D model has been developed. This model, implemented in EES, simulates the fuel cell steady-state operation and, validated with experimental data, it has been used to compare the I-V characteristics of the cell, electrical power and cell efficiency. Additionally, the 0D model allows to determine the composition of the exhaust gas by applying simultaneously the laws of mass conservation and chemical equilibrium.

The fuel cell configuration under study is based on a planar design with air and fuel gas streams in a co-flow configuration. The geometric and performance related data of the SOFC are based on the design of Elcogen's commercial single cells.

Owed to the complexity of the physical and chemical processes occurring in SOFCs, for the development of the present model the following main assumptions have been used:

1. Steady state operation.
2. H_2 electro-oxidation responsible for the electrical flow.
3. CO only participates in the water-gas shift reaction and CH_4 in the steam methane reforming reaction.
4. The flowing gases behave as ideal gases at the temperature and pressure of operation of the SOFC in both the fuel and air channels.
5. The temperature was assumed to be uniform, thus the model was assumed to be isothermal.
6. The pressure drop in the SOFC was neglected.
7. Chemical equilibrium for the reforming and shifting reactions.

8. The cathode stream was assumed to be composed of 21% oxygen and 79% nitrogen.
9. Anode inlet stream is composed of three different compositions, as described in section 4.1, consisting of CH_4, CO, CO_2, H_2, and H_2O.
10. The current density and operating temperature are considered as input values.

Accordingly, in this work, it is assumed that the electrochemical oxidation of the CO does not occur, i.e, SOFC only oxidizes H_2, whereas the CO in the fuel stream participates in the electrical production through the conversion to H_2 in the shift reaction and then through the H_2 electrochemical reaction. This assumption, dealing with the CO consumption within the cell, is largely adopted in papers about the numerical simulation of the SOFC electrochemical reactions [273, 274], since it is reported that the reaction rate of the electrochemical oxidation of carbon monoxide is 2-5 times slower than that of hydrogen, while the rapid water-gas shift reaction becomes the dominant reaction.

A.1.1. Internal reforming model

The considered reactions occurring inside the cell are:

$$\text{Reforming :} \quad \overset{x}{\text{CH}_4} + \text{H}_2\text{O} \longrightarrow \text{CO} + 3\,\text{H}_2 \tag{A.1a}$$

$$\text{Shifting :} \quad \overset{y}{\text{CO}} + \text{H}_2\text{O} \longrightarrow \text{CO}_2 + \text{H}_2 \tag{A.1b}$$

$$\text{Electrochemical :} \quad \overset{z}{\text{H}_2} + \text{O}^{2-} \longrightarrow \text{H}_2\text{O} + 2\,\text{e}^- \tag{A.1c}$$

The equilibrium constants in the reforming and shifting processes are temperature dependent and can be expressed by the following polynomial equation [192, 275]:

$$log\left(K_{eq,p}\right) = AT^4 + BT^3 + CT^2 + DT + E \tag{A.2}$$

where the corresponding constant values A, B, C, D and E are [192, 275, 276]:

	Reforming	Shifting
A	$-2.6312x10^{-11}$	$5.47x10^{-12}$
B	$1.2406x10^{-7}$	$-2.574x10^{-8}$
C	$2.2523x10^{-4}$	$4.6374x10^{-5}$
D	$1.95027x10^{-1}$	$-3.91500x10^{-2}$
E	-66.139488	13.209723

Assuming that the reforming and shifting reactions are in equilibrium, the equilibrium constants can also be calculated from the partial pressure of the reactants and products at the exit by:

$$K_{eq,SMR} = \frac{p_{H_2}^3 p_{CO}}{p_{CH_4} p_{H_2O}} \tag{A.3}$$

$$K_{eq,WGS} = \frac{p_{CO_2} p_{H_2}}{p_{CO} p_{H_2O}} \tag{A.4}$$

If x, y and z from Eq. (A.1)a to Eq. (A.1)c are the respective molar rates of CH_4, CO and H_2 participating in the reactions, then a molar balance at the exit of the fuel electrode is stated as:

$$CH_4^e = CH_4^i - x \tag{A.5a}$$
$$CO^e = CO^i + x - y \tag{A.5b}$$
$$CO_2^e = CO_2^i + y \tag{A.5c}$$
$$H_2^e = H_2^i + 3x + y - z \tag{A.5d}$$
$$H_2O^e = H_2O^i - x - y + z \tag{A.5e}$$
$$NTM^e = NTM^i + 2x \tag{A.5f}$$

where superscript i indicates the inlet and e indicates the exit. NTM is the total molar rate, and the chemical symbols represent the molar rates of the corresponding species.

Accordingly, at the exit of the anode, the total molar rate is the sum of the terms of the right-hand side of the Eq. (A.5). Thus, the equilibrium conditions can now written as:

$$K_{eq,SMR} = \frac{\left(\frac{CO^i + x - y}{NTM^i + 2x}\right)\left(\frac{H_2^i + 3x + y - z}{NTM^i + 2x}\right)^3 \left(\frac{p}{p_{ref}}\right)^2}{\left(\frac{CH_4^i - x}{NTM^i + 2x}\right)\left(\frac{H_2O^i - x - y + z}{NTM^i + 2x}\right)} \tag{A.6}$$

$$K_{eq,WGS} = \frac{\left(\frac{H_2^i + 3x + y - z}{NTM^i + 2x}\right)\left(\frac{CO_2^i + y}{NTM^i + 2x}\right)}{\left(\frac{CO^i + x - y}{NTM^i + 2x}\right)\left(\frac{H_2O^i - x - y + z}{NTM^i + 2x}\right)} \tag{A.7}$$

$$z = i/n_e F \tag{A.8}$$

As the temperature is known, the equilibrium constants, $K_{eq,SMR}$ and $K_{eq,WGS}$ can be calculated from Eq. (A.2), and unknowns x, y and z are determined by solving simultaneously Eqs. (A.6)-(A.8) at a given electrical current and flow inlet conditions. The equation system (basically Eq. (A.6) and Eq. (A.7)) is solved using a classical Newton-Raphson method.

Thus, the composition of the exhaust gas can be calculated by applying simultaneously the laws of conservation of mass and the laws of chemical equilibrium at the exit of the cell.

A.1.2. Electrochemical model

The voltage evaluation has been carried out based on the knowledge of the cell open-circuit potential. Accordingly, for a H_2-O_2 reacting SOFC with known partial pressures of reactants and products, the reversible cell potential can be calculated from the Nernst equation, Eq. (2.12).

The Nernst potential is reduced due to the following irreversibilities (already described in section 2.2.3): 1) ohmic overpotential, η_{ohm}; 2) activation overpotential, η_{act}; and 3) concentration overpotential, η_{conc}. Thus, the output voltage of the SOFC is expressed according to Eq. (2.17).

A.1.2.1. Ohmic losses

The overall ohmic overpotential, η_{ohm}, has been evaluated using the Ohm's law, Eq. (2.13).

From Eq. (2.13), R_{ohm} is the ASR, which includes contribution of the anode, cathode, GDC interlayer and electrolyte. However, as the model should be applicable over a wide temperature range, the temperature dependence of $R_{ohm}(T)$ must be precisely predicted. For thermally activated charge transport mechanisms, such as the oxygen ion conduction in YSZ, in general the following

relationship, derived from the Arrhenius equation, holds [42].

$$R_{ohm}(T) = \frac{T}{B_{ohm}} \exp\left(\frac{E_{act,ohm}}{RT}\right) \tag{A.9}$$

T denotes the absolute temperature in Kelvin, $E_{act,ohm}$ the activation energy in kJ/mol, and B_{ohm} is a material-specific constant in $[SK/m^2]$. The unknown parameters B_{ohm} and $E_{act,ohm}$ are the first two to be determined from the knowledge of the ASR or R_{ohm} at two different temperatures. Accordingly, the ASR has been determined from open-circuit impedance measurements carried out at 650 °C and 700 °C.

A.1.2.2. Activation losses

The activation overpotential is calculated separately for anode and cathode, in both cases using the Butler-Volmer equation, Eq. (2.14).

In this equation, $j_{0,el}$ is the exchange current density for anode or cathode, n_e the number of exchanged electrons, α_{el} the apparent charge transfer coefficient, and $\eta_{act,el}$ the activation overpotential of the corresponding electrode. The unknown parameters required for modelling ($j_{0,el}$ and α_{el}) are taken from [42], where they have been determined experimentally for a similar cell.

Partial pressure dependency of the exchange current densities $j_{0,an}$ and $j_{0,cat}$ of anode and cathode, respectively, is frequently described by the semi-empirical Eq. (A.10) and Eq. (A.11). They contain a power law relation for the partial pressure dependency as well as an Arrhenius-type temperature dependency.

$$j_{0,an} = i_{an} \left(\frac{p_{\mathrm{H_2},an}}{p}\right)^{\gamma_{\mathrm{H_2}}} \left(\frac{p_{\mathrm{H_2O},an}}{p}\right)^{\gamma_{\mathrm{H_2O}}} \exp\left(-\frac{E_{act,an}}{RT}\right) \tag{A.10}$$

$$j_{0,cat} = i_{cat} \left(\frac{p_{\mathrm{O_2},cat}}{p}\right)^{\gamma_{\mathrm{O_2}}} \exp\left(-\frac{E_{act,cat}}{RT}\right) \tag{A.11}$$

The pre-exponential factors i_{an} and i_{cat}, the exponents $\gamma_{\mathrm{H_2}}$, $\gamma_{\mathrm{H_2O}}$, and $\gamma_{\mathrm{O_2}}$, as well as the activation energies $E_{act,an}$ and $E_{act,cat}$, are also taken from [42], where all of them have been experimentally determined for an ASC.

A.1.2.3. Concentration losses

Regarding mass transport, Fick's model is the simplest diffusion model used in porous media [200]. Therefore, concentration overpotentials were calculated taking into account Fick's law and introducing binary and Fuller diffusion models. Accordingly, calculations of the concentration overpotentials for anode and cathode are based on the following equations [42, 191, 244, 275]:

$$\eta_{conc,an} = \frac{RT}{2F} \ln \left(\frac{1 + \frac{j_{cell}}{j_{L,\mathrm{H_2O}}}}{1 - \frac{j_{cell}}{j_{L,\mathrm{H_2}}}} \right) \tag{A.12}$$

$$\eta_{conc,cat} = \frac{RT}{4F} \ln \left(\frac{1}{1 - \frac{j_{cell}}{j_{L,\mathrm{O_2}}}} \right) \tag{A.13}$$

From the above two expressions, $j_{L,i}$ is the limiting current density for diffusion of gas species i through the corresponding electrode. Calculation of limiting current density in the anode is given by [42, 191, 244]:

$$j_{L,i} = \frac{2FD_i^{eff}}{RTL_{an}} p_{i,an} \tag{A.14}$$

whereas at the cathode it is calculated as:

$$j_{L,i} = \frac{4FD_i^{eff}}{RTL_{cat}(1 - p_{i,cat}/p)} p_{i,cat} \tag{A.15}$$

When replacing the corresponding terms of Eq. (A.14) and Eq. (A.15) into Eq. (A.12) and Eq. (A.13), it can be observed that results the same already presented Eq. (2.15) and Eq. (2.16).

From the above expressions, D_i^{eff} in Fick's law is the effective diffusion coefficient of species i, which takes into account the composition of the gas mixture. Since in the studied gas mixtures there are several components, thus the effective diffusion coefficient D_i^{eff} for a component i in the mixture depends of the molecular interaction of species i with the other components in the mixture as stated by Fairbanks [277]. Therefore, the calculation of D_i^{eff} can be carried out following Eq. (A.16) [277, 278], where $D_{i,j}$ is the binary diffusion coefficient of species i, ε and τ are the porosity and tortuosity of the corresponding porous electrode, respectively.

$$D_i^{eff} = \frac{\varepsilon_{el}}{\tau_{el}^2} \cdot \frac{1 - y_i}{\sum_{i,j \neq i} \frac{y_j}{D_{ij}^{eff}}} \tag{A.16}$$

Based on the kinetic gas theory, the binary diffusion coefficients $D_{i,j}$ were calculated by the Fuller correlation, Eq. (A.17) [279, 280]:

$$D_{ij} = \frac{0.001 T^{1.75} (1/M_i + 1/M_j)^{1/2}}{\left(\nu_i^{1/3} + \nu_j^{1/3}\right)^2 p} \tag{A.17}$$

where ν_i are the specific atom diffussion volumes for the different species in the mixture, taken also from [279–281].

A.1.2.4. Electrical power and efficiency

The cell electrical power has been calculated as the product of cell current intensity by the cell electrodes voltage, according to Eq. (A.18).

$$\dot{W} = Vi \tag{A.18}$$

Overall efficiency, η, was associated with the ratio of the real operating voltage of the fuel cell (V) to the thermodynamically reversible cell voltage (V_{Nernst}). This cell efficiency is based on the second-law efficiency [39]:

$$\eta = \frac{V}{V_{Nernst}} \tag{A.19}$$

In this study, this efficiency is named voltage efficiency. Voltage efficiency incorporates the losses due to irreversible kinetic effects in the fuel cell [27]. Recall from section 3.1.2 that these losses are captured in the operational I-V curve.

In the present section the model has just briefly described, however, for more detailed information the entire implemented code is also available.

A.2. Finite-difference model

In this section the 2D model implemented in Matlab for the local prediction of the current density distribution is described. This very simple model is based on finite differences. However, taking advantage of the spot-sampling set-up, the experimental temperature distribution is taken as an input or known parameter, in such a way that the governing equations of fluid dynamics -momentum and energy equations- are not solved, except for the continuity one.

Therefore, experimental data have been useful to predict locally the behavior of the cell and correlate them with the internal reforming phenomena. That is, based on the local temperature measurements and on the corresponding experimental OCV, the experimental map of current density distribution and fuel utilization throughout the anode under predetermined conditions is calculated.

For this model, the main assumptions are listed below:

1. Steady-state condition.
2. Temperature distribution is known.
3. The ideal or Nernst voltage is known (experimental OCV).
4. The total pressure gradient inside the electrode is assumed to be negligible, i.e., pressure drops are not taken into account.
5. Ideal gas approximation.
6. Flow rate and gas inlet concentrations are uniform at the entrance of each channel.
7. Electrical potential is considered constant on the surface of the electrodes since they are good electrical conductors.
8. Total current density is considered as input value.
9. H_2 electro-oxidation responsible for the electrical flow.
10. CO and CH_4 only participate in the WGS reaction and in the SMR reaction, respectively.
11. Chemical equilibrium.
12. The cathode stream is assumed to be composed of 21% oxygen and 79% nitrogen.
13. Anode inlet stream consists of any of the three different compositions described in section 4.1, consisting of CH_4, CO, CO_2, H_2, and/or H_2O.

As observed, several assumptions for this model are common for the 0D model as well. This is because basically, the currently described model is based in the same internal reforming and electrochemical models, already described in section A.1.1 and section A.1.2, respectively.

Regarding the anode discretization, in Fig. A.1 it is schematically shown the way in which the the domain has been discretized.

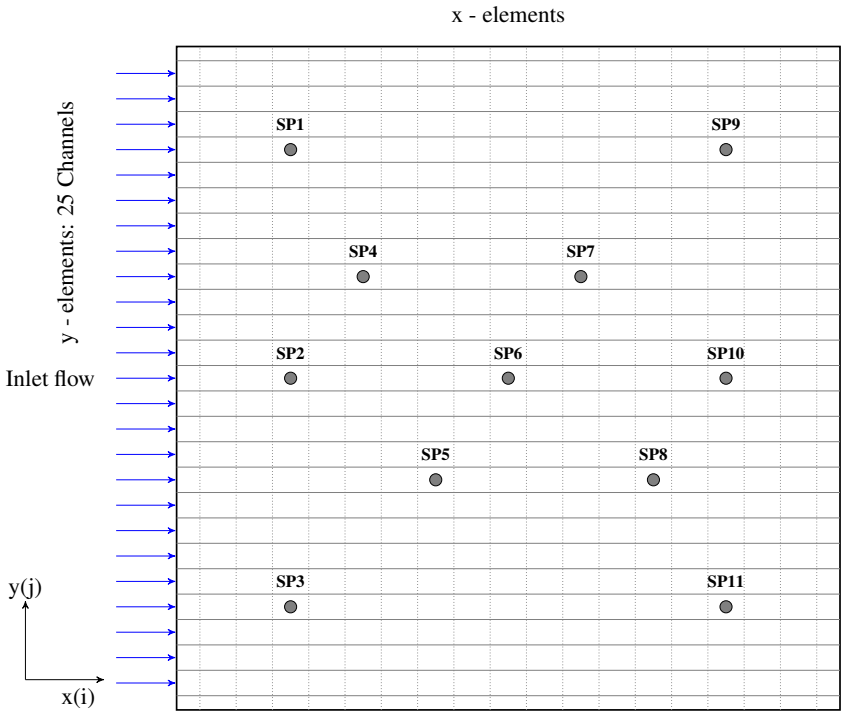

Figure A.1. *Schematic representation of the anode discretization.*

As observed, in the y-direction there have been considered only 25 elements, which correspond to the 25 channels themselves. Meanwhile, in the x-direction, according to the mesh sensitivity analysis, the cell is discretized in 145 elements. In Fig. A.1 the number of elements in x-direction does not correspond with the used for the present analysis. It is just an example of the discretization method, highlighting that all elements (25x145) have the same size.

On the other hand, the temperature mapping used in the model is based on a paraboloid fitting of the corresponding 11 temperature data. Since the anode temperature measurements were carried out in the 11 sampling points shown in Fig. A.1, it has been thus possible to use these data and calculate a temperature mapping over all the anode under each analyzed condition.

Regarding the input parameters, it has been also established that, unlike the 0D model, in this case the Nernst voltage or numerical OCV is not calculated numerically, rather it is directly taken from the experimental OCV. Recalling the main assumptions for the present model, it has been clarified that the inlet flows to each single channel are all considered uniform.

Hence, according to the discretization above described and to the assumptions already established, an electrochemical analysis based on deviations from the ideal performance (experimental OCV) is proposed at each element. The same irreversibilities considered for the 0D model, i.e. activation, ohmic and concentration losses, that cause voltage losses from the ideal voltage and have a negative impact on fuel cell performance, have been considered for this model as well. Thus, the

way in which each of them is evaluated has been already presented in section A.1.2. Meanwhile, the compositions considering chemical equilibrium, used for the overpotentials calculations, have been also determined based on the internal reforming model for the 0D model already described in section A.1.1.

Considering the electrodes to be equipotential surfaces [35], and in order to satisfy the conservation of current, the current density at each element is calculated as suggested in the corresponding algorithm shown in Fig. 5.42 and Fig. 5.43. That is, once ideal voltage and overpotentials are known, the operating voltage, initially considering an uniform current distribution at each single element of the cell, is evaluated according to Eq. (2.17). Afterward, from this voltage distribution, an average voltage is calculated, V_{ref}.

Thus, calculated the average voltage, V_{ref}, and set the temperature field of the cell, there is only one value of current density satisfying Eq. (2.17) at each element. Then, a continuity equation is applied at each single element after solving Eq. (2.17), and it is in this way that the current density distribution all over the anode is obtained.

Finally, as earlier mentioned, this model is essentially based on the 0D model already described in section A.1.

NOMENCLATURE

Symbol	Units	Meaning
α	Dimensionless	Charge transfer coefficient
A_{cell}	cm^2	Cell active area
a	Dimensionless	Chemical activity
ASR	$\Omega\,cm^2$	Area-specific resistance
D_i^{eff}	$cm^2\,s^{-1}$	Effective diffusion coefficient of species i
ΔE_N	%	Voltage loss due to leakage
$\Delta\hat{g}$	$kJ\,kmol^{-1}$	Molar Gibbs free energy
$\Delta\hat{g}^0$	$kJ\,kmol^{-1}$	Standard-state molar Gibbs free energy change
ΔG	kJ	Gibbs free energy change
ΔG^0	$kJ\,kmol^{-1}$	Gibbs free energy change at standard temperature and pressure
$\Delta\hat{h}$	$kJ\,kmol^{-1}$	Molar enthalpy
ΔH^0	$kJ\,kmol^{-1}$	Enthalpy change at standard temperature and pressure
DR	%/h	Degradation rate of the cell
$\Delta\hat{s}$	$kJ\,kmol^{-1}\,K^{-1}$	Molar entropy
ΔT	°C	Temperature difference
ΔV	mV	Voltage difference
ΔV_{loss}	mV	Total voltage loss
ε	Dimensionless	Porosity
ξ	Dimensionless	Error
E_a	$kJ\,kmol^{-1}$	Activation energy
E^0	V	Standard voltage
E_N	V	Nernst voltage
F	$C\,mol^{-1}$	Faraday constant, 96 485 C/mol
f	Hz	Frequency
G	kJ	Gibbs free energy
H	kJ	Enthalpy
i	A	Current

j	$\mathrm{A\,cm^{-2}}$	Current density
j_0	$\mathrm{A\,cm^{-2}}$	Exchange current density
K	Dimensionless	Equilibrium constant
λ	Dimensionless	Regularization parameter
L	m	Electrode thickness
$\dot{m}$	$\mathrm{kg\,s^{-1}}$	Mass flow rate
M	$\mathrm{kg\,kmol^{-1}}$	Molar mass
η	%	Efficiency
η_{ohm}	V	Ohmic overpotential
η_{act}	V	Activation overpotential
η_{conc}	V	Concentration overpotential
$\dot{n}$	$\mathrm{mol\,s^{-1}}$	Molar flow rate
n_e	Dimensionless	Number of electrons involved in the reaction
n_{rxn}	mol	Number of moles reacting electrochemically
OCV	mV	Open-circuit voltage
p	Pa	Pressure
PD	$\mathrm{W\,cm^{-2}}$	Power density
R	$\mathrm{kJ\,kmol^{-1}\,K^{-1}}$	Universal ideal gas constant, $8.314\,\mathrm{kJ/kmol\,K}$
R_0	$\Omega\,\mathrm{cm^2}$	Ohmic resistance
R_{ohm}	$\Omega\,\mathrm{cm^2}$	Overall ohmic resistance
R_{pol}	$\Omega\,\mathrm{cm^2}$	Polarization resistance
R_T	$\Omega\,\mathrm{cm^2}$	Total cell resistance from EIS
R_{cell}	$\Omega\,\mathrm{cm^2}$	Total cell resistance from I-V curves
S	$\mathrm{kJ\,K^{-1}}$	Entropy
τ	Dimensionless	Tortuosity
T	K	Temperature
$T_{mean,as}$	°C	Mean temperature of the anode
t	h	Operation time per region
V	V	Voltage
V_f	mV	Final cell voltage
V_i	mV	Initial cell voltage
$V(i)$	mV	Cell voltage at a given current
V_{ohm}	mV	Ohmic overpotential
V_{pol}	mV	Polarization overpotential
$\dot{V}$	$\mathrm{ml\,min^{-1}}$	Volume flow rate
ω	Hz	Radial frequency
$\dot{W}$	W	Power

W	$\mathrm{kW\,kmol^{-1}}$	Electrical work
y	Dimensionless	Molar fraction
Z	Ω	Impedance
Z'	$\Omega\,\mathrm{cm^2}$	Real part of the impedance spectra
Z''	$\Omega\,\mathrm{cm^2}$	Imaginary part of the impedance spectra

Subscripts

Symbol	Meaning
an	Anode
avg	Average
cat	Cathode
act	Activation
$conc$	Concentration
e	Exit
el	Electrode
$elect$	Electrical
eq	Equilibrium
i	Species
in	Inlet
L	Limiting point
max	Maximum
min	Minimum
N	Nernst
th	Theoretical
ohm	Ohmic
ox	Oxidation
red	Reduction
ref	Reformate
$r-WGS$	Reverse water gas-shift
rxn	Reaction
SMR	Steam methane reforming
WGS	Water gas-shift

Superscripts

Symbol	Meaning
e	Exit
eff	Effective
in	Inlet
r	Reacting
out	Outlet

Abbreviations

Symbol	Meaning
AFL	Anode functional layer
CIR	Complete internal reforming
DIR	Direct internal reforming
DRT	Distribution of relaxation times
EDS	Energy dispersive X-ray spectroscopy
EES	Engineering equation solver
EIS	Electrochemical impedance spectroscopy
FID	Flame ionization detector
FU	Fuel utilization
GC	Gas chromatography
GDC	Gadolina-doped ceria
GDP	Gas diffusion plate
$H-SOFC$	Proton conducting solid oxide fuel cell
IIR	Intermediate internal reforming
IT	Intermediate temperature
$K-K$	Kramers-Kroning
LIR	Low internal reforming
LSC	Lanthanum strontium cobaltite
$LSCF$	Lanthanum strontium cobalt ferrite
OCV	Open-circuit voltage
O/C	Oxygen-to-carbon ratio
SC	Single cell

S/C	Steam-to-carbon ratio
SEM	Scanning electron microscopy
SMR	Steam methane reforming
$SOFC$	Solid oxide fuel cell
$SOEC$	Solid oxide electrolysis cell
SP	Sampling point
TEM	Transmission electron microscopy
TCD	Thermal conductivity detector
TPB	Triple-phase boundary
WGS	Water-gas shift
XRD	X-ray diffraction
YSZ	Yttria-stabilized zirconia

CONTRIBUTIONS

- D.M. Silva-Mosqueda, F. Elizalde-Blancas, D. Pumiglia, F. Santoni, C. Boigues-Munñoz, and S.J. McPhail, "Intermediate temperature solid oxide fuel cell under internal reforming: Critical operating conditions, associated problems and their impact on the performance", *Applied Energy*, vol. 235, pp. 625-640, 2019.

- F. Santoni, D.M. Silva-Mosqueda, D. Pumiglia, E. Viceconti, B. Conti, C. Boigues-Muñoz, B. Bosio, S. Ulgiati, and S. J. McPhail, "In-situ study of the gas-phase composition and temperature of an intermediate-temperature solid oxide fuel cell anode surface fed by reformate natural gas", *Journal of power sources*, Vol. 370, pp. 36-44, 2017.

- D.M. Silva-Mosqueda, D. Pumiglia, F. Elizalde-Blancas, S.J. McPhail, F. Santoni and C. Boigues-Muñoz, " Performance and degradation phenomena of a planar IT-SOFC under critical operating conditions", 7th European Fuel Cell Technology & Applications Conference-Piero Lunghi Conference (Naples, Italy), December 12-15, 2017.

Bibliography

[1] J. Larminie, A. Dicks, and M. S. McDonald, *Fuel cell systems explained*, vol. 2. J. Wiley Chichester, UK, second ed., 2003.

[2] K. Sundmacher, A. Kienle, H. J. Pesch, J. F. Berndt, and G. Huppmann, *Molten carbonate fuel cells: modeling, analysis, simulation, and control*. John Wiley & Sons, 2007.

[3] 2017. http://www.vttresearch.com/Impulse/Pages/Impulse-2-2016.aspx.

[4] M. Steil, S. Nobrega, S. Georges, P. Gelin, S. Uhlenbruck, and F. Fonseca, "Durable direct ethanol anode-supported solid oxide fuel cell," *Applied Energy*, vol. 199, pp. 180–186, 2017.

[5] J. Qu, W. Wang, Y. Chen, F. Wang, R. Ran, and Z. Shao, "Ethylene glycol as a new sustainable fuel for solid oxide fuel cells with conventional nickel-based anodes," *Applied energy*, vol. 148, pp. 1–9, 2015.

[6] J. Qu, W. Wang, Y. Chen, X. Deng, and Z. Shao, "Stable direct-methane solid oxide fuel cells with calcium-oxide-modified nickel-based anodes operating at reduced temperatures," *Applied energy*, vol. 164, pp. 563–571, 2016.

[7] W. Wang, C. Su, Y. Wu, R. Ran, and Z. Shao, "Progress in solid oxide fuel cells with nickel-based anodes operating on methane and related fuels," *Chemical reviews*, vol. 113, no. 10, pp. 8104–8151, 2013.

[8] A. Da Silva, N. Bion, F. Epron, S. Baraka, F. Fonseca, R. Rabelo-Neto, L. Mattos, and F. Noronha, "Effect of the type of ceria dopant on the performance of Ni/CeO2 SOFC anode for ethanol internal reforming," *Applied Catalysis B: Environmental*, vol. 206, pp. 626–641, 2017.

[9] E. M. Mokheimer, M. I. Hussain, S. Ahmed, M. A. Habib, and A. A. Al-Qutub, "On the modeling of steam methane reforming," *Journal of Energy Resources Technology*, vol. 137, no. 1, p. 012001, 2015.

[10] L. Hu, *Molten carbonate fuel cells for electrolysis*. PhD thesis, KTH Royal Institute of Technology, 2016.

[11] T.-I. Tsai, L. Troskialina, A. Majewski, and R. Steinberger-Wilckens, "Methane internal reforming in solid oxide fuel cells with anode off-gas recirculation," *International Journal of Hydrogen Energy*, vol. 41, no. 1, pp. 553–561, 2016.

[12] F. Cells and H. J. Undertaking, "Fuel cell and hydrogen technology: Europe's journey to a greener world," 2017.

[13] A. Ideris, E. Croiset, M. Pritzker, and A. Amin, "Direct-methane solid oxide fuel cell (SOFC) with Ni-SDC anode-supported cell," *International Journal of Hydrogen Energy*, vol. 42, no. 36, pp. 23118–23129, 2017.

[14] A. Baldinelli, L. Barelli, G. Bidini, A. Di Michele, and R. Vivani, "SOFC direct fuelling with high-methane gases: Optimal strategies for fuel dilution and upgrade to avoid quick degradation," *Energy Conversion and Management*, vol. 124, pp. 492–503, 2016.

[15] D. Mogensen, J.-D. Grunwaldt, P. V. Hendriksen, K. Dam-Johansen, and J. Nielsen, "Internal steam reforming in solid oxide fuel cells: Status and opportunities of kinetic studies and their impact on modelling," *Journal of Power Sources*, vol. 196, no. 1, pp. 25–38, 2011.

[16] M. Andersson, J. Yuan, and B. Sundén, "Review on modeling development for multiscale chemical reactions coupled transport phenomena in solid oxide fuel cells," *Applied Energy*, vol. 87, no. 5, pp. 1461–1476, 2010.

[17] R. Peters, R. Dahl, U. Klüttgen, C. Palm, and D. Stolten, "Internal reforming of methane in solid oxide fuel cell systems," *Journal of Power Sources*, vol. 106, no. 1, pp. 238–244, 2002.

[18] E. D. Wachsman and K. T. Lee, "Lowering the temperature of solid oxide fuel cells," *Science*, vol. 334, no. 6058, pp. 935–939, 2011.

[19] K. T. Lee, H. S. Yoon, and E. D. Wachsman, "The evolution of low temperature solid oxide fuel cells," *Journal of Materials Research*, vol. 27, no. 16, p. 2063, 2012.

[20] S. Badwal, "Stability of solid oxide fuel cell components," *Solid State Ionics*, vol. 143, no. 1, pp. 39–46, 2001.

[21] M. Gandiglio, A. Lanzini, and M. Santarelli, "Large stationary solid oxide fuel cell (SOFC) power plants," in *Modeling, design, construction, and operation of power generators with solid oxide fuel cells*, pp. 233–261, Springer, 2018.

[22] K. Wandelt, "Encyclopedia of interfacial chemistry: surface science and electrochemistry," 2017.

[23] Y. Fu, *Theoretical and experimental study of solid oxide fuel cell (SOFC) using impedance spectra*. PhD thesis, Massachusetts Institute of Technology, 2014.

[24] M. Guida, F. Postiglione, and G. Pulcini, "A random-effects model for long-term degradation analysis of solid oxide fuel cells," *Reliability Engineering & System Safety*, vol. 140, pp. 88–98, 2015.

[25] A. Hauch, M. Mogensen, and A. Hagen, "Ni/YSZ electrode degradation studied by impedance spectroscopyEffect of p (H2O)," *Solid State Ionics*, vol. 192, no. 1, pp. 547–551, 2011.

[26] S. C. Singhal, "Advances in solid oxide fuel cell technology," *Solid State Ionics*, vol. 135, no. 1, pp. 305–313, 2000.

[27] R. O'hayre, S.-W. Cha, F. B. Prinz, and W. Colella, *Fuel cell fundamentals*. John Wiley & Sons, 2016.

[28] M. J. Moran, H. N. Shapiro, D. D. Boettner, and M. B. Bailey, *Fundamentals of engineering thermodynamics*. John Wiley & Sons, 2010.

[29] "Fuel cell and hydrogen energy association-the bussiness case for fuel cells 2015: powering corporate sustainability," 2015.

[30] A. Kromp, A. Weber, and E. Ivers-Tiffée, "Electrochemistry of reformate fueled Ni/8YSZ anodes for solid oxide fuel cells," *ECS Transactions*, vol. 57, no. 1, pp. 3063–3075, 2013.

[31] A. Kromp, *Model-based interpretation of the performance and degradation of reformate fueled solid oxide fuel cells*. KIT Scientific Publishing, 2013.

[32] M. Turco, A. Ausiello, and L. Micoli, "Fuel cells operating and structural features of MCFCs and SOFCs," in *Treatment of Biogas for Feeding High Temperature Fuel Cells*, pp. 31–76, Springer, 2016.

[33] T. Franco, M. Haydn, A. Weber, W. Schafbauer, L. Blum, U. Packbier, D. Roehrens, N. H. Menzler, J. Rechberger, A. Venskutonis, *et al.*, "The status of metal-supported sofc development and industrialization at plansee," *ECS Transactions*, vol. 57, no. 1, pp. 471–480, 2013.

[34] H. Iwai, Y. Yamamoto, M. Saito, and H. Yoshida, "Numerical simulation of intermediate-temperature direct-internal-reforming planar solid oxide fuel cell," *Energy*, vol. 36, no. 4, pp. 2225–2234, 2011.

[35] D. Ferrero, A. Lanzini, P. Leone, and M. Santarelli, "Reversible operation of solid oxide cells under electrolysis and fuel cell modes: Experimental study and model validation," *Chemical Engineering Journal*, vol. 274, pp. 143–155, 2015.

[36] Y. Fujimaki, K. Mizuno, Y. Kimura, T. Nakamura, K. Develos-Bagarinao, K. Yamaji, K. Yashiro, T. Kawada, F. Iguchi, H. Yugami, *et al.*, "Contribution of triple-phase boundary reaction in cathodic reaction of solid oxide fuel cell," *ECS Transactions*, vol. 78, no. 1, pp. 847–853, 2017.

[37] J. Ugartemendia, J. X. Ostolaza, and I. Zubia, "Operating point optimization of a hydrogen fueled hybrid solid oxide fuel cell-steam turbine (SOFC-ST) plant," *Energies*, vol. 6, no. 10, pp. 5046–5068, 2013.

[38] C. M. Stoots, J. S. Herring, J. J. Hartvigsen, *et al.*, "Syngas production via high-temperature coelectrolysis of steam and carbon dioxide," *Journal of fuel cell science and technology*, vol. 6, no. 1, p. 011014, 2009.

[39] K. Wark Jr, *Advanced thermodynamics for engineers*. McGraw-Hill: New York, 1995.

[40] T. Oswell, *Investigation of performance of reformate fuels on SOFC anodes*. PhD thesis, University of Calgary, 2013.

[41] D. Pumiglia, *Intermediate temperature solid oxide fuel cells fed with syngas: an evaluation of electrochemical phenomena*. PhD thesis, Università Degli Study Della Tuscia Di Viterbo, 2017.

[42] A. Leonide, *SOFC modelling and parameter identification by means of impedance spectroscopy*. PhD thesis, Karlsruher Institut für Technologie, 2010.

[43] C. B. Muñoz, *Computational simulation of solid oxide fuel cells - integrating numerical and experimental approaches*. PhD thesis, Università Politecnica Delle Marche, 2015.

[44] A. Yahya, D. Ferrero, H. Dhahri, P. Leone, K. Slimi, and M. Santarelli, "Electrochemical performance of solid oxide fuel cell: Experimental study and calibrated model," *Energy*, vol. 142, pp. 932–943, 2018.

[45] H.-T. Lim, S. C. Hwang, and J. S. Ahn, "Performance of anode-supported solid oxide fuel cell in planar-cell channel-type setup," *Ceramics International*, vol. 39, pp. S659–S662, 2013.

[46] M. Lang, C. Bohn, M. Henke, G. Schiller, C. Willich, and F. Hauler, "Understanding the current-voltage behavior of high temperature solid oxide fuel cell stacks," *Journal of The Electrochemical Society*, vol. 164, no. 13, pp. F1460–F1470, 2017.

[47] Z. Wuillemin, S. Ceschini, Y. Antonetti, C. Beetschen, S. Modena, D. Montinaro, T. Cornu, O. Bucheli, and M. Bertoldi, "High-performance SOFC stacks tested under different reformate compositions," in *11th Eur. SOFC SOE Forum, Lucerne*, 2014.

[48] B. M. White, W. L. Lundberg, and J. F. Pierre, "Accomplishments, status, and road map for the US department of energy's fossil energy SOFC program," *ECS Transactions*, vol. 68, no. 1, pp. 23–38, 2015.

[49] May 2018.

[50] S. D. Angeli, G. Monteleone, A. Giaconia, and A. A. Lemonidou, "State-of-the-art catalysts for CH4 steam reforming at low temperature," *International Journal of Hydrogen Energy*, vol. 39, no. 5, pp. 1979–1997, 2014.

[51] H.-T. Lim, C. Yang, S. Hwang, and Y.-J. Choi, "Experimental study of internal reforming on large-area anode supported solid oxide fuel cells," *Fuel Cells*, vol. 15, no. 4, pp. 555–565, 2015.

[52] K. Eguchi, "Performance and degradation of Ni-based cermet anode for solid oxide fuel cells," *Journal of the Japan Petroleum Institute*, vol. 58, no. 2, pp. 79–85, 2015.

[53] L. Hu, G. Lindbergh, and C. Lagergren, "Electrode kinetics of the Ni porous electrode for hydrogen production in a Molten Carbonate Electrolysis Cell (MCEC)," *Journal of The Electrochemical Society*, vol. 162, no. 9, pp. F1020–F1028, 2015.

[54] T. Iida, M. Kawano, T. Matsui, R. Kikuchi, and K. Eguchi, "Internal reforming of SOFCs carbon deposition on fuel electrode and subsequent deterioration of cell," *Journal of the Electrochemical Society*, vol. 154, no. 2, pp. B234–B241, 2007.

[55] N. Minh, J. Mizusaki, and S. C. Singhal, "Advances in solid oxide fuel cells: review of progress through three decades of the international symposia on solid oxide fuel cells," *ECS Transactions*, vol. 78, no. 1, pp. 63–73, 2017.

[56] J. Nielsen, T. Jacobsen, and M. Wandel, "Impedance of porous IT-SOFC LSCF: CGO composite cathodes," *Electrochimica Acta*, vol. 56, no. 23, pp. 7963–7974, 2011.

[57] A. Kromp, S. Dierickx, A. Leonide, A. Weber, and E. Ivers-Tiffée, "Electrochemical analysis of sulfur-poisoning in anode supported SOFCs fuelled with a model reformate," *Journal of The Electrochemical Society*, vol. 159, no. 5, pp. B597–B601, 2012.

[58] J. Hjelm, M. Søgaard, R. Knibbe, A. Hagen, and M. Mogensen, "Electrochemical characterization of planar anode supported SOFC with strontium-doped lanthanum cobalt oxide cathodes," *ECS transactions*, vol. 13, no. 26, pp. 285–299, 2008.

[59] P. Shearing, D. Brett, and N. Brandon, "Towards intelligent engineering of SOFC electrodes: a review of advanced microstructural characterisation techniques," *International Materials Reviews*, vol. 55, no. 6, pp. 347–363, 2010.

[60] K. Sasaki, T. Yoshizumi, K. Haga, H. Yoshitomi, T. Hosoi, Y. Shiratori, and S. Taniguchi, "Chemical degradation of SOFCs: external impurity poisoning and internal diffusion-related phenomena," *ECS Transactions*, vol. 57, no. 1, pp. 315–323, 2013.

[61] Y. Kikuchi, J. Matsuda, Y. Tachikawa, Y. Shiratori, S. Taniguchi, and K. Sasaki, "Degradation of SOFCs by various impurities: impedance spectroscopy and microstructural analysis," *ECS Transactions*, vol. 78, pp. 1253–1260, may 2017.

[62] R. M. C. Clemmer, *The processing and characterization of porous Ni/YSZ and NiO/YSZ composites used in solid oxide fuel cell applications*. PhD thesis, University of Waterloo, 2006.

[63] Y. Zhang, Y. Chen, and F. Chen, "In-situ quantification of solid oxide fuel cell electrode microstructure by electrochemical impedance spectroscopy," *Journal of Power Sources*, vol. 277, pp. 277–285, 2015.

[64] D. Pumiglia, F. Santoni, E. Viceconti, B. Conti, C. B. Muñoz, B. Bosio, M. Carlini, and S. J. McPhail, "SOFC anode process characterization by means of a spot-sampling set-up for in-operando gas analysis," *ECS Transactions*, vol. 75, no. 49, pp. 1–8, 2017.

[65] J. Nielsen, A. Hagen, and Y.-L. Liu, "Effect of cathode gas humidification on performance and durability of solid oxide fuel cells," *Solid State Ionics*, vol. 181, no. 11, pp. 517–524, 2010.

[66] Ö. Aydn, H. Nakajima, and T. Kitahara, "Current and temperature distributions in-situ acquired by electrode-segmentation along a microtubular solid oxide fuel cell operating with syngas," *Journal of Power Sources*, vol. 293, pp. 1053–1061, 2015.

[67] Ö. Aydn, T. Koshiyama, H. Nakajima, and T. Kitahara, "In-situ diagnosis and assessment of longitudinal current variation by electrode-segmentation method in anode-supported microtubular solid oxide fuel cells," *Journal of Power Sources*, vol. 279, pp. 218–223, 2015.

[68] M. Santarelli, P. Leone, M. Calì, and G. Orsello, "Experimental evaluation of the sensitivity to fuel utilization and air management on a 100kW SOFC system," *Journal of Power Sources*, vol. 171, no. 1, pp. 155–168, 2007.

[69] A. Lanzini, P. Leone, M. Pieroni, M. Santarelli, D. Beretta, and S. Ginocchio, "Experimental investigations and modeling of direct internal reforming of biogases in tubular solid oxide fuel cells," *Fuel Cells*, vol. 11, no. 5, pp. 697–710, 2011.

[70] O. Razbani, I. Wærnhus, and M. Assadi, "Experimental investigation of temperature distribution over a planar solid oxide fuel cell," *Applied energy*, vol. 105, pp. 155–160, 2013.

[71] B. Morel, R. Roberge, S. Savoie, T. W. Napporn, and M. Meunier, "An experimental evaluation of the temperature gradient in solid oxide fuel cells," *Electrochemical and solid-state letters*, vol. 10, no. 2, pp. B31–B33, 2007.

[72] A. Donazzi, M. Rahmanipour, M. Maestri, G. Groppi, L. Bardini, A. Pappacena, and M. Boaro, "Experimental and model analysis of the co-oxidative behavior of syngas feed in an intermediate temperature solid oxide fuel cell," *Journal of Power Sources*, vol. 306, pp. 467–480, 2016.

[73] W. G. Bessler, S. Gewies, C. Willich, G. Schiller, and K. A. Friedrich, "Spatial distribution of electrochemical performance in a segmented SOFC: A combined modeling and experimental study," *Fuel Cells*, vol. 10, no. 3, pp. 411–418, 2010.

[74] F. Santoni, D. S. Mosqueda, D. Pumiglia, E. Viceconti, B. Conti, C. B. Muñoz, B. Bosio, S. Ulgiati, and S. McPhail, "In-situ study of the gas-phase composition and temperature of an intermediate-temperature solid oxide fuel cell anode surface fed by reformate natural gas," *Journal of Power Sources*, vol. 370, pp. 36–44, 2017.

[75] J. Saunders and M. Davy, "High-temperature vibrational Raman spectroscopy of gaseous species for solid-oxide fuel cell research," *international journal of hydrogen energy*, vol. 37, no. 4, pp. 3403–3414, 2012.

[76] G. Schiller, E. Gülzow, M. Schulze, N. Wagner, and K. A. Friedrich, "Analytical investigation of fuel cells by using in situ and ex situ diagnostic methods," in *Materials Science Forum*, vol. 638, pp. 1125–1130, Trans Tech Publ, 2010.

[77] A. Kromp, A. Leonide, H. Timmermann, A. Weber, and E. Ivers-Tiffée, "Internal reforming kinetics in SOFC-anodes," *ECS Transactions*, vol. 28, no. 11, pp. 205–215, 2010.

[78] H. Timmermann, W. Sawady, R. Reimert, and E. Ivers-Tiffée, "Kinetics of (reversible) internal reforming of methane in solid oxide fuel cells under stationary and APU conditions," *Journal of Power Sources*, vol. 195, no. 1, pp. 214–222, 2010.

[79] A. Leonide, S. Hansmann, A. Weber, and E. Ivers-Tiffée, "Performance simulation of current/voltage-characteristics for SOFC single cell by means of detailed impedance analysis," *Journal of Power Sources*, vol. 196, no. 17, pp. 7343–7346, 2011.

[80] H.-T. Lim, S. Hwang, M. Jung, H. Park, M. Park, S.-S. Lee, and Y.-G. Jung, "Degradation mechanism of anode-supported solid oxide fuel cell in planar-cell channel-type setup," *Fuel cells*, vol. 13, no. 5, pp. 712–719, 2013.

[81] H.-T. Lim, S. C. Hwang, Y. M. Park, and I. S. Lee, "Performance and long term stability of large area anode supported solid oxide fuel cells (SOFCs)," *Solid State Ionics*, vol. 225, pp. 124–130, 2012.

[82] J. Nielsen and M. Mogensen, "SOFC LSM: YSZ cathode degradation induced by moisture: An impedance spectroscopy study," *Solid State Ionics*, vol. 189, no. 1, pp. 74–81, 2011.

[83] R. Barfod, M. Mogensen, T. Klemensø, A. Hagen, Y.-L. Liu, and P. V. Hendriksen, "Detailed characterization of anode-supported SOFCs by impedance spectroscopy," *Journal of The Electrochemical Society*, vol. 154, no. 4, pp. B371–B378, 2007.

[84] A. Kromp, A. Leonide, A. Weber, and E. Ivers-Tiffée, "Electrochemical analysis of reformate-fuelled anode supported SOFC," *Journal of The Electrochemical Society*, vol. 158, no. 8, pp. B980–B986, 2011.

[85] C. Boigues Muñoz, D. Pumiglia, S. J. McPhail, D. Montinaro, G. Comodi, G. Santori, M. Carlini, and F. Polonara, "More accurate macro-models of solid oxide fuel cells through electrochemical and microstructural parameter estimation-part I: Experimentation," *Journal of Power Sources*, vol. 294, pp. 658–668, 2015.

[86] T.-H. Lee, K.-Y. Park, J.-T. Kim, Y. Seo, K. B. Kim, S.-J. Song, B. Park, and J.-Y. Park, "Degradation analysis of anode-supported intermediate temperature-solid oxide fuel cells under various failure modes," *Journal of Power Sources*, vol. 276, pp. 120–132, 2015.

[87] H. Schichlein, A. C. Müller, M. Voigts, A. Krügel, and E. Ivers-Tiffée, "Deconvolution of electrochemical impedance spectra for the identification of electrode reaction mechanisms in solid oxide fuel cells," *Journal of Applied Electrochemistry*, vol. 32, no. 8, pp. 875–882, 2002.

[88] S. Primdahl and M. Mogensen, "Gas conversion impedance: A test geometry effect in characterization of solid oxide fuel cell anodes," *Journal of the Electrochemical Society*, vol. 145, no. 7, pp. 2431–2438, 1998.

[89] D. Papurello, D. Menichini, and A. Lanzini, "Distributed relaxation times technique for the determination of fuel cell losses with an equivalent circuit model to identify physicochemical processes," *Electrochimica Acta*, vol. 258, pp. 98–109, 2017.

[90] E. Ivers-Tiffée, A. A. Weber, E. Ivers-Tiffée, and A. A. Weber, "Evaluation of electrochemical impedance spectra by the distribution of relaxation times," *Journal of the Ceramic Society of Japan*, vol. 125, no. 4, pp. 193–201, 2017.

[91] A. Weiß, S. Schindler, S. Galbiati, M. A. Danzer, and R. Zeis, "Distribution of relaxation times analysis of high-temperature PEM fuel cell impedance spectra," *Electrochimica Acta*, vol. 230, pp. 391–398, 2017.

[92] A. Leonide, Y. Apel, and E. Ivers-Tiffee, "Sofc modeling and parameter identification by means of impedance spectroscopy," *ECS Transactions*, vol. 19, no. 20, pp. 81–109, 2009.

[93] A. Kromp, H. Geisler, A. Weber, and E. Ivers-Tiffée, "Electrochemical impedance modeling of gas transport and reforming kinetics in reformate fueled solid oxide fuel cell anodes," *Electrochimica Acta*, vol. 106, pp. 418–424, 2013.

[94] A. Leonide, V. Sonn, A. Weber, and E. Ivers-Tiffée, "Evaluation and modeling of the cell resistance in anode-supported solid oxide fuel cells," *Journal of The Electrochemical Society*, vol. 155, no. 1, pp. B36–B41, 2008.

[95] P. Hjalmarsson, M. Søgaard, and M. Mogensen, "Electrochemical performance and degradation of (La 0.6 Sr 0.4) 0.99 CoO 3- δ as porous SOFC-cathode," *Solid State Ionics*, vol. 179, no. 27, pp. 1422–1426, 2008.

[96] B. Stoeckl, V. Subotić, D. Reichholf, H. Schroettner, and C. Hochenauer, "Extensive analysis of large planar SOFC: Operation with humidified methane and carbon monoxide to examine carbon deposition based degradation," *Electrochimica acta*, vol. 256, pp. 325–336, 2017.

[97] B. Liu, H. Muroyama, T. Matsui, K. Tomida, T. Kabata, and K. Eguchi, "Analysis of impedance spectra for segmented-in-series tubular solid oxide fuel cells," *Journal of The Electrochemical Society*, vol. 157, no. 12, pp. B1858–B1864, 2010.

[98] C. Boigues Muñoz, D. Pumiglia, F. Santoni, S. J. McPhail, G. Comodi, and M. Carlini, "Performance degradation prediction of a low-temperature SOFC via impedance spectroscopy and CFD modelling," *ECS Transactions*, vol. 68, no. 1, pp. 2227–2235, 2015.

[99] A. Ploner, A. Hagen, and A. Hauch, "Study of operating parameters for accelerated anode degradation in SOFCs," *Fuel Cells*, vol. 17, no. 4, pp. 498–507, 2017.

[100] G. Nurk, M. Vestli, P. Möller, R. Jaaniso, M. Kodu, H. Mändar, T. Romann, R. Kanarbik, and E. Lust, "Mobility of Sr in gadolinia doped ceria barrier layers prepared using spray pyrolysis, pulsed laser deposition and magnetron sputtering methods," *Journal of The Electrochemical Society*, vol. 163, no. 2, pp. F88–F96, 2016.

[101] D. Pumiglia, S. Vaccaro, A. Masi, S. J. McPhail, M. Falconieri, S. Gagliardi, L. Della Seta, and M. Carlini, "Aggravated test of intermediate temperature solid oxide fuel cells fed with tar-contaminated syngas," *Journal of Power Sources*, vol. 340, pp. 150–159, 2017.

[102] D. Lee, J.-K. Lin, C.-H. Tsai, S.-H. Wu, Y.-N. Cheng, and R.-Y. Lee, "Analysis of long-term and thermal cycling tests for a commercial solid oxide fuel cell," *Journal of Electrochemical Energy Conversion and Storage*, vol. 14, no. 4, p. 041002, 2017.

[103] H.-S. Noh, J.-W. Son, H. Lee, J.-S. Park, H.-W. Lee, and J.-H. Lee, "Direct applicability of La0. 6Sr0. 4CoO3–δ thin film cathode to yttria stabilised zirconia electrolytes at T $\leq$ 650 C," *Fuel Cells*, vol. 10, no. 6, pp. 1057–1065, 2010.

[104] J. Saunders and M. Davy, "In-situ studies of gas phase composition and anode surface temperature through a model DIR-SOFC steam-methane reformer at 973.15 K," *International Journal of Hydrogen Energy*, vol. 38, no. 31, pp. 13762–13773, 2013.

[105] R. R. Liu, S. H. Kim, S. Taniguchi, T. Oshima, Y. Shiratori, K. Ito, and K. Sasaki, "Influence of water vapor on long-term performance and accelerated degradation of solid oxide fuel cell cathodes," *Journal of power Sources*, vol. 196, no. 17, pp. 7090–7096, 2011.

[106] S. H. Kim, T. Ohshima, Y. Shiratori, K. Itoh, and K. Sasaki, "Effect of water vapor and SOx in air on the cathodes of solid oxide fuel cells," *Mater. Res. Soc. Symp. Proc.*, vol. 1041, pp. R3–10, 2008.

[107] D. Lee, J. Myung, J. Tan, S.-H. Hyun, J. T. Irvine, J. Kim, and J. Moon, "Direct methane solid oxide fuel cells based on catalytic partial oxidation enabling complete coking tolerance of Ni-based anodes," *Journal of Power Sources*, vol. 345, pp. 30–40, 2017.

[108] L. Holzer, B. Iwanschitz, T. Hocker, B. Münch, M. Prestat, D. Wiedenmann, U. Vogt, P. Holtappels, J. Sfeir, A. Mai, *et al.*, "Microstructure degradation of cermet anodes for solid oxide fuel cells: Quantification of nickel grain growth in dry and in humid atmospheres," *Journal of Power Sources*, vol. 196, no. 3, pp. 1279–1294, 2011.

[109] H.-C. Yu, F. Zhao, A. V. Virkar, and K.-Z. Fung, "Electrochemical characterization and performance evaluation of intermediate temperature solid oxide fuel cell with La0. 75Sr0. 25CuO2. 5- δ cathode," *Journal of power sources*, vol. 152, pp. 22–26, 2005.

[110] T. Dang-Long, T. Quang-Tuyen, and Y. Shiratori, "Catalytic and electrochemical behaviour of solid oxide fuel cell operated with simulated-biogas mixtures," in *AIP Conference Proceedings*, vol. 1737, p. 060012, AIP Publishing, 2016.

[111] T. Kushi, "Performance and durability evaluation of dry reforming in solid oxide fuel cells," *International Journal of Hydrogen Energy*, vol. 41, no. 39, pp. 17567–17576, 2016.

[112] V. Subotić, C. Schluckner, J. Strasser, V. Lawlor, J. Mathe, J. Rechberger, H. Schroettner, and C. Hochenauer, "In-situ electrochemical characterization methods for industrial-sized planar solid oxide fuel cells Part I: Methodology, qualification and detection of carbon deposition," *Electrochimica Acta*, vol. 207, pp. 224–236, 2016.

[113] Y. J. Kim and H.-T. Lim, "Performance of solid oxide fuel cells with direct internal reforming of methane," *Journal of the Korean Ceramic Society*, vol. 52, no. 5, pp. 325–330, 2015.

[114] T. Zhu, Z. Yang, and M. Han, "Performance evaluation of solid oxide fuel cell with in-situ methane reforming," *Fuel*, vol. 161, pp. 168–173, 2015.

[115] C. Boigues Muñoz, G. Santori, S. J. McPhail, and F. Polonara, "Thermochemical model and experimental validation of a tubular SOFC cell comprised in a 1 kWel stack designed for μCHP applications," *International Journal of Hydrogen Energy*, vol. 39, no. 36, pp. 21714–21723, 2014.

[116] V. N. Nguyen, Q. Fang, U. Packbier, and L. Blum, "Long-term tests of a Jülich planar short stack with reversible solid oxide cells in both fuel cell and electrolysis modes," *International Journal of Hydrogen Energy*, vol. 38, no. 11, pp. 4281–4290, 2013.

[117] D. Papurello, R. Borchiellini, P. Bareschino, V. Chiodo, S. Freni, A. Lanzini, F. Pepe, G. Ortigoza, and M. Santarelli, "Performance of a solid oxide fuel cell short-stack with biogas feeding," *Applied Energy*, vol. 125, pp. 254–263, 2014.

[118] M. Halinen, J. Saarinen, M. Noponen, I. Vinke, and J. Kiviaho, "Experimental analysis on performance and durability of SOFC demonstration unit," *Fuel Cells*, vol. 10, no. 3, pp. 440–452, 2010.

[119] A. Hauch and M. B. Mogensen, "Testing of electrodes, cells, and short stacks," in *Advances in medium and high temperature solid oxide fuel cell technology*, pp. 31–76, Springer, 2017.

[120] A. Baratella, R. Bove, and P. Lunghi, "A methodology for assessing fuel cell performance under a wide range of operational conditions: Results for single cells," *Journal of Fuel Cell Science and Technology*, vol. 3, no. 3, pp. 226–233, 2006.

[121] C. Boigues-Muñoz, D. Pumiglia, S. J. McPhail, G. Santori, D. Montinaro, G. Comodi, M. Carlini, and F. Polonara, "More accurate macro-models of solid oxide fuel cells through electrochemical and microstructural parameter estimation-Part II: Parameter estimation," *Journal of Power Sources*, vol. 286, pp. 321–329, 2015.

[122] S. D. Ebbesen and M. Mogensen, "Kinetics of oxidation of H2 and reduction of H2O in Ni-YSZ based solid oxide cells," *ECS Transactions*, vol. 50, no. 49, pp. 167–182, 2013.

[123] J. Hjelm, M. Søgaard, M. Wandel, M. Menon, M. Mogensen, and A. Hagen, "Electrochemical impedance studies of SOFC cathodes," *ECS Transactions*, vol. 7, no. 1, pp. 1261–1270, 2007.

[124] A. Hagen, Y. L. Liu, R. Barfod, and P. V. Hendriksen, "Anode supported solid oxide fuel cells-deconvolution of degradation into cathode and anode contributions," *ECS Transactions*, vol. 7, no. 1, pp. 301–309, 2007.

[125] M. Kornely, N. Menzler, A. Weber, and E. Ivers-Tiffée, "Degradation of a high performance SOFC cathode by Cr-poisoning at OCV-conditions," *Fuel Cells*, vol. 13, no. 4, pp. 506–510, 2013.

[126] S. Koch, P. V. Hendriksen, M. Mogensen, Y.-L. Liu, N. Dekker, B. Rietveld, B. De Haart, and F. Tietz, "Solid oxide fuel cell performance under severe operating conditions," *Fuel Cells*, vol. 6, no. 2, pp. 130–136, 2006.

[127] A. Müller, A. Weber, H. J. Beie, A. Krügel, D. Gerthsen, and E. Ivers-Tiffée, "Influence of current density and fuel utilization on the degradation of the anode," in *Proc. of 3rd European Solid Oxide Fuel Cell Forum*, pp. 353–362, 1998.

[128] M. Santarelli, F. Quesito, V. Novaresio, C. Guerra, A. Lanzini, and D. Beretta, "Direct reforming of biogas on Ni-based SOFC anodes: Modelling of heterogeneous reactions and validation with experiments," *Journal of Power Sources*, vol. 242, pp. 405–414, 2013.

[129] A. Baldinelli, L. Barelli, and G. Bidini, "Performance characterization and modelling of syngas-fed SOFCs (solid oxide fuel cells) varying fuel composition," *Energy*, vol. 90, pp. 2070–2084, 2015.

[130] F. Zhao and A. V. Virkar, "Dependence of polarization in anode-supported solid oxide fuel cells on various cell parameters," *Journal of power sources*, vol. 141, no. 1, pp. 79–95, 2005.

[131] M. Ni, "Modeling of SOFC running on partially pre-reformed gas mixture," *International journal of hydrogen energy*, vol. 37, no. 2, pp. 1731–1745, 2012.

[132] M. Fardadi, D. F. McLarty, and F. Jabbari, "Investigation of thermal control for different SOFC flow geometries," *Applied Energy*, vol. 178, pp. 43–55, 2016.

[133] S. Campanari and P. Iora, "Comparison of finite volume SOFC models for the simulation of a planar cell geometry," *Fuel Cells*, vol. 5, no. 1, pp. 34–51, 2005.

[134] T. Choudhary *et al.*, "Computational analysis of IR-SOFC: Thermodynamic, electrochemical process and flow configuration dependency," *International Journal of Hydrogen Energy*, vol. 41, no. 2, pp. 1259–1271, 2016.

[135] V. Chiodo, A. Galvagno, A. Lanzini, D. Papurello, F. Urbani, M. Santarelli, and S. Freni, "Biogas reforming process investigation for SOFC application," *Energy Conversion and Management*, vol. 98, pp. 252–258, 2015.

[136] Y. Shiratori, T. Ijichi, T. Oshima, and K. Sasaki, "Internal reforming SOFC running on biogas," *International Journal of Hydrogen Energy*, vol. 35, no. 15, pp. 7905–7912, 2010.

[137] A. Lanzini and P. Leone, "Experimental investigation of direct internal reforming of biogas in solid oxide fuel cells," *International Journal of Hydrogen Energy*, vol. 35, no. 6, pp. 2463–2476, 2010.

[138] F. Manenti, R. Pelosato, P. Vallevi, A. R. Leon-Garzon, G. Dotelli, A. Vita, M. L. Faro, G. Maggio, L. Pino, and A. S. Aricò, "Biogas-fed solid oxide fuel cell (SOFC) coupled to tri-reforming process: Modelling and simulation," *International Journal of Hydrogen Energy*, vol. 40, no. 42, pp. 14640–14650, 2015.

[139] H.-S. Roh and K.-W. Jun, "Low temperature methane steam reforming for hydrogen production for fuel cells," *Bulletin of the Korean Chemical Society*, vol. 30, no. 1, pp. 153–156, 2009.

[140] M. L. Faro, S. Trocino, S. Zignani, V. Antonucci, and A. Aricò, "Production of syngas by solid oxide electrolysis: A case study," *International Journal of Hydrogen Energy*, July 2017.

[141] N. Nakagawa, H. Sagara, and K. Kato, "Catalytic activity of Ni-YSZ-CeO2 anode for the steam reforming of methane in a direct internal-reforming solid oxide fuel cell," *Journal of Power Sources*, vol. 92, no. 1, pp. 88–94, 2001.

[142] G. Brus, R. Nowak, J. S. Szmyd, Y. Komatsu, and S. Kimijima, "An experimental and theoretical approach for the carbon deposition problem during steam reforming of model biogas," *Journal of Theoretical and Applied Mechanics*, vol. 53, no. 2, pp. 273–284, 2015.

[143] T. Takeguchi, Y. Kani, T. Yano, R. Kikuchi, K. Eguchi, K. Tsujimoto, Y. Uchida, A. Ueno, K. Omoshiki, and M. Aizawa, "Study on steam reforming of CH4 and C2 hydrocarbons and carbon deposition on Ni-YSZ cermets," *Journal of Power Sources*, vol. 112, no. 2, pp. 588–595, 2002.

[144] J.-H. Koh, Y.-S. Yoo, J.-W. Park, and H. C. Lim, "Carbon deposition and cell performance of Ni-YSZ anode support SOFC with methane fuel," *Solid State Ionics*, vol. 149, no. 3-4, pp. 157–166, 2002.

[145] V. Alzate-Restrepo and J. M. Hill, "Effect of anodic polarization on carbon deposition on Ni/YSZ anodes exposed to methane," *Applied Catalysis A: General*, vol. 342, no. 1-2, pp. 49–55, 2008.

[146] Z. Chen, L. Bian, L. Wang, N. Chen, H. Zhao, F. Li, and K. Chou, "Effect of hydrogen and carbon dioxide on the performance of methane fueled solid oxide fuel cell," *International Journal of Hydrogen Energy*, vol. 41, no. 18, pp. 7453–7463, 2016.

[147] A. Weber, B. Sauer, A. C. Müller, D. Herbstritt, and E. Ivers-Tiffée, "Oxidation of H2, CO and methane in SOFCs with Ni/YSZ-cermet anodes," *Solid State Ionics*, vol. 152, pp. 543–550, 2002.

[148] A. M. Sukeshini, B. Habibzadeh, B. P. Becker, C. A. Stoltz, B. W. Eichhorn, and G. S. Jackson, "Electrochemical oxidation of H2, CO, and CO/ H2 mixtures on patterned Ni anodes on YSZ electrolytes," *Journal of the Electrochemical Society*, vol. 153, no. 4, pp. A705–A715, 2006.

[149] Y. Matsuzaki and I. Yasuda, "Electrochemical oxidation of H2 and CO in a H2-H2O-CO-CO2 system at the interface of a Ni-YSZ cermet electrode and YSZ electrolyte," *Journal of the Electrochemical Society*, vol. 147, no. 5, pp. 1630–1635, 2000.

[150] J. Hanna, W. Y. Lee, Y. Shi, and A. Ghoniem, "Fundamentals of electro-and thermochemistry in the anode of solid-oxide fuel cells with hydrocarbon and syngas fuels," *Progress in Energy and Combustion Science*, vol. 40, pp. 74–111, 2014.

[151] B. Steele, I. Kelly, H. Middleton, and R. Rudkin, "Oxidation of methane in solid state electrochemical reactors," *Solid State Ionics*, vol. 28, pp. 1547–1552, 1988.

[152] S. Park, R. Craciun, J. M. Vohs, and R. J. Gorte, "Direct oxidation of hydrocarbons in a solid oxide fuel cell: I. methane oxidation," *Journal of the Electrochemical Society*, vol. 146, no. 10, pp. 3603–3605, 1999.

[153] S. Park, J. M. Vohs, and R. J. Gorte, "Direct oxidation of hydrocarbons in a solid-oxide fuel cell," *Nature*, vol. 404, no. 6775, p. 265, 2000.

[154] E. P. Murray, T. Tsai, and S. Barnett, "A direct-methane fuel cell with a ceria-based anode," *Nature*, vol. 400, no. 6745, pp. 649–651, 1999.

[155] W. Guan, H. Zhai, L. Jin, C. Xu, and W. Wang, "Temperature measurement and distribution inside planar SOFC stacks," *Fuel cells*, vol. 12, no. 1, pp. 24–31, 2012.

[156] W. Yao, *Hydrogen and carbon monoxide electrochemical oxidation reaction kinetics on solid oxide fuel cell anodes*. PhD thesis, 2013.

[157] H. Ö. Sigurdsson and S. K. Kær, "Steam reforming of methane over Pt/Rh based wire mesh catalyst in single channel reformer for small scale syngas production," in *ECOS 2012International Conference on Efficiency, Cost, Optimization, Simulation and Environmental Impact of Energy Systems*, pp. 1–10, Firenze University Press, 2012.

[158] H. Sumi, Y.-H. Lee, H. Muroyama, T. Matsui, and K. Eguchi, "Comparison between internal steam and CO2 reforming of methane for Ni-YSZ and Ni-ScSZ SOFC anodes," *Journal of The Electrochemical Society*, vol. 157, no. 8, pp. B1118–B1125, 2010.

[159] H. Aslannejad, L. Barelli, A. Babaie, and S. Bozorgmehri, "Effect of air addition to methane on performance stability and coking over NiO-YSZ anodes of SOFC," *Applied Energy*, vol. 177, pp. 179–186, 2016.

[160] E. S. Hecht, G. K. Gupta, H. Zhu, A. M. Dean, R. J. Kee, L. Maier, and O. Deutschmann, "Methane reforming kinetics within a Ni-YSZ SOFC anode support," *Applied Catalysis A: General*, vol. 295, no. 1, pp. 40–51, 2005.

[161] Z. Jiao, A. Ueno, and N. Shikazono, "Study on the correlation between solid oxide fuel cell Ni-YSZ anode performance and reduction temperature," in *Journal of Physics: Conference Series*, vol. 745, p. 32146, IOP Publishing, 2016.

[162] D. L. King, J. J. Strohm, X. Wang, H.-S. Roh, C. Wang, Y.-H. Chin, Y. Wang, Y. Lin, R. Rozmiarek, and P. Singh, "Effect of nickel microstructure on methane steam-reforming activity of Ni-YSZ cermet anode catalyst," *journal of Catalysis*, vol. 258, no. 2, pp. 356–365, 2008.

[163] H. Yokokawa, H. Tu, B. Iwanschitz, and A. Mai, "Fundamental mechanisms limiting solid oxide fuel cell durability," *Journal of Power Sources*, vol. 182, no. 2, pp. 400–412, 2008.

[164] T. Horita, K. Yamaji, T. Kato, H. Kishimoto, Y. Xiong, N. Sakai, M. E. Brito, and H. Yokokawa, "Imaging of CH4 decomposition around the Ni/YSZ interfaces under anodic polarization," *Journal of power sources*, vol. 145, no. 2, pp. 133–138, 2005.

[165] Y. Lin, Z. Zhan, J. Liu, and S. A. Barnett, "Direct operation of solid oxide fuel cells with methane fuel," *Solid State Ionics*, vol. 176, no. 23, pp. 1827–1835, 2005.

[166] L. Lei, J. M. Keels, Z. Tao, J. Zhang, and F. Chen, "Thermodynamic and experimental assessment of proton conducting solid oxide fuel cells with internal methane steam reforming," *Applied Energy*, vol. 224, pp. 280–288, 2018.

[167] M. Pillai, Y. Lin, H. Zhu, R. J. Kee, and S. A. Barnett, "Stability and coking of direct-methane solid oxide fuel cells: Effect of CO2 and air additions," *Journal of power sources*, vol. 195, no. 1, pp. 271–279, 2010.

[168] V. Menon, A. Banerjee, J. Dailly, and O. Deutschmann, "Numerical analysis of mass and heat transport in proton-conducting SOFCs with direct internal reforming," *Applied Energy*, vol. 149, pp. 161–175, 2015.

[169] M. Hanasaki, C. Uryu, T. Daio, T. Kawabata, Y. Tachikawa, S. Lyth, Y. Shiratori, S. Taniguchi, and K. Sasaki, "SOFC durability against standby and shutdown cycling," *Journal of The Electrochemical Society*, vol. 161, no. 9, pp. F850–F860, 2014.

[170] M. Andersson, J. Yuan, and B. Sundén, "SOFC modeling considering electrochemical reactions at the active three phase boundaries," *International journal of heat and mass transfer*, vol. 55, no. 4, pp. 773–788, 2012.

[171] Y. Shiratori, T. Oshima, and K. Sasaki, "Feasibility of direct-biogas SOFC," *International Journal of Hydrogen Energy*, vol. 33, no. 21, pp. 6316–6321, 2008.

[172] K. Park, S. Yu, J. Bae, H. Kim, and Y. Ko, "Fast performance degradation of sofc caused by cathode delamination in long-term testing," *International Journal of Hydrogen Energy*, vol. 35, no. 16, pp. 8670–8677, 2010.

[173] Y.-H. Lee, H. Muroyama, T. Matsui, and K. Eguchi, "Degradation of nickel-yttria-stabilized zirconia anode in solid oxide fuel cells under changing temperature and humidity conditions," *Journal of Power Sources*, vol. 262, pp. 451–456, 2014.

[174] A. Hagen, K. Neufeld, and Y.-L. Liu, "Effect of humidity in air on performance and long-term durability of SOFCs," *Journal of The Electrochemical Society*, vol. 157, no. 10, pp. B1343–B1348, 2010.

[175] P. Pianko-Oprych, T. Zinko, and Z. Jaworski, "CFD modelling of hydrogen starvation conditions in a planar solid oxide fuel cell," *Polish Journal of Chemical Technology*, vol. 19, no. 2, pp. 16–25, 2017.

[176] Y. Tao, J. Shao, W. G. Wang, and J. Wang, "Optimisation and evaluation of La0.6Sr0.4CoO3-δ cathode for intermediate temperature solid oxide fuel cells," *Fuel Cells*, vol. 9, no. 5, pp. 679–683, 2009.

[177] A. Hagen, R. Barfod, P. Vang Hendriksen, Y.-L. Liu, and S. Ramousse, "Degradation of anode supported SOFCs as a function of temperature and current load," *Journal of The Electrochemical Society*, vol. 153, no. 6, pp. A1165–A1171, 2006.

[178] B. Lin, Y. Shi, and N. Cai, "Numerical simulation of cell-to-cell performance variation within a syngas-fuelled planar solid oxide fuel cell stack," *Applied Thermal Engineering*, vol. 114, pp. 653–662, 2017.

[179] F. Ramadhani, M. Hussain, H. Mokhlis, and S. Hajimolana, "Optimization strategies for Solid Oxide Fuel Cell (SOFC) application: A literature survey," *Renewable and Sustainable Energy Reviews*, vol. 76, pp. 460–484, 2017.

[180] M. Hussain, X. Li, and I. Dincer, "Mathematical modeling of transport phenomena in porous SOFC anodes," *International Journal of Thermal Sciences*, vol. 46, no. 1, pp. 48–56, 2007.

[181] J. Yuan, Y. Huang, B. Sundén, and W. G. Wang, "Analysis of parameter effects on chemical reaction coupled transport phenomena in SOFC anodes," *Heat and Mass Transfer*, vol. 45, no. 4, pp. 471–484, 2009.

[182] R. Suwanwarangkul, E. Croiset, M. Fowler, P. Douglas, E. Entchev, and M. Douglas, "Performance comparison of Ficks, dusty-gas and Stefan-Maxwell models to predict the concentration overpotential of a SOFC anode," *Journal of Power Sources*, vol. 122, no. 1, pp. 9–18, 2003.

[183] B. Haberman and J. Young, "Three-dimensional simulation of chemically reacting gas flows in the porous support structure of an integrated-planar solid oxide fuel cell," *International Journal of Heat and Mass Transfer*, vol. 47, no. 17-18, pp. 3617–3629, 2004.

[184] K. Tseronis, I. Kookos, and C. Theodoropoulos, "Modelling mass transport in solid oxide fuel cell anodes: a case for a multidimensional dusty gas-based model," *Chemical Engineering Science*, vol. 63, no. 23, pp. 5626–5638, 2008.

[185] H. Yakabe, M. Hishinuma, M. Uratani, Y. Matsuzaki, and I. Yasuda, "Evaluation and modeling of performance of anode-supported solid oxide fuel cell," *Journal of Power Sources*, vol. 86, no. 1-2, pp. 423–431, 2000.

[186] R. Bove and S. Ubertini, "Modeling solid oxide fuel cell operation: Approaches, techniques and results," *Journal of Power Sources*, vol. 159, no. 1, pp. 543–559, 2006.

[187] Z. Qu, *Simulation and analysis of an anode-supported solid oxide fuel cell and stack*. PhD thesis, TU Delft, Delft University of Technology, 2011.

[188] Y. Shi, N. Cai, C. Li, C. Bao, E. Croiset, J. Qian, Q. Hu, and S. Wang, "Modeling of an anode-supported Ni–YSZ— Ni–ScSZ— ScSZ— LSM–ScSZ multiple layers SOFC cell: Part I. experiments, model development and validation," *Journal of Power Sources*, vol. 172, no. 1, pp. 235–245, 2007.

[189] M. Xu, T. S. Li, M. Yang, M. Andersson, I. Fransson, T. Larsson, and B. Sundén, "Modeling of an anode supported solid oxide fuel cell focusing on thermal stresses," *International Journal of Hydrogen Energy*, vol. 41, no. 33, pp. 14927–14940, 2016.

[190] H. Paradis, M. Andersson, J. Yuan, and B. Sundén, "CFD modeling: different kinetic approaches for internal reforming reactions in an anode-supported SOFC," *Journal of Fuel Cell Science and Technology*, vol. 8, no. 3, p. 031014, 2011.

[191] A. V. Akkaya, "Electrochemical model for performance analysis of a tubular SOFC," *International Journal of Energy Research*, vol. 31, no. 1, pp. 79–98, 2007.

[192] A. F. Massardo and F. Lubelli, "Internal reforming solid oxide fuel cell-gas turbine combined cycles (IRSOFC-GT): Part A- cell model and cycle thermodynamic analysis," *Journal of Engineering for Gas Turbines and Power*, vol. 122, pp. 27–35, October 2000.

[193] S. Chan, K. Khor, and Z. Xia, "A complete polarization model of a solid oxide fuel cell and its sensitivity to the change of cell component thickness," *Journal of Power Sources*, vol. 93, no. 1, pp. 130–140, 2001.

[194] P. Hofmann, K. Panopoulos, L. Fryda, and E. Kakaras, "Comparison between two methane reforming models applied to a quasi-two-dimensional planar solid oxide fuel cell model," *Energy*, vol. 34, no. 12, pp. 2151–2157, 2009.

[195] T. W. Song, J. L. Sohn, J. H. Kim, T. S. Kim, S. T. Ro, and K. Suzuki, "Performance analysis of a tubular solid oxide fuel cell/micro gas turbine hybrid power system based on a quasi-two dimensional model," *Journal of Power Sources*, vol. 142, no. 1, pp. 30–42, 2005.

[196] K. Tseronis, I. S. Fragkopoulos, I. Bonis, and C. Theodoropoulos, "Detailed multi-dimensional modeling of direct internal reforming solid oxide fuel cells," *Fuel Cells*, vol. 16, no. 3, pp. 294–312, 2016.

[197] A. Amiri, P. Vijay, M. O. Tadé, K. Ahmed, G. D. Ingram, V. Pareek, and R. Utikar, "Planar SOFC system modelling and simulation including a 3D stack module," *International Journal of Hydrogen Energy*, vol. 41, no. 4, pp. 2919–2930, 2016.

[198] C. Schluckner, V. Subotić, V. Lawlor, and C. Hochenauer, "Three-dimensional numerical and experimental investigation of an industrial-sized SOFC fueled by diesel reformat-Part II: Detailed reforming chemistry and carbon deposition analysis," *International Journal of Hydrogen Energy*, vol. 40, no. 34, pp. 10943–10959, 2015.

[199] J. Yuan and B. Sundén, "Analysis of chemically reacting transport phenomena in an anode duct of intermediate temperature SOFCs," *Journal of fuel cell science and technology*, vol. 3, no. 2, pp. 89–98, 2006.

[200] A. Pramuanjaroenkij, S. Kakaç, and X. Y. Zhou, "Mathematical analysis of planar solid oxide fuel cells," in *Mini-Micro Fuel Cells*, pp. 359–390, Springer, 2008.

[201] K. Tseronis, I. Kookos, and K. Theodoropoulos, "Modelling and design of the solid oxide fuel cell anode," in *COMSOL users conference Birmingham*, 2006.

[202] P. Aguiar, C. Adjiman, and N. P. Brandon, "Anode-supported intermediate temperature direct internal reforming solid oxide fuel cell. I: model-based steady-state performance," *Journal of Power Sources*, vol. 138, no. 1, pp. 120–136, 2004.

[203] S. Chan, C. Low, and O. Ding, "Energy and exergy analysis of simple solid-oxide fuel-cell power systems," *Journal of Power Sources*, vol. 103, no. 2, pp. 188–200, 2002.

[204] V. A. Chakravarthula, R. A. Roberts, and M. Wolff, "Dynamic Model of Solid Oxide Fuel Cell Integrated with Fan and Exhaust Nozzle," in *14th International Energy Conversion Engineering Conference*, p. 4718, 2016.

[205] L. Barelli, G. Bidini, and A. Ottaviano, "Solid oxide fuel cell modelling: Electrochemical performance and thermal management during load-following operation," *Energy*, vol. 115, pp. 107–119, 2016.

[206] W. Bi, D. Chen, and Z. Lin, "A key geometric parameter for the flow uniformity in planar solid oxide fuel cell stacks," *international journal of hydrogen energy*, vol. 34, no. 9, pp. 3873–3884, 2009.

[207] M. Andersson, J. Yuan, B. Sundén, T. S. Li, and W. G. Wang, "Modeling validation and simulation of an anode supported SOFC including mass and heat transport, fluid flow and chemical reactions," in *ASME 2011 9th International Conference on Fuel Cell Science, Engineering and Technology collocated with ASME 2011 5th International Conference on Energy Sustainability*, pp. 317–327, American Society of Mechanical Engineers, 2011.

[208] E. Guk, J.-S. Kim, M. Ranaweera, V. Venkatesan, and L. Jackson, "In-situ monitoring of temperature distribution in operating solid oxide fuel cell cathode using proprietary sensory techniques versus commercial thermocouples," *Applied Energy*, vol. 230, pp. 551–562, 2018.

[209] D. L. Damm and A. G. Fedorov, "Local thermal non-equilibrium effects in porous electrodes of the hydrogen-fueled SOFC," *Journal of Power Sources*, vol. 159, no. 2, pp. 1153–1157, 2006.

[210] Y. Fu, Y. Jiang, S. Poizeau, A. Dutta, A. Mohanram, J. D. Pietras, and M. Z. Bazant, "Multicomponent gas diffusion in porous electrodes," *Journal of The Electrochemical Society*, vol. 162, no. 6, pp. F613–F621, 2015.

[211] F. Priyakorn, N. Laosiripojana, and S. Assabumrungrat, "Modeling of solid oxide fuel cell with internal reforming operation fueled by natural gas," *gas*, vol. 11, p. 2, 2011.

[212] V. M. Janardhanan and O. Deutschmann, "CFD analysis of a solid oxide fuel cell with internal reforming: Coupled interactions of transport, heterogeneous catalysis and electrochemical processes," *Journal of Power Sources*, vol. 162, no. 2, pp. 1192–1202, 2006.

[213] P. Ivanov, "Thermodynamic modeling of the power plant based on the SOFC with internal steam reforming of methane," *Electrochimica acta*, vol. 52, no. 12, pp. 3921–3928, 2007.

[214] J. H. Nam and D. H. Jeon, "A comprehensive micro-scale model for transport and reaction in intermediate temperature solid oxide fuel cells," *Electrochimica Acta*, vol. 51, no. 17, pp. 3446–3460, 2006.

[215] J. Shi and X. Xue, "CFD analysis of a symmetrical planar SOFC with heterogeneous electrode properties," *Electrochimica Acta*, vol. 55, no. 18, pp. 5263–5273, 2010.

[216] M. Ni, M. K. Leung, and D. Y. Leung, "Micro-scale modelling of solid oxide fuel cells with micro-structurally graded electrodes," *Journal of Power Sources*, vol. 168, no. 2, pp. 369–378, 2007.

[217] Y. Shi, N. Cai, and C. Li, "Numerical modeling of an anode-supported SOFC button cell considering anodic surface diffusion," *Journal of Power Sources*, vol. 164, no. 2, pp. 639–648, 2007.

[218] D. Kanno, N. Shikazono, N. Takagi, K. Matsuzaki, and N. Kasagi, "Evaluation of SOFC anode polarization simulation using three-dimensional microstructures reconstructed by FIB tomography," *Electrochimica Acta*, vol. 56, no. 11, pp. 4015–4021, 2011.

[219] H. Iwai, N. Shikazono, T. Matsui, H. Teshima, M. Kishimoto, R. Kishida, D. Hayashi, K. Matsuzaki, D. Kanno, M. Saito, *et al.*, "Quantification of SOFC anode microstructure based on dual beam FIB-SEM technique," *Journal of Power Sources*, vol. 195, no. 4, pp. 955–961, 2010.

[220] V. M. Janardhanan, V. Heuveline, and O. Deutschmann, "Performance analysis of a SOFC under direct internal reforming conditions," *Journal of Power Sources*, vol. 172, no. 1, pp. 296–307, 2007.

[221] D. Sanchez, R. Chacartegui, A. Munoz, and T. Sanchez, "On the effect of methane internal reforming modelling in solid oxide fuel cells," *International Journal of Hydrogen Energy*, vol. 33, no. 7, pp. 1834–1844, 2008.

[222] R. Suwanwarangkul, E. Croiset, E. Entchev, S. Charojrochkul, M. Pritzker, M. Fowler, P. Douglas, S. Chewathanakup, and H. Mahaudom, "Experimental and modeling study of solid oxide fuel cell operating with syngas fuel," *Journal of Power Sources*, vol. 161, no. 1, pp. 308–322, 2006.

[223] E. Hernández-Pacheco, D. Singh, P. N. Hutton, N. Patel, and M. D. Mann, "A macro-level model for determining the performance characteristics of solid oxide fuel cells," *Journal of Power Sources*, vol. 138, no. 1, pp. 174–186, 2004.

[224] D. S. Monder, V. G. Polisetty, P. V. Jampana, and V. M. Janardhanan, "A distributed parameter model for a solid oxide fuel cell: simulating realistic operating conditions," *IFAC-PapersOnLine*, vol. 48, no. 8, pp. 734–739, 2015.

[225] F. Elizalde-Blancas, S. Pakalapati, F. Cayan, C. Xu, I. Celik, H. Finklea, and J. Zondlo, "A full 3D computational model for SOFC running on syngas," *Submitted to Journal of Fuel Cell Science and Technology*, 2009.

[226] Y. Patcharavorachot, A. Arpornwichanop, and A. Chuachuensuk, "Electrochemical study of a planar solid oxide fuel cell: Role of support structures," *Journal of Power Sources*, vol. 177, no. 2, pp. 254–261, 2008.

[227] W. G. Bessler, M. Vogler, H. Störmer, D. Gerthsen, A. Utz, A. Weber, and E. Ivers-Tiffée, "Model anodes and anode models for understanding the mechanism of hydrogen oxidation in solid oxide fuel cells," *Physical Chemistry Chemical Physics*, vol. 12, no. 42, pp. 13888–13903, 2010.

[228] W. G. Bessler, S. Gewies, and M. Vogler, "A new framework for physically based modeling of solid oxide fuel cells," *Electrochimica Acta*, vol. 53, no. 4, pp. 1782–1800, 2007.

[229] M. Ni, D. Y. Leung, and M. K. Leung, "Modeling of methane fed solid oxide fuel cells: comparison between proton conducting electrolyte and oxygen ion conducting electrolyte," *Journal of Power sources*, vol. 183, no. 1, pp. 133–142, 2008.

[230] W. Lehnert, J. Meusinger, and F. Thom, "Modelling of gas transport phenomena in SOFC anodes," *Journal of Power Sources*, vol. 87, no. 1-2, pp. 57–63, 2000.

[231] J.-M. Klein, Y. Bultel, S. Georges, and M. Pons, "Modeling of a SOFC fuelled by methane: From direct internal reforming to gradual internal reforming," *Chemical Engineering Science*, vol. 62, no. 6, pp. 1636–1649, 2007.

[232] F. P. Nagel, T. J. Schildhauer, S. M. Biollaz, and S. Stucki, "Charge, mass and heat transfer interactions in solid oxide fuel cells operated with different fuel gases-a sensitivity analysis," *Journal of Power Sources*, vol. 184, no. 1, pp. 129–142, 2008.

[233] L. Wang, H. Zhang, and S. Weng, "Modeling and simulation of solid oxide fuel cell based on the volume-resistance characteristic modeling technique," *Journal of Power Sources*, vol. 177, no. 2, pp. 579–589, 2008.

[234] J.-M. Klein, M. Hénault, C. Roux, Y. Bultel, and S. Georges, "Direct methane solid oxide fuel cell working by gradual internal steam reforming: Analysis of operation," *Journal of Power Sources*, vol. 193, no. 1, pp. 331–337, 2009.

[235] H. Zhu, R. J. Kee, V. M. Janardhanan, O. Deutschmann, and D. G. Goodwin, "Modeling elementary heterogeneous chemistry and electrochemistry in solid-oxide fuel cells," *Journal of the electrochemical society*, vol. 152, no. 12, pp. A2427–A2440, 2005.

[236] E. Vakouftsi, G. Marnellos, C. Athanasiou, and F. Coutelieris, "CFD modeling of a biogas fuelled SOFC," *Solid State Ionics*, vol. 192, no. 1, pp. 458–463, 2011.

[237] P. Aguiar, C. Adjiman, and N. Brandon, "Anode-supported intermediate-temperature direct internal reforming solid oxide fuel cell: II. Model-based dynamic performance and control," *Journal of Power Sources*, vol. 147, no. 1, pp. 136–147, 2005.

[238] R. Torii, Y. Tachikawa, K. Sasaki, and K. Ito, "Anode gas recirculation for improving the performance and cost of a 5-kW solid oxide fuel cell system," *Journal of Power Sources*, vol. 325, pp. 229–237, 2016.

[239] A. Lasia, "Electrochemical impedance spectroscopy and its applications," in *Modern aspects of electrochemistry*, pp. 143–248, Springer, 2002.

[240] Q.-A. Huang, R. Hui, B. Wang, and J. Zhang, "A review of AC impedance modeling and validation in SOFC diagnosis," *Electrochimica Acta*, vol. 52, no. 28, pp. 8144–8164, 2007.

[241] J. Nielsen and J. Hjelm, "Impedance of SOFC electrodes: A review and a comprehensive case study on the impedance of LSM: YSZ cathodes," *Electrochimica Acta*, vol. 115, pp. 31–45, 2014.

[242] D. Klotz, *Characterization and modeling of electrochemical energy conversion systems by impedance techniques*. KIT Scientific Publishing, 2014.

[243] M. C. Williams *et al.*, "Fuel cell handbook," *EG&G Technical Services, National Energy Technology Laboratory, US Department of Energy*, 2004.

[244] S. C. Singhal and K. Kendall, *High-temperature solid oxide fuel cells: fundamentals, design and applications*. Elsevier, 2003.

[245] July 2018.

[246] B. A. Boukamp, "A linear Kronig-Kramers transform test for immittance data validation," *Journal of the electrochemical society*, vol. 142, no. 6, pp. 1885–1894, 1995.

[247] "Gas chromatography," July 2018.

[248] 2017.

[249] "SEM analysis," July 2018.

[250] "Analysis via scanning electron microscopy / energy dispersive x-ray spectroscopy (SEM/EDS)," July 2018.

[251] B. Hafner, "Energy Dispersive Spectroscopy on the SEM," *Characterization Facility, University of Minnesota, USA*, 2011.

[252] R. Peters, R. Deja, L. Blum, J. Pennanen, J. Kiviaho, and T. Hakala, "Analysis of solid oxide fuel cell system concepts with anode recycling," *International Journal of hydrogen energy*, vol. 38, no. 16, pp. 6809–6820, 2013.

[253] M. Engelbracht, R. Peters, L. Blum, and D. Stolten, "Analysis of a solid oxide fuel cell system with low temperature anode off-gas recirculation," *Journal of The Electrochemical Society*, vol. 162, no. 9, pp. F982–F987, 2015.

[254] R. Peters, R. Deja, M. Engelbracht, M. Frank, V. N. Nguyen, L. Blum, and D. Stolten, "Efficiency analysis of a hydrogen-fueled solid oxide fuel cell system with anode off-gas recirculation," *Journal of Power Sources*, vol. 328, pp. 105–113, 2016.

[255] C. Willich, "Local characterisation of solid oxide fuel cells," 2012.

[256] D. M. Silva-Mosqueda, F. Elizalde-Blancas, D. Pumiglia, F. Santoni, C. Boigues-Muñoz, and S. J. McPhail, "Intermediate temperature solid oxide fuel cell under internal reforming: Critical operating conditions, associated problems and their impact on the performance," *Applied Energy*, vol. 235, pp. 625–640, 2019.

[257] H. Miao, W. G. Wang, T. S. Li, T. Chen, S. S. Sun, and C. Xu, "Effects of coal syngas major compositions on Ni/YSZ anode-supported solid oxide fuel cells," *Journal of Power Sources*, vol. 195, no. 8, pp. 2230–2235, 2010.

[258] F. Elizalde-Blancas, *Modeling issues for solid oxide fuel cells operating with coal syngas*. PhD thesis, West Virginia University, 2009.

[259] H. Zhu, A. Kromp, A. Leonide, E. Ivers-Tiffée, O. Deutschmann, and R. J. Kee, "A model-based interpretation of the influence of anode surface chemistry on solid oxide fuel cell electrochemical impedance spectra," *Journal of The Electrochemical Society*, vol. 159, no. 7, pp. F255–F266, 2012.

[260] M. Boaro and A. S. Aricò, *Advances in medium and high temperature solid oxide fuel cell technology*, vol. 574. Springer, 2017.

[261] V. Sonn, A. Leonide, and E. Ivers-Tiffée, "Combined deconvolution and CNLS fitting approach applied on the impedance response of technical Ni/ 8YSZ cermet electrodes," *Journal of The Electrochemical Society*, vol. 155, no. 7, pp. B675–B679, 2008.

[262] A. Bertei, G. Arcolini, J. Ouweltjes, Z. Wuillemin, P. Piccardo, and C. Nicolella, "Physically-based deconvolution of impedance spectra: interpretation, fitting and validation of a numerical model for lanthanum strontium cobalt ferrite-based solid oxide fuel cells," *Electrochimica Acta*, vol. 208, pp. 129–141, 2016.

[263] Z. Lyu, W. Shi, and M. Han, "Electrochemical characteristics and carbon tolerance of solid oxide fuel cells with direct internal dry reforming of methane," *Applied energy*, vol. 228, pp. 556–567, 2018.

[264] G. De Lorenzo and P. Fragiacomo, "Energy analysis of an sofc system fed by syngas," *Energy Conversion and Management*, vol. 93, pp. 175–186, 2015.

[265] V. Liso, M. P. Nielsen, and S. K. Kær, "Influence of anodic gas recirculation on solid oxide fuel cells in a micro combined heat and power system," *Sustainable Energy Technologies and Assessments*, vol. 8, pp. 99–108, 2014.

[266] Agilent , "Troubleshooting tips and tricks for your GC analyzer & CFT application," Oct. 2014.

[267] Ö. Aydın, H. Nakajima, and T. Kitahara, "Reliability of the numerical SOFC models for estimating the spatial current and temperature variations," *International Journal of Hydrogen Energy*, vol. 41, no. 34, pp. 15311–15324, 2016.

[268] J.-W. Kim, A. V. Virkar, K.-Z. Fung, K. Mehta, and S. C. Singhal, "Polarization effects in intermediate temperature, anode-supported solid oxide fuel cells," *Journal of the Electrochemical Society*, vol. 146, no. 1, pp. 69–78, 1999.

[269] M. Andersson, H. Paradis, J. Yuan, and B. Sundén, "Three dimensional modeling of an solid oxide fuel cell coupling charge transfer phenomena with transport processes and heat generation," *Electrochimica Acta*, vol. 109, pp. 881–893, 2013.

[270] K. Ahmed and K. Föger, "Analysis of equilibrium and kinetic models of internal reforming on solid oxide fuel cell anodes: Effect on voltage, current and temperature distribution," *Journal of Power Sources*, vol. 343, pp. 83–93, 2017.

[271] A. Hagen, Y.-L. Liu, R. Barfod, and P. V. Hendriksen, "Assessment of the cathode contribution to the degradation of anode-supported solid oxide fuel cells," *Journal of the Electrochemical Society*, vol. 155, no. 10, pp. B1047–B1052, 2008.

[272] Y. L. Liu and C. Jiao, "Microstructure degradation of an anode/electrolyte interface in SOFC studied by transmission electron microscopy," *Solid State Ionics*, vol. 176, no. 5-6, pp. 435–442, 2005.

[273] F. Calise, M. D. dAccadia, A. Palombo, and L. Vanoli, "One-dimensional model of a tubular solid oxide fuel cell," *Journal of Fuel Cell Science and Technology*, vol. 5, no. 2, p. 021014, 2008.

[274] X. Zhang, G. Li, J. Li, and Z. Feng, "Numerical study on electric characteristics of solid oxide fuel cells," *Energy Conversion and Management*, vol. 48, no. 3, pp. 977–989, 2007.

[275] S. Chan, H. Ho, and Y. Tian, "Multi-level modeling of SOFC–gas turbine hybrid system," *International Journal of Hydrogen Energy*, vol. 28, no. 8, pp. 889–900, 2003.

[276] A. Massardo and F. Lubelli, "Internal reforming solid oxide fuel cell-gas turbine combined cycles (IRSOFC-GT): Part ACell model and cycle thermodynamic analysis," in *ASME 1998 International Gas Turbine and Aeroengine Congress and Exhibition*, pp. V003T08A028–V003T08A028, American Society of Mechanical Engineers, 1998.

[277] D. Fairbanks and C. Wilke, "Diffusion coefficients in multicomponent gas mixtures," *Industrial & Engineering Chemistry*, vol. 42, no. 3, pp. 471–475, 1950.

[278] J. Yuan and B. Sundén, "On mechanisms and models of multi-component gas diffusion in porous structures of fuel cell electrodes," *International Journal of Heat and Mass Transfer*, vol. 69, pp. 358–374, 2014.

[279] E. N. Fuller, P. D. Schettler, and J. C. Giddings, "New method for prediction of binary gas-phase diffusion coefficients," *Industrial & Engineering Chemistry*, vol. 58, no. 5, pp. 18–27, 1966.

[280] Ö. Aydin and H. Nakajima, "Concentration gradient of reactants extending from reaction sites inward inlet periphery of fuel cells," *Journal of The Electrochemical Society*, vol. 165, no. 5, pp. F365–F374, 2018.

[281] B. Todd and J. Young, "Thermodynamic and transport properties of gases for use in solid oxide fuel cell modelling," *Journal of power Sources*, vol. 110, no. 1, pp. 186–200, 2002.

Salamanca, Gto., a 2 de Septiembre del 2019.

M. en I. HERIBERTO GUTIÉRREZ MARTIN
JEFE DE LA UNIDAD DE ADMINISTRACIÓN ESCOLAR
P R E S E N T E-

Por medio de la presente, se otorga autorización para proceder a los trámites de impresión, empastado de tesis y titulación al alumno(a) Dulce María Silva Mosqueda del ***Programa de Maestría en*** Ingeniería Mecánica y cuyo número de ***NUA*** es: 387719 del cual soy director. El título de la tesis es: "Experimental Study on the performance of a single SOFC during internal reforming".

Hago constar que he revisado dicho trabajo y he tenido comunicación con los sinodales asignados para la revisión de la tesis, por lo que no hay impedimento alguno para fijar la fecha de examen de titulación.

ATENTAMENTE

Francisco Elizalde Blancas
NOMBRE Y FIRMA
DIRECTOR DE TESIS
SECRETARIO

Stephen J. McPhail
NOMBRE Y FIRMA
DIRECTOR DE TESIS

Sergio Cano Andrade
NOMBRE Y FIRMA
PRESIDENTE

Cesar E. Damián Ascencio
NOMBRE Y FIRMA
VOCAL